Two hole extrusion and the effects of M[subscript g2 Si, Si and Fe on the extrudability of 6xxx series aluminium alloys.

Markides, Christopher Andrew

Two-Hole Extrusion and the Effects of Mg_2Si, Si and Fe on the Extrudability of 6xxx series Aluminium Alloys.

by

Christopher A. Markides

A thesis submitted for the
degree of Doctor of Philosophy
of the University of London

December 1999

Materials Engineering and
Manufacturing Group
King's College, London.

Abstract

The present study deals with the specifics of two-hole extrusion of aluminium 6xxx series alloys, and the effects of alloying additions of Mg, Si and Fe are investigated. Three different dies were designed and made with holes for rod extrusion. The diameters of the holes were 16 and 8, 16 and 6 and 16 and 4 mm. All had a constant die land length of 3mm. A number of remelted AA6063 billets were extruded to varying degrees through the dies to ascertain the characteristics of the extrusion process. Each extrusion yielded varying lengths of material through each die orifice. The length ratio, using identical processing conditions, can be construed to be a measure of the extrudability of the alloy.

A total of 54 special alloys were cast using a standard gravity die technique and three billets of each were extruded – one through each die. The alloys had varying amounts of Mg, Si and Fe and the length ratios, through one of the dies, were used to define the extrudability of each. It was found that although Fe is conventionally considered deleterious to extrusion properties, an increase in extrudability ensues with small additions of Fe.

A novel ageing treatment has been investigated and found to perform better than the conventional treatments used in industry. The process is based on a two-stage treatment to facilitate maximum nucleation and growth rates of the metastable precipitates.

Acknowledgements

I would like to express my sincere thanks to the following for the realisation of this project:

1. BOAL BV. and Deeside Aluminium for supplying the material used.
2. Dr. Michael P. Clode for the initiation and supervision of the project.
3. Dr. Hayder Ahmed and Dr. Min Zhou for their constructive input throughout the study.
4. Mr. K. Nielsen of BOAL BV., Mr. Simon Faulkner and Mr. Barry Price of Deeside Aluminium for their assistance in understanding the industrial applications of the work.
5. For their superb technical advice, Mr. Melvyn Andrews, Mr. Adrian Caden, Mr. Mike Flynn and Mr. Paul Leforte.
6. Members of the Materials Processing Group at the Department of Materials, Imperial College, especially Dr. Leo Christodoulou and Mr. Richard Thackray.
7. Mr. Norman Carr for providing food for thought through stimulating conversation.
8. Mr. T. Ioannou, director of the Cyprus Productivity Centre, for use of the facilities of the centre.
9. My brother, Constantine, for his continuous support and encouragement.
10. Although only my name appears on this thesis, credit must be attributed to Ms. Simoni Ioannou. Thank you for your support and help in realising this work.
11. Last, but by no means least, my parents, Athos and Stella for their undying love and support. This thesis is dedicated to them with all my love.

This thesis is dedicated to the memory of

James Murray

and

Christakis Nicolaou

and to my parents, Athos and Stella,

with all my love

Table of Contents:

List of Figures

List of Tables

Chapter 1

Introduction

1. Introduction:

The aluminium industry is today at one of its most productive and profitable times of its relatively short life, with better yet to come. "It's hard to imagine a better time to be in the aluminium business"[1], the words of Jerry Sheehan, the chairman of Reynolds Metals, one of the world's largest aluminium producers.

The main reason for this, apart from aluminium's classic characteristics - high strength-to-weight ratio, good corrosion resistance, electrical conductivity and ease of fabrication, - is the world's shift towards more environmentally friendly materials and procedures. Aluminium fulfils this category admirably, as it boasts being the most recyclable mass-produced material available on the world market.

Western markets last year accounted for more than half the world's aluminium consumption, as shown in figure 1.1(a), with Japan also taking an impressive 12 % share. Figure 1.1(b) shows how the western world share of consumption is split into the separate end-use industries.

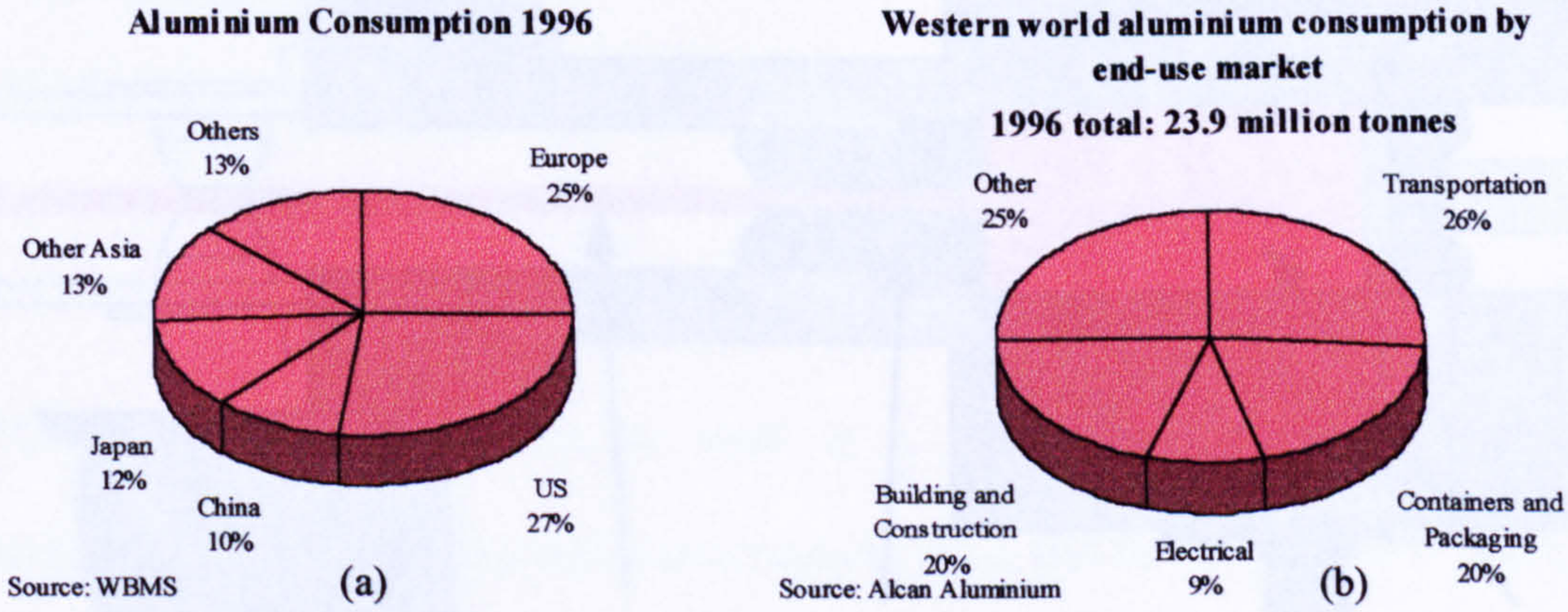

Figure 1.1 Local consumption and end-use markets of aluminium in 1996[1]

The Aluminium Association defines extrusion as: "a deformation process (usually hot) whereby a billet is forced through an orifice in a die by a large compressive force achieving large deformation ratios".

The first patent recorded which may be considered the original extrusion press was in England in 1797 by Bramah. This machine was used "for making pipes of lead or other soft metals of all dimensions and any given length". Molten lead was poured into a container and forced through an orifice by means of a manually operated ram. Cooling was effected at the outlet to aid solidification of the metal.

The pioneer of modern-day extrusion was born in Germany in 1838. In 1894, Alexander Dick applied for and obtained a patent (Pat. no. 83,388) [2] for a hydraulic extrusion press, an outline of which may be seen in figure 1.2. His design incorporates a surprising number of features which may still be seen on today's extrusion rigs.

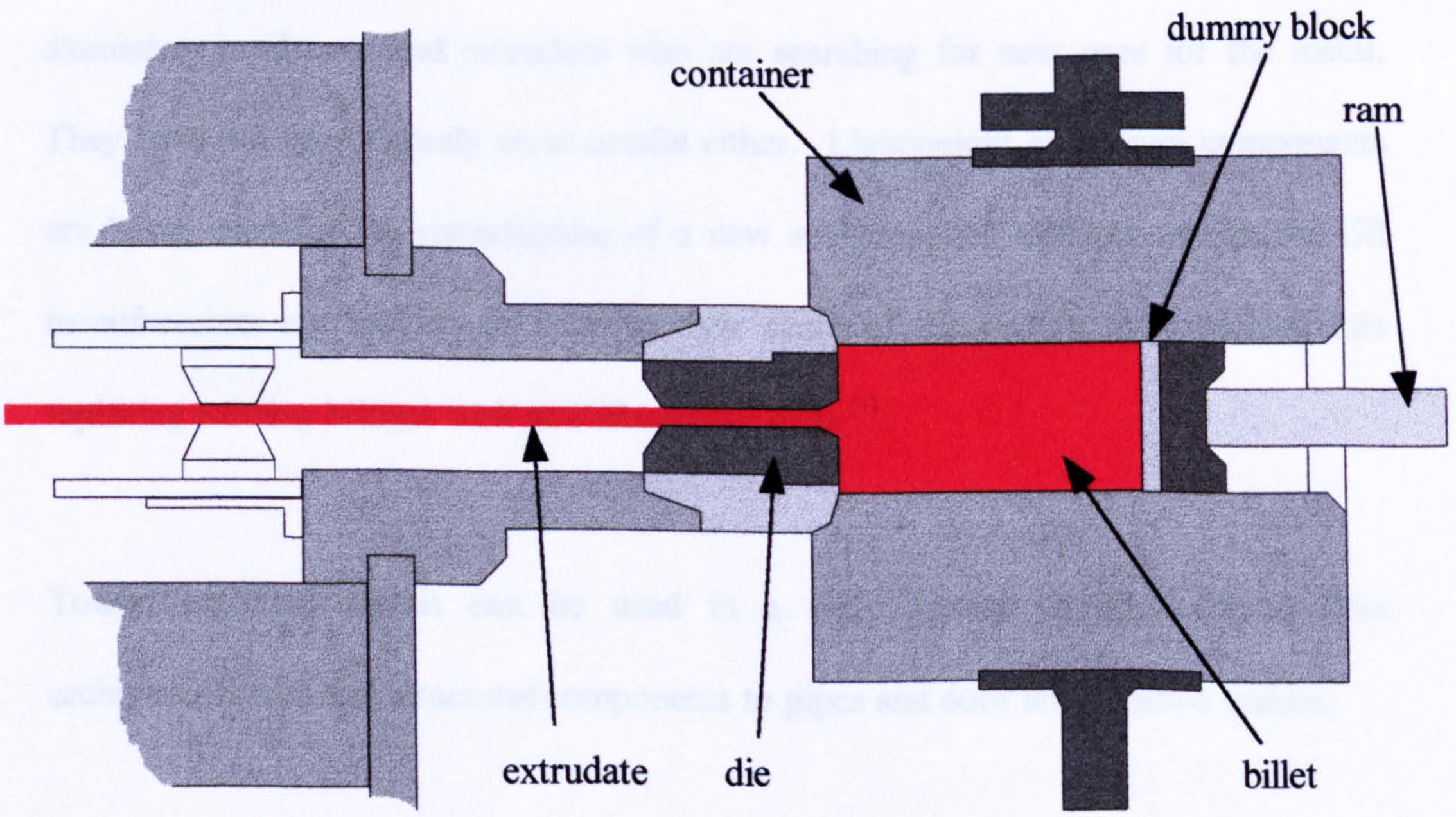

Figure 1.2. Alexander Dick's original Extrusion Press (German Patent No. 83,388) [2]

The two methods of extrusion which are commonly used today are Direct and Indirect extrusion. The former is the most widely, industrially, used of the two mainly because the billet requires little or no tooling in comparison with the more complex tooling required for the latter (which involves pushing the die into the billet instead of the reverse). Indirect extrusion, however, is beginning to find more specific applications relating to hard aluminium alloys and free cutting brass alloys. This is due, mainly, to the lower load required and the slightly more uniform flow patterns yielded when the indirect method is applied.

Aluminium extrusions are mainly utilised in building and construction work, which over the last few years has seen a decline in the proportion of total aluminium consumption used. This is partly due to the increase in the transport and packaging share of the market and partly due to the competition of the more traditional materials in the sector, such as steel and wood. The situation is attempting to be rectified by the aluminium producers and extruders who are searching for new uses for the metal. They have not been entirely unsuccessful either. Lightweight aluminium components are being used for the manufacture of a new self-propelled elevator and in the US manufacturers are looking to improve their share of the market by branching into replacing existing bridges with new aluminium ones [1].

Today, extruded metals can be used in a wide variety of applications; from architectural trim and structural components to pipes and door and window frames.

Chapter 2

Literature Review

Nomenclature – Chapter 2

A''	Constant
A'	Constant
a	Atomic spacing
A	Hot working constant
A_x	Cross-sectional area of specimen
b	Burger's vector
D	Diffusion coefficient
D_0	Diffusivity
D_b	Billet Diameter
D_e	Extrudate diameter
d_s	Subgrain diameter
G	Universal gas constant
G_s	Shear modulus
k	Shear yield stress of material
L	Billet length
m	Strain rate sensitivity
n	Hot working constant
P	Steady state extrusion pressure
R	Extrusion ratio
s	Internal state variable
$\dot{s}$	Variation of internal state variable
s_m	Saturation value of internal state variable
S_p	Interparticle spacing
T	Absolute temperature
t	Time
V	Ram Velocity
V_M	Maximum Possible Ram Velocity
Z	Temperature compensated strain rate
ΔH	Activation energy
Δn_{Mg}	Concentration differential of Mg atoms
Δn_{Mg0}	Concentration differential of Mg atoms when time = 0
α	DMZ angle
α	Hot working constant
ε_r	Relaxation strain constant
$\dot{\varepsilon}$	Strain rate
$\dot{\varepsilon}_{vp}$	Viscoplastic strain rate
μ	Frictional coefficient
ω	Relaxation time
λ	Shape Factor
σ	Mean equivalent flow stress
σ_y	Tensile yield strength
$\bar{\sigma}$	Flow stress
$\bar{\sigma}_s$	Steady state flow stress
$\bar{\sigma}_0$	Initial flow stress
$\bar{\sigma}_{0.1}$	Flow stress at a strain of 0.1

2. Literature Survey:

2.1. Industrial Extrusion:

On an industrial scale the material to be extruded goes through three distinct stages in the process:

Homogenisation: On delivery from the casting plant the aluminium billets are normally inhomogeneous due to the rapid nature of the cooling program during DC casting. This inhomogeneity is manifested in the form of macro- and micro-segregation of certain alloying elements and second phases in the alloy. To alleviate this problem homogenisation is employed, i.e. a long soak at elevated temperatures, which causes the alloying additions to return to solution, followed by a controlled cooling process.

Extrusion: The homogenised billets are, in turn, put through the extrusion press and extruded into the shape required by the customer.

Age Hardening: Because of the high temperatures employed during extrusion microstructural restoration occurs, either in static or dynamic processes. This causes the aluminium product to become soft, thus subsequent hardening is required. Via a low temperature heating procedure, a sequence of metastable particle dispersions are formed which inhibit dislocation motion and strengthen the material.

2.2. Direct-Chill-Casting and non-equilibrium solidification.

Semi-continuous direct chill casting is the most popular casting process for commercial Al alloys, with roots stretching back to the 1940's when rod or narrow strip was successfully continuously cast and coiled [3].

The DC cast process consists of liquid metal forced through pressurised pipes into a mould where it is rapidly cooled. Primary cooling is incurred by the heat conduction through the water cooled mould and secondary cooling which is applied by water jets on the solid shell as it emerges from the mould. The process is shown schematically in figure 2.1. As the liquid freezes, it contracts, creating an air gap between the solid shell and the mould wall. Control of the size of the air gap is important as, if the gap is too deep, and the metal level too high, the primary cooling through the mould wall would be greatly reduced, possibly leading to the shell remelting before secondary cooling can take place. Thus, the risk of surface defects on the casting increases. A continuous flow of lubricant against the mould wall can be applied in order to avoid sticking of the cast shell to the mould wall.

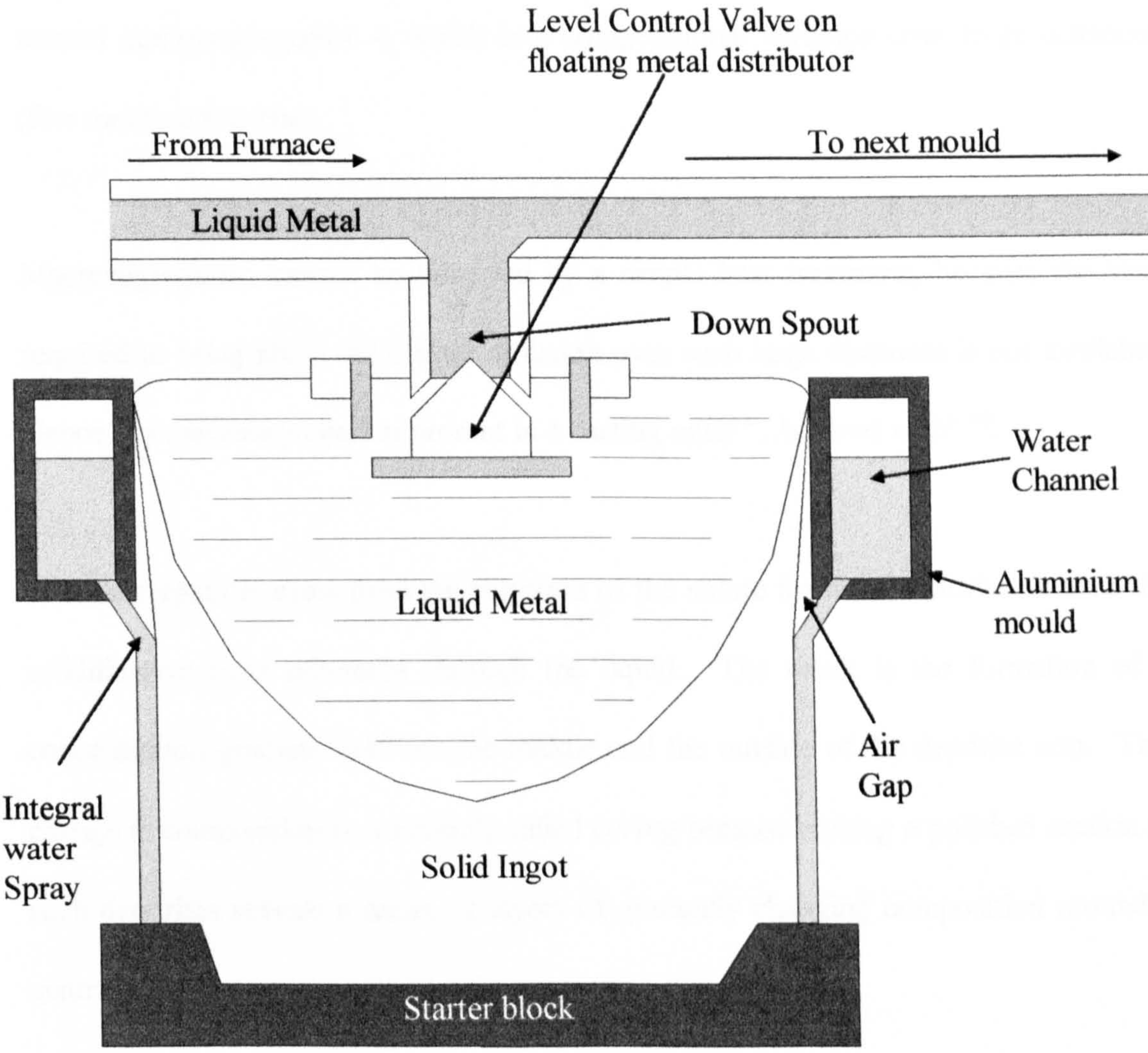

Figure 2.1. Schematic Diagram of Vertical Casting as commonly practised (After Emley [3])

The structure resulting from DC casting consists of predominantly columnar growth bordered by an outer chill zone, of varying thickness, and an inner band of equiaxed grains.

Because of the rapidity of solidification during DC casting, and the slow nature of solid state diffusion, it is impossible to achieve castings without compositional variations. These compositional variations are termed *segregation*. Segregation can occur both microscopically - termed *microsegregation* - which is defined as a localised

compositional variation over very small distances (few μm) and macroscopically - termed *macrosegregation* -, which is a compositional variation over large distances (few mm to a few cm).

Macrosegregation cannot be removed by a simple heat treatment, because the time required to bring about solid-state diffusion over such large distances is not available. Hence any macrosegregation present in a casting must '...be lived with' [4].

Microsegregation arises from the rejection of the solute from the dendrite arms as the solidification front advances through the liquid. The result is the formation of a concentration gradient between the middle and the outside of the dendrite arm. This change in composition is commonly called *coring* because etching a polished section of such dendrites reveals a series of layers of gradually changing composition around a central core.

The sideways rejection of solute into the liquid as the dendrite grows into the melt can lead to a form of macrosegregation widely known as *inverse segregation*. This is displayed in figure 2.2. As the dendrites solidify, liquid flows back towards the mould to accommodate solidification shrinkage and in doing so carries progressively more solute towards the dendrite roots.

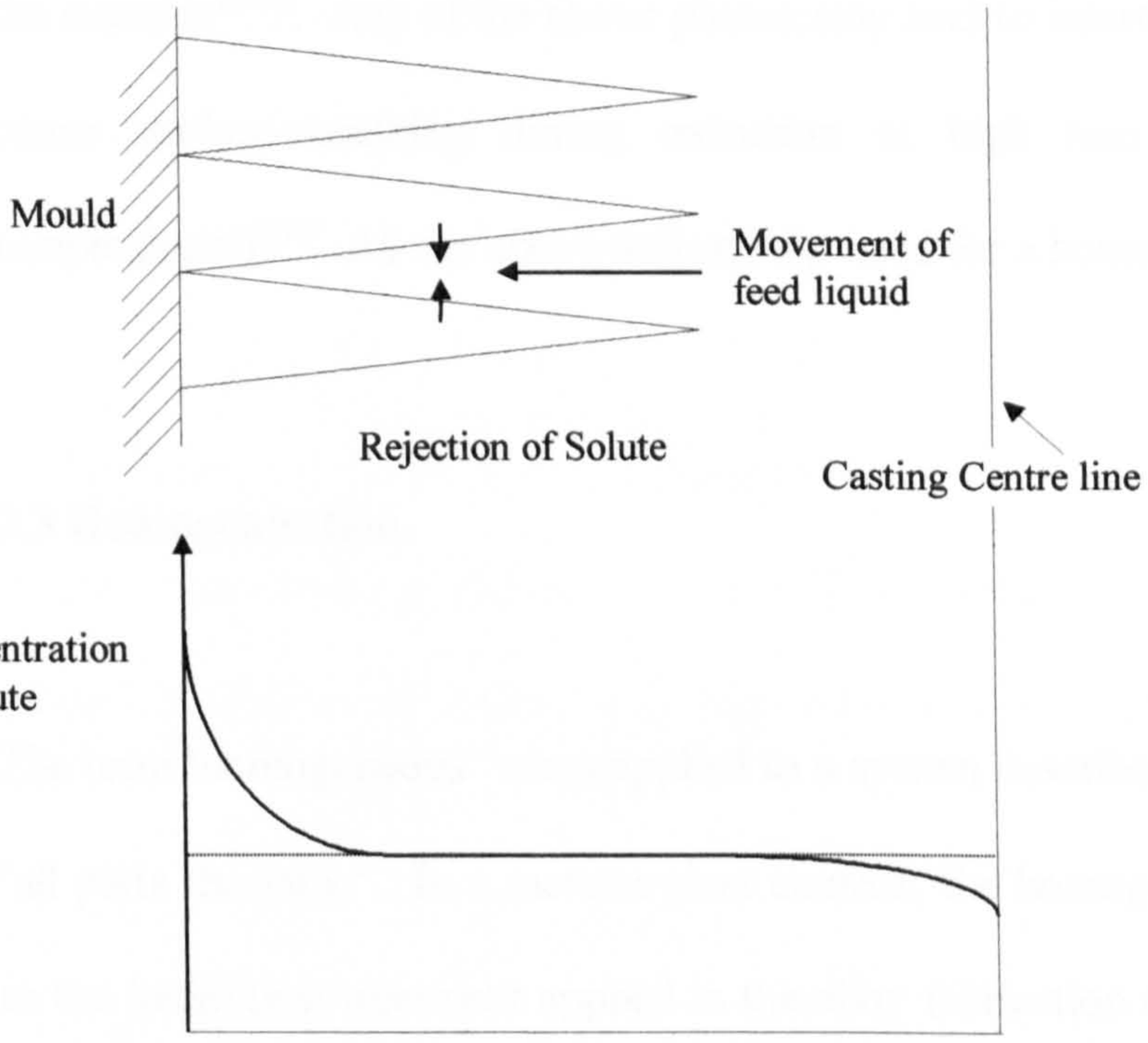

Figure 2.2. Normal dendritic segregation (inverse segregation) arising as a result of the combined actions of solute rejection and shrinkage during solidification in a temperature gradient (After Campbell[4])

It has been reported [5] that in Al-Mg-Si alloys solidified under non-equilibrium conditions (such as those created by DC casting), there exists a tendency for the formation of Si crystals in alloys where all the Si should be tied up as Mg_2Si. In addition, as would be expected, because of coring, Mg_2Si or Mg_5Al_8 may appear in alloys that consist of a single phase at equilibrium[6].

Particles segregated during casting of Al-Mg-Si alloys are usually AlFeSi [7,8], but also $FeAl_3$[9]. The former occur in the spheroidal α form or the more detrimental acicular β form, which can be avoided by rapid solidification or slowly transformed later by homogenisation. This transformation is discussed in a subsequent section.

Additionally there may also be present large particles rich in Mg or Si associated with the eutectic [8,10]. Any of the above phases may lead to interfacial cracking which could cause surface cracking during extrusion at high ram speeds (and low billet temperatures)[11]. All the above indicate the need for a homogenisation heat treatment.

2.3 Homogenisation.

The term 'homogeneous' when applied to a system describes the said system as having 'all parts the same'. In a metallurgical context, the homogenisation of an alloy refers to the initial heat treatment applied in the alloy fabrication route [12]. As mentioned in the previous section, all cast billets contain inhomogeneities in the form of coring or inverse segregation. Thus a homogenisation cycle is required prior to hot working, to equilibrate the chemical gradients across the alloy. In addition to this, coring may result in the formation of low melting point (such as Mg_5Al_8, M.P.: 451°C) or other detrimental phases (such as β-AlFeSi). The former may remelt during a hot working operation and result in a localised melting defect called 'hot shortness' and ultimately failure due to cracking [13].

It was noted by Reiso [8,10] that the larger Mg or Si rich particles could produce small molten eutectic patches, upon interaction with the constituent particles, increasing the risk of interfacial cracking along grain boundaries or dendrite arms at lower maximum ram velocities than those associated with intergranular fracture of the Al matrix (The maximum ram velocity, V_M, which is limited by the billet temperature and acceptable surface finish, is considered by many workers to be a measure of extrudability because

it quantifies plant productivity [8,10]). This effect was reported to occur within the deformation zone of the billet after rapid preheating (e.g. by induction), when there is no time for dissolution. Thus V_M decreases with an increase in size and quantity of the particles - brought about by excesses of Mg or Si in the alloy.

A theory was proposed for the kinetics of homogenisation in 1969 [14] assuming the solute concentration gradients were linear between the middle of the dendrite arms and the centre of the region enclosed by adjacent dendrites as shown in figure 2.3.

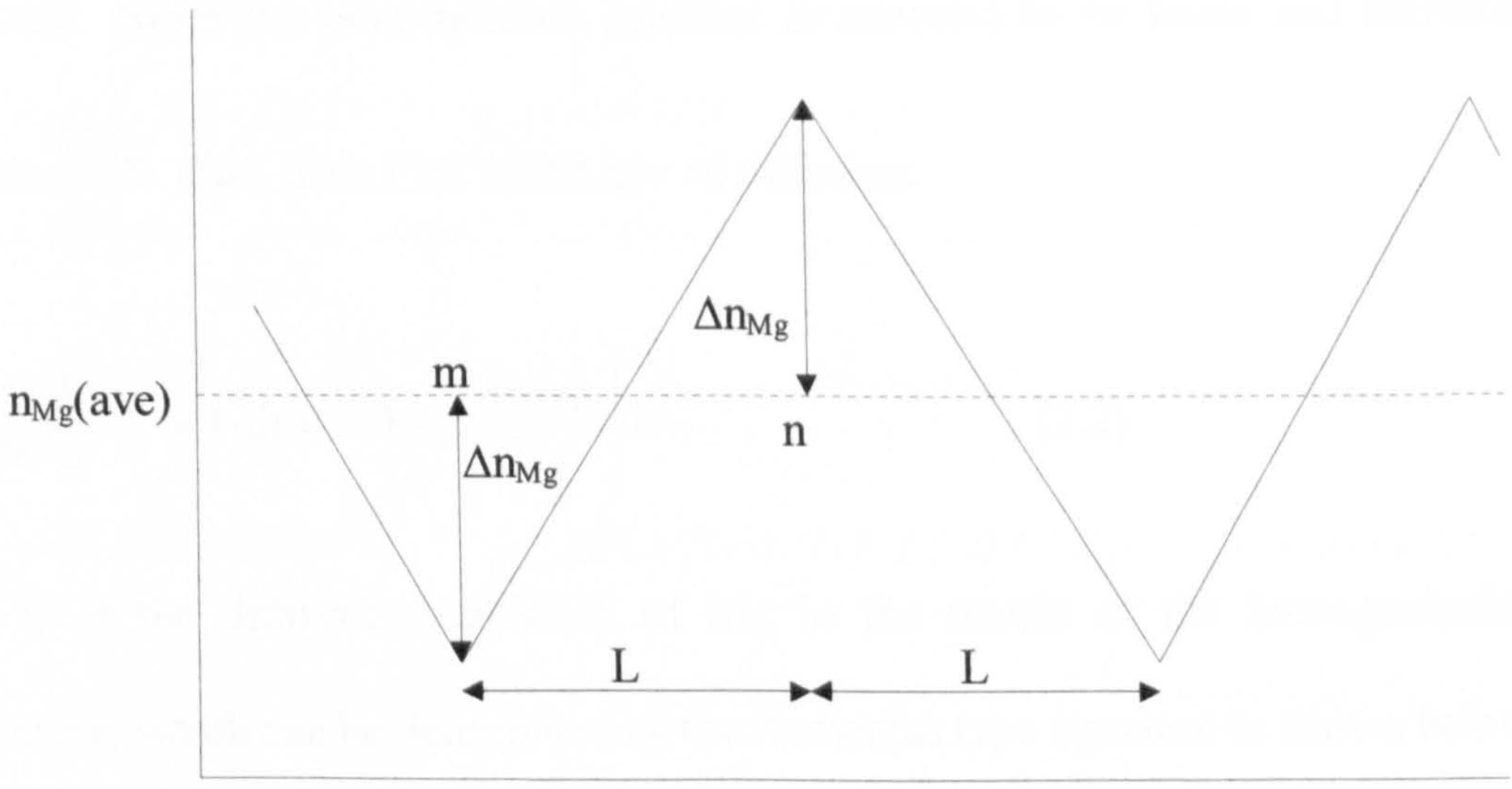

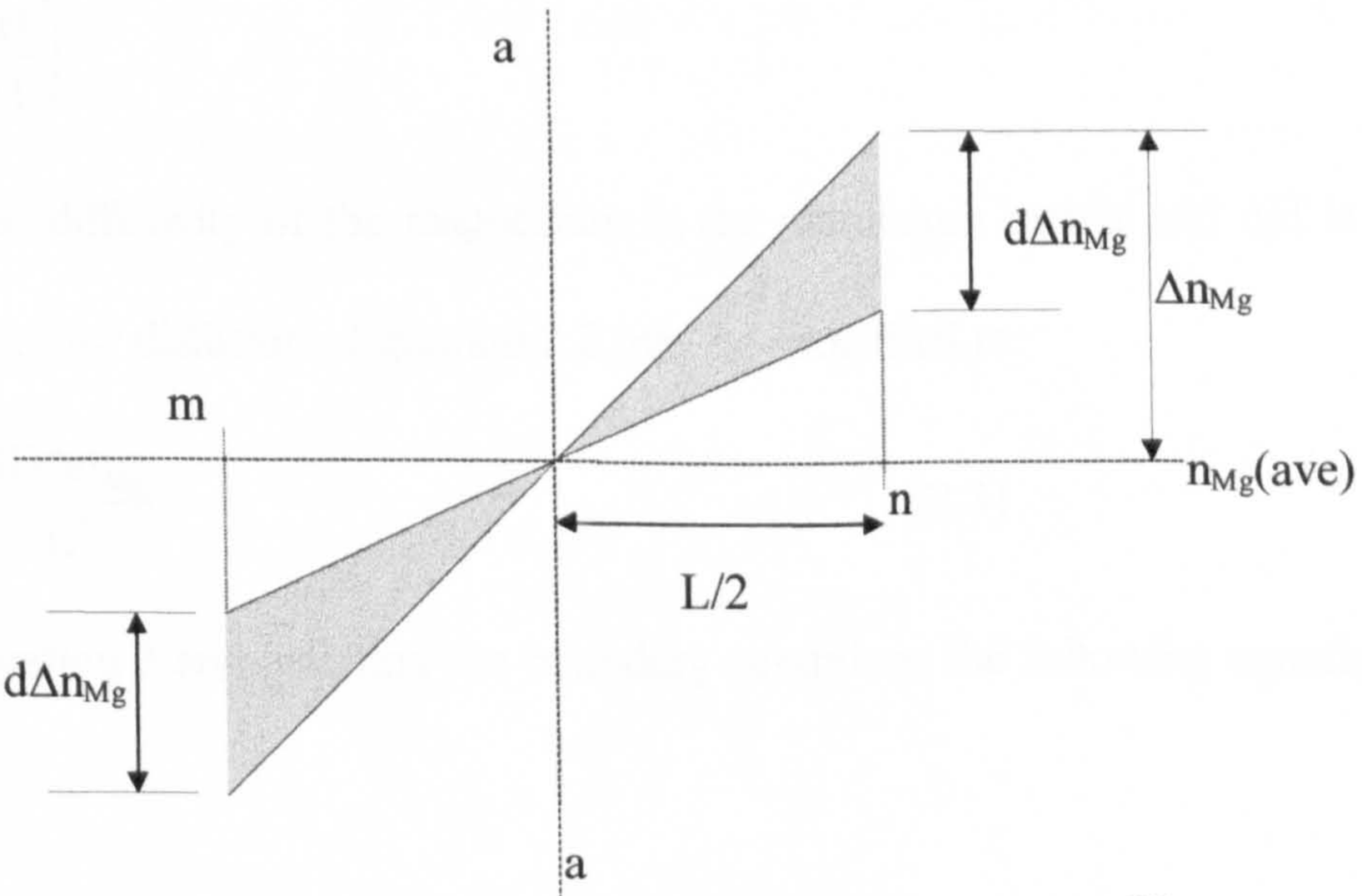

Figure 2.3. An assumed linear concentration gradient in a cored Al - Mg specimen [14]

In a time interval dt, the concentration of Mg in the Al matrix at point m may be assumed to increase by $d\Delta n_{Mg}$, while at point n it should decrease by the same amount. In order for this to happen a number of Mg atoms equal to

$$d(\Delta n_{Mg})\frac{L}{4}A_x \qquad (2.1)$$

where A_x is the cross-sectional area of the specimen, has to pass through the cross-section aa, where $d(\Delta n_{Mg})\frac{L}{4}$ is the area of one of the small cross-hatched triangles. This number can be equated to J dt where J is the flux of Mg atoms per second past section aa. Since the concentration gradient is assumed to be linear and therefore equal to $\frac{\Delta n_{Mg}}{L/2}$ thus, from Fick's first law of diffusion:

$$d\left(\Delta n_{Mg}\right)\frac{L}{4}A_x = J\cdot dt = -DA_x\left(\frac{\Delta n_{Mg}}{L/2}\right)dt \qquad (2.2)$$

where D is the diffusion coefficient of Mg in the matrix at the homogenisation temperature, which can be determined by the Arrhenius type equation as shown below:

$$D = D_0 \exp\left(\frac{\Delta H}{GT}\right)$$

where D_0 is the diffusivity of the magnesium in the aluminium matrix and ΔH is the activation energy for diffusion. Equation 2.2 may be simplified to:

$$\frac{d(\Delta n_{Mg})}{dt} = -\frac{8D\Delta n_{Mg}}{L^2} \qquad (2.3)$$

Integrating equation 3 and inserting the boundary conditions the following equation is arrived at:

$$\Delta n_{Mg} = \Delta n_{Mg_o} \exp\left(-\frac{8D}{L^2}t\right) \qquad (2.4)$$

where Δn_{Mg_o} is the concentration differential when the time is zero. The quantity $\frac{L^2}{8D}$ is equivalent to a relaxation time, ω, thus

$$\Delta n_{Mg} = \Delta n_{Mg_o} \exp\left(-\frac{t}{\omega}\right) \qquad (2.5)$$

However, a somewhat better approximation is that the concentration gradient varies sinusoidally with distance rather than linearly. This type of variation corresponds to a relaxation time of $\omega = \frac{L^2}{\pi^2 D}$ instead of $\frac{L^2}{8D}$ [14]. The significance of the relaxation time is that it is the time required, at the homogenisation temperature, for the concentration differential at any point in the system to decrease by a factor of $\frac{1}{e}$. In a typically cored specimen, the dendrite arm spacing is approximately 70μm and the diffusion coefficient of Mg in Al at the temperature at which maximum solid solubility occurs (450°C) is $8.05 \times 10^{-12} m^2/s$ [5]. Using these values gives a relaxation time of

$$\omega = \frac{L^2}{\pi^2 D_{Mg}} = \frac{4.9 \times 10^{-9}}{\pi^2 8.05 \times 10^{-12}} \approx 60 \text{ seconds.}$$

Hence the magnesium concentration gradient present in the cored structure will quickly achieve equilibrium. However, iron and chromium have diffusion coefficients 7 and 6 orders of magnitude less than Mg respectively [5]. Thus for iron

$$\omega = \frac{L^2}{\pi^2 D_{Fe}} = \frac{4.9x10^{-9}}{\pi^2 1.109x10^{-18}} \approx 10^{10} \text{ seconds} \approx 14 \text{ years}$$

This result shows clearly that for the Fe concentration gradient to achieve equilibrium across the cast ingot, is practically impossible. This is the reason for the willingness to extract as much of the iron as possible from the aluminium alloy during casting.

So, the time required for homogenisation to be completed changes depending on the dendrite arm spacing. It is thus preferable to have as small a dendrite arm spacing as possible (minimising the distance required for diffusion). Generally apart from solute redistribution, homogenisation at 420-600°C (depending on the alloy) is required for:

- The shrinkage and spherodisation of the constituent particles.
- The elimination of non-equilibrium eutectics and particles.
- Relief of residual stresses produced during the rapid cooling involved in the DC casting process.

Specifically for the Al-Mg-Si system homogenisation [7,9,10,15,16] is used to:

- Dissolve the Mg and Si rich particles and eutectics.
- Eliminate coring within the alloy increasing the uniformity of the matrix.
- Refinement of the βAl-Fe-Si phase to the less detrimental α phase.

- Ideally produce an even distribution of fine Mg_2Si particles and a solute level according to the solvus line in the pseudo-binary phase diagram (in balanced alloys: Mg/Si=1.72)

2.4. Effect of alloying additions in AA6xxx alloys

Mg_2Si:

This is the primary hardening phase present in these alloys (Mg / Si = 1.73:1 to form equilibrium Mg_2Si). Its solubility at 600°C is 1.85 wt %. It provides an increase in tensile strength but a decrease in extrudability. This was attributed to an increase in the deformational heating [17]. Scharf [18] reported that an increase of the Mg_2Si content from 0.5 to 0.95 and 1.35 wt % resulted in a decrease in the extrusion speed by 40 and 70 % respectively. However, even though the extrusion speed is reduced, if the *overall* productivity of the profile production process is considered (i.e. billet pre-heating, extrusion and ageing) an opposite effect has been observed. As the Mg_2Si content of the alloy is increased, a gain in the overall productivity is achieved. This is due to the storage time, between extrusion and artificial ageing, which can be reduced from several days at low Mg_2Si contents (< 0.35 wt %) to a few hours at high concentrations. The storage time requirements are not yet fully understood but are believed to be associated with the growth of fine precipitates [19].

To obtain full age hardenable properties Mg_2Si should be retained in solution during extrusion. To achieve this a very fine dispersion of particles is required before extrusion. These are formed by use of a suitable homogenisation treatment, followed by rapid cooling and a good casting practice (control of melt temperature, mould temperature, avoidance of inhomogeneities in the melt, ensure homogenous cooling

etc). These must be followed by rapid heating to the extrusion temperature. Fine particles will dissolve. Large particles, however, would require longer pre-extrusion soaking times.

The process of precipitation of fine Mg_2Si particles is aided by the presence of minor alloying addition containing dispersoids (such as TAlMgSi, $ZrAl_3$ or αAlMnSi) which act as nucleation sites and aid the refinement.

The critical temperature for precipitation of Mg_2Si is between 316°C and 427°C and results in coarse and rapid precipitation. Thus during cooling after homogenisation, this temperature regime must be passed as quickly as possible [20].

Mondolfo [21] suggested that slow cooling of the alloy after homogenisation (as low as 36°C/hr) provides precipitation and coagulation of Mg_2Si, improving extrudability without the loss of properties. This finding is surprising and conflicts with the findings of a number of workers [16,22] as well as with established homogenisation practice.

Indeed previous work highlighted the problem of agglomerated precipitates present in the matrix during extrusion. At around 545°C a sharp drop in ductility was observed by Gjestland et al. [23] which was believed to have been induced by incipient melting of agglomerates of α–Al(Fe,Mn)Si + Mg_2Si + Si + Al. On the other hand, incipient melting may be avoided by controlled cooling after homogenisation to result in large Mg_2Si (>0.5μm) and fewer low melting point phases.

It is possible to induce dynamic precipitation of Mg_2Si particles during deformation of a fully solution treated billet [24-33]. This results in a high initial flow stress, followed by gradual work softening. In the region 250 - 350 °C it is particularly evident, because the particles formed are very fine and impede dislocation motion very strongly. Subgrain formation and, hence, dynamic recovery are also reduced. The drop in flow stress (work softening) is produced by rapid agglomeration of the particles under pressure [24,26-31]

Coarse Mg_2Si can cause a dull anodised finish. Fine precipitates do not seem to have any effect on the bright anodised finish [34].

Silicon (Si):

It is widely accepted that Si tends to form intermetallic compounds with Fe preferentially to Mg. Stoichiometric calculations by Traenkner [16] yielded the following equations:

Si required to form equilibrium $Mg_2Si = 0.58$ (%Mg)

Si remaining to form equilibrium Mg_2Si = %Si - 0.25(%Fe + %Mn).

The effects of the AlFeSi phase will be discussed in the next section.

Excess Si in the structure (over that required to form Mg_2Si) leads to refinement of the Mg_2Si precipitate structure, increasing the strength and decreasing the ductility [35]. A large proportion of this Si is deposited at the grain boundaries as elemental Si. This

probably constitutes the reason for the reduction in ductility and toughness in excess Si alloys.

Evans and Autcote [35] postulated that the intergrannular mode of fracture, induced in excess Si alloys is due to the size, distribution and nature of the grain boundary precipitates, rather than the weak precipitate free zones.

Si, in solid solution, reduces the extrudability of the alloy. However, undissolved coarse Mg - Si phases in the structure, as it enters the die, also result in a sharp reduction in extrudability. This effect has been attributed to the change in failure mechanism, because of the local weakness these phases represent. An incipient melting mechanism is proposed [8, 10].

Low Si (and Mg) contents, on the other hand can become the cause for surface tearing during extrusion due to insufficient strength of the Al matrix at high extrusion ratios and speeds. As the speed (and, hence, temperature) is increased the Al matrix can no longer withstand the frictional forces developed at the die and tearing results [10]. Industrial wrought alloys are normally formulated with a balance of Mg and Si or with excess Si. This is due to the less detrimental effect that Si has, on the hot workability of the alloy, than Mg [16,36,37].

Excess Si in the structure is also reported to increase the sensitivity towards intergrannular fracture during tensile failure. This is caused by a slow quench after homogenisation in alloys which do not contain significant dispersoid forming elements.

Such a quench would result in Mg_2Si precipitation at grain boundaries accompanied by broad precipitate free zones [38].

Magnesium (Mg):

Mg has repeatedly been reported to have detrimental effects on the extrudability of the alloy. Thus, although it does provide a small amount of solid solution strengthening, it is not desirable to have Mg present in amounts larger than those required to form Mg_2Si [16,20]

Mg is also reported to improve the corrosion resistance of the alloy [5].

Iron (Fe):

Iron is present in most wrought aluminium alloys as a controlled impurity and forms two different phases in the Al-Mg-Si matrix; αAlFeSi and βAlFeSi. These are abbreviations for $Al_{12}Fe_3Si_2$ and $Al_{4.5}FeSi$ respectively. The latter is a hard eutectic phase which has been reported to be detrimental to the hot working (extrusion) properties of the alloy. Thus its transformation to the less detrimental α phase is desirable, during any homogenisation practice [5,7].

Other studies have suggested that it is not the β to α transformation which improves the extrudability of the alloy but the refinement of the Mg_2Si distribution [39].

Particular difficulty is incurred to transform β- to α-AlFeSi if the alloy in question has excess Si, which tends to stabilise the β phase [39].

Fe has, however, been reported to increase the toughness in excess Si alloys by overting silicon segregetion to the grain boundaries and by refining the Mg_2Si dispersion.

Minor alloying additions:

Manganese (Mn):

Manganese additions are reported to have beneficial effects on the properties of 6XXX extrusion alloys. A major advantage of small Mn additions involves the β to α transformation, which is caused to occur at a greater rate [39]. At an alloying content of 0.01 wt % Mn the transformation is reported to take around 20h. This may be reduced to only 20min at 0.1 wt % Mn [16,39]. Mn was also found to increase the tensile ductility because of a reduction in the amount of Si segregating to the grain boundaries [40].

In a study, involving alloy AA6013 [41], designed to study the AlFeSi particles, which were found to promote recrystallisation, and the MnFeAlSi particles, which retard it, it was found that increasing the Mn content of the alloy had no serious effect as it increased the numbers of both classes of particles. However, reducing the amount of

Fe resulted in an improvement in the resistance to static recrystallisation, because the MnFeAlSi intermetallic seemed to form preferentially.

Mn forms dispersoids of the form AlMnSi which act as grain refiners and nucleation sites for Mg_2Si particles aiding a fine distribution, thus decreasing the solution heating time required.

Surface finish is said to be improved, decreasing the tendency for pick-up formation[38,40]. However, it is reported to slightly reduce the strength after aging [40] and has a detrimental effect on the extrudability and quench sensitivity of the alloy[42,43].

Zirconium (Zr):

It has been reported that Zr additions of up to 0.1 wt % *in combination with* up to 0.4 wt % addition of Mn to an alloy containing excess Si, influence the mechanical properties, toughness and weldability of the alloy. The impact strength of the alloy was drastically improved; Heat Affected Zone microcracking was also reported to have been avoided using the above additions [44].

These effects were explained with reference to the microstructural influence which Zr and Mn appear to have on the alloy. They tend to aid the development of a fibre structure by increasing the activation energy for, and thus inhibiting, recrystallisation after hot working.

Zr alone forms particles of $(Al,Si)_3Zr$, but when it is in the presence of Mn, the inclusion of Si is inhibited in the intermetallic allowing formation of $ZrAl_3$, which acts as a recrystallisation inhibitor and nucleation site for Mg_2Si [44].

Copper (Cu):

Cu is generally unacceptable as an alloying addition in Europe because of its detrimental effect on the corrosion resistance of the alloy [34,42,45,46].

It is accepted that minor additions of Cu improve the mechanical properties of 6XXX alloys in proportion to the amount used [35,42], but other effects of Cu on the structure and properties of 6XXX alloys still remain unclear. It was reported by Lang and Castle [46] that Cu additions tend to slightly improve the impact resistance of the alloys if present in combination with Cr and Mn additions, the total combination of which does not exceed 0.1 wt %. The same authors, however, also point out that the same combination yields a significant increase in the extrusion load. This effect has been confirmed by other workers [35].

Chromium (Cr):

The effects of chromium are very similar to those of Mn as it is a dispersoid forming element (it forms a metastable TAlCrMg phase), thus inhibiting recrystallisation by grain boundary pinning, and aiding the refinement of the Mg_2Si dispersion. Cr rich dispersoids are reported to aid in the preservation of the fibrous structure after extrusion thus affecting toughness [42].

As does Mn, chromium reduces the amount of Mg_2Si and elemental Si which precipitates onto the grain boundaries, thus improving the toughness of the alloy. Mn, however, is used more frequently than Cr as an alloying addition because, although it has a more pronounced effect on the quench sensitivity of the alloy, it is less detrimental to the extrusion speed and surface finish quality [20].

Other minor alloying additions:

Strontium (Sr) has been found to promote the transformation of the β to αAlFeSi phases. As little as 0.015 wt % has been reported to result in the above transformation. The same amount was also found to act as a grain-refining agent in the medium strength alloy AA6201 [47].

Lead (Pb) is added to improve machinability [5].

TiB_2 acts as a grain-refining agent but is detrimental to extrudability and surface finish quality [38].

Zinc (Zn) exists in the matrix as a controlled impurity but can have minor strengthening effects by solid solution strengthening [5].

2.5. Phase Transformations in Al - Mg - Si (Fe) alloys

As mentioned previously iron is never added intentionally to such alloys, but is present in small amounts as a controlled impurity. In the absence of iron the silicon present in the alloy may occur as Mg_2Si, elemental Si or dissolved in the aluminium matrix. Excess magnesium, however (necessary to suppress the formation of elemental Si) is taken into solid solution and may prove detrimental to the casting process (coring) [6].

The ternary Al - Mg - Si phase diagram is well established and is shown in figure 2.4.

The invariant reactions which take place are tabulated below:

Reaction	Composition				Temp (K)
	Liquid		Solid solution		
	%Mg	%Si	%Mg	%Si	
$L \rightarrow Al_{ss} + Si$	-	12.5	-	1.65	850
$L \rightarrow Al_{ss} + Mg_5Al_8$	34.0	-	17.4	-	723
$L \rightarrow Al_{ss} + Mg_2Si$ quasibinary	8.15	7.75	1.17	0.68	868
$L \rightarrow Al_{ss} + Mg_2Si + Si$	4.96	12.95	0.85	1.10	828
$L \rightarrow Al_{ss} + Mg_2Si + Mg_5Al_8$	32.2	0.37	15.3	0.05	722

Table 2.1. List of invariant reactions occurring in Al - Mg - Si ternary alloys [5]

The phases present - Si, Mg_5Al_8 and Mg_2Si - may be assumed to be close to the stoichiometric composition. It has been reported [5] that in the liquid phase, Mg and Si atoms tend to cluster together to form Mg_2Si 'molecules'.

Temperature (°K)	A	B		C		D		E
	%Mg	%Mg	%Si	%Mg	%Si	%Mg	%Si	%Si
868	-	-	-	1.17	0.68	-	-	-
850	-	-	-	1.10	0.63	-	-	1.65
825	-	-	-	1.00	0.57	0.83	1.06	1.30
800	-	-	-	0.83	0.47	0.6	0.8	-
775	-	-	-	0.70	0.40	0.5	0.65	0.8
725	17.4	15.3	0.1	0.48	0.27	0.3	0.45	0.48
675	13.5	11	0.0X	0.33	0.19	0.22	0.3	0.29
575	6.7	5	0.0X	0.19	0.11	0.1	0.15	0.06

Table 2.2. Location of points in figure 2.4 (b)

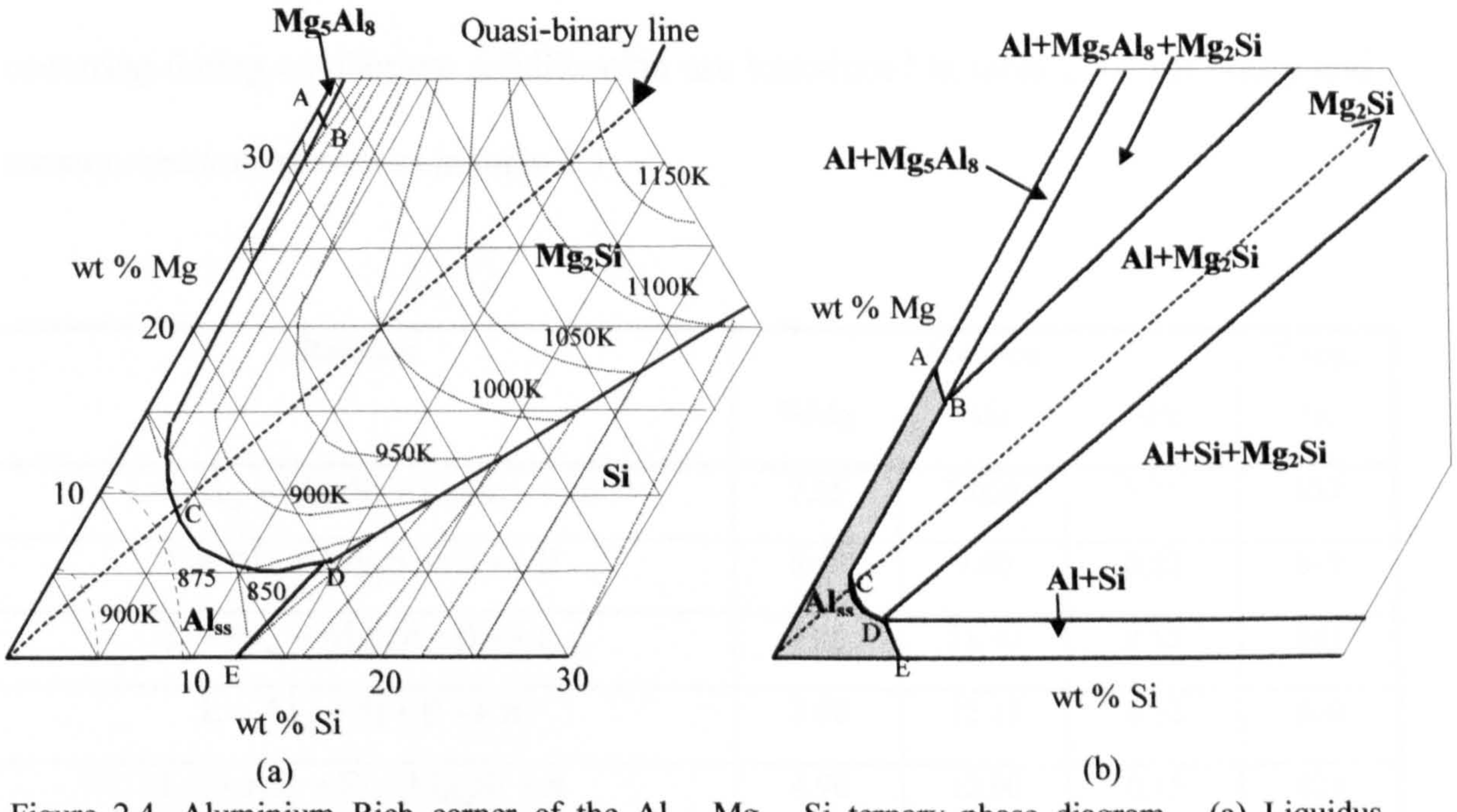

Figure 2.4. Aluminium Rich corner of the Al - Mg - Si ternary phase diagram. (a) Liquidus projection, (b) Isothermal section; Points A, B, C, D and E are located as shown in the table 2.2:

The stoichiometry and structure of the compound Mg_5Al_8 has been widely discussed among the scientific community. Initially it was believed to have a cubic structure with 227 atoms per unit cell, (belonging to the space group Fd3m), loosely related to Mg_2Al_3 stoichiometry [48], but later the Mg_5Al_8 stoichiometry was established after studies by Perlitz [49]. Perlitz supported that the compound has a complex fcc structure containing 1172 atoms, belonging to the space group Fd3m. Sampson [50] later reported a partially disordered lattice with 1168 atoms per unit cell.

Mg_2Si has a cubic structure with 12 atoms per unit cell and belongs to the space group Fm3m [5].

If Fe is not altogether absent from the alloy, the quaternary invariant reactions occurring during equilibrium solidification are introduced in table 2.3. All binary and ternary reactions remain as in table 2.1.

Reaction	Location			Temp.
	%Mg	%Si	%Fe	°K
$L + Al_{ss} + Mg_2Si + FeAl_3 \rightarrow \alpha$	7.25	7.055	1.35	859
$L + Al_{ss} + Mg_2Si + \alpha \rightarrow \beta$	6.45	9.80	0.82	849
$L + Al_{ss} + Mg_2Si + \beta \rightarrow \pi$	6.00	11.40	0.55	841
$L + Al_{ss} + Si + \beta \rightarrow \pi$	2.90	12.15	0.52	840
$L \rightarrow Al_{ss} + Si + Mg_2Si + \pi$	4.90	12.90	0.15	828
$L \rightarrow Al_{ss} + Mg_2Si + Mg_5Al_8 + FeAl_3$	33.3	0.35	0.11	724

Table 2.3. Positions of quaternary invariant reactions in the Al - Mg - Si - Fe system.

It has been suggested that the compound designated $FeAl_3$ does not exist as such at room temperature but breaks up into Fe_2Al_5 and Fe_2Al_7 [6]. Hultgren et al. [51] suggested that it has a base centred monoclinic structure. Nowhere has $FeAl_3$ been reported to be capable of dissolving even small amounts of Mg. The two phases designated α and β are AlFeSi phases with approximate stoichiometries $Fe_3Si_2Al_{12}$ [52] and $Fe_2Si_2Al_9$ [53] respectively. α is, as mentioned already, the less detrimental of the two, on the properties of the alloy and is formed peritectically from $FeAl_3$ [54]. As it is widely accepted that peritectic reactions are rarely completed because of poor diffusion characteristics, it may be found in envelopes around $FeAl_3$ crystals or in characteristic 'Chinese Script' formations if it has directly crystallised from the melt. It has been postulated that it has a hexagonal crystal structure with a = 12.3 Å and c = 26.2 Å [55]. The β phase is formed peritectically from α. It is a hard and brittle

eutectic phase, richer in Si than α and has been reported to have a monoclinic structure with a = b = 6.12 Å, c = 41.5 Å and β = 91° [53]. The quaternary eutectic phase which appears in Al - Mg - Si - Fe alloys is designated π and may loosely be associated with the stoichiometry $Al_8Mg_3Si_6Fe$. Perlitz and Westgren [56] suggested that it is a perfectly stoichiometric compound with a hexagonal structure (having a = 6.62 Å and c = 7.92 Å) with 18 atoms per unit cell. It belongs to either $H\bar{6}m$ or D^3_{3h} space groups.

2.6. Extrusion:

Introduction:

Extrusion is a complex method of metal forming, the specifics of which have been extensively discussed elsewhere [57-60] and is summarised in the next section. In short extrusion is the forming process during which a billet of material of area A_B is placed in a heated container and struck by a ram moving at velocity V. Under the applied pressure, the billet upsets to fill the container and is forced through an orifice to produce a length of uniform cross-section of area A_E. The ratio A_B/A_E is designated R and termed the Extrusion Ratio. The true strain applied to the billet is therefore lnR.

2.6.1. General Pressure Equation Considerations:

Extrusion, as mentioned earlier, has been examined, over the years, by a number of workers.

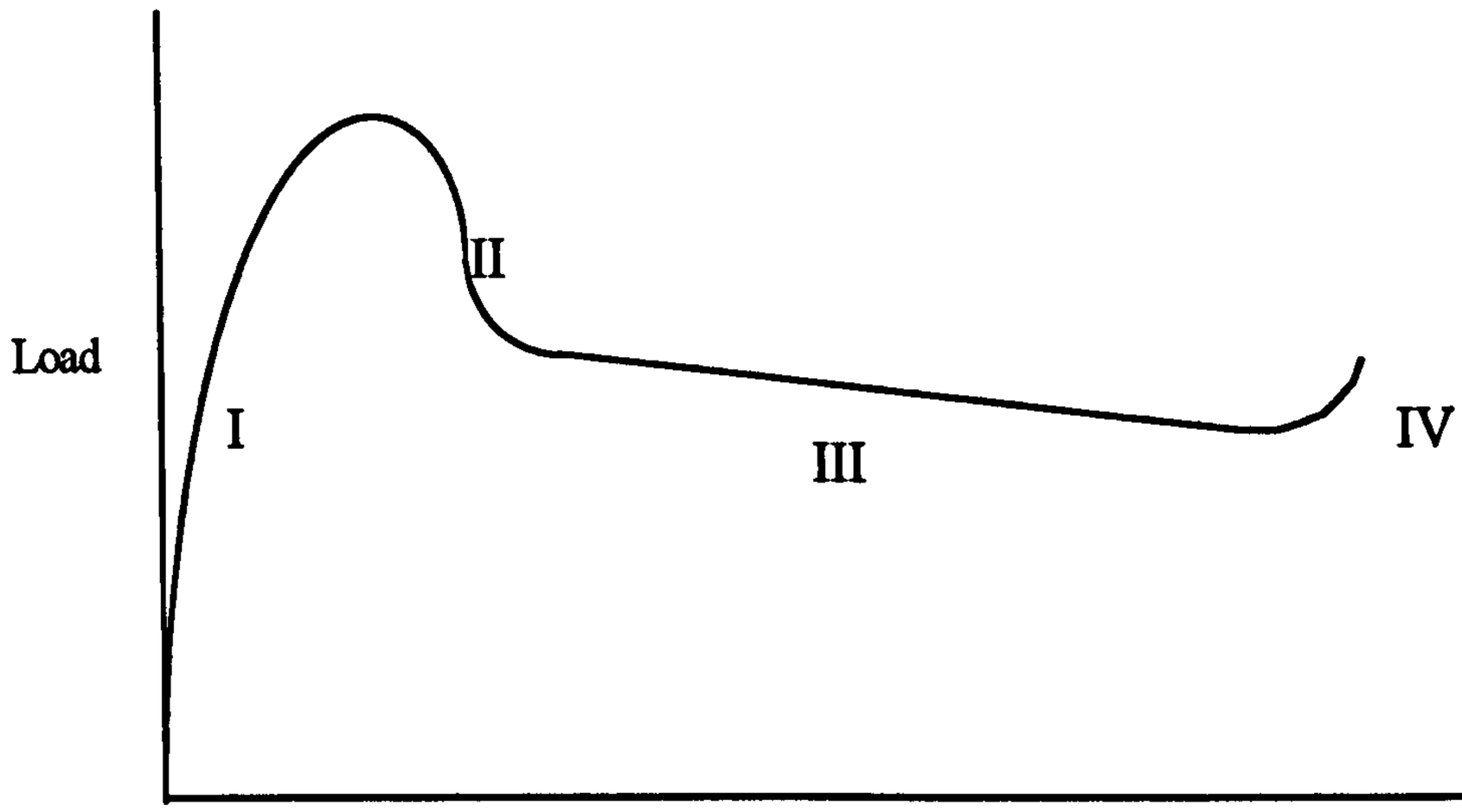

Figure 2.5. Schematic Load - Displacement Diagram for Direct Extrusion.

An explanation of the various sections of the diagram shown in figure 2.5 designated by the Roman numerals is made below:

I. There is an increase in pressure as the billet is upset to fill the container. Some extrusion takes place during this stage [61,62]. This is of the order of the extrude diameter in length [63].

II. The sharp drop in extrusion pressure, for complex alloys (or those containing second phase particles), e.g. 2xxx and 5xxx series aluminium alloys, may be due to the pressure drop observed once a certain threshold stress has been attained. This threshold stress arises from the dislocation pile-ups formed during the upsetting of the billet. Grain boundaries and especially second phase particles pin the dislocations requiring a large stress to release them into the system.

III. After the peak load is attained, the load gradual decreases as the length of the billet is reduced and the frictional forces between the container and the billet decrease [61]. This effect is made more prominent by the temperature rise generated during the extrusion cycle. The increase in temperature creates a drop in the flow stress of the material causing the observed decrease in load. This effect is greater in those tests performed at low temperatures and high strain rates, i.e. large values of the temperature compensated strain rate, Z [63].

IV. This decrease continues until near completion, where a sharp increase occurs because of the excess pressure required to affect flow in the remaining small part of the billet. It is, however, common practice to end the extrusion run before this point, as this is the time during which the 'funnel' defect may arise. This occurs because of inhomogeneous flow - the centre flowing faster than the surface - causing a funnel shaped defect to appear in the discard. This sometimes extends into the extrudate if an insufficient discard length is left.

Various other explanations have been voiced over the years concerning the prominent peak discussed above (II):

Sheppard and other workers [57,62,64-67] have, over the years, attributed the peak to the formation of the deformation zone before much heating has been introduced into the

billet. When the temperature does rise, as extrusion proceeds, deformation occurs more easily.

Wilson [68] suggested that it results from the transition from sticking friction to full-film lubrication. It is however doubtful that such conditions of full-film lubrication exist when extruding light alloys, although it has been shown to be present during high temperature extrusion, (i.e. steels etc.). This study by Wilson was performed by mathematical analysis.

Ziegler [69] observed the peak during indirect extrusion in which the frictional effects between the billet and the container are zero. In other analyses of indirect extrusion the observed peak was considerably reduced in size in alloys such as AA2014 [61] and was barely detectable in dilute alloys such as AA6063 [63]. Peaks have been observed during indirect extrusion. However, these were not in the hot working regime but at temperatures well below that, indicating that perhaps the billet is not free to flow over the die face.

Other explanations involve a temperature effect [70] due to the temperature differential between the die and the billet or connected to the entry angle of the die [71]. These, though, have both been disproved and thus appear dubious. Avitzur [72] suggested a connection with the formation of the dead metal zone.

The presence of the peak and its magnitude will not be considered in this study because of its apparent absence when extruding AA6063. The general pressure

equation will only be analysed assuming the pressure, wherever mentioned, to be the steady state extrusion pressure.

Alexander [60] via a slip-line field theory analysis found that for plane strain conditions, flat-faced dies and direct extrusion, formulae of the type shown below may be used to calculate the extrusion pressure, taking account of friction.

$$\frac{P}{2k} = a + b\ln R + cl \qquad (2.6)$$

where P is the steady-state extrusion pressure, k is the (constant) shear yield stress of the material, R is the extrusion ratio, l is the length of the billet remaining and a, b and c are constants. Slip-line field theory, however is limited by experimental constraints and applies only at low extrusion ratios which is not the case in industrial extrusion.

This equation was suggested to be also applied to cases in which work hardening is present during extrusion, by including a mean value of the variable k. This has been discussed elsewhere [73] and will not be included in this study.

The total work required for deformation is made up of three contributing terms, in equation 2.6, as follows:

- blnR represents the useful work required to reach the applied strain, since lnR is a measure of the true strain suffered by the material.
- cl represents the work done to overcome the frictional forces present during deformation.

- *a* represents the redundant work used to change the internal energy of the material associated with the structure alteration suffered by the material, and the residual stresses in the alloy.

Hirst and Ursell [74] used a form of equation 2.6 to calculate the friction contribution:

$$\frac{P}{\sigma_y} = a' + b' \ln R \qquad (2.7)$$

where σ_y is the yield stress assuming the Tresca yield criterion holds true. The assumption shown in figure 2.6 is that the pressure along any distinct transverse plane is constant.

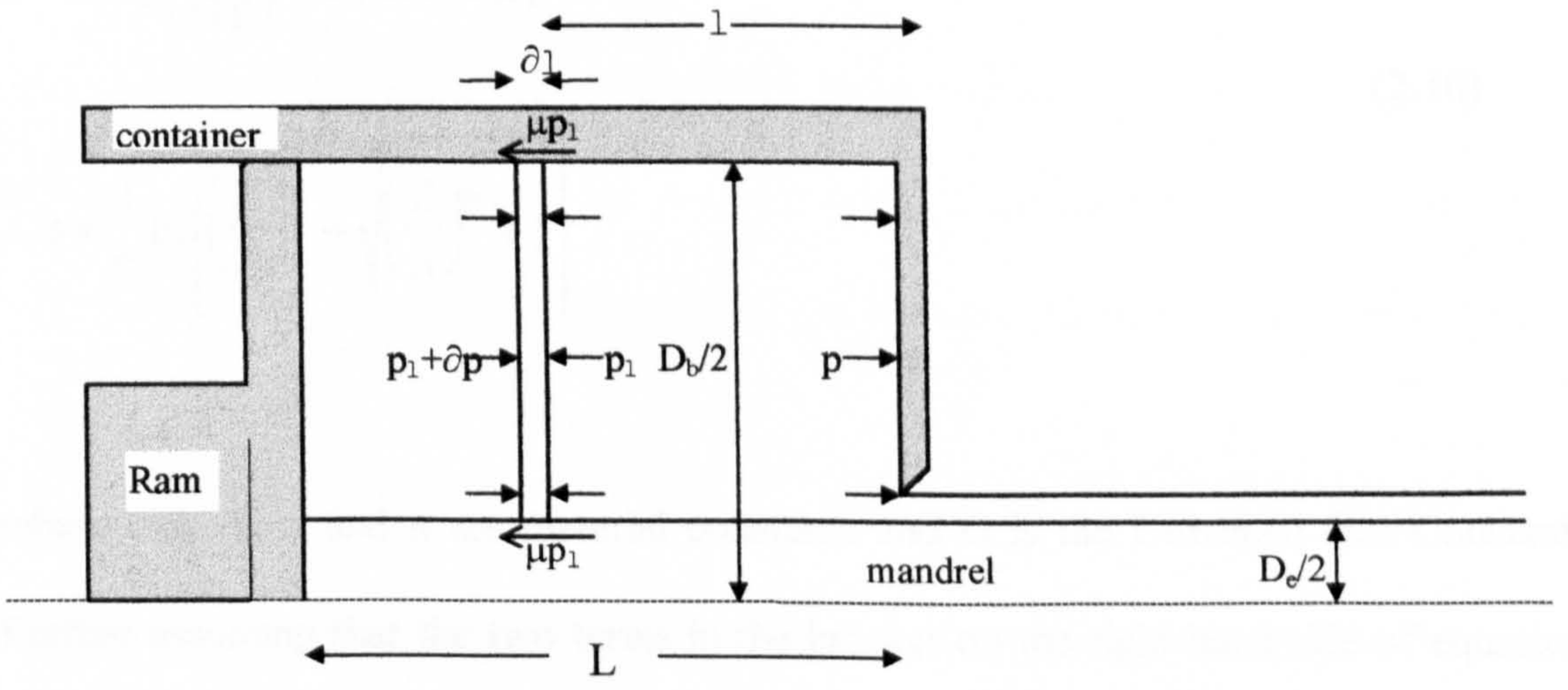

Figure 2.6. Construction by Hirst and Ursell to calculate the frictional contribution.

Considering the elemental slice shown it is obvious that:

$$\partial p_l \frac{\pi}{4}\left(D_b^2 - D_e^2\right) = \mu p_l \pi \left(D_b + D_e\right) \partial l$$

where μ is the frictional coefficient which arises between the container and the billet and inserting the boundary condition $p_l = p$ at $l = 0$ then we may derive [74]:

$$\frac{p_1}{\sigma_y} = (a' + b' \ln R) \exp \frac{4\mu L}{D_b - D_e} \qquad (2.8)$$

Equation 2.8 may be written as:

$$\frac{P}{\sigma} = A' + B' \ln R \qquad (2.9)$$

where σ is the mean equivalent flow stress [60]. Assuming that σ has a value approximating the steady state flow stress, it may be evaluated using the hot-working equation.

$$Z = \dot{\varepsilon} \exp\left(\frac{\Delta H}{GT}\right) = A\{\sinh(\alpha\sigma)\}^n \qquad (2.10)$$

$$\therefore \sigma = \frac{1}{\alpha} \ln\left\{\left(\frac{Z}{A}\right)^{\frac{1}{n}} + \sqrt{\left(\frac{Z}{A}\right)^{\frac{2}{n}} + 1}\right\}$$

where ΔH, A, α and n are material constants and G is the Universal Gas Constant. Further assuming that the two terms in the bracket on the right hand side of equation 2.10 are approximately equal, it may be reduced to:

$$\sigma \approx \frac{0.7}{\alpha} + \frac{1}{\alpha n} \ln\left(\frac{Z}{A}\right) \qquad (2.11)$$

Combining equations 2.9 and 2.11 gives:

$$P=\left(\frac{0.7}{\alpha}+\frac{1}{\alpha n}\ln\left(\frac{Z}{A}\right)\right).(A'+B'\ln R) \qquad (2.12)$$

This equation combines terms based on temperature, strain rate and extrusion ratio and defines the pressure required to extrude an alloy given certain conditions. Equation 2.12 also bears resemblance to empirical equations formulated by Tutcher [75] and Vierod [61] and thus can be more conveniently presented in an equation of the form shown below:

$$P=\frac{1}{\alpha n}\left(A''+B''\ln R+C\ln\left(\frac{Z}{A}\right)\right) \qquad (2.13)$$

This equation was validated by Clode [63] by using multiple regression analysis on data collected from tests conducted on AA6063 alloy. The results compared favourably with the theoretical results indicating that the equation may be applied over a wide range of temperatures and strain rates.

The major limitations of equation 2.13 is that it applies to specific billet dimensions and does not necessarily take into account frictional effects.

Considering the analysis of friction shown earlier, Vierod [61] included a frictional term as follows:

$$P=\frac{1}{\alpha n}\left(A''+B''\ln R+C\ln\left(\frac{Z}{A}\right)+D\ln\left(\frac{Z}{A}\right)\cdot\exp\left(\frac{4\mu L}{D_b}\right)\right) \qquad (2.14)$$

The same worker attempted a validation of the above equation but found a decrease in the correlation coefficients, which he attributed to the experimental error derived from the small increase observed in the experimental values of the *peak* pressure with billet length, L. The experimental data was collected from tests involving 2xxx series alloys. No literature was found applying equation 2.14 to alloys which do not exhibit the peak pressure phenomenon. It is difficult to determine the value of the frictional coefficient, μ, for alloys such as AA6063 because of the negligible change in the extrusion pressure during the quasi-static deformation involved in extrusion.

The other limitation involving the billet dimensions is not as critical as the frictional term because most industrial and laboratory researchers would not alter the size of the billet.

2.6.2. Evaluation Of Strain Rate During Extrusion

There exist a variety of methods by which the strain rate during extrusion may be estimated. None of these, however, are absolute, but are applied by taking boundary conditions and making a number of simplifying assumptions.

Simple strain rate calculation:

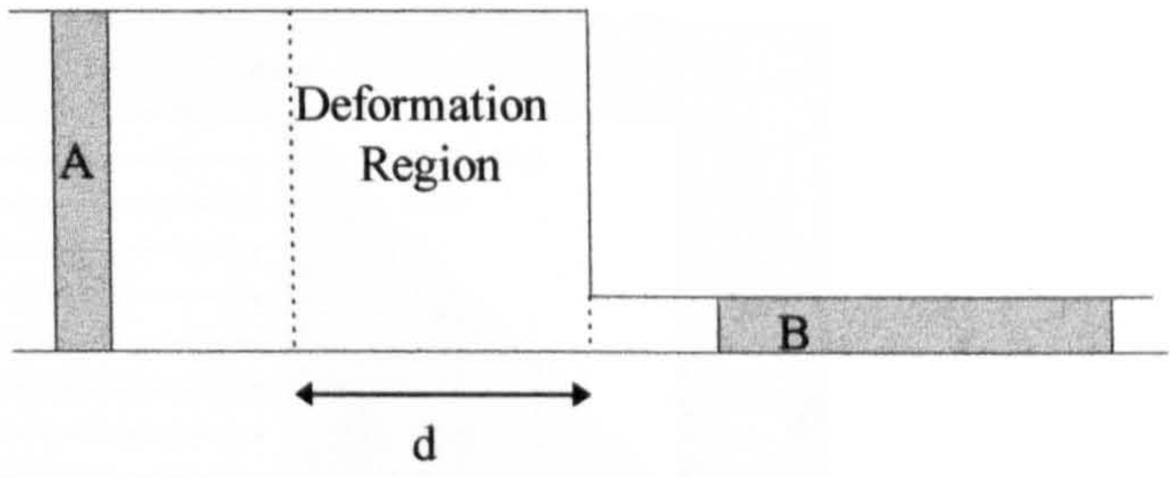

Figure 2.7. Assumptions for a simple strain rate calculation.

This is applied assuming an element of undeformed material, A, will be deformed into a corresponding element, B, after extrusion. Thus we have:

$$\dot{\varepsilon} = \frac{\partial \varepsilon}{\partial t} = \frac{\Delta \varepsilon}{\Delta t}$$

Hence:

$$\dot{\varepsilon} = \frac{\ln R}{t} = \frac{\ln R.V}{d} \qquad (2.15)$$

where R is the extrusion ratio and V is the ram speed.

Feltham Approach:

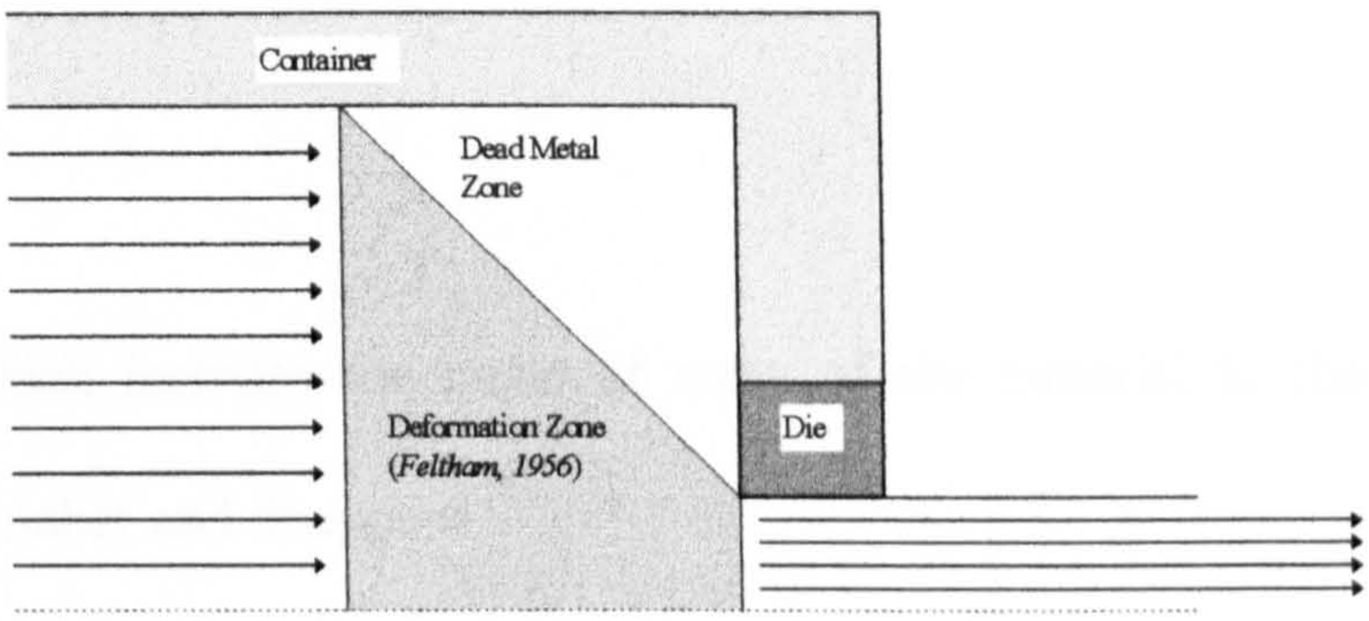

Figure 2.8. Assumptions made by Feltham [58]

Feltham [58] assumed the dead metal region to be bound by a planar conical surface and all the deformation occurring within the shaded region shown in figure 2.8.

This equation is calculated to be:

$$\dot{\varepsilon} = \frac{6V}{D_b} \ln R \qquad (2.16)$$

where D_b is the billet diameter. A major assumption made by Feltham was that the angle formed by the dead metal zone with the container is 45°.

This approach has been used and improved by various workers:

Hirst and Ursell [74] and later Alexander [60] showed that:

$$\dot{\varepsilon} = (0.47 + 1.2R) \frac{6D_b^2 V}{D_b^3 - D_e^3} \qquad (2.17)$$

where D_e is the extrude diameter. Equation 2.17 incorporates friction against the walls of the container during the extrusion process, assuming a constant frictional coefficient of 0.5.

An equation which includes the angle of entry of the material to the die, α, was suggested by Tutcher and Sheppard [76]:

$$\dot{\varepsilon} = \frac{6D_b^2 V \tan\alpha}{D_b^3 - D_e^3} \ln R \qquad (2.18)$$

For strain-rate sensitive materials, Chandra and Jonas [77] have shown that an appropriate measure of strain rate is the root mean power strain rate:

$$\dot{\varepsilon}_{rmp} = \left[\frac{1}{\ln R} \int_0^{\ln R} (\dot{\varepsilon})^m d\varepsilon \right]^{1/m} \qquad (2.19)$$

where m is the strain-rate sensitivity which can be determined from a the slope of a plot of $\log \bar{\sigma}$ Vs $\log \dot{\varepsilon}$, and is defined as [13]:

$$m = \left(\frac{\partial \ln \bar{\sigma}}{\partial \ln \dot{\varepsilon}} \right)_{\varepsilon,T}$$

From observations of flow patterns during extrusion, it is obvious that the assumptions made by Feltham [58] are not strictly the case. The volume to which strain rate should be attributed is a *hollow* cone around the die entry as shown in figure 2.9.

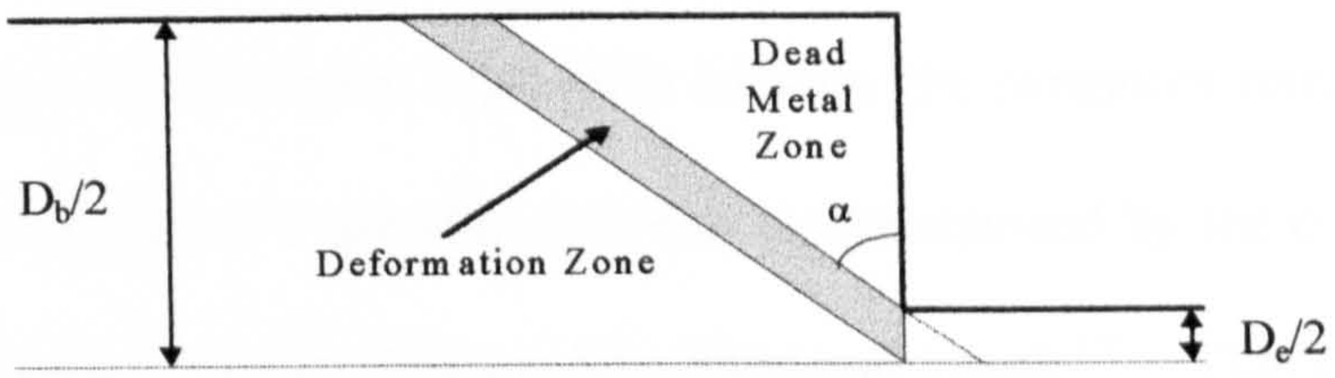

Figure 2.9. Assumptions made for present study.

Following working by Feltham [58] the volume of the deformation zone is:

$$\text{Volume} = \frac{\pi D_e^2 (D_b - D_e)}{4 \tan \alpha}$$

With this in mind and assuming volumetric incompressibility the mean equivalent strain-rate, may be calculated to be:

$$\dot{\bar{\varepsilon}} = \frac{4 D_b^2 V}{D_e^2 (D_b - D_e)} \ln R \tan \alpha \qquad (2.20)$$

This equation is similar to the one proposed by other workers [76] but does not account for deformation within the whole cone, but only part of it as shown in figure 2.9.

2.6.3. Extrudability

The commercial extrusion product must satisfy strict specifications in properties, geometry and appearance. Thus it is imperative that the extrusion process variables (ram speed, extrusion ratio and temperature) are controlled, in order to achieve these specifications. For example, extruding too quickly, i.e. if the ram velocity is too high,

will result in unsatisfactory surface finish, or using a billet temperature which is too low, will render the extrusion impossible because the pressures required will be too high. This behaviour of a specific alloy can be summarised by the construction of an extrusion limit diagram, first proposed by Hirst and Ursell [74]. This diagram identifies the operating area for the alloy by positioning a specific pressure line to denote the load limitation and an incipient melting line for the temperature limitation. A typical extrusion limit diagram is shown in figure 2.10.

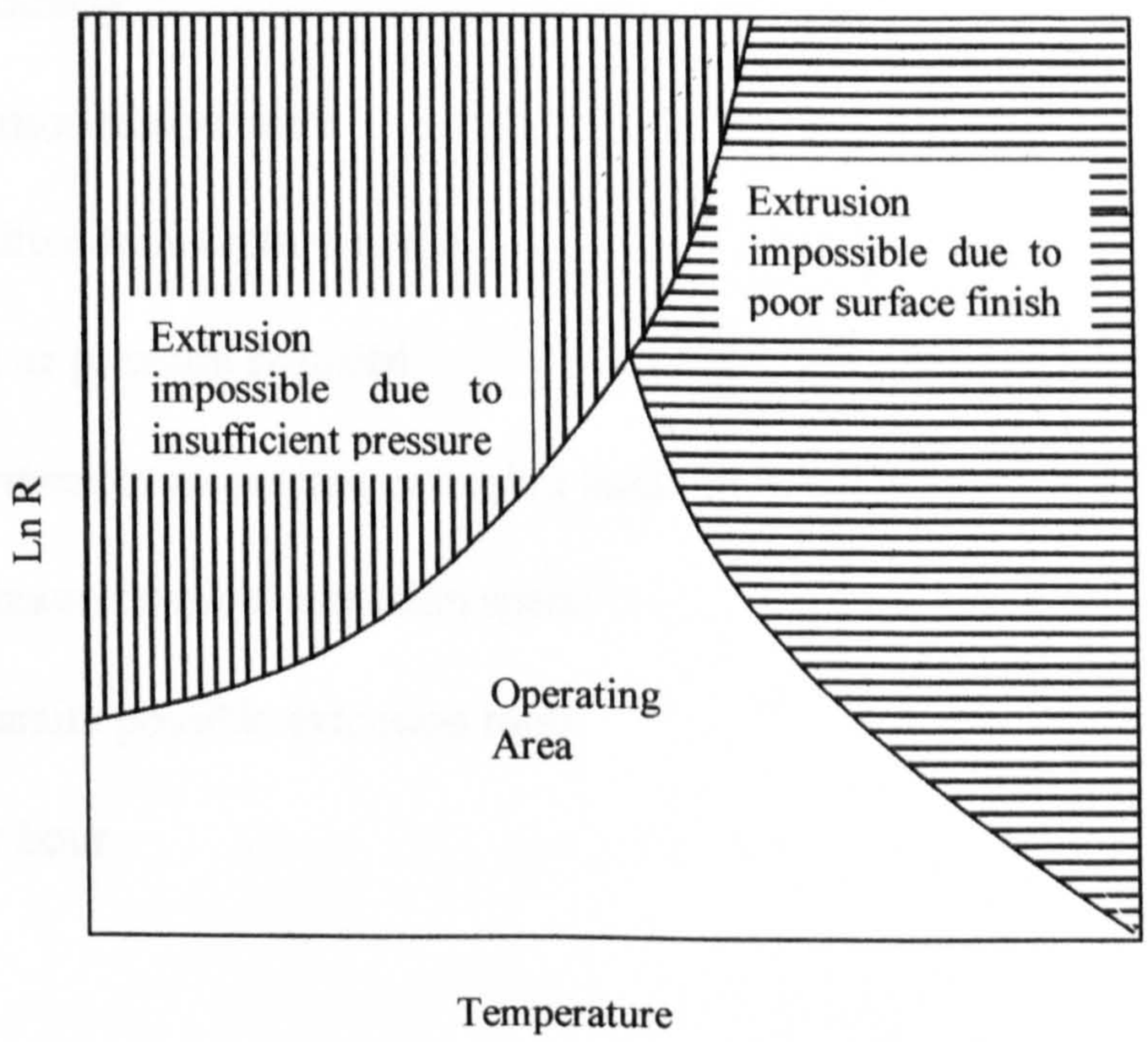

Figure 2.10 Typical Extrusion Limit Diagram

The construction of extrusion limit diagrams is beyond the scope of this study but has been discussed extensively elsewhere [57, 63, 74, 78]. It is important to note, however, that within the operating area of the press may be more lines, which contain structural or topological information (such as the formation of pick up or die lines) [78].

In a large number of previous studies, extrudability has been defined as the maximum extrusion velocity that is possible without compromising the surface finish quality of the profile [10, 16, 36, 38, 79, 80, 81]. Laue and Stenger [64] identified a *workability* term (the ratio of the flow stress, under given conditions, to the ductility of the alloy) as a deformation parameter, which can be used as a relative value for extrudability. However, extrudability is assessed according to a large variety of parameters, which may include [64]:

a. Workability
b. Extrusion temperature
c. Permitted temperature range
d. Load or pressure required
e. Exit speed at a constant extrusion load
f. Maximum possible extrusion speed
g. Maximum possible extrusion ratio
h. £ per hour

It is generally accepted that the comparison of the extrudability of alloys is difficult since many factors may influence the results. For example, the homogenising practice of the billet may influence the maximum extrusion speed. Other factors such as extrusion temperature or even billet length affect the way a billet extrudes. If extrusion is to be performed at conditions along the line of poor surface finish in figure 2.10 then the problem in assessing extrudability is no longer limited to productivity but also to quality. There now exists the need to distinguish 'good' from 'poor' extrusion quality [82].

A standard extrudability die was proposed by Lang and Castle [46]. This die consisted of two solid bars connected by a thin rod. One of the bars had 15 'ribs' attached to it, each with an area of 1 mm^2. Abrasion or breakage of the ribs helped the workers detect poor extrudability. Other workers [10, 83] modified the die proposed by Lang and Castle [46] but the methodology followed to measure extrudability continued to be consistent with previous work.

Limiting flow rate during extrusion was again used as a measure of assessing extrudability by Bondarev et al. [84]. This was associated to the resistance of the material to deformation in a similar way as the present study associates the length ratio to the resistance to deformation (see chapter 5). The flow stress of the material was used to quantify the resistance to deformation and the value of the limiting flow rate, V_M, was found to approximately obey the following law:

$$\mathrm{Log}V_M = a + b\bar{\sigma}^{-1/2}$$

Where a and b are constants and $\bar{\sigma}$ is the flow stress of the alloy.

Laue [85] suggested that the shape of a profile influences the difficulty with which an alloy can be extruded, even if the extrusion ratio remains the same. The study classifies profile shape into 13 categories according to the difficulty to extrude. In a subsequent study [86] a shape factor, λ, is introduced in order to quantify this influence of the profile shape. Thus, the influence of the die geometry can be partly included in the analysis of the extrusion process. Table 2.4 shows both the classifications.

Category	Section Type	Example	λ
A	Simple bar		2.8
B	Shaped bar	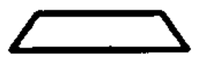	
C	Standard sections		4.8
D	Simple solid sections		6.8
E	Semi-hollow sections	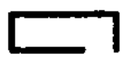	21
F	Sections with abrupt changes, thin walls, wide sections		54
G	Sections with difficult tongues, narrow inlets	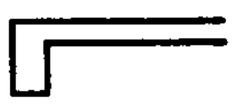	46
H	Tubes		40
J	Simple hollow sections		82
K	Difficult hollow sections		90
L	Tubes with projections		120
M	Tubes with internal projections		130
N	Large or wide hollow sections	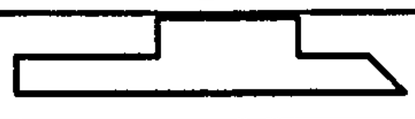	N/A

Table 2.4. Influence of shape on extrudability (After Sheppard [86])

Sheppard [86] stated that one measure of extrudability of an alloy could be considered its flow stress, since this parameter determines the pressure locus on the extrusion limit diagram. A classification of alloy extrudability has been established from empirical evidence and the experience of professional extruders. This classification is based on how difficult an alloy is to extrude and is expressed as a percentage of the extrudability of AA6063. Table 2.5 displays a selection of alloys and their relative extrudability as described above – the larger the extrudability number the more extrudable the alloy.

Alloy	Extrudability	Alloy	Extrudability
1000	150	5052	60
1100	137	5083	20
3003	101	2024	15
6063	100	2011	15
6105	89	7075	10
6061	60		

Table 2.5 Experts' Extrudability Chart (After Mondolfo and Peel [21])

A study by Mondolfo and Peel [21, 87] attempted to further the premise of resistance to deformation by using a two-hole die and comparing the lengths of rod extruded through each orifice. This study is discussed in more detail in chapter 5. On a related subject, the mechanics of two-hole extrusion was investigated by means of a two-dimensional upper bound model [88, 89]. However, the study did not intend to analyse the extrudability issue but rather to formulate a model that would be able to assist in the solution of problems such as the determination of die land lengths or the optimisation of the positions of die orifices.

The effects of alloying additions on extrudability have been discussed in section 2.4. Apart from alloying additions though, other factors have been reported to affect extrudability. Reiso [8, 10] reported that the extrudability of aluminium alloys is affected by the homogenisation treatment of the billet and especially the cooling rate after homogenisation. This is due to the coarse Mg_2Si particles, which result from a slow cooling rate and cause a decrease in the maximum extrusion velocity. Scharf and Lossack [79] showed that there exists a relationship between the maximum extrusion

velocity and the dendritic cell size. Thus, as the grain size in the extrusion billet decreases, there is a corresponding increase in the extrudability of the alloy.

Many studies have been performed which relate a variety of factors (both microstructural and process related) to the extrudability of aluminium alloys. However, as discussed above, extrudability is a parameter that is very difficult to determine and compare. In the following chapters, the concept of extrudability is discussed further and a standard test is proposed.

2.6.4. Constitutive Equations:

Tests to assess the hot working characteristics of materials are normally carried out in compression or torsion. There are certain disadvantages to both methods and the selection of the process is usually down to the range of strains and strain-rates to be used. Compression tests can only be carried out to moderate strains and friction with the platens causes barrelling and hence non-uniform strains and strain rates. A relatively constant strain rate can be achieved by gradually reducing the anvil velocity through the test. Conversely, torsion can achieve unlimited strain, but both strain and strain-rate vary radially through the sample even if twisting is performed at a constant rate [90-92]. To alleviate this problem it was suggested that hollow specimens be used[93].

Flow stress dependence on strain rate and temperature:

A number of studies have compared the hot working conditions for simple metals and alloys to the conditions existing during creep [94-99]. Hence the same form of empirical equations were employed:

$$\dot{\varepsilon} = A'\overline{\sigma}^{\eta} \qquad (2.21a)$$

or

$$\dot{\varepsilon} = A''\exp(\beta\overline{\sigma}) \qquad (2.21b)$$

or

$$Z = \dot{\varepsilon}\exp\left(\frac{Q}{GT}\right) = A\left[\sinh(\alpha\overline{\sigma})\right]^{n} \qquad (2.22)$$

where $A, A', A'', \alpha, n, \eta, Q, G = 8.314$ kJ/mol/kg and $\beta=\alpha\eta$ are constants for a material of known microstructure and strain history. Equation 2.21a has proved the most appropriate for low stresses where the strain rate ranges between 10^{-8} s^{-1} and 10^{-4} s^{-1}. For higher strain rates (ranging from 10^{-3} to 10^{2} s^{-1}) equation 2.21b is deemed more suitable. Over the entire range, equation 2.22 is accepted to approximate the previous two equations at extreme $\overline{\sigma}$ [100]. This equation is known as the *Zener-Holomon equation* and the Z term is the Temperature Compensated Strain-Rate or the Zener-Holomon parameter. In many Al alloys the 150 kJ/mol value which is found as the activation energy, Q, is approximately equal to the activation energy for self diffusion (vacancy diffusion) and as such is consistent with restoration by dynamic recovery. The specifics of dynamic recovery will be discussed in a subsequent section but briefly, it can be described as follows:

During hot working, grains elongate in the primary deformation direction and contract in the others. This results in an increase in the flow stress because of the increase in

dislocation density and work hardening. At the same time within the deforming grains a substructure - usually equiaxed - is developed by dislocation annihilation and formation of low angle grain boundaries. In high stacking fault energy (SFE) materials such as aluminium alloys, the recovery process completely balances any strain hardening and a steady state is achieved.

In a more recent study [101] considering viscoplastic flow during hot torsion, it was suggested that the introduction of an internal variable into equation 2.22 could characterise the present state of the material as follows:

$$\dot{\varepsilon}_{vp} = A\left[\sinh\left(\frac{\bar{\sigma}}{s}\right)\right]^{n} \exp\left(-\frac{\Delta H}{GT}\right) \qquad (2.23)$$

where $\dot{\varepsilon}_{vp}$ is the rate of viscoplastic strain and s is the internal state variable which varies as follows:

$$\dot{s} = \chi(s_m - s)\dot{\varepsilon}_{vp} \qquad (2.24)$$

where $\chi s_m \dot{\varepsilon}_{vp}$ represents the assumed linear strain hardening and $-\chi s\dot{\varepsilon}_{vp}$ represents the strain softening due to dynamic recovery. s_m is the saturation value of the internal state variable, s, which is attained when a steady state sub-structure has been formed, and χ is a constant. It is obvious now that at steady state $\dot{s} = 0$ because $s=s_m$ (in high SFE materials no residual work hardening exists as it is completely balanced by the dynamic restoration processes [101]) and the steady state flow stress, $\bar{\sigma}_s$, can now be described as:

$$\overline{\sigma}_s = s_m \sinh^{-1}\left[\frac{\dot{\varepsilon}}{A}\exp\left(-\frac{\Delta H}{GT}\right)\right]^{1/n} \qquad (2.25)$$

Another relationship that has been used to calculate flow stress of materials is:

$$\overline{\sigma} = \sigma_0 + (\sigma_s - \sigma_0)\left[1-\exp\left(-\frac{\varepsilon}{\varepsilon_r}\right)\right]^m \qquad (2.26)$$

where $\overline{\sigma}$ is the equivalent flow stress, σ_0 is the initial flow stress, σ_s is the steady state flow stress and ε_r is the relaxation, or transient, strain constant. Amongst others, this relationship was used by Shi et al. [102] in the development of a thermomechanical model of processing operations of aluminium alloys. ε_r is determined from the following relationship:

$$\varepsilon_r = -0.1\left\{\ln\left[1-\left(\frac{\sigma_{0.1}-\sigma_0}{\sigma_s-\sigma_0}\right)^{1/m}\right]\right\}^{-1} \qquad (2.27)$$

as used for steels, where $\sigma_{0.1}$ is the flow stress at a permanent strain of 0.1 and m is the strain-rate sensitivity. However $\sigma_{0.1}$ is well into the hardening range and inadequately describes the hot deformation of aluminium alloys. To better approximate the behaviour of these it was found by work hardening and recovery analysis that

$$\varepsilon_r = a\sigma_s^2 \qquad (2.28)$$

where a is constant. This model (equation 2.26) was found to approximate very well the stress strain behaviour of the aluminium alloys tested (1xxx and 3xxx series).

2.6.5. Dynamic Recovery

As mentioned earlier, the basic mechanism of high temperature recovery is the movement of dislocations resulting from plastic deformation, into subgrain or cell boundaries. If this occurs during deformation it is termed *dynamic* recovery.

The driving force for recovery is derived from the strain energy stored in the metallic system due to plastic deformation. Since the free energy of the system is directly linked to the strain energy, a thermodynamic driving force for recovery is established. The simplest form of recovery is the interaction of two dislocations of opposite sign on the same slip plane; this would result mutual annihilation, but does not, however, lead to any significant softening in the material. In non-ideal alloys, dislocations must re-order, i.e. more dislocations are required to slip in and out of their preferential slip planes to avoid sessile locking.

The extent to which any observable recovery occurs, in a material, depends on the ability of the dislocations to move from one slip plane to another, which contains the screw component of their Burger's vector. This effect is called *cross-slip* and can occur by one of two mechanisms, depending on the strain rate.

At high strain rates cross-slip is achieved by the formation of a stair rod dislocation to allow for the extended dislocation to move from one slip plane to the other. In high SFE alloys, however cross-slip is achieved by thermally activated cross-slip which is

normal at creep strain rates. The mechanism involves the constriction of the extended dislocation as shown in figure 2.11. Constriction is the thermally activated process which involves the two partials uniting to form a total dislocation of length L. The dislocation then breaks into two partials on the cross slip plane. Finally, if sufficient shear stress is present, the extended dislocation moves onto the slip plane. The length of the constriction has a critical value: Below this the constriction is unstable and collapses back to its original slip plane.

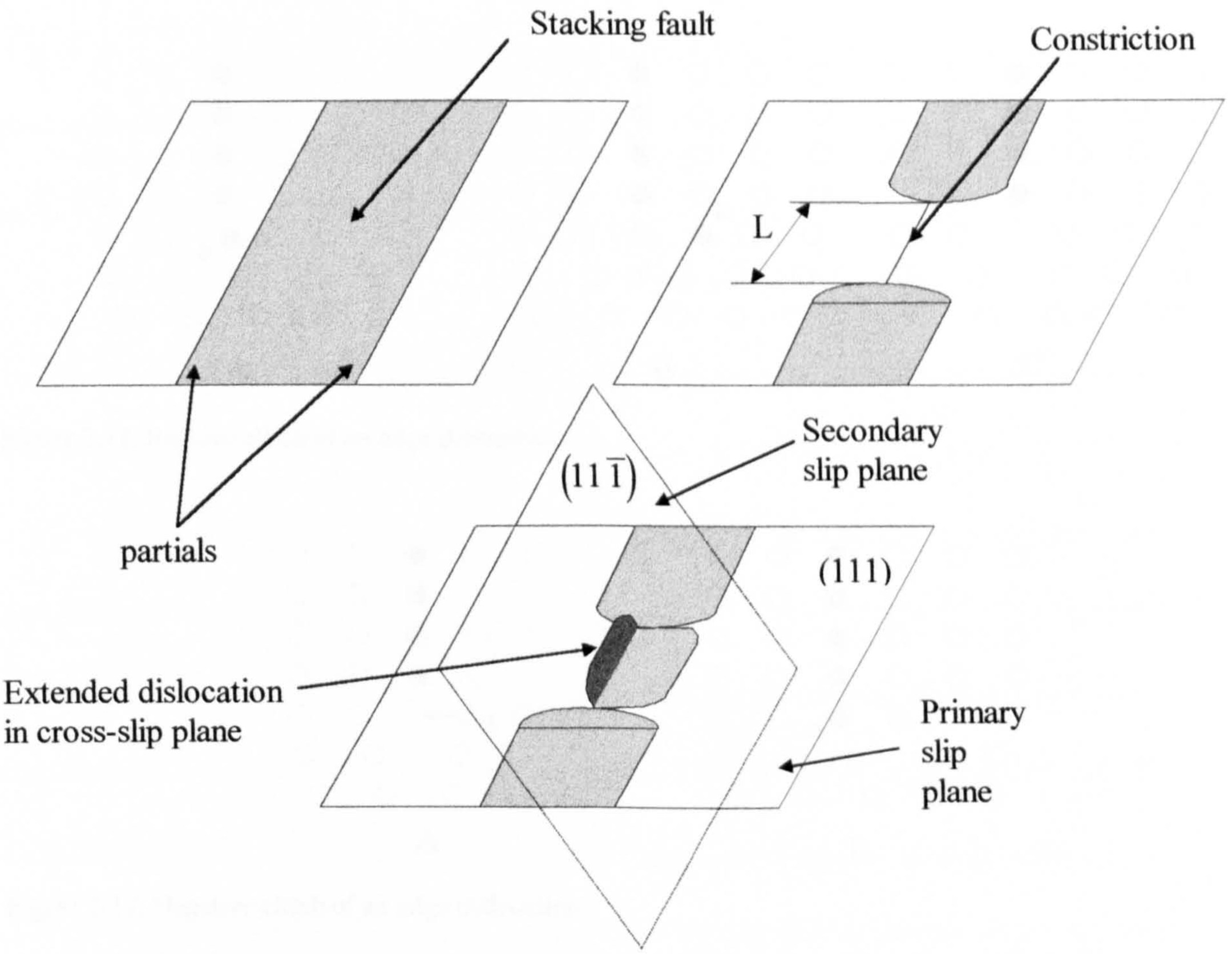

Figure 2.11. Thermally activated cross-slip of an extended dislocation.

Note that the constriction process requires additional strain energy, so it is easier for a total dislocation rather that an extended dislocation to cross-slip.

Because of the high SFE it is now obvious that cross-slip is easy in Al alloys and α-Fe at any strain rate, so the predominant softening mechanism is dynamic recovery.

Cross-slip is the movement of the screw component of dislocations. Edge dislocations move by means of climb. Simple climb of edge dislocations depends on the diffusion of vacancies towards (positive climb) or away (negative climb) from the dislocation. These processes are depicted graphically in figures 2.12 and 2.13. Atom a is the atom which moves in the opposite direction to the vacancy and atom c (grey) represents the next atom of the edge lying just beneath the plane of the paper.

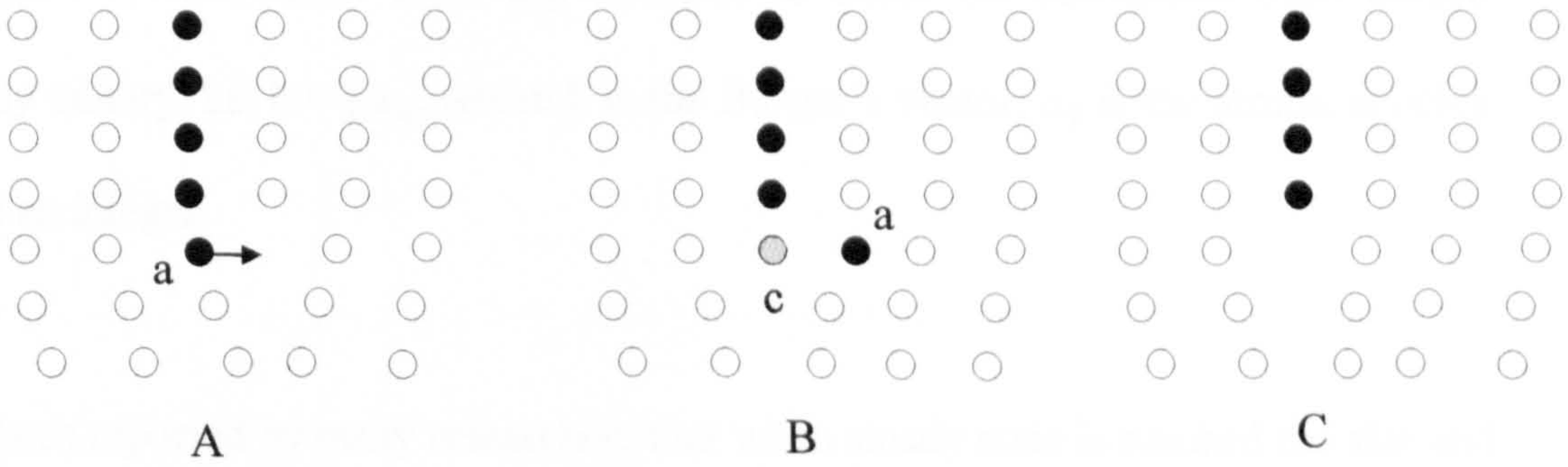

Figure 2.12. Positive climb of an edge dislocation.

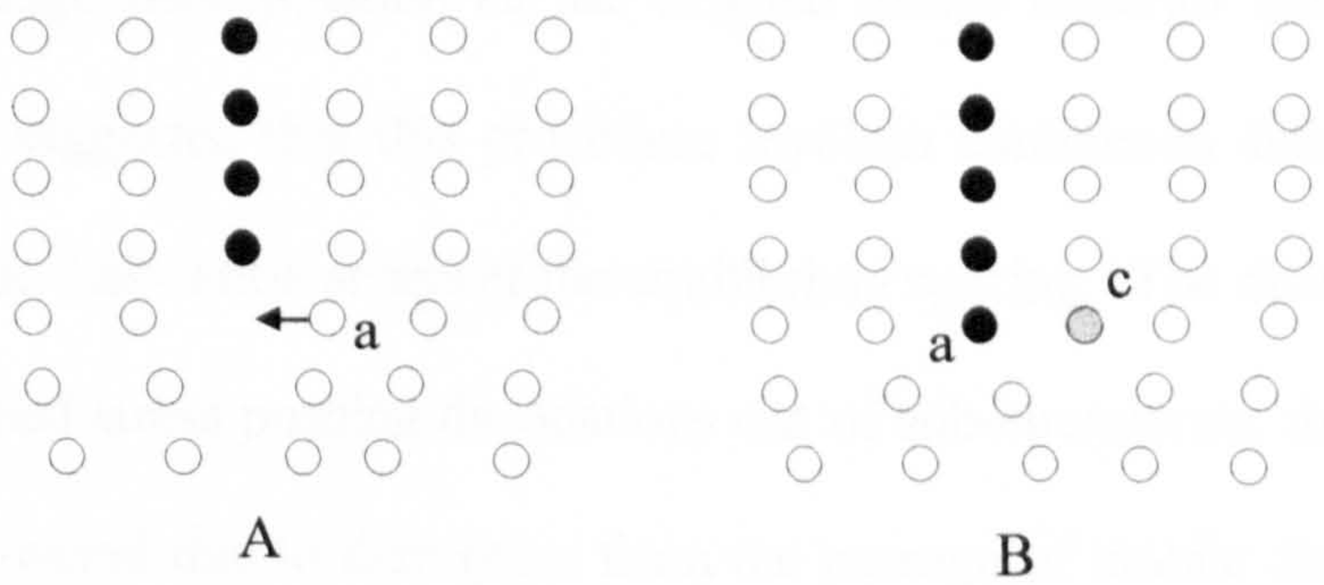

Figure 2.13. Negative climb of an edge dislocation.

In cold working conditions, dislocation climb is not activated (due to the lower temperature) and therefore recovery must depend on cross-slip alone. Hence, the flow stress increases with temperature due to the inability of the recovery rate to keep up with the work hardening rate. Although subgrains formed under these conditions do not change size with respect to their number density, they do elongate, however, in the

direction of flow under the applied stress. As the temperature rises or the strain rate is lowered, the steady state subgrains adopt a larger, more perfect shape [95]. The subgrain diameter varies according to equation 2.26.

$$d_s^{-1} = a + b \ln Z \qquad (2.26)$$

where d_s is the subgrain diameter, Z is the Zener-Hollomon Parameter and a and b are constants [103]. For either cross-slip or climb to occur the dislocation must remain perfectly unitary, i.e. $b = j\, a_{sp}$, where b is the Burger's vector, a_{sp} is the atomic spacing and j is an integer.

It has been reported by many researchers that when steady state is reached the size and shape of the subgrains remains constant. For this to occur, the subgrain boundaries must be able to change their position as the original grains undergo deformation. McQueen et al. [104] suggested that this procedure involves continuous disintegration and reformation of the dislocation arrays at the equilibrium spacing. The disintegration proceeds by the applied stress pushing dislocations out of sub-boundaries, the stability of which has been lowered due to disruption from the passage of mobile dislocations. The process is assisted by a limited amount of sub-boundary migration, which is made possible by the enhanced climb of dislocations produced by the deformation. The overall process is termed *repolygonisation*.

It is well established that the subgrain boundaries are low angle boundaries [95, 104, 105]. Misorientations were observed to lie between 1 and 4 degrees.

The energy which acts as a driving force for the formation of dislocation arrays is derived from the external energy applied during the hot working process. Most of this energy is dissipated in the form of heat. A small portion of it, though, is stored by the material as elastic strain energy. An additional amount is retained in the form of point defects and acts as a driving force to the movement of vacancies in the structure. The total amount of stored energy was reported to be in the range of 0.4 - 4 kJ/kg [106], and it may be released, partly or fully, during the recovery process, by the rearrangement of the dislocation tangles and the eventual formation of low angle sub-boundaries by dislocation climb and glide.

Low angle grain boundaries are low energy configurations consisting of vertical arrays of dislocations on a number of parallel slip planes. The compressive region of a dislocation is counteracted by the tensile region of the adjacent one. This effect lowers the strain energy present in the crystal and is called *polygonisation*. The process described above refers to single crystal materials; where polycrystalline materials are concerned the polygonisation process is much more complex.

The first observation of a subgrain structure in a metallic system was in 1951 by Gay et al. [107], who deduced the existence of a dislocation cellular network, the outer walls of which had a very high dislocation density, whereas the interior was for all intents and purposes dislocation free.

Sheppard [108] suggested a mechanism for the formation of low angle grain boundaries (or tilt boundaries) considering hot deformation activated climb. Piled-up dislocation climb perpendicular to the glide plane (111). By this process a tilt boundary is formed

which grows by further migration of dislocations. Since edge dislocations glide in the (111) plane in the [101] direction, the tilt boundary can be expected to form on the (101) plane. Similarly pure twist boundaries form on the $(11\bar{1})$ cross-slip plane. The (111) [101] slip system, though, is the least active slip system in the fcc lattice and hence the pure twist nature of the boundary is less likely to be destroyed by the slip of mixed dislocations in the $(11\bar{1})$ plane. Clearly, on activation of further slip systems, sub-boundaries may be formed on other slip planes by the same process. Generally boundaries will be of a mixed nature, having both twist and tilt components.

Subsequent annealing of the dynamically recovered structure resulted in the sub-boundaries becoming more distinct and the interior becoming further depleted of dislocations. The sharpness of the cell walls was found to be dependent on the SFE of the material, hence metals such as aluminium and ferritic iron alloys exhibit well defined cellular structures which become much sharper during subsequent heat treatment.

2.7. Non Equilibrium and Metastable Phase Transformations.

Heat treatable alloys, Al-Mg-Si, Al-Cu and Al-Mg-Zn alloys, gain their strength from a fine dispersion of metastable particles. Such particles are intermediate stages before the formation of the equilibrium phase - for Al-Mg-Si alloys this is Mg_2Si and for Al-Cu alloys $AlCu_2$. The process by which precipitation of metastable precipitates occurs is called age hardening.

The hardening sequence in Al-Mg-Si alloys is shown below:

$$\text{GPzones} \rightarrow \beta'' \rightarrow \beta' \rightarrow \beta(Mg_2Si)$$

GP zones manifest themselves as very small, spherical clusters of Mg and Si atoms which very early grow into needles of β″, the major axis being along the [100] direction. β″ has been reported to have a monoclinic structure with a = b = 6.16 Å, c=7.1 Å and γ = 72° and orientation relationship with the matrix [5]:

$$(100)\ \beta'' \parallel (110)_{Al}\ ;\ [110]\ \beta'' \parallel [001]_{Al}$$

These needles are coherent with the matrix (although some compressive coherency strains have been reported, [5] which, in some cases, may reach the yield point) and vary in size from 16 to about 200 nm in length and 1.5 to 6 nm in diameter. Guinier and Lambot [109] and later, Thomas [110] observed a second form of zones, needle-like in appearance which comprised of a row of Si atoms bounded by two rows of Mg atoms. The dimensions of these zones were 10-20Å wide and about 100Å long. It is the opinion of the present worker that these were simply β″ needles at the beginning of their formation.

During further growth, the needles begin to lose coherency with the matrix and grow into rods of a phase termed as β′. This metastable phase is reported to have a cubic [5] (a = 6.42 Å) or a hexagonal lattice [111, 112] with a = 7.05 Å, c = 4.05 Å. It forms an orientation relationship with the matrix as follows [112]:

$$(001)\ \beta' \parallel (100)_{Al}\ ;\ [100]\ \beta' \parallel [011]_{Al}$$

These semi-coherent rods reach a maximum size of approximately 0.03 μm before softening begins. This represents a figure, which is an order of magnitude less than that observed in other age hardenable alloys (e.g. 2xxx series) [5].

AA6061 alloys (which contain a small amount of Cu) have been reported to contain an additional metastable particle (which to avoid confusion will be designated B′) similar in structure to the quaternary phase Q ($Al_5Cu_2Mg_8Si_6$) [113]. This precipitate was lath-like in appearance and was seen to occupy any of four habit planes: $(\bar{1}50)_{Al}$, $(150)_{Al}$, $(510)_{Al}$ or $(5\bar{1}0)_{Al}$. The most possible structure for B′ was considered to be hexagonal with a = 10.4 Å and c = 4.05 Å. The four possible orientation relationships with the matrix are:

$$[10\bar{1}0]_{B'} \parallel (\bar{1}50)_{Al}$$

$$[10\bar{1}0]_{B'} \parallel (150)_{Al}$$

$$[10\bar{1}0]_{B'} \parallel (510)_{Al}$$

$$[10\bar{1}0]_{B'} \parallel (5\bar{1}0)_{Al}$$

The final phase in the ageing sequence is equilibrium Mg_2Si or β. This appears as platelets and its structure has been established as that mentioned earlier. The orientation relationship with the matrix is [5, 111, 112]:

$$(100)_{Mg2Si} \parallel (100)_{Al} ; [110]_{Mg2Si} \parallel [001]_{Al}$$

Westengen and Ryum [111] observed a separate form of β precipitates, which appeared to have a cubic morphology, if the samples were quenched rapidly enough in water after solutionising. The orientation relationship with the matrix was shown to be:

$$(001)_{Mg2Si\text{-}cubes} \parallel (001)_{Al} ; [100]_{Mg2Si\text{-}cubes} \parallel [100]_{Al}$$

2.8. Precipitation Ageing

2.8.1. The precipitation process

The phases mentioned above represent the hardening particles of AlMgSi alloys. In order for the sequence of particles to begin nucleating and grow, a low temperature heat treatment is required known as Artificial Ageing. Consider the phase diagram in figure 2.12. Each intermediate phase has its own solvus line. Consider an alloy of composition X_1 held at a temperature T_1. Obviously, at this temperature, all the alloying component is held in solid solution. If the alloy is subsequently quenched rapidly to room temperature, the alloy will become supersaturated - because diffusion is suppressed by the speed of the quench - and a massive driving force for precipitation is achieved.

Increasing the temperature now to a value below T_3 will result, not in the formation of the equilibrium phase, but the formation of small precipitates of phase 1 (which are normally rich in the alloying element). This may be explained by the relative activation energy barriers required to form each of the transition phases. Because the change in structure between the transition phases is relatively small - compared to the equilibrium phase - and the loss of coherency of the particles with the matrix is gradual, the activation barrier for the formation of each intermediate phase is less than that of the equilibrium phase. This is represented graphically in figure 2.15.

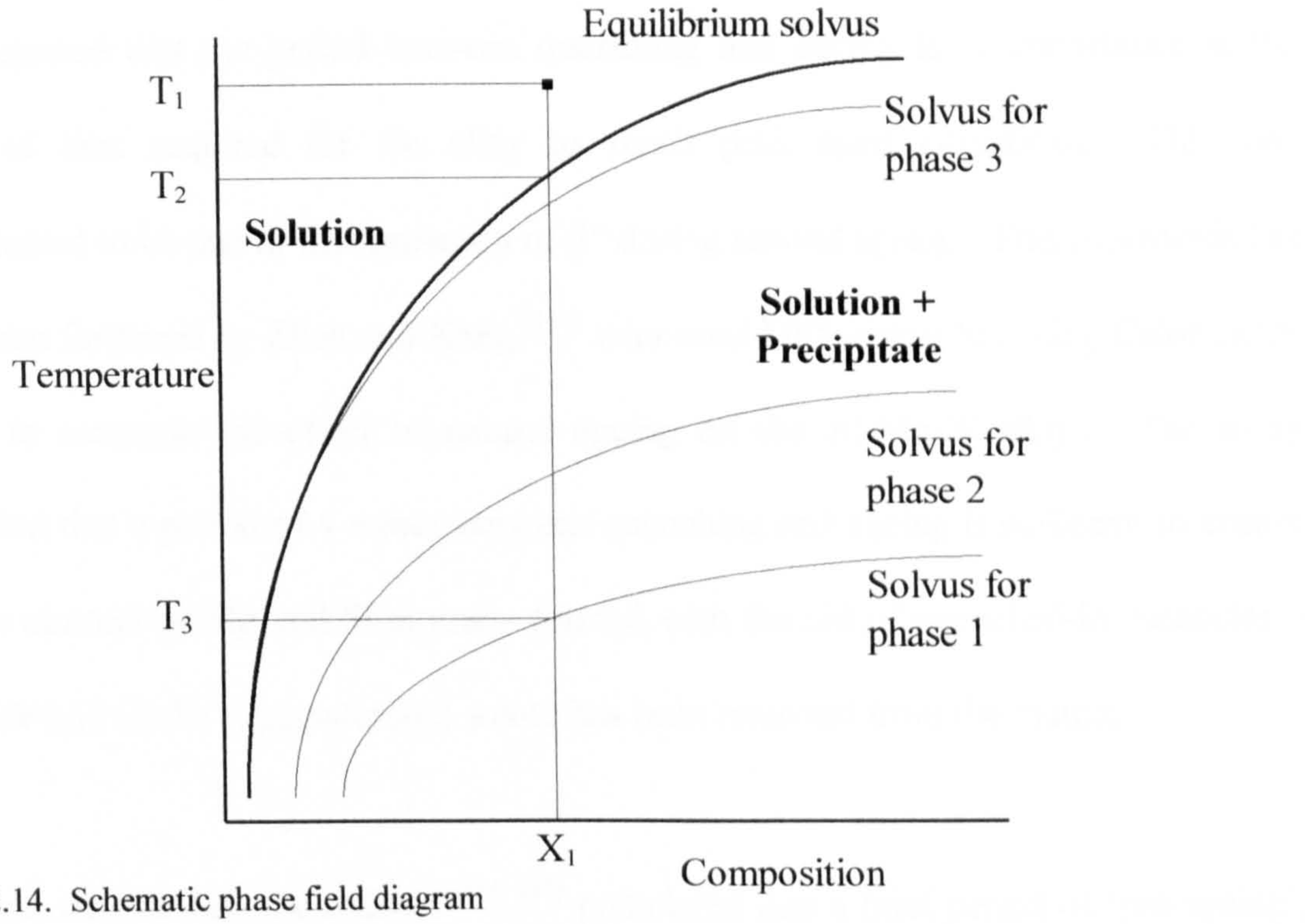

Figure 2.14. Schematic phase field diagram

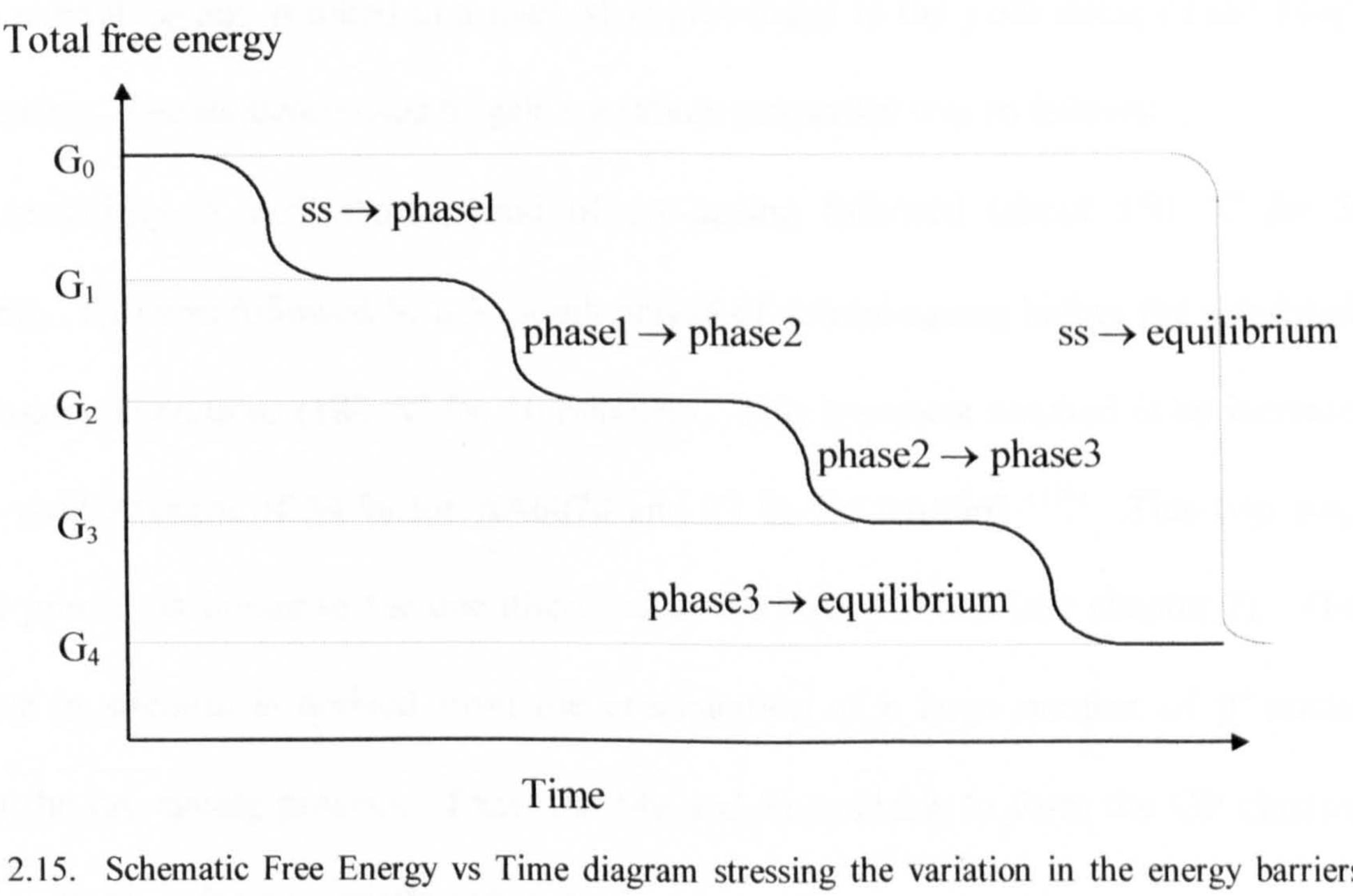

Figure 2.15. Schematic Free Energy vs Time diagram stressing the variation in the energy barriers between the transition phases, compared to the direct formation of the equilibrium phase from solid solution (ss). (After Porter & Easterling [114])

A variety of studies have been performed regarding the ageing process. Pashley et al. [115] suggested that the period between quenching and ageing is of importance in the length of time required for the alloy to reach peak aged conditions. This was hypothesised to be due to the formation of β″ during natural ageing. This hypothesis has since been furthered by Zhen and Kang [116] who used Differential Scanning Calorimetry (DSC) to ascertain the effect of natural ageing on the Al-Mg-Si alloys. The study concluded that a period of 4 weeks between quenching and ageing is sufficient to ensure that the clusters of Mg and Si atoms – formed with the aid of quenched-in vacancies – are stable and all the supersaturated solute has been removed from the matrix.

Moving a step further, the authors [116, 117] postulated that a brief period of 'pre-ageing', before natural ageing, resulted in a marked improvement in the yield stress of the alloy after ageing. The sequence used to gain maximum properties was as follows:

After quenching, a very short period of pre-ageing followed (about 150 °C for 5 minutes). This was followed by a 3-month period of natural ageing before the simulated paint baking conditions (180 °C for 30 minutes). This treatment resulted in an increase in the yield strength of 34 % for AA6070 and 23 % for AA6063 [116]. This two step ageing process is similar to the one discussed in the present study (see chapter 7). The increase in strength is derived from the precipitation of a large number of β″ nuclei during the pre-ageing process. Thus, the Mg and Si available to form the GP clusters during natural ageing are greatly reduced.

It has also been postulated [120] that a treatment involving a cyclically changing ageing temperature, of the same length as a conventional ageing treatment, can lead to the improvement of properties such as toughness and plasticity. However, the strength characteristics of the alloy are somewhat decreased in comparison to conventional

ageing. This was hypothesised to be due to the more dispersed precipitation of the metastable hardening phases that was induced by the thermal cycling treatment.

Westengen and Ryum [111], who suggested the new cubic form of the β precipitates, postulated that these could be formed using a two step ageing technique. The two stages are (a) the high temperature annealing (550 °C) and (b) a lower temperature process (180 – 350 °C) that causes the precipitation of the β. The first stage of the ageing process was said to form vacancy/solute atom agglomerates and quench vacancies, which acted as nucleation sites for the β precipitates.

The use of two step ageing treatments are also common in 7xxx series alloys. This is also known as 'duplex ageing'. Fuelled by the need for aircraft alloys with high strength to weight ratios in the 1930s and 1940s, alloys belonging to the 7xxx received special attention regarding their ageing response. Similar to the alloys of the 2xxx series, it was found that the common practice of ageing at a single temperature resulted in an increase in the alloy's tensile strength. Ageing at a temperature within the range 120°C -135°C, the hardening response was due to the precipitation of GP zones. Ageing at temperatures within the range 160°C -170°C also resulted in an increase in strength due to the precipitation of a fine dispersion of η′ phase. Whilst the increase in strength was not as great as ageing in the lower temperature range, the increase in the alloy's resistance to Stress Corrosion Cracking (SCC) was significantly improved. The need for higher strengths, coupled with good SCC resistance, lead to the adoption of a two-step ageing treatment. The designated temper, T73, comprises of a first-step ageing treatment in the range 120°C -135°C followed by a second-step exposure in the temperature range 160°C -170°C. It was found that such a treatment resulted in precipitation of a finer dispersion

of the η′ phase in the second-step, which nucleated from the pre-existing GP zones from the first-step. The two step ageing treatment resulted in a slight reduction in the maximum obtainable strength in the T6 temper but resulted in an acceptable combination of high strength with good SCC resistance. For example, the tensile properties of 7075-T73 are some 15% below those for 7075-T6. In a similar study, Fridlyander et al. [118] describes the effect of a two step ageing process on the V95 alloy (Russian designation which approximates to AA7075). This involved ageing for 3 hours at 120°C and then up to 40 hours at a higher temperature (usually between 165 and 175 °C). The process results in a decrease in the time required to reach peak ageing conditions in the same way as it is shown in the present study. The same alloy was subjected to a step-like ageing process involving 15 minutes at 180 °C between two 24-hour periods at 120 °C [119]. This resulted in the improvement of the strength characteristics due to the refinement of the η′ phase distribution in the alloy. Further examples of this form of ageing treatment and its application can be found elsewhere [118,161-163].

2.8.2. Hardening Mechanisms

When particles are introduced into a matrix, the application of an external stress will cause the dislocations present therein to move and find ways in which to by-pass the particles. This can be done in a number of ways: dislocations can shear through them, climb over (or under) them or bow around them. Any of these techniques requires varying amounts of additional energy, thus providing an increase in the strength of the alloy.

Coherent particles - such as GP zones - allow the dislocations present to shear through them. The energy required to perform this depends on the size and distribution of the

particles and on the size of the misfit strain field around them. Thus, the strength of an alloy containing coherent particles will increase with increasing size, number and misfit of the precipitates. The shearing of a spherical particle by a dislocation is shown schematically in figure 2.16.

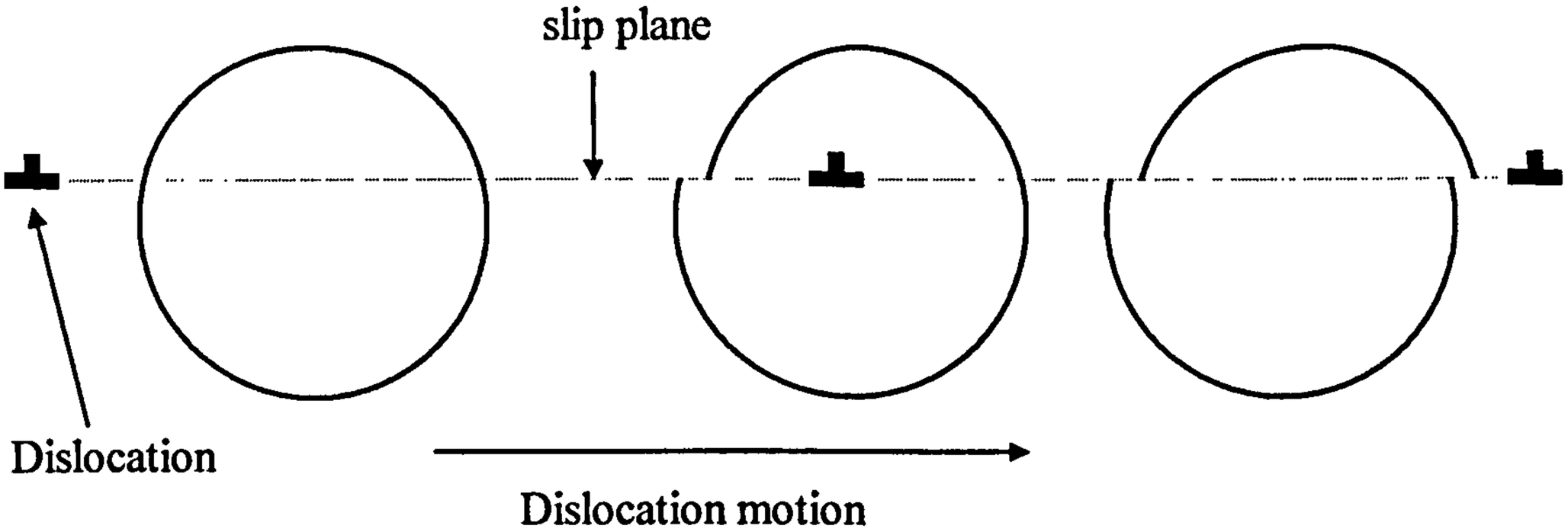

Figure 2.16. Dislocation shear of a coherent particle

Particles with one or more incoherent face cannot be sheared through the incoherent interface. Thus, the dislocation must devise another way to bypass the particle. For particles below a certain size, this is achieved by climb (described in section 2.6.5). The strength of the alloy is determined by the rate at which dislocations can climb around such particles without causing pile-ups. In hot working processes, as the strain rate increases, so does the dislocation generation, thus at low strain rates the size of particle which can be climbed is large. This decreases however as the number of dislocations in the matrix increases, so at high strain rates the only particles that can be climbed without generating pile-ups are very small ones. Therefore, in hot working processes, such as extrusion, the flow stress of the alloy depends on the strain rate.

Another mechanism, which is now believed to apply for larger particles (> 0.1 μm) [12], was proposed by Orowan in 1954 [121]. The mechanism, aptly named after its proposer,

involves the formation of dislocation loops around particles in its path. A schematic of the process is shown in figure 2.17.

Unlike climb, which depends on particle size to induce strengthening, the hardening due to Orowan bowing is inversely proportional to the interparticle spacing (equation 2.27)

$$\tau = \frac{2G_s b}{S_p} \qquad (2.27)$$

where τ is the shear stress required for a dislocation to bow around a particle, G_s is the shear modulus, b is the dislocation's Burger's vector and S_p is the interparticle spacing.

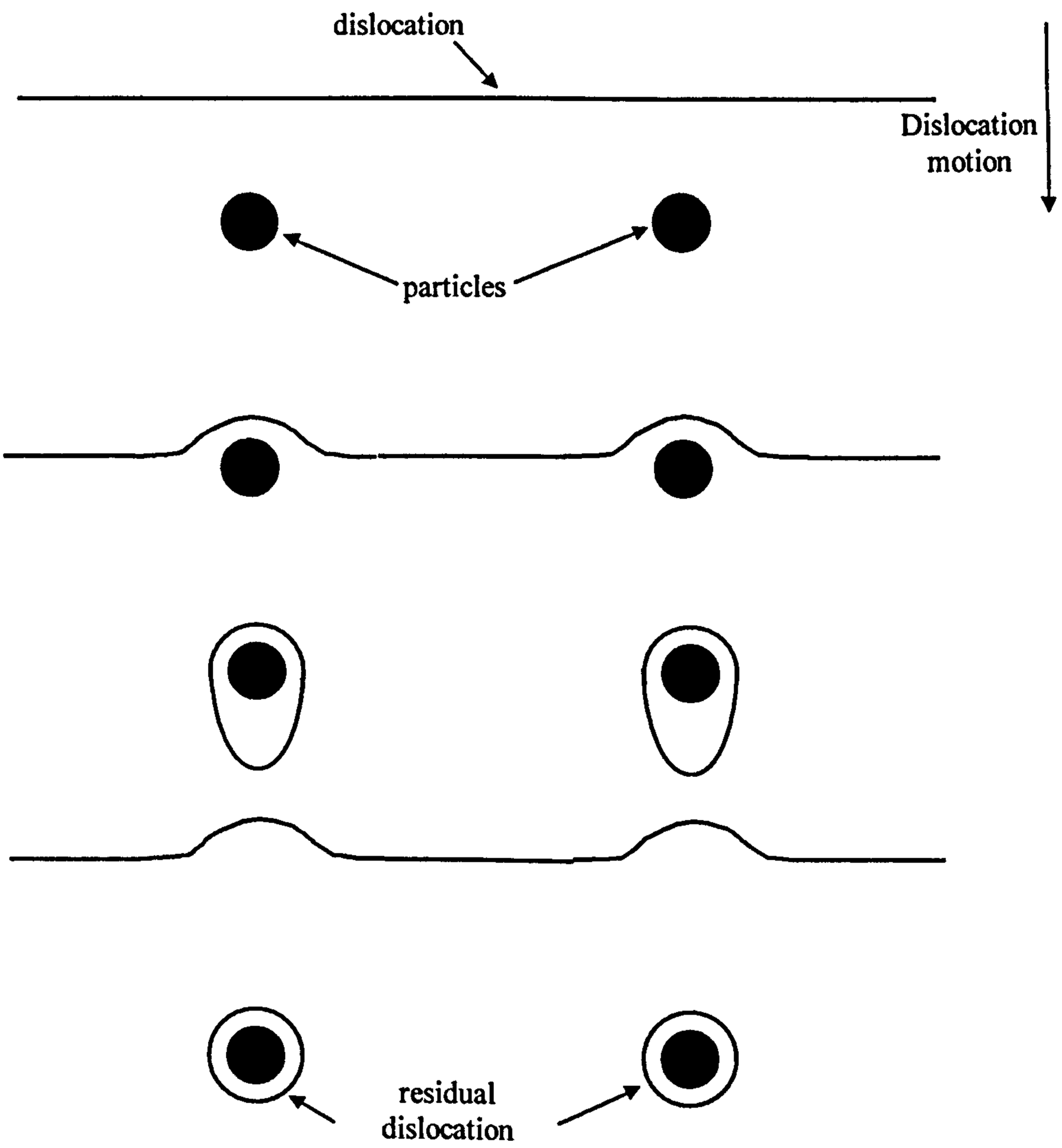

Figure 2.17. The Orowan bowing mechanism (After Orowan [121])

Chapter 3

Theory

Nomenclature – Chapter 3

F_E	Extrusion Force
F_C	Frictional Resistance the container interface
F_D	Deformation Force
F_F	Frictional Resistance at the die land
P_E	Extrusion Pressure
R	Extrusion Ratio
p_i	Pseudo billet radius
d	Die land length
r_1, r_2	Orifice radii
r_0	Billet radius
τ	Shear stress
$\bar{\sigma}$	Flow stress
L	Length of billet remaining in the container
w_a	External work
ε	Strain
V_0	Initial billet volume
V_i	Extrudate volume

3. Theory

3.1. Force Balance in Axisymmetric Extrusion:

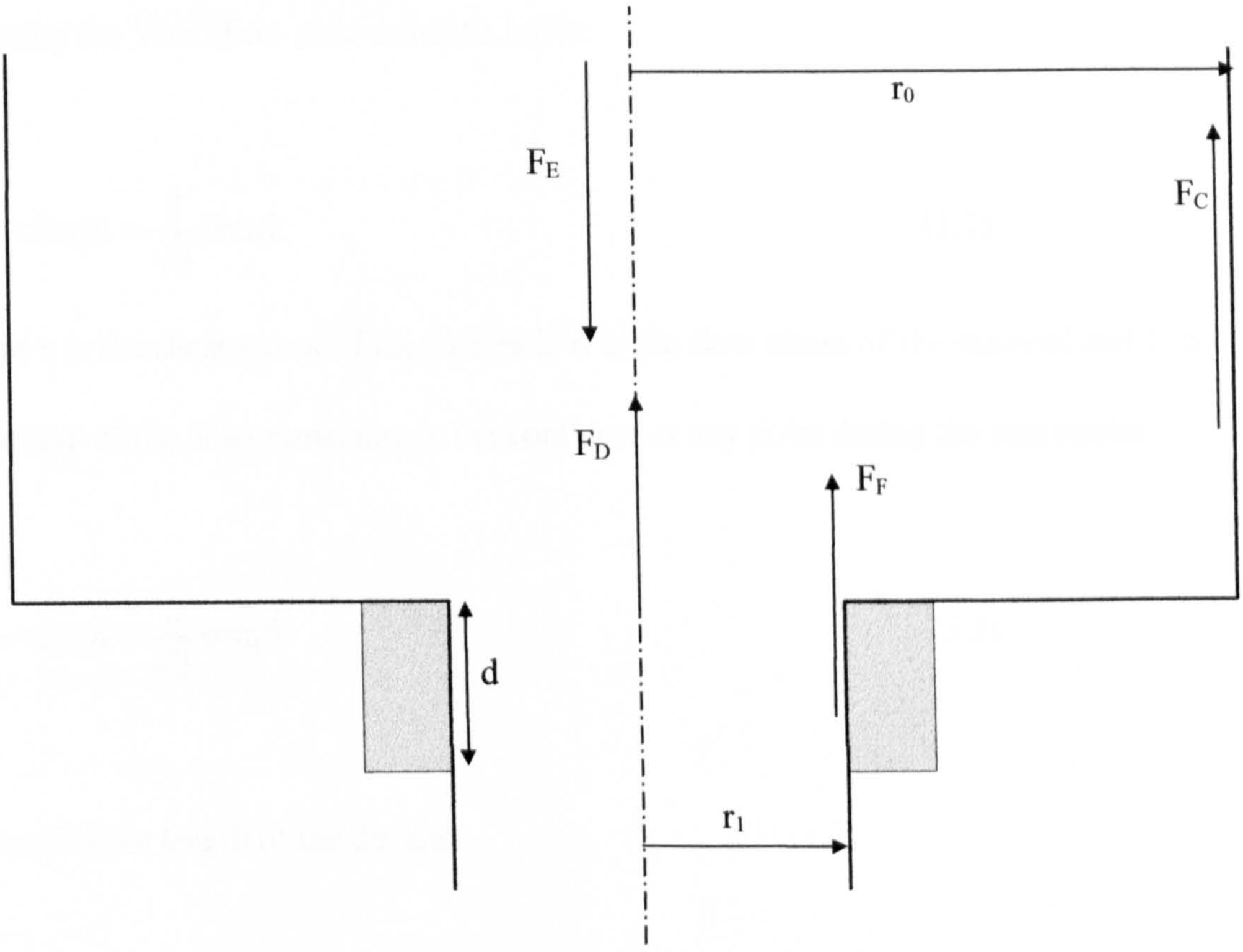

Figure 3.1. Forces present in axisymmetric extrusion

From normal static analysis:

$$F_E=F_C+F_D+F_F \tag{3.1}$$

where F_E is the applied extrusion force, F_C is the drag generated from friction with the container, F_F is the drag generated from friction with the die land area and F_D is the force required to deform the billet.

Because frictional coefficients are difficult to determine, the frictional forces can be approximated assuming that a thin film of aluminium adheres to, either the die face, or the container surface, and internal shear occurs to push the material through. Hence, assuming the Von Mises yield criterion holds:

$$F_C = \tau 2\pi r_0 L = \frac{2}{\sqrt{3}} \bar{\sigma} \pi r_0 L \qquad (3.2)$$

where τ is the shear stress of the material, $\bar{\sigma}$ is the flow stress of the material and L is the length of the billet remaining in the container at any point during the ram stroke.

$$F_F = \tau 2\pi r_1 d = \frac{2}{\sqrt{3}} \bar{\sigma} \pi r_1 d \qquad (3.3)$$

where d is the length of the die land.

The determination of the deformation force is slightly more complex. A lower bound solution can be found assuming ideal deformation conditions. The applied work under ideal conditions, is all used to deform the material.

So, external work, w_a, is equal to the extrusion force times the change in length, or:

$$w_a = F_E \, DL \qquad (3.4)$$

per unit volume the above equation becomes:

$$w_a = \frac{F_E \Delta L}{A_0 \Delta L} = \frac{F_E}{A_0} \qquad (3.5)$$

but F_E/A_0 is the extrusion pressure, P_E.

The work done in an ideal system is the area under the true-stress true strain curve, i.e.:

$$w_a = \int_0^{\varepsilon} \bar{\sigma} d\varepsilon = P_E = \frac{F_E}{A_0} \qquad (3.6)$$

Thus the deformation force in a non-ideal system, i.e. one that includes friction and other redundant work, like extrusion, is:

$$F_D = A_0 \int_0^{\ln R} \bar{\sigma} d\varepsilon \qquad (3.7)$$

or for a material under hot working conditions:

$$F_D = \pi r_0^2 \bar{\sigma} \ln R \qquad (3.8)$$

Thus the extrusion force at any point of the ram stroke is shown in equation 3.9:

$$F_E = \pi \bar{\sigma} \left[\frac{2}{\sqrt{3}} r_0 L + \frac{2}{\sqrt{3}} r_1 d + r_0^2 \ln R \right] \qquad (3.9)$$

3.2 Force Balance for two –hole extrusion

If this model is translated for a two-hole extrusion process, two more forces must be introduced as shown below:

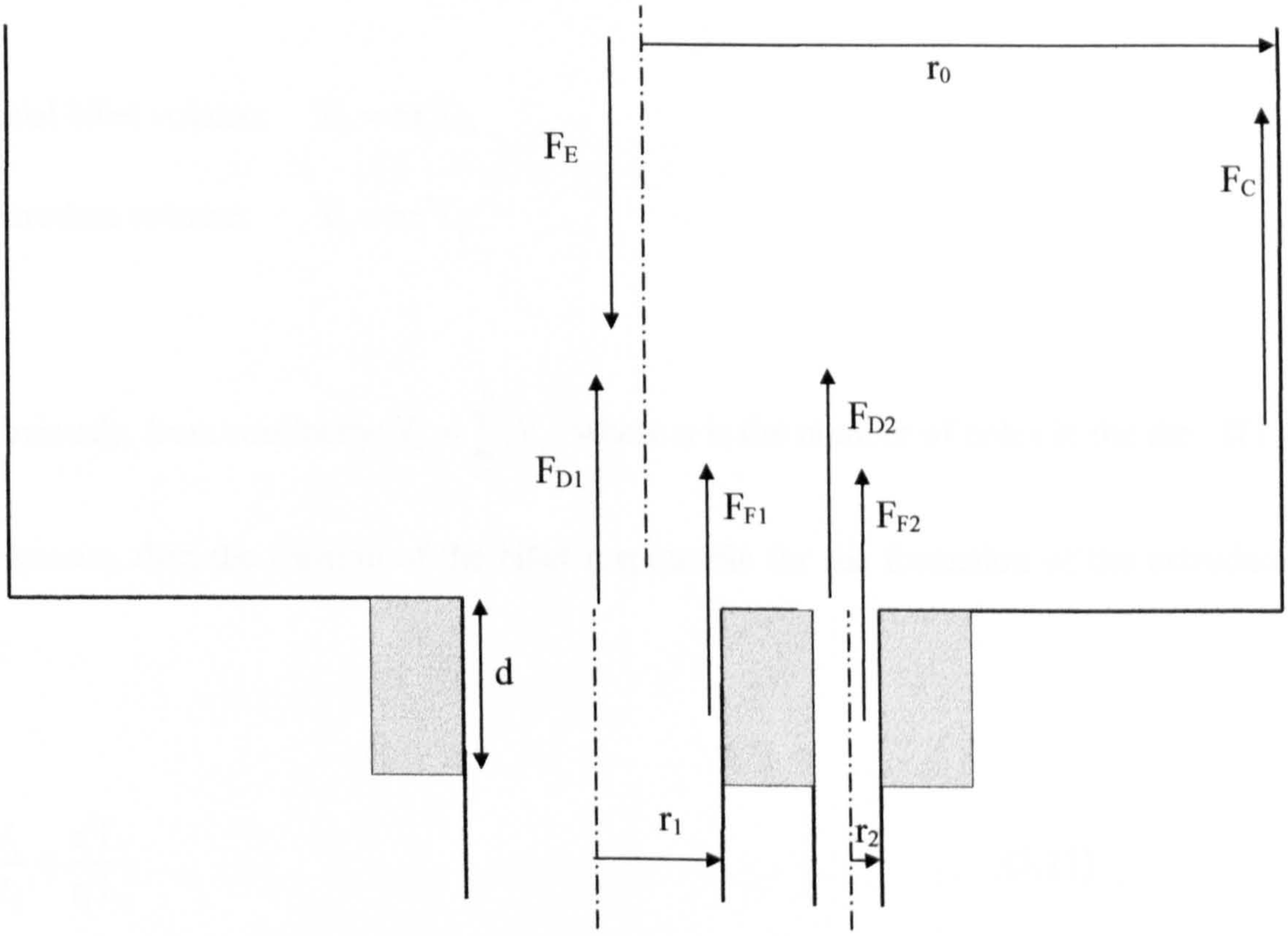

Figure 3.2. Forces present in two-hole extrusion

The frictional forces (F_C, F_{F1}, F_{F2}) can be calculated as before. The deformation forces (F_{D1}, F_{D2}) can be calculated as above but the problem is determining the strain required to form each extrudate.

$$F_{Di} = A\bar{\sigma}\int_0^{\varepsilon_i} d\varepsilon = \pi r_0^2 \bar{\sigma}\varepsilon_i \qquad (3.10)$$

Given the lengths of the extrudates, L_i, it is possible to work backwards to determine the diameter of a '*pseudo-billet*', that would form the extrudate of length L_i if no other extrudate was generated.

Initial billet volume: $V_0 = \pi r_0^2 L_0$

Extrudate volume: $V_i = \pi r_i^2 L_i$

Obviously, from continuity: $V_0 = \sum_{i=1}^{n} V_i$, where n is the number of holes in the die. If L_i is known, then the fraction of the billet responsible for the formation of the extrudate is:

$$\frac{V_i}{V_0} = \frac{r_i^2 L_i}{r_0^2 L_0} \qquad (3.11)$$

Given the original length of the billet, L_0, a value may be calculated for the radius, p, of the pseudo-billet:

$$p = \sqrt{\frac{r_i^2 L_i}{L_0}} \qquad (3.12)$$

Thus:

$$F_{Di} = A\bar{\sigma}\varepsilon_i$$
$$= A\bar{\sigma}\ln\frac{p^2}{r_i^2} \qquad (3.13)$$
$$= \pi p_i^2\bar{\sigma}\ln\frac{L_i}{L_0}$$

So, if the Von Mises yield criterion holds true, the extrusion force for multi-hole extrusion is:

$$F_E = \pi\bar{\sigma}\left[\frac{2}{\sqrt{3}}r_0L + \sum_{i=1}^{n}\frac{2}{\sqrt{3}}r_id + \sum_{i=1}^{n}p_i^2\ln\frac{L_i}{L_0}\right] \qquad (3.14)$$

where n is the number of holes in the die.

A force that accounts for other redundant work such as internal deformation and heat generation should also be included. It should also be noted that this model does not account for any heat generation during extrusion (which could be quite significant) and assumes isothermal deformation.

Chapter 4

Experimental Procedure

4. Experimental Procedure

4.1 Casting:

The alloys used in the present study were all made especially for the project and most are not available commercially. The die utilised was a custom-made gravity die a schematic of which is shown in figure 4.1.

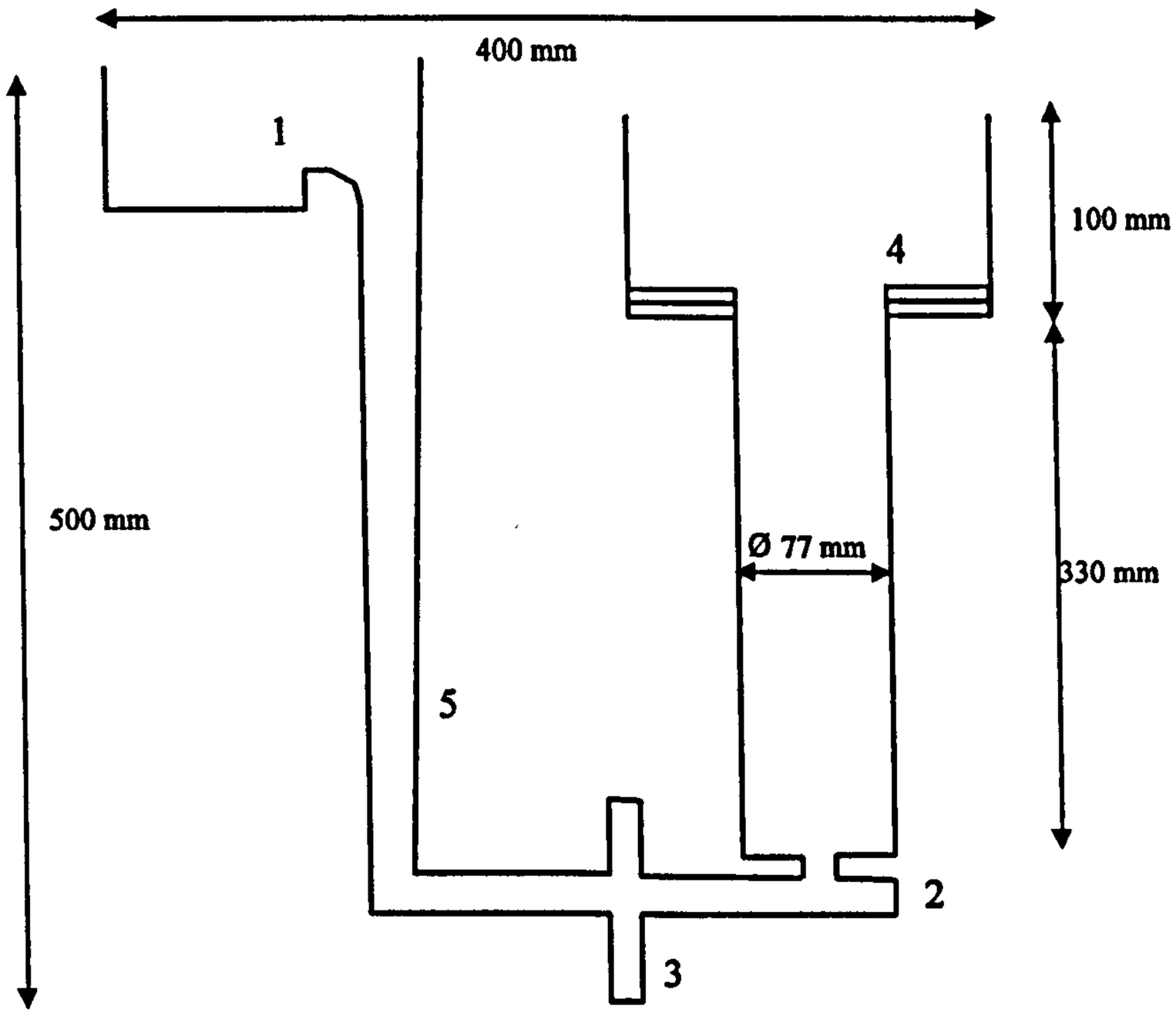

Figure 4.1. Schematic drawing of the cross-section of the cast iron Gravity Die used for the casting of the special alloys used in the present study.

A variety of features were included in the design of the mould in order to provide a clean and as oxide free as possible product. The features marked 1-5 on the diagram are the most important and their function is explained below:

1. The pouring lip: This was included to ensure homogeneous filling of the sprue and to avoid bubble formation.

2. This feature is common for most gravity dies and provides the means to avoid fold-over in the surface of the billet thus minimising internal oxide formation.
3. Ceramic filter: As well as homogenising the flow the carbon filter also stops any unwanted inclusions from entering the sensitive area of the mould.
4. Ceramic paper washers: Their function is purely for the ease of extraction of the casting as during solidification contraction of the aluminium occurs along the axis of the billet pinning it in the mould. The aluminium silicate washers take up the volume, which contracts and help avoid subsequent solidification cracking.
5. Tapering sprue: The taper in the sprue increases the velocity of the molten metal as it proceeds towards the billet.

Melting of the aluminium was performed in a RAMSELL-NABER programmable furnace with a maximum capacity of approximately 200 kg of aluminium, which can be held at temperatures of up to 1000 °C. The raw materials were supplied by Deeside Aluminium and their compositions are detailed in table 4.1.

Addition	Form	Al wt %	Mg wt %	Si wt %	Fe wt %	Mn wt %	other wt %
Al (CP)	15 kg ingots	bal.	0.017	0.135	0.1	0.06	< 0.1
Al (SP)	1.5 kg ingots	99.999	< 0.0003	< 0.0001	< 0.0007	-	bal.
Mg	1.5 kg ingots	bal.	90	-	-	-	< 0.2
Si	granules	-	-	100	-	-	-
Fe	pellets	bal.	-	-	75	-	< 0.2

Table 4.1. Compositions of the raw materials and the alloying additions used.

The mould and pouring ladle were heated using propane + air blowtorches. Temperatures reached before casting were at least 600 °C for the ladle, 760 °C for the melt and 150 °C for the mould. Temperature regulation was conducted using a Pt /

Pt-13% Rh touch thermocouple for the mould and a similar dip thermocouple for the melt.

The alloys were made by first melting the primary aluminium and then adding the alloying additions in small enough increments. Of course, this is more time consuming as dissolution and homogenisation time is required after each silicon addition. At high temperatures Si forms a protective oxide layer and is very difficult to dissolve in the aluminium melt. In order to avoid the formation of the oxide layer all the Si granules were wrapped in Al foil (regular kitchen foil) and plunged to the bottom of the crucible. This gives the Si a layer of Al around it, which inhibits oxygen penetration and suppresses the oxide formation thus decreasing the time required for dissolution. Stirring of the melt was performed using an inert carbon rod.

The magnesium was added just before each cast and plunged straight to the bottom of the melt because it takes very little time to dissolve and such practice provides minimal Mg losses.

Errors:

Compositional: Exact compositions and ratios cannot be predicted because of the nature of the furnace. Cumulative errors arise due to the weighing of what comes out of the crucible instead of what is actually still in. Losses include ladle residue and skimmed material. It is also known that at the operating temperatures of the furnace, Mg tends to burn off at the surface of the melt. Thus, it was calculated that slight overestimation of the amount of Mg, to be added to the melt was required.

Billet Homogeneity: In some cases, complete filling of the mould was not possible because of low mould temperature. The top part of these billets has a matt finish, which indicates oxide build-up. Upon microstructural investigation, some billets, with high silicon contents, were noted to contain large Si particles, which originated from undissolved Si in the melt.

The alloys cast with the above process had the compositions as listed in table A.1 in Appendix A. It may be easier to view the compositions in graphical form, depicted in figures A.1-5. These compositions were found by Spark Emission Spectrometry (using an inert argon atmosphere) on a sample of each alloy taken before filling of the die. The average of three readings with Residual Standard Deviation (RSD) of less than 1 were taken from each sample.

4.2. Extrusion

After the special alloys had been cast, they were cut into three billets and turned down to a diameter of 73 mm and a length of 90 mm and subsequently homogenised at 580 °C for 6 hours followed by an air cool. The oxidised surface layer was then machined off (resulting in a final diameter of 72 mm) and the billets were pre-heated to 450 °C. Extrusion was performed on a 5 MN vertical press using a container temperature 50 °C below the billet temperature. The ram velocity, at 12 mm/s, was the highest the hydraulics of the press could produce. The dies were custom made and comprised of two holes- diameters 16 and 8, 16 and 6 and 16 and 4 mm respectively, with identical land lengths. Schematics of the dies are shown in figure 4.2.

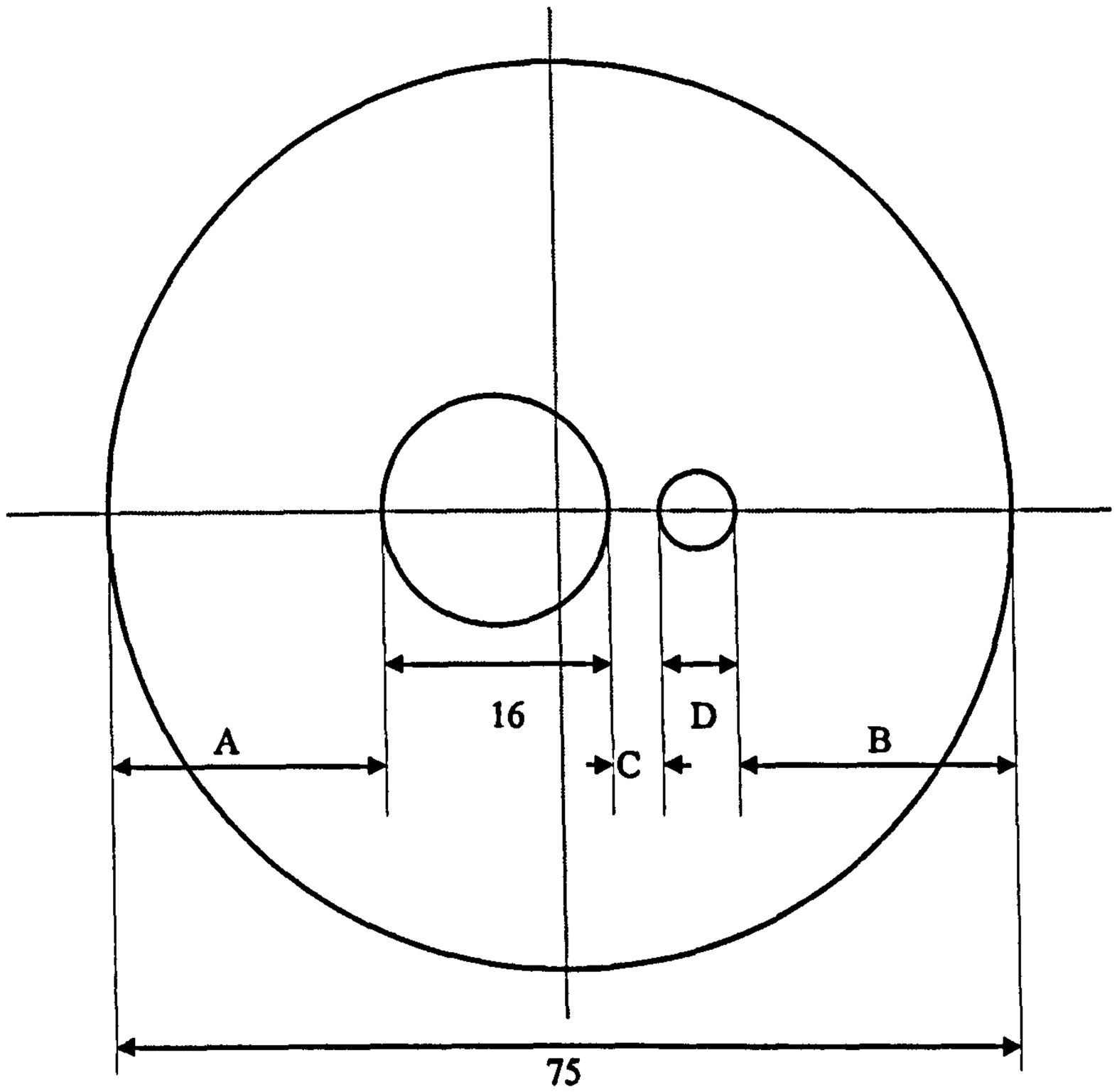

Figure 4.2. Schematic of the custom made dies used. All distances in mm. The values for lengths A, B, C and D are shown in Table 4.3.

Die	A	B	C	D
1	23.5	22.5	5	8
2	24	24	5	6
3	24.5	25.5	5	4

Table 4.2. Values for lengths shown in figure 4.2. All distances in mm.

A number of partial extrusions were also performed on a standard AA6063 alloy in order to assess the flow through the dies. All these extrusions were performed under

exactly the same conditions as mentioned above, the only variable being the percentage of the billet extruded. Two series of six identical billets each were extruded varying the billet temperature (from 350 to 580 °C) and the ram velocity (from 2.3 to 12 mm/s) respectively. The compositions of these billets as well as that of the standard 6063 alloy are shown in table 4.3.

Alloy	Mg (wt %)	Si (wt %)	Fe (wt %)	Others (wt %)	Al (wt %)
1	0.62	0.35	0.35	0.5	Bal.
2	0.67	0.92	0.11	<0.1	Bal.
3	0.62	1.47	0.11	< 0.1	Bal.

Table 4.3. Composition of alloys used to investigate the two-hole extrusion process. Billets of alloy 1 were extruded to varying degrees, those of alloy 2 at different ram speeds and those of alloy 3 at different temperatures.

All the results of the extrusion of the above alloys can be seen in tables B.1-B.4 in Appendix B.

4.3. Artificial Ageing

Extruded strips of Primary Equivalent Recycled Aluminium (PERAl), the composition of which is shown in Table 4.4, were supplied by Deeside Aluminium, in the T4 condition. PERAl has been proven through previous tests [122] to behave in a similar manner to primary aluminium during the ageing sequence, therefore it is safe to assume that any findings in the present study would reflect the behaviour of primary alloys as well.

Si	Mg	Fe	Cu	Mn	Cr	Zn	Ti	B	Other	Al
.39-.45	.41-.47	.15	< .05	<.05	<.02	<.02	.03	<.001	.1	Bal.

Table 4.4. Composition of PERAl alloy used in present study

The strips were solutionised at 500, 520 and 540 °C, quenched, aged as detailed in Table A.2 (Appendix A) and quenched again. The ageing took place in an air circulated pie oven pre-heated to the initial temperature. The temperature was regulated using a thermocouple inserted into a control sample

The aged samples were then Hardness tested using an AVERY Direct Reading Rockwell Hardness testing machine and a VICKERS Hardness Tester and tensile tests were performed. Several duplicate samples and averaging multiple indents were used to reduce scatter. Because the samples were supplied as strip (instead of rod) a special form of tensile specimen had to be designed to accommodate both the tensile machine and the form of the sample. This design is shown in figure 4.3. Tensile tests were performed on a JJ Instruments tensile tester with a 10 kN Load Cell, and a constant cross-head speed of 2.5 mm/min.

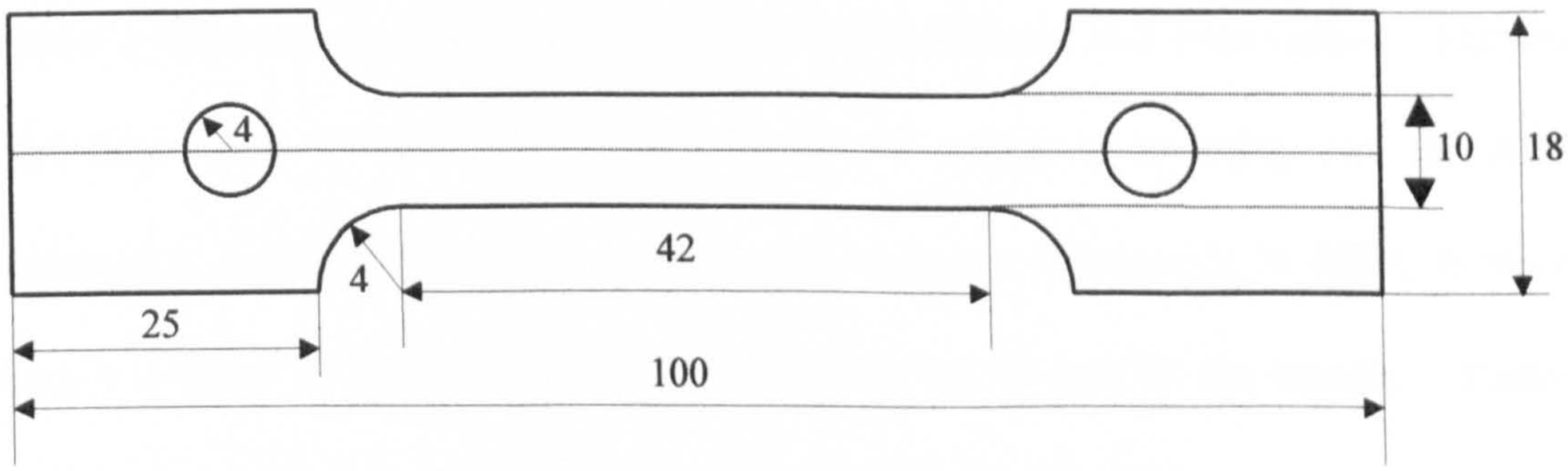

Figure 4.3. Design of tensile specimen for ageing analysis. Constant thickness 4 mm.

Certain ageing experiments were conducted after the samples had been strained. The deformation was applied by cold rolling in the extrusion direction using a simple two-

high mill press. The reduction in thickness involved a multi-stage rolling process of the sample by approximately 2 % each time. Once the desired separation of the mills was attained, all the samples were passed through a number of times to ensure that the thickness was uniform and no localised deformation occurred. However, the problem that arises from use of rolling for this type of application is that the rolled strips were unable to stay flat and most of them became 'wavy'. This caused problems in the subsequent testing, as the hardness tester requires flat samples for an accurate reading. Although care was taken to take hardness readings at a flat point on each strip, the error which arises from the hardness testing should be considered to increase as the amount of deformation increases. Samples were pre-strained to 1, 5, 7, 10, 15 and 20 %.

4.4. Optical Microscopy

Selective microscopy was performed on samples of the as-cast, homogenised, partially extruded billet and extruded product. The samples were ground and polished and then etched using a variety of chemical etchants, depending on the details that were to be shown. A macro etch* was used on all the partially extruded billets in order to bring out the grains and determine whether any recrystallisation had taken place. The other specimens were etched first with a 0.5 % HF solution, to bring out the AlFeSi precipitates, followed by an electroetch with Barker's solution (2 % HBF_4 in water), using a voltage between 15 and 20 V depending on the size of the sample. Barker's samples were viewed under cross-polarised light, using a quarter wavelength plate to increase the contrast of the grains.

---

* The macro-etchant used consisted of 45 % conc. HCl, 15 % conc. HNO_3, 15 % conc. HF, 25 % H_2O

Chapter 5

Mechanics of two-hole extrusion

Nomenclature – Chapter 5

A'	Area of orifice / Area of die-land
a, b	Distances as in figure 5.7
b, w	Bearing length and width
B, W	Reference bearing length and width
c_p	Specific heat capacity
D	Die/Billet diameter
d, d_i	Die land length (of orifice i)
e	Eccentricity of die
e_i	Eccentricity of orifice i
f_i	Flow factor
F_i	Frictional force at orifice i
G	Universal gas constant
L_i	Length of extrudate
m	Mass extruded
p_i	Pseudo billet radius corresponding to orifice i
Q	Minimum radius of circle concentric with the die that circumscribes all orifices
q	Distance of section to die centre
R_D	Inherent resistance to deformation
r_{eff}	Effective radius
r_i	Radius of orifice i
$\mathbf{r}_m$	Positional vector of centre of gravity
T	Absolute temperature
V	Ram velocity
V_i	Volume of extrudate
$\bar{\mathbf{x}}_i$	Positional vector of orifice centre
Z_i	Temperature compensated strain rate
ΔH	Activation energy
ΔT	Temperature rise
α,A,n	Material constants
δ	$\lvert\bar{\mathbf{x}}_1\rvert+\lvert\bar{\mathbf{x}}_2\rvert$
$\dot{\varepsilon}$	Strain rate
η	Material constant
ρ	Density
$\bar{\sigma}$	Flow stress
τ	Shear strength

5. Mechanics of two-hole Extrusion

Introduction and Background:

As detailed in section 2.6. a great deal of work has been performed pertaining to axisymmetric single hole extrusion. Given that the industrial applications of single hole extrusion are limited, it is surprising that multi hole extrusion has not been researched as thoroughly. A selection of the work most relevant to the present study is presented below.

The flow of material through a two-hole die was investigated by Valberg et al. [123] using a novel flow visualisation technique. Flow was observed and explained for two different alloys extruded through two-hole dies (r_1/r_2=1 equispaced from the centre of the die). However, no reference was made to the products of the extrusion, only which part of the billet contributed to which extrudate. The alloys extruded were the very 'extrudable' AA6063, and AA7018, classified as having "...medium extrudability". It is interesting to observe the dead metal zone (DMZ) formation for the two dies (with different hole spacing). The closer the two holes are to each other, as is the case in the present study, the smaller the DMZ is formed between them. When the spacing is increased a funnel shaped zone is formed between the holes similar to that created in the corners of the billet extruded axisymmetrically. This effect is verified by the results of Romana and Zasadzinski [124]. The flow through the dies was classified as alloy dependent in that internal shear was more difficult in the Al-Mg-Zn (7xxx) alloy increasing the retention of material in the container and increasing the size of the

DMZ. Therefore, towards the end of the extrusion cycle the flow from the outer regions of the billet exceeded that of the softer Al-Mg-Si (6xxx) alloy.

A test similar to the one performed in the present study was carried out by Mondolfo and Peel [21]. In this study, five dies were used with similar hole area ratios but with a large distance between the holes. The centres of the holes were, as before, equidistant from the centre of the die. No mention of the die-land lengths is made (it is assumed that they are the same for both holes). It will be shown later in this chapter that the die land length is a critical factor in determining the flow of material through the hole. Of great interest is the normalisation technique employed by the authors. The area/circumference ratio of each hole on the die was used to normalise the L_1/L_2 index. A similar approach is employed in the present work including a term to account for the change in hole area ratio.

This normalisation is justified, by considering that the holes' area/circumference ratio is a measure of the amount of material moving through the die orifice and the friction encountered at the die land.

5.1. Material Flow:

There is a sequence of events, prior to the extrusion of a billet, which leads to the emergence of the product. This sequence is detailed in the following points:

The ram strikes the billet. The press utilised in this study incorporates a fast approach mechanism to minimise heat losses of the billet to the environment. When a load of 2

tons is reached, the ram slows down from its fast approach and then accelerates (if necessary) to the desired speed. The billet then upsets to fill the container and, when breakthrough pressure is reached, the extrudates begin to emerge together. The fact that both extrudates emerge at the same time is postulation. There is no visual access to the die exit. The assumption is made by considering the load extension-diagram: One peak only is observed - which corresponds with breakthrough. If one had begun to extrude before the other, a double peak would have been observed. The displacement diagram apart, it is somewhat logical that the two extrudates should emerge at the maximum pressure point. If one required a larger breakthrough pressure than the other, it would never actually emerge, as the pressure drops after the extrudate begins to emerge. A typical load–ram displacement diagram is shown in figure 5.1. The increase in extrusion force at the very end of the stroke is due to the deformation of the Dead Metal Zone. Obviously, the DMZ is formed in the position at which the least energy is required for deformation. Once the ram begins to interact with the material in the high shear areas of the billet, the DMZ shape is disturbed and a new formation is created, which increases the force required to extrude.

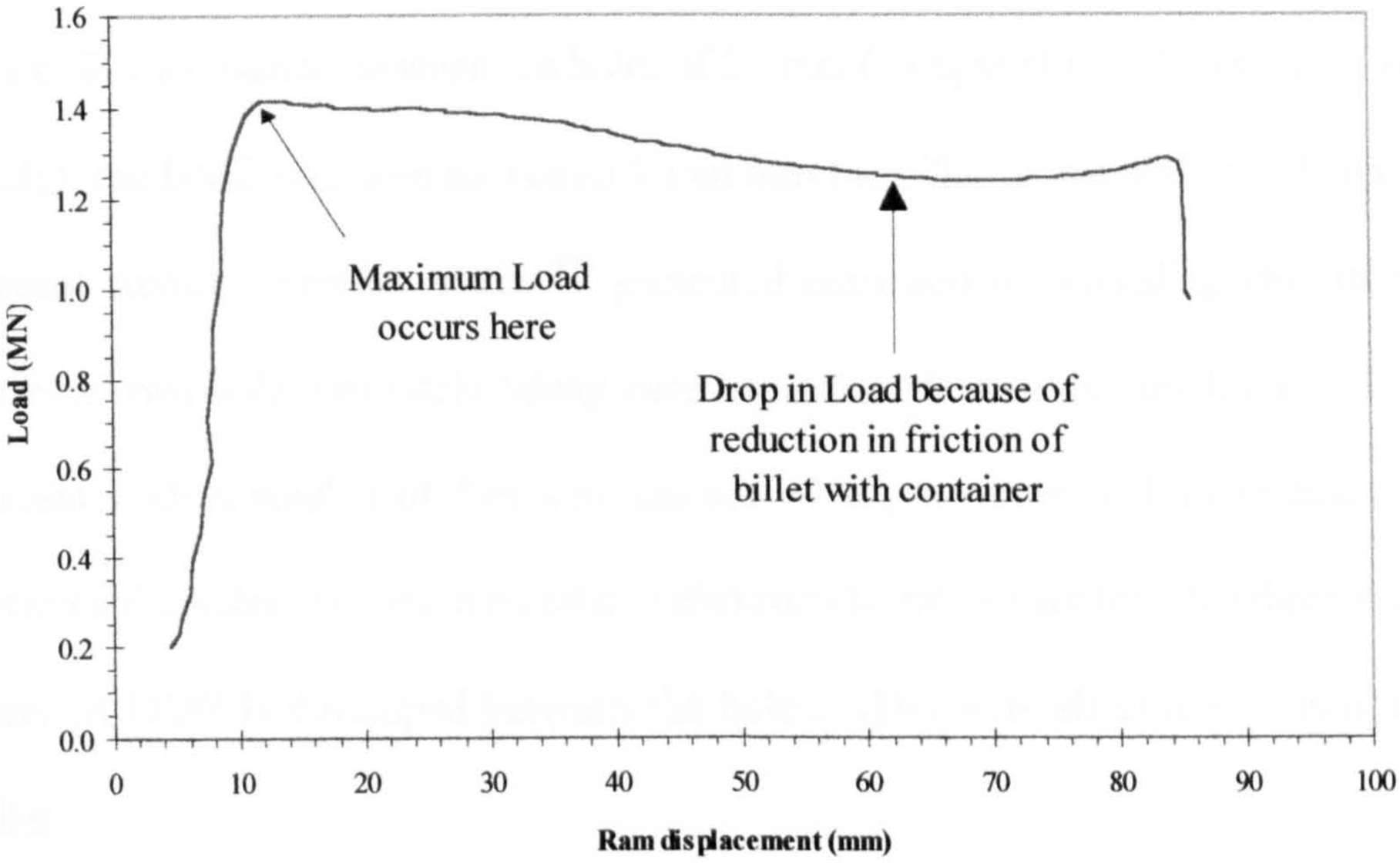

Figure 5.1. Typical load -ram displacement curve (alloy 422 through die 1).

A DMZ of considerable volume is formed around the two holes, but only a very small one between them. As reported by Valberg et al. [123], this would not be the case if there were a greater distance between the holes. In the situation presented in this study, the die orifices are close enough together to allow the formation of only a small DMZ because of sticking friction. In an analysis of material flow through a single-hole flat-faced die, Clode [63] indicated the existence of a small deformation region adjacent to the die throat on the face of the die. The region between the two holes in the present study presents a similar picture. Deformation of material in close proximity to the die orifice occurs by internal shear around the layer dead metal between the two holes. This gives the appearance of a 'dynamic' layer in the region. Because the distance between the holes remained constant for all the dies used it would be difficult to postulate at exactly which point the DMZ would begin to form. However, comparing the size of the DMZ with that observed in similar studies [21, 125] the depth of

the DMZ into the billet (between the holes) increases rapidly as the holes move further apart. For a distance between the holes of 20 mm (compared with 5 mm in the present study), the DMZ was seen to extend 7 mm into the billet (compared to < 1 mm in the present study). Another study [88] presented extrusion of modelling clay through a series of two hole dies while taking care to ensure plain strain conditions. As in the present study a number of dies were utilised which, however, had a constant distance between the holes (18 mm in an 80 mm die) significantly larger than the three dies used here. A DMZ is developed between the holes, which extends around 5 mm into the billet.

The depth of this DMZ is approximately 15 mm at the container interface. This can be seen on the flow of the billet extruded partially to 48 %, shown in figure 5.2.

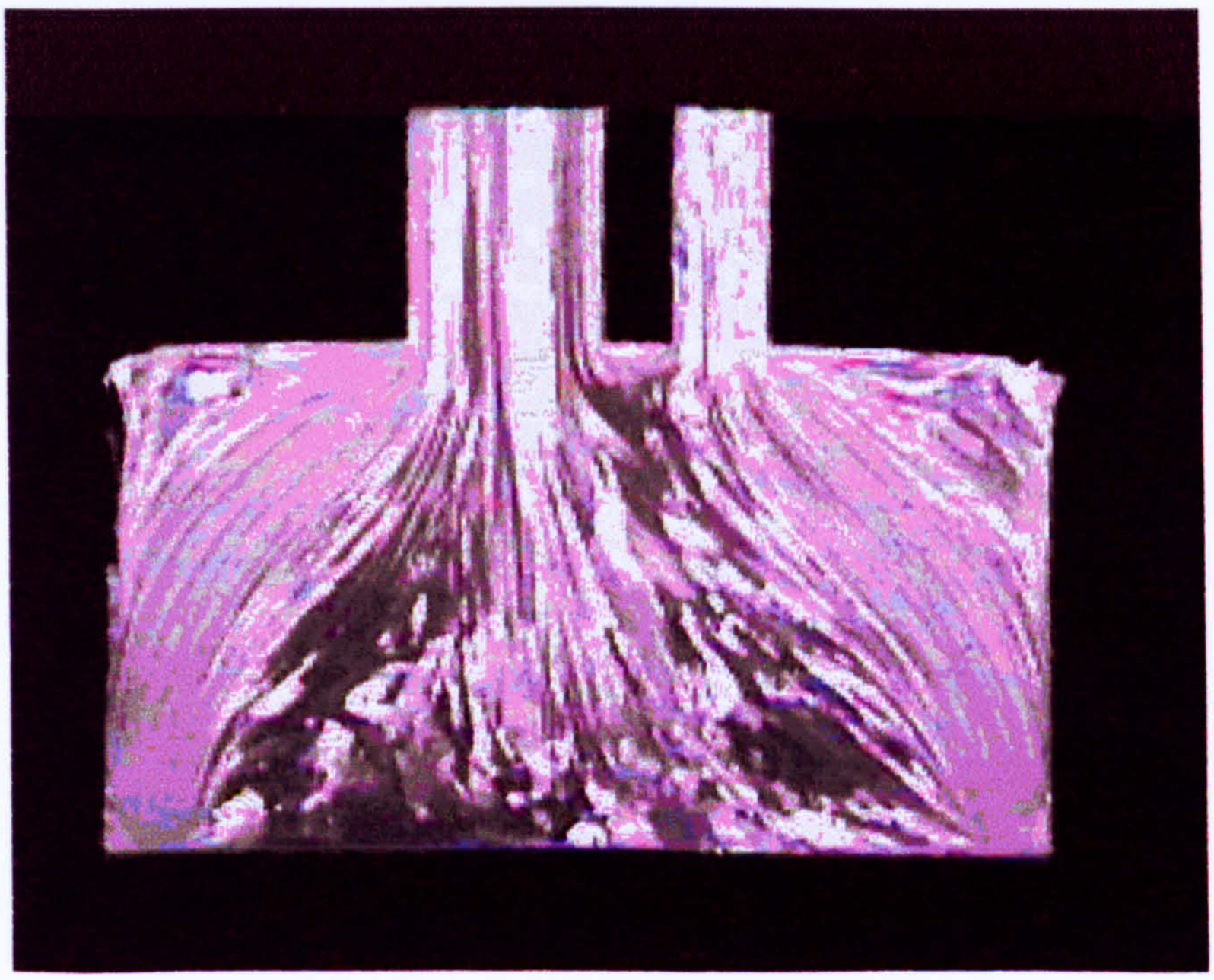

Figure 5.2. Longitudinal section of the discard of a billet extruded to 48 %

The exit velocities of the two extrudates increase as the ram stroke proceeds up to the first 20 % of the billet length. This is a sign that the ram velocity is not constant at the beginning of the stroke, but when the fast approach cuts off, the ram overshoots the

target speed and then immediately accelerates to the set speed. This effect is seen in the velocity plot in figure 5.3 and the typical ram displacement-time diagram in figure 5.4. The velocities were calculated using the lengths of the extrudates measured from each partial, and the extrusion time calculated using the ram velocity (measured by the data capture software) and the volumetric incompressibility.

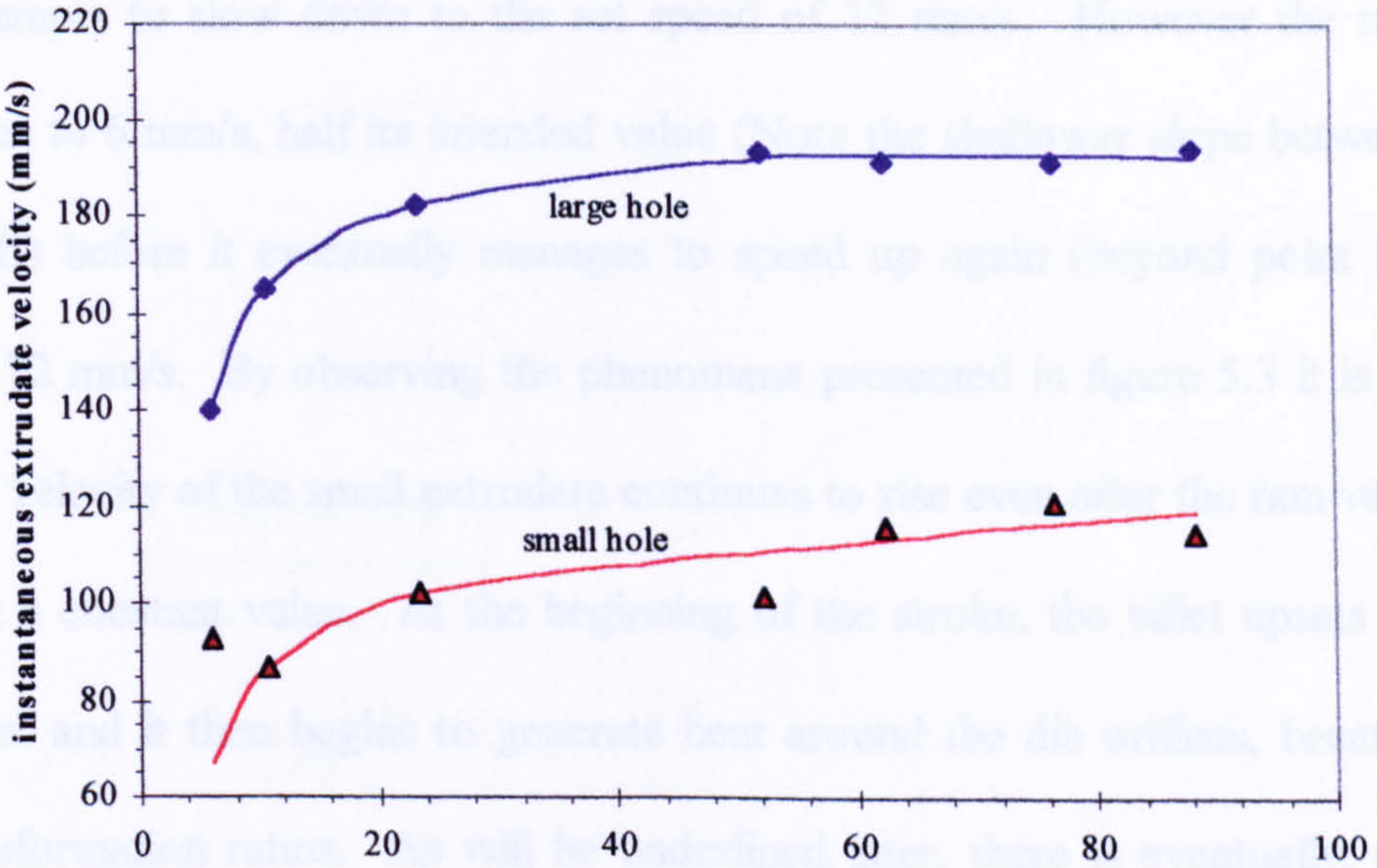

Figure 5.3. Velocity variation of the extrudates as they emerge from the die.

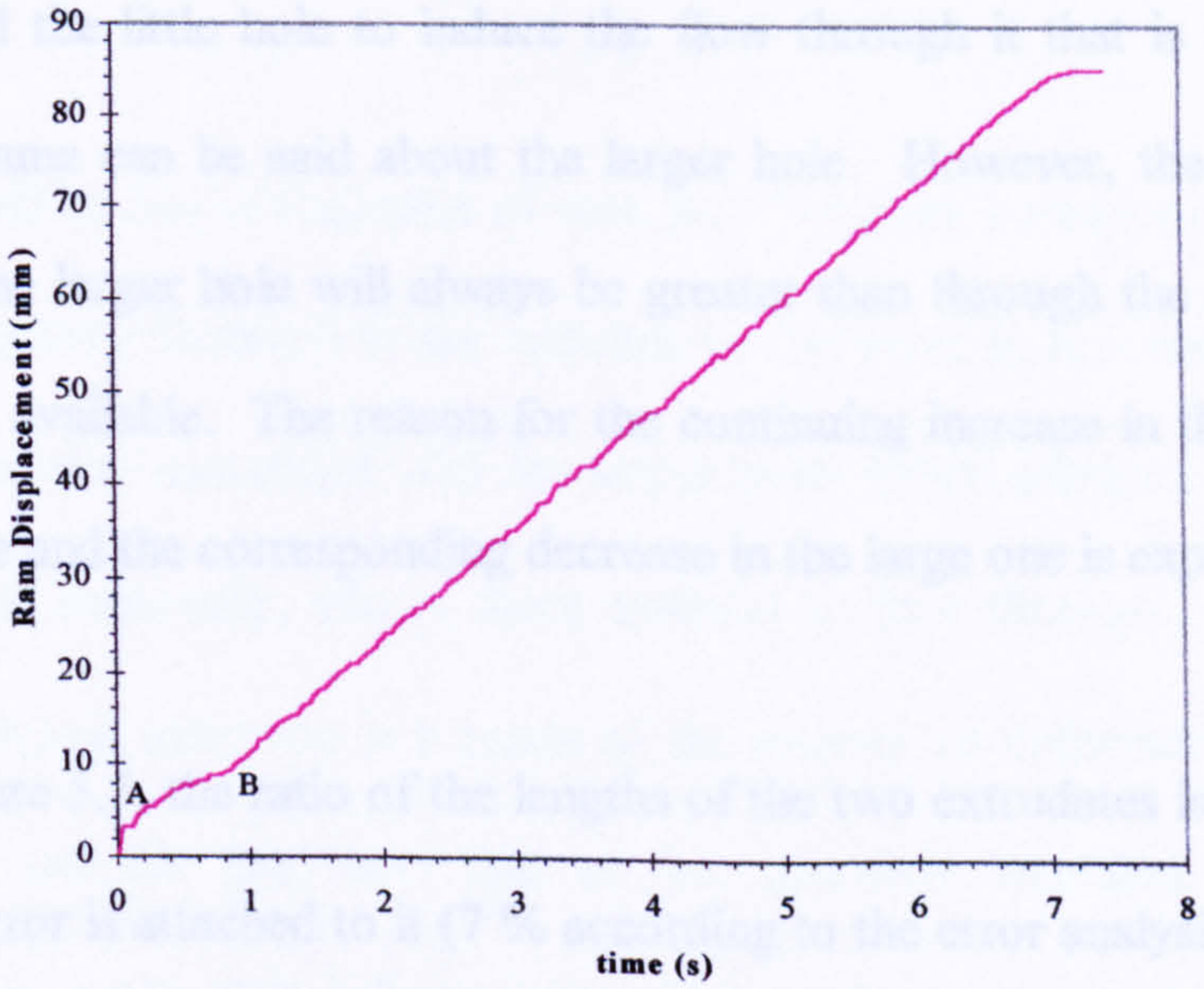

Figure 5.4. Typical Ram displacement Vs Time diagram (alloy 422 die 1)

It is evident that the material extruded through the large hole is emerging faster than that through the little hole. It is, again, about 20 % of the stroke before the velocities of the extrudates begin to reach a steady state, because of the press overshooting its set speed. Figure 5.4 indicates how the ram reduces velocity after the cut off of the fast approach. Point A, at the very beginning of the stroke, is the point at which the ram attempts to slow down to the set speed of 12 mm/s. However the ram speed decreases to 6 mm/s, half its intended value (Note the shallower slope between points A and B) before it eventually manages to speed up again (beyond point B) to the desired 12 mm/s. By observing the phenomena presented in figure 5.3 it is proposed that the velocity of the small extrudate continues to rise even after the ram velocity has reached a constant value. At the beginning of the stroke, the billet upsets to fill the container and it then begins to generate heat around the die orifices, because of the large deformation ratios. As will be underlined later, there is eventually, more heat generated around the small hole than the larger one. Hence, at the beginning of the stroke, when the extrudates first begin to emerge, the level of heat generation is not enough around the little hole to induce the flow through it that is seen later in the stroke. The same can be said about the larger hole. However, the volumetric flow rate through the larger hole will always be greater than through the other because of the larger area available. The reason for the continuing increase in the velocity of the small extrudate and the corresponding decrease in the large one is explained later.

As seen in figure 5.5, the ratio of the lengths of the two extrudates is quite erratic and a significant error is attached to it (7 % according to the error analysis. The individual lengths can be measured to within 5 % - no tension is placed on the end of the extrudates so when they emerge they are not straight – in industrial practice, a puller

would be used to keep the profiles straight). In order to gain a more representative picture of how the length ratio is affected by the ram stroke, a corrected L_1/L_2 ratio is calculated, and plotted (red line). This new variable seems to rise steeply at the very beginning of the stroke - when the two extrudates emerge simultaneously having infinitesimal lengths- reaches a peak and then suffers a shallow decline as the stroke progresses.

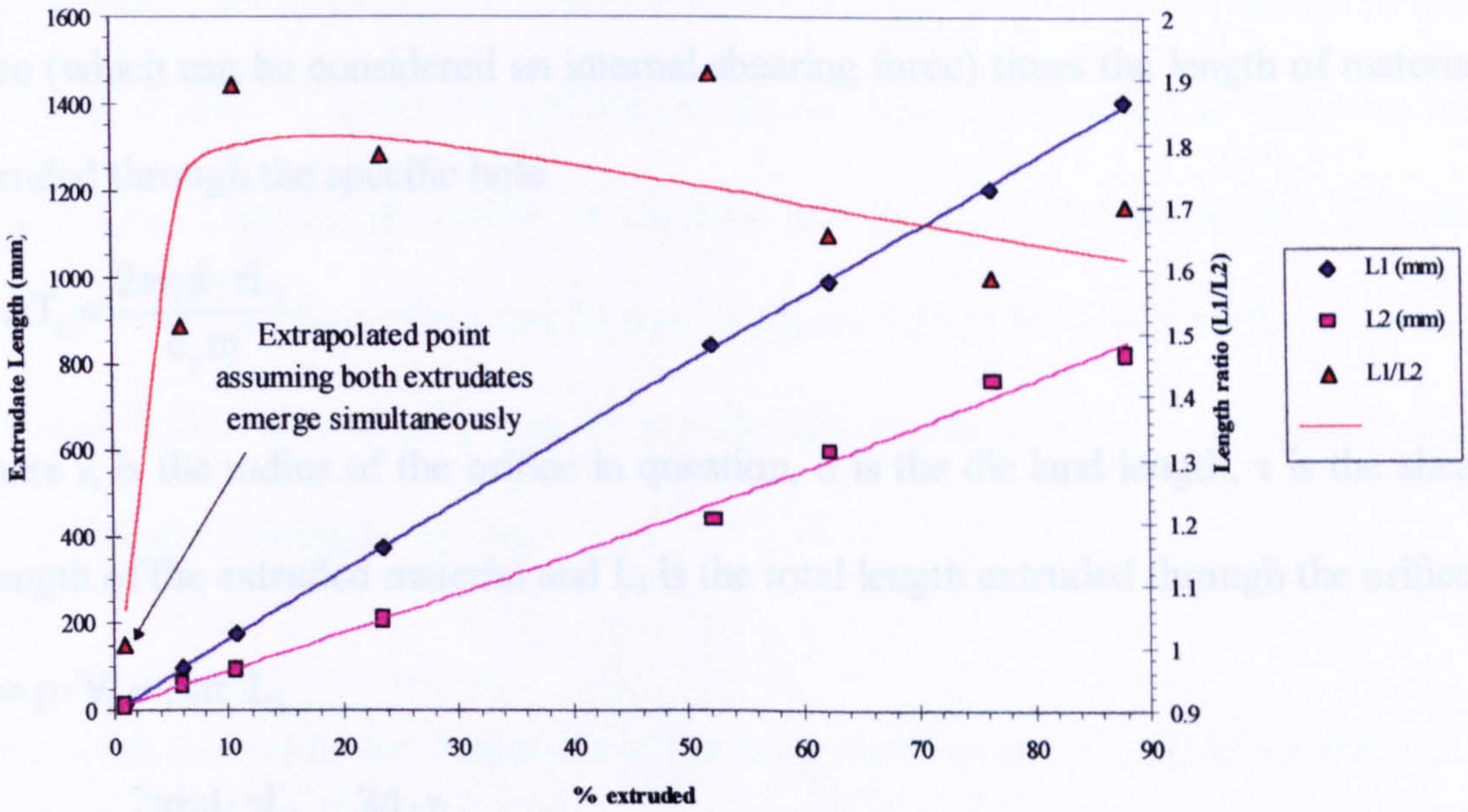

Figure 5.4. Variation of the extrudate lengths and the length ratio with % extruded.

This effect could be due to a number of reasons. The most probable of these, however is that the high shear incurred at the entrance to the small hole, causes a temperature rise (larger than that associated with the larger hole) which effects a drop in the local flow stress and, eventually, allows more material to flow through. The temperature rise incurred during extrusion is a result of the amount of deformation, the frictional opposition at the die land and that at the container interface. However, the temperature rise due to bulk deformation (which is alloy dependent) and the friction at the container interface is common for both holes. The difference in the temperature

rise between the two holes will be due to the effects of the frictional resistance at each die land. This is shown below. If all work done to oppose friction at the die land is transformed into heat, we have:

$$\text{Temperature Rise due to friction} = \Delta T = \frac{\text{Work Done}}{c_p m}$$

Where c_p is the specific heat capacity of the extruded metal and m is the mass of the extruded length. Now, the total work done to oppose friction is equal to the frictional force (which can be considered an internal shearing force) times the length of material extruded through the specific hole.

$$\Rightarrow \Delta T_i = \frac{2\pi r_i d \cdot \tau L_i}{c_p m}$$

Where r_i is the radius of the orifice in question, d is the die land length, τ is the shear strength of the extruded material and L_i is the total length extruded through the orifice.

$$m = \rho \cdot V_i = \rho \pi r_i^2 L_i$$

$$\text{So } \Delta T_i = \frac{2\pi r_i d \cdot \tau L_i}{c_p \pi r_i^2 L_i \rho} = \frac{2d \cdot \tau}{c_p r_i \rho}$$

Assuming that the shear strength of the extruded material is approximately constant for small changes in temperature, (this is definitely not the case but it will be assumed so for comparison purposes) the ratio of temperature changes in the two extrudates can be seen to be inversely proportional to the ratio of their diameters.

$$\frac{\Delta T_1}{\Delta T_2} = \frac{r_2}{r_1}$$

So in the case of the dies used in the present study the temperature rise in the material around the smaller extrudate is twice as much as the temperature rise around the large hole for die 1. This increases to 2.7 times for die 2 and 4 times as much for die 3. For

an AA6063 alloy calculations from the above analysis yield a typical increase of 18 °C in the temperature of the larger extrudate *due to the friction at the die land.*

As stated earlier, at the beginning of the stroke, both extrudates increase in speed to accommodate the acceleration of the ram. Later as the ram is moving at a constant speed, the heat generated around the little hole locally decreases the local flow stress and the exit velocity increases. As a result, the exit speed of the other extrudate must decrease slightly to allow for volumetric equilibrium. Obviously as one extrudate speeds up and the ram is feeding the material into the die at a constant rate, the other must slow down. This effect can be seen in figure 5.3. After about 50 % of the billet has been extruded, when the ram is moving at a constant velocity, the speed of the small extrudate continues to rise.

Other reasons include the formation of the dead metal zone. The DMZ on the side of the smaller hole would require higher energies because of the greater shear involved. Once the formation of the DMZ is complete flow through the smaller hole increases.

5.2 Extrudability Measurements

It was discussed earlier (section 2.6.3) that extrudability is not a universal measure with a standard test, which can be performed to evaluate it. An example of a constant, which is alloy dependent and is measured using a standard test, is the hardenability of steels. Although hardenability is not an easily defined constant a test has been devised (the Jominy Test) that allows its universal standardisation. Extrudability should be a number, which depends only on the material extruded, and defines how easy, or

difficult it is to extrude. However, until today, on an industrial basis, extrudability has been roughly measured as the maximum extrusion velocity, which results in an adequate surface finish. For comparison of different materials, though, this method lacks the analytical nature required. For example, if a standard test method were defined, like the Jominy test for hardenability, a more objective and reliable comparison could be made between different alloys. After the work by Mondolfo and Peel [21, 87], extrusion through a two-hole die provides the information necessary to quantify the still abstract quantity known as extrudability. This is furthered in the present work.

In the following sections, the effects of changes in the process parameters will be examined with respect to the calculation of the extrudability term.

5.2.1. Eccentricity Calculations

In order to assess the extrudability of an alloy, using the two-hole die construction and multiple dies with different hole sizes, and configurations, it is necessary to eliminate the geometric factor of the die in some way. This can be accomplished by assigning a scalar number to each hole, which describes its size and position relative to the centre of the die. This number is called the *eccentricity* of the hole. For symmetric dies it is possible to determine the eccentricity of the die as a whole (after Castle [125]). In the same way that each hole is characterised by an eccentricity, it would be possible to assign a shape factor to each hole depending on the orifice shape. Applying a shape factor is not appropriate in the present study because both profiles have a circular cross-section.

Considerations for the effects of the die-land length are made in section 5.2.2.

For the present study, two different methods were considered for the calculation of the eccentricity:

5.2.1.1. Eccentricity Calculation for the whole die

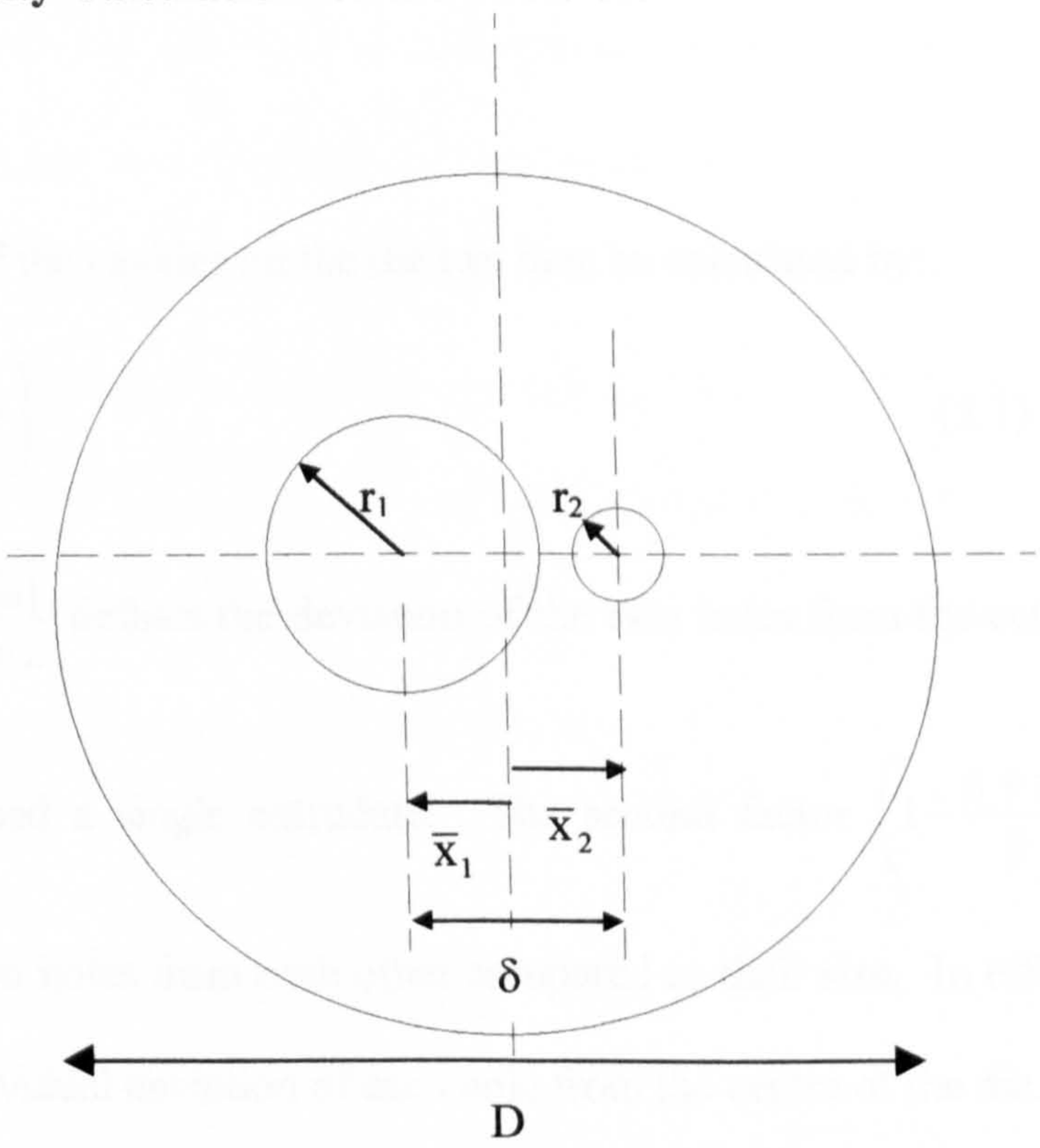

Figure 5.6. Eccentricity calculations for the whole die

The centre of gravity is used in industrial practice to centre large profiles on a die. By placing the centre of gravity of a profile on the centre of the die (assuming the die contains only a single cavity) extruders (die designers) ensure that flow through the profile occurs through the fastest part of the billet [126]. In the present study, if the two extrudates are considered to be a single profile, the distance of the centre of gravity from the centre of the die, $\mathbf{r}_m$, can be calculated using basic mathematical formulae as follows:

$$\mathbf{r}_m = \frac{\bar{\mathbf{x}}_1 r_1^2 + \bar{\mathbf{x}}_2 r_2^2}{r_1^2 + r_2^2}$$

Where $\bar{\mathbf{x}}_1$ and $\bar{\mathbf{x}}_2$ are the positional vectors of the centres of the two holes from the centre of the die. Thus, $\mathbf{r}_m$ is also calculated as a vector. Depending on the choice of the positive direction (the calculations above are based on unidirectional space along the diameter of the die) $\mathbf{r}_m$ will adopt the appropriate sign depending on which side of the centre it is on.

The eccentricity of the cavities on the die can then be calculated by:

$$e = \frac{|\mathbf{r}_m|}{D/2}\left(1 - \frac{r_1 + r_2}{\delta}\right) \qquad (5.1)$$

The first factor $\frac{|\mathbf{r}_m|}{D/2}$ defines the deviation of the two holes from the centre of the die as if they produced a single extrudate. The second factor $\left(1 - \frac{r_1 + r_2}{\delta}\right)$ gives the distance of the two holes from each other compared to their size. In effect, this factor quantifies the individual deviation of each hole from the centre of the die.

The significance of the eccentricity factor becomes clearer if the possibility is considered where $\mathbf{r}_m = 0$ (i.e. the centre of gravity lies on the middle of the die) and $\delta = r_1 + r_2$ (i.e. the two holes form a single extrudate). In this case $e = 0$ which signifies the optimum positioning of the die orifices for extrusion. Note also that the value of e will always be less than 1. A value of 1 can never be achieved, however, because $r_1 + r_2$ cannot be zero. As the eccentricity of the die increases, extrusion becomes more

difficult as the two holes tend towards the edge of the die, or the bulk of material is required to be extruded from slower parts of the billet.

In the present study the eccentricities for the three dies are e_1=0.024, e_2=0.032 and e_3=0.036.

The disadvantage of using this method of eccentricity calculation is that no indication is given of the relative flow through the two holes. It is a basic assumption that a single extrudate is formed – the two holes connected by a thin rod of negligible mass. In this case, eccentricity will provide only an idea of the effect of the die layout on the ease of extrusion. The rate of flow of material through the die will obviously not be affected because of volumetric incompressibility. The only factor that could influence the rate of material flow would be the ram velocity.

5.2.1.2. Eccentricity Calculation for each hole

Contrary to the previous normalisation technique, in this case the eccentricities of each hole in the die are calculated separately (after Castle [125]): $e = \frac{b}{a+b}$. If no part of the hole was on the face of the die, i.e. the hole didn't exist, e=1 and if it were at the middle of the die e=0.

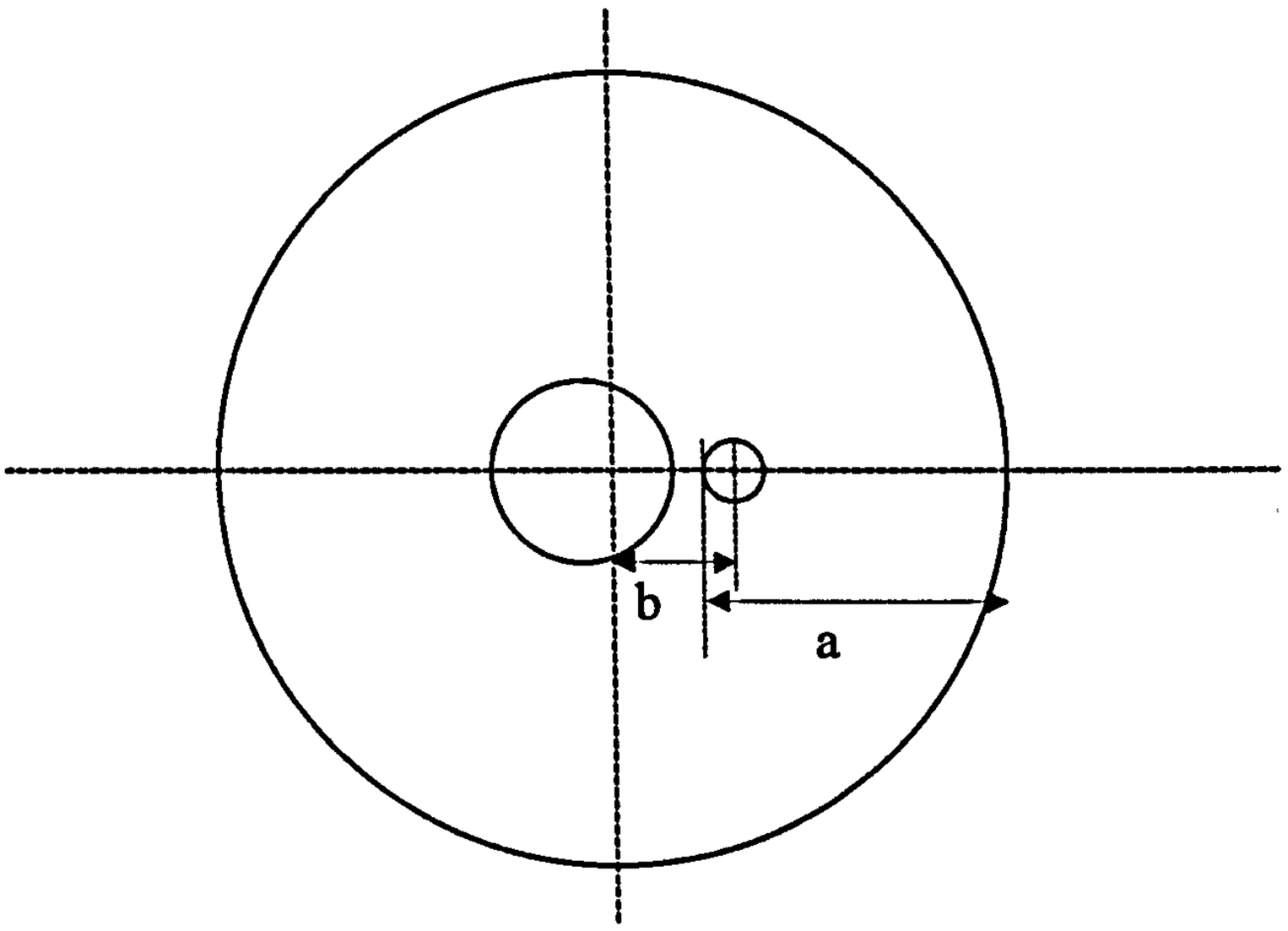

Figure 5.7. Eccentricity calculations for each hole

Figure 5.8 shows the maximum possible eccentricity as a function of the hole size. The limiting factor is obviously that no part of the orifice may be off the die.

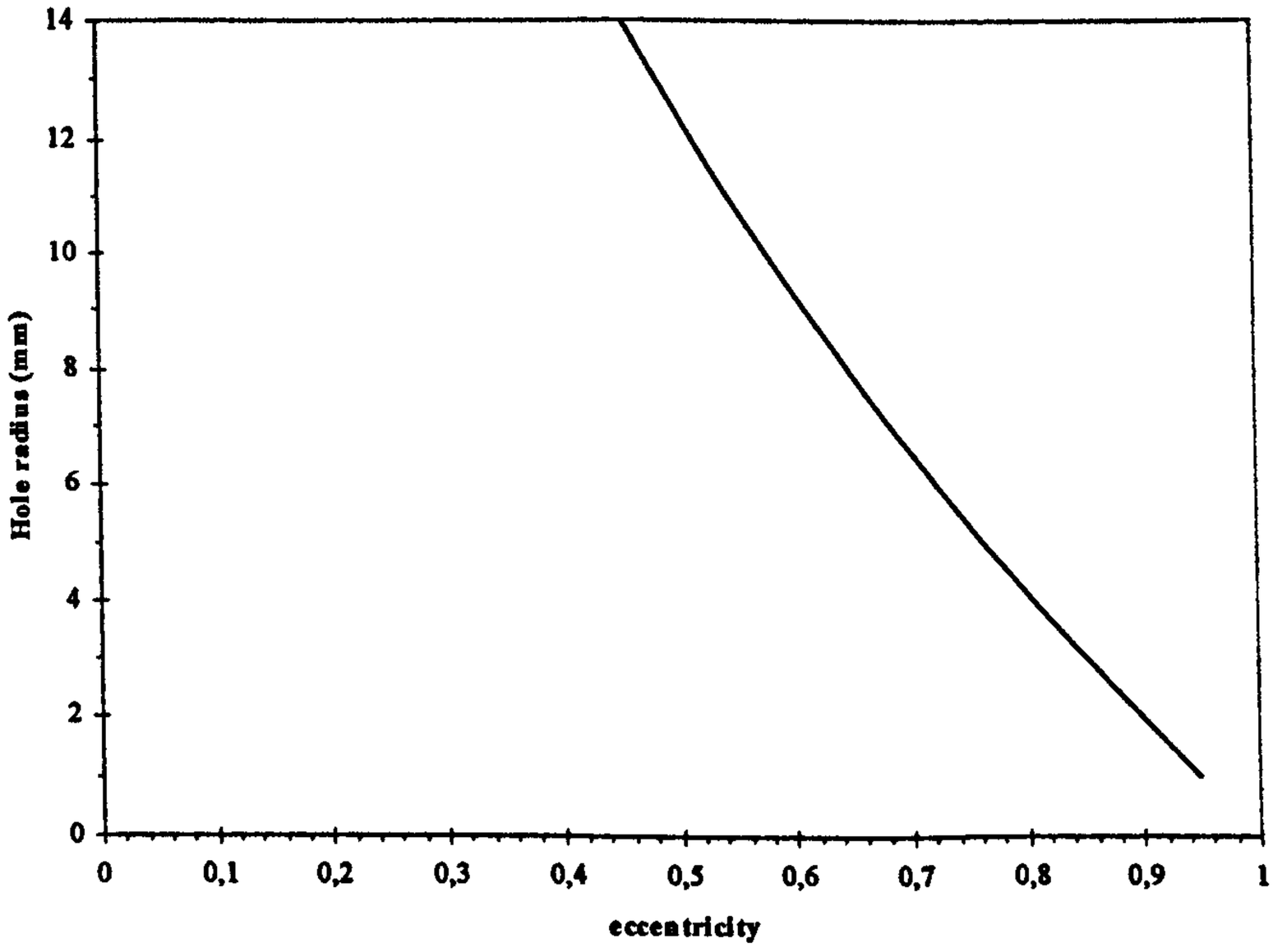

Figure 5.8. Maximum eccentricity as a function of the radius of the orifice. These calculations were performed assuming a die radius of 75 mm.

The analysis that follows has been performed using the second method of eccentricity calculations.

It is obvious that flow through the little hole will diminish as its diameter decreases. The eccentricity values alone are not enough to reflect this though. A further factor is required to quantify the friction per unit area extruded. To do this the ratio of the cross-section of the extrudate area to the area of the die land (A') of each hole is required. A' is a unitless variable, which is calculated by dividing the force required to extrude, by the force opposing extrusion at the die land. In general, the frictional force opposing extrusion increases with increases to the circumference and bearing length of the orifice and the force required to extrude increases with the area of the orifice. Combining these two factors gives a unitless scalar figure, f_i, which gives a measure of the flow allowed through the hole:

$$\begin{aligned} f_i &= A_i'(1-e_i) \\ &= \frac{\pi r_i^2 \overline{\sigma}}{2\pi r_i d\tau}(1-e_i) \\ &= \frac{\sqrt{3} r_i}{2d}(1-e_i) \end{aligned} \qquad (5.2)$$

assuming Von Mises' yield criterion holds, where i represents the hole number and d is the die land length. Note the use of the eccentricity factor in equation 5.2. Limiting conditions of $e_i = 0$ and $e_i = 1$ exist. In these extreme cases, the hole is placed either exactly in the middle of the die ($e_i = 0$) or it does not exist ($e_i = 1$). Previous examinations of the empirical rules governing bearing length calculation [126, 127] have indicated that the die land length increases linearly as the hole moves away from the centre of the die. Since the calculation of extrudability is a linear representation of the

distance of the hole from the centre of the die, equation 5.2 may be seen to have its basis in empirical rules. Thus, for example an eccentricity of $e_i = 0.5$ would give half the flow factor, f_i, of an identical hole with $e_i = 0$. The larger f is, the more flow occurs through the hole. This analysis assumes that the die is choked and the full length of the die land is used to oppose deformation. The possibility exists that the dies were not choked, and there was no practical way of removing the dies between extrusions to ascertain the full use of the die land. Observations by Clode [63] indicate that the surface finish of the extrudates is influenced by the adherence of a thin layer of aluminium to the front end of the die. The fact that the back end is bare, gives rise to surface defects such as pick up and die lines. Dies such as the ones used in a previous study [21, 87] have very small diameter holes combined with long die land lengths. In cases such as these it is probable that most of the die land remains unused and an effective die land length should be used in calculations.

Die	e_1	e_2	f_1	f_2
1	0.132	0.265	2.004	0.849
2	0.12	0.259	2.032	0.641
3	0.11	0.253	2.055	0.431

Table 5.1. Eccentricities and flow factors for all the holes in the dies

Mondolfo and Peel [21, 87] based their analysis of two-hole extrusion around the assumption that:

$$\frac{L_1}{L_2} \propto \frac{R_D + F_2}{R_D + F_1}$$

Where R_D is the inherent resistance to deformation and F_1 and F_2 are the frictional forces opposing flow at each die orifice. A similar theoretical premise was used in the

present study. In other words, the ratio of the lengths extruded through each hole is dependent on the relative sizes of the inherent resistance to deformation, R_D, and the resistance incurred at each of the die orifices (F_1, F_2). The L_1/L_2 parameter can be construed to be a measure of the extrudability of an alloy if it is considered that:

1. L_1/L_2 will be large if a material is easy to deform, because R_D will be small compared to the frictional resistance at the entry to the die orifices, thus the material will flow mainly through the large hole.
2. L_1/L_2 will tend to unity if a material is difficult to deform, because R_D will be much greater than F_1 and F_2. Thus, the flow will divide more evenly through the holes.

This approach can be modified by considering that the length ratio of the extrudates will not only be influenced by frictional factors, but also by the position of the holes. Moving a step further and implementing the flow factor, f_i, for each hole, relative flow through the holes would be:

$$\frac{L_1}{L_2} \propto \frac{R_D + \left(1/f_2\right)^{\eta}}{R_D + \left(1/f_1\right)^{\eta}} \qquad (5.3)$$

Where R_D is the inherent resistance of the material to deformation and η is a material constant which reflects the sensitivity of the material to the geometry of the die it is being extruded through. A material's resistance to deformation can be simply expressed as its flow stress. However, flow stress is temperature and strain rate dependent. In order to incorporate these variables into equation 5.3, established hot working theory could be applied, viz.

$$\frac{L_1}{L_2} \propto \frac{\frac{1}{\alpha n}\ln\left(\frac{Z_2}{A}\right)+\left(1/f_2\right)^{\eta}}{\frac{1}{\alpha n}\ln\left(\frac{Z_1}{A}\right)+\left(1/f_1\right)^{\eta}} \qquad (5.4)$$

Where α, A and n are material constants and Z_1 and Z_2 are the Zener-Hollomon parameters or temperature compensated strain rates associated with each hole. Equation 5.4 is a refined version of the relationship suggested by Mondolfo and Peel [21, 87].

The main advantage of equation 5.4 over the approach suggested by Mondolfo and Peel is its sensitivity to the individual changes in the conditions around each hole. For example, it is evident and widely accepted that changes in temperature and strain rate affect the flow stress of a material. Because of the differences in geometry of the two holes – in dies both in the present study and elsewhere [21, 87] – local changes in temperature and strain rate around the die orifices result in a variation in of the local resistance to deformation. This is not reflected in the work by Mondolfo and Peel. Moreover, a measure has been established (f_i) to quantify how flow will be affected by the size and position of the hole. Because of the similarity in the present study and in the work by Mondolfo and Peel [21, 87] the findings in the two pieces of work can be easily compared. Figure 5.9 compares the findings of Mondolfo and Peel [21,87] with those of the present study regarding the effect of temperature on the extrudability of a commercial alloy.

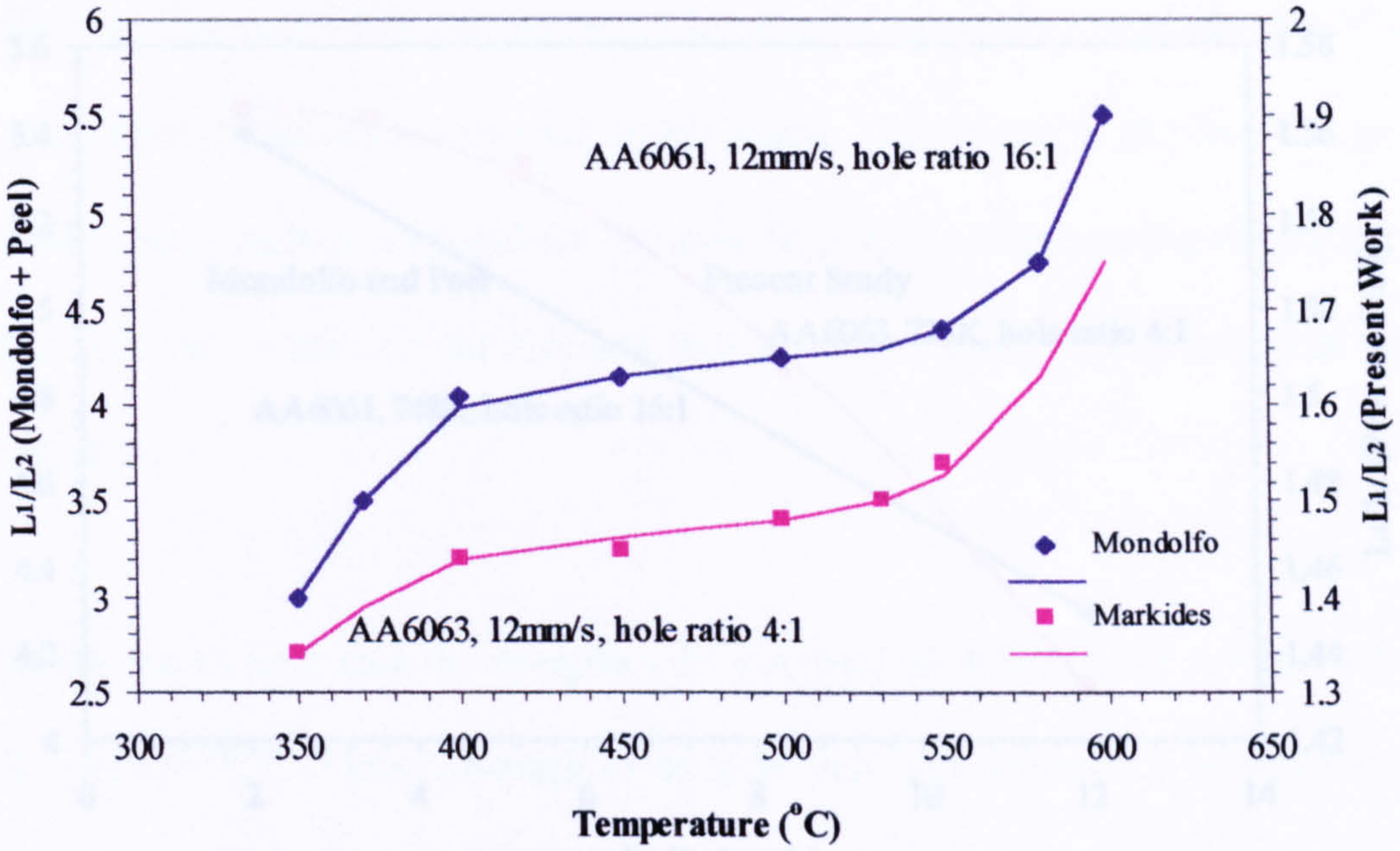

Figure 5.9. Effect of temperature on L_1/L_2 ratio

The trends shown in figure 5.9 are similar for both pieces of work and can be explained by considering the following: at low temperatures the extrudability of the alloy increases rapidly as the recrystallisation temperature is reached. It slows in the region 400 – 550 °C and then rises rapidly again as eutectic melting begins during extrusion. The differences in the absolute values between the two studies are due to the different die configurations used. A similar comparison may be drawn if the effect of ram velocity is considered (Figure 5.10). The decrease in extrudability with increase in ram velocity is natural and expected since the faster speeds will cause the frictional resistance both at the container interface and at the die land to increase. The study by Mondolfo and Peel only included two different ram velocities because of the limitations of the press used. Again, in figure 5.10 the difference in the absolute values of the extrudability between the two studies can be attributed to the difference in the die configurations used.

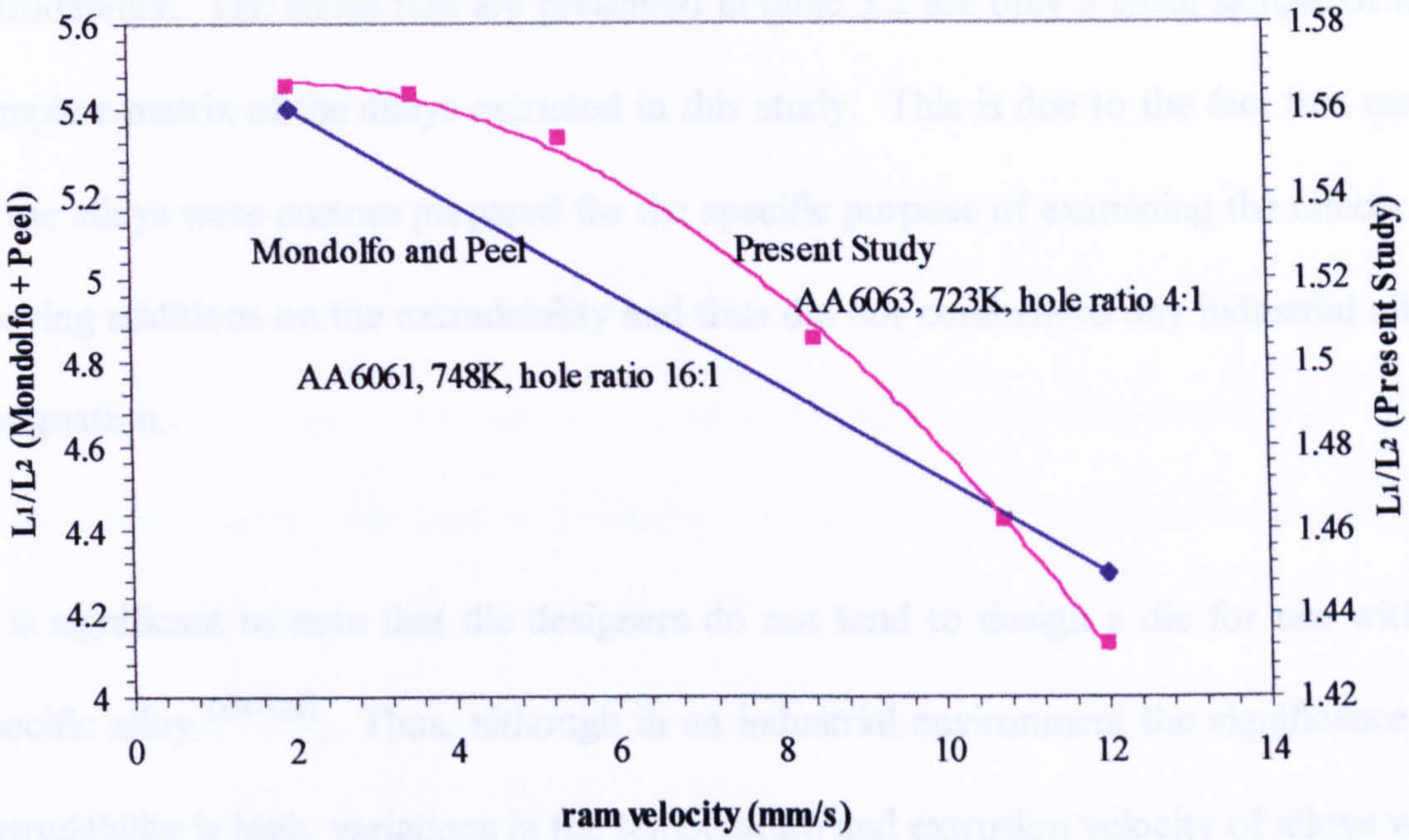

Figure 5.10. Effect of ram velocity on the L_1/L_2 ratio

Alloy	Number	L_1/L_2	% 6063	Mondolfo	Expert's % 6063
6463	421	5.85	122		105
6063	422	4.81	100	100	100
6105	432, 433	4.70	98	89	
6101	441, 422	3.62	75		100
6061	472, 501	3.18	66	86	60

Table 5.2 L_1/L_2 ratios compared to the expert's extrudability chart

The L_1/L_2 ratio, as a measure of extrudability, correlates well with the expert's extrudability chart, which was derived, based on extruder's experience and the results presented in the study by Mondolfo and Peel (Table 5.2). The discrepancy observed with alloy 6101 can be explained by considering the amount of Fe present in such alloys. Alloys 441 and 442 have a high Fe content (0.53 wt %) which is improbable in an industrial alloy. As underlined later (section 6.3), high Fe contents adversely affect

extrudability. The alloys that are presented in table 5.2 are only a small sample of the complete matrix of the alloys extruded in this study. This is due to the fact that most of the alloys were custom prepared for the specific purpose of examining the effects of alloying additions on the extrudability and thus did not conform to any industrial alloy designation.

It is significant to note that die designers do not tend to design a die for use with a specific alloy [126-128]. Thus, although in an industrial environment the significance of extrudability is high, variations in the temperature and extrusion velocity of alloys with different properties can minimise the effects of the inherent resistance of the material, leaving the designers to use the empirical rules of their trade to achieve the desired results.

A recent theoretical study by Keife [88] calculates the length ratio of the extrudates using a complex eight-triangle upper bound solution. The results were validated using modelling clay extruded indirectly. However, it seems that the theoretical results are not entirely reflected by the experiments. The analysis suggests a dead metal zone formed around the die orifices. This is not the case with the split modelling clay billets presented in the study. Also there is a great deal of scatter in the experimental results (up to 50 %) through which it would be relatively easy to infer any theoretical extrapolation. The gridded modelling clay extruded billets shown in the study underline the previously stated fact that material flow through the centre of the die is greater than that further out. The extrudates (produced through knife-edge die orifices) bend away from the middle of the die as soon as they begin to emerge. This is

a sign that the inside edge of the extrudate is being provided with material at a greater rate than the outer edge.

As was mentioned earlier the strain rate associated with each hole on the die varies depending on the hole size and the amount of material flowing through it. The pseudo-billet theory, explained in chapter 3, can be applied to ascertain the strain rates of the two extrudates, using the Feltham [58] approach (equation 2.16). Figure 5.11 shows how the strain rate of each hole changes depending on the material flowing through it. It can be seen in the figure that the change in strain rate for each extrudate, with extrudate length, is negligible compared to the difference between the strain rates of the two holes. In this way, although exact strain rates cannot be calculated they may be estimated by the size of the holes.

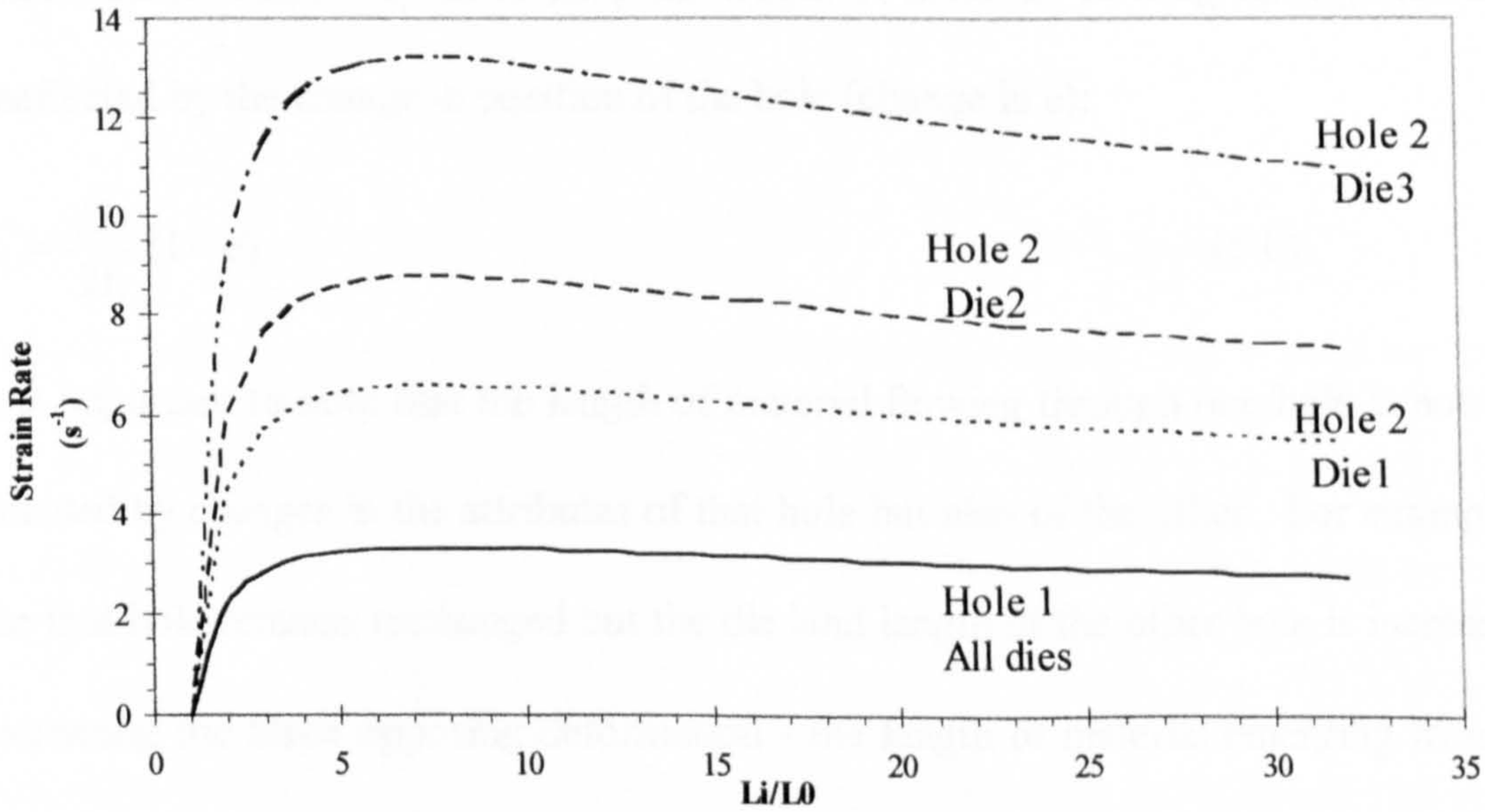

Figure 5.11. The strain rates of the extrudates against the ratio of the lengths of the original billet (L_0) to the length of the extrudate (L_i) calculated using the Feltham approach.

5.2.2. Calculation of the experimental extrudability

Obviously, from equation 5.2, the same length of material would be generated if we had a smaller hole (smaller r_i) closer to the centre of the die (decreased e_i) - or, conversely, a larger hole, further from the centre of the die. Thus it is possible to calculate the equivalent size of a hole in the middle of the die that would yield the same length of material. In the same way, while the size of the hole may remain constant, the length of the die land may vary to balance the change in position of the hole. The effective radius of a die orifice - the radius of the hole if it were positioned axisymmetrically in the die, i.e. in the centre - is:

$$r_{eff} = \frac{2}{\sqrt{3}} d_i \cdot f_i \qquad (5.5)$$

Where f is the flow factor of the orifice. Similarly, the die land length may be calculated in such a way as to keep the length of material, flowing through the hole, unaffected by the change in position of the hole (change in e):

$$d_i = \frac{\sqrt{3} r_i}{2 f_i} (1 - e) \qquad (5.6)$$

It is important to note that the length of material flowing through one hole is not only affected by changes in the attributes of that hole but also of the other. For example, if the first hole remains unchanged but the die land length of the other hole is increased - increasing the force opposing deformation - the length of material emerging from the first hole will increase. Industrial practices work on a theory similar to this. Die dressers and designers work on the principle of concentric circles from the die centre. At the centre a certain die land length is used which decreases as the component moves towards the outer rims of the die. The amount by which the die land is decreased is

also dependent on the size of the component to be extruded. A thinner profile will have a smaller die land length than a thicker one. A series of empirical rules have been published [126, 128] and are currently implemented by die dressers in industry.

An empirical equation [127], based on the above rules can be used to relate the land length, b, at a section of width w, to the reference bearing length, B, at a section of width W:

$$\frac{b}{w} = \frac{B}{W}(1 + C(Q - q)) \qquad (5.7)$$

Where C is a constant for a given die, Q is the minimum radius of a circle concentric with the die, which circumscribes all orifices, and q is the distance from the section to the die centre. The reference bearing length and width are always chosen as those furthest from the die centre or those that apply to the 'slowest' part of the profile. Qualitatively, equations 5.7 and 5.6 are similar as they both define the bearing length as increasing from the outer parts of the die towards its centre.

Equation 5.6 requires some modification before it can be implemented on an industrial basis because it was developed specifically for the purposes of the present study, i.e. two circular holes in a flat-faced die. On the other hand equation 5.7 is based entirely on the experience of die dressers and has no theoretical basis. The two methods can be compared by their prediction of the bearing length for a hole whose size and position varies, using a reference orifice with fixed size, position and bearing length. It can be seen from figures 5.12 and 5.13 that the two methods are in extremely good agreement. The flow factor approach introduced in this study shows that a theoretical

basis for die design can be implemented without the existing empirical rules being compromised.

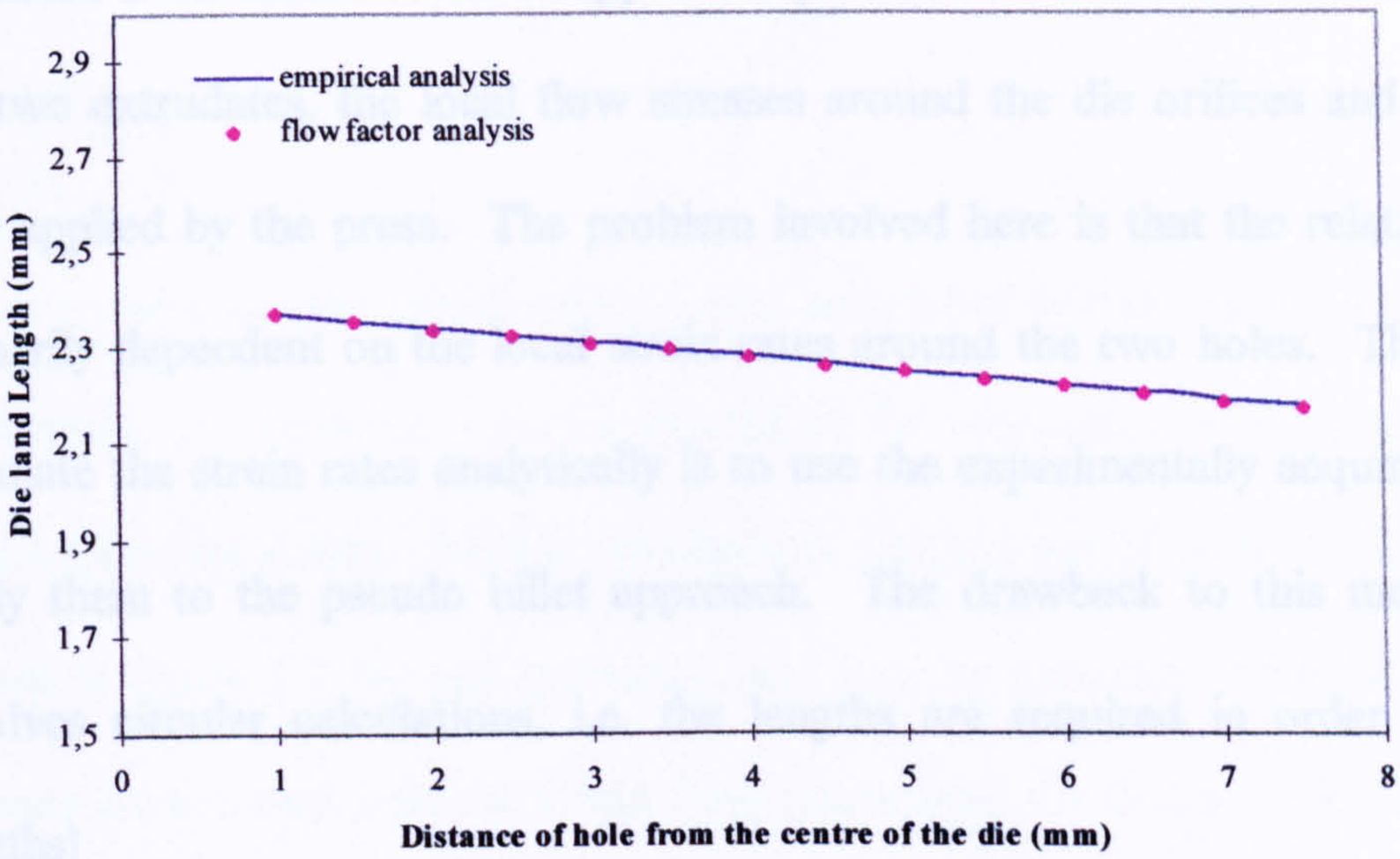

Figure 5.12 The predicted die land length for both the empirical and the flow factor approach as a function of the distance of the hole from the centre of the die.

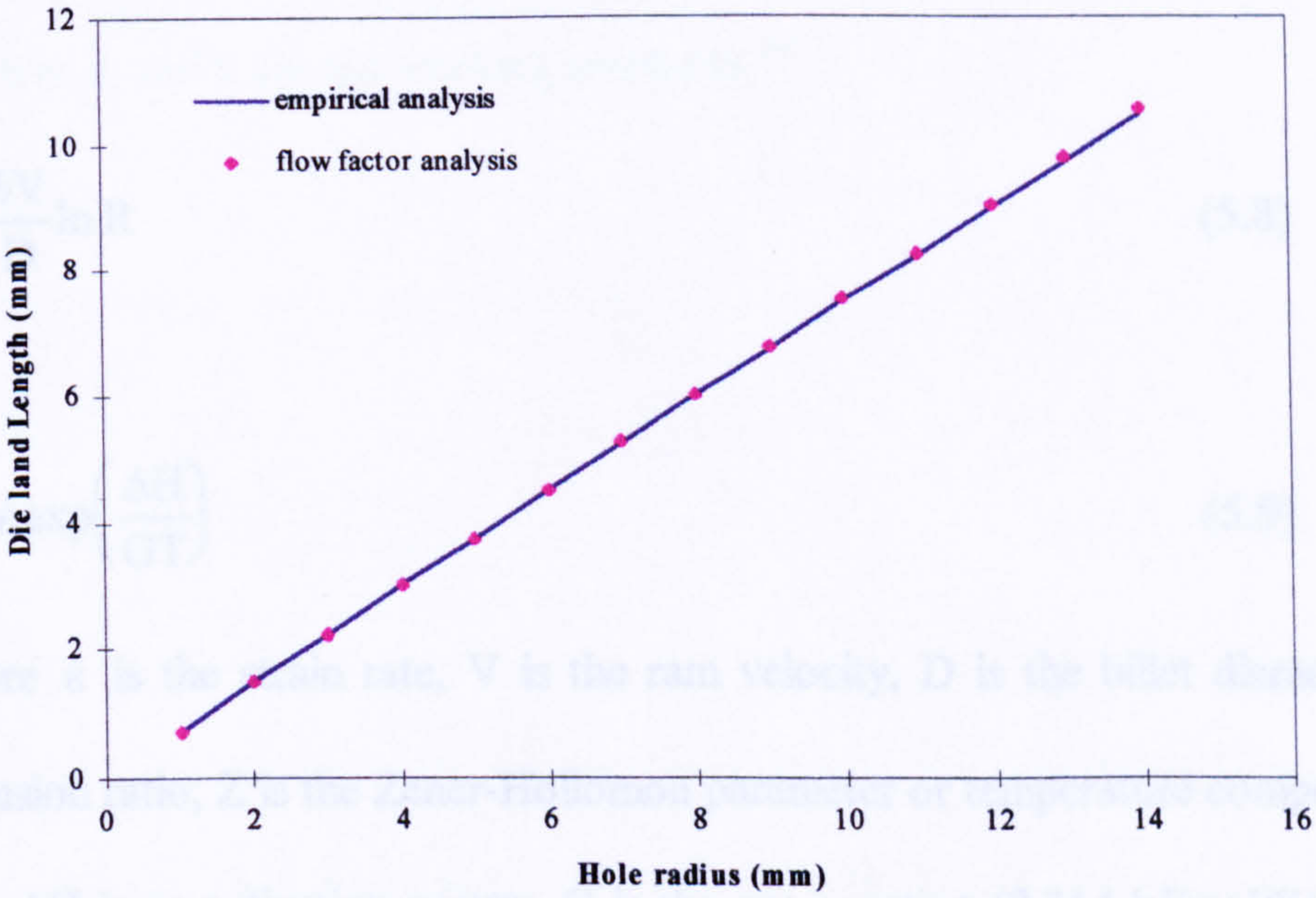

Figure 5.13 The predicted die land length for both the empirical and the flow factor approach as a function of the radius of the hole.

5.3 Force Balance

The theory of the force balance model is detailed in chapter 3. It would, however be beneficial if the model could be applied to predict variables such as the length ratio of the two extrudates, the local flow stresses around the die orifices and the maximum load applied by the press. The problem involved here is that the relative lengths are primarily dependent on the local strain rates around the two holes. The only way to calculate the strain rates analytically is to use the experimentally acquired lengths and apply them to the pseudo billet approach. The drawback to this method is that it involves circular calculations, i.e. the lengths are required in order to predict the lengths!

In order to find the variables mentioned above, an estimation of the strain rates and Z parameters must be made. From established theory [58]:

$$\dot{\varepsilon} = \frac{6V}{D} \ln R \tag{5.8}$$

and

$$Z = \dot{\varepsilon} \exp\left(\frac{\Delta H}{GT}\right) \tag{5.9}$$

Where $\dot{\varepsilon}$ is the strain rate, V is the ram velocity, D is the billet diameter, R is the extrusion ratio, Z is the Zener-Hollomon parameter or temperature compensated strain rate, ΔH is an activation energy, G is the gas constant (8.314 kJ/mol/K) and T is the absolute temperature. Equation 5.8 cannot be applied directly to the data for two-hole extrusion because the diameter of the billet does not apply for both holes. The theory

of the pseudo-billet - i.e. the diameter of a billet, which would account for the formation of each extrudate - can be applied to equation 5.8, which becomes:

$$\dot{\varepsilon}_i = \frac{3V}{p_i} \ln \frac{p_i^2}{r_i^2} \qquad (5.10)$$

where p_i and r_i are the pseudo-billet radius and radius of hole i in the die. The pseudo-billet radius is calculated from the lengths of the extrudates, which must be estimated from experimental data. Simple calculations, though, can be made to create the curves shown in figure 5.7 for any geometry, and give an estimate of the strain rates. The stresses around each hole are found from rearranging the Zener-Hollomon equation:

$$\bar{\sigma}_i = \frac{1}{\alpha} \ln \left[\left(\frac{Z_i}{A} \right)^{1/n} + \sqrt{\left(\frac{Z_i}{A} \right)^{2/n} + 1} \right] \qquad (5.11)$$

where α, A and n are hot working constants [63].

5.4 Microstructural Evolution in AA6063

The structure before and after extrusion and the restoration processes that the alloy undergoes as it is being extruded will be examined in this section.

5.4.1. As cast and Homogenised Microstructures

Homogenisation has two main functions in this study. One was to alleviate any coring or segregation that may have existed from the gravity die casting process and the other was to aid the β to α AlFeSi phase transformation.

5.4.1.1. AlFeSi phase transformation

Figures 5.14, 5.15 and 5.16, 5.17 show the structure of the Fe phase before and after homogenisation, respectively, for two different alloys (with high Fe contents and differing Si contents). What is immediately evident, in the unhomogenised material, is that the dark phase (AlFeSi) is aligned as acicular particles along the grain boundaries. These particles tend to split up, after homogenisation into the conventional chinese-script type particles, which are traditionally associated with the α-AlFeSi phase.

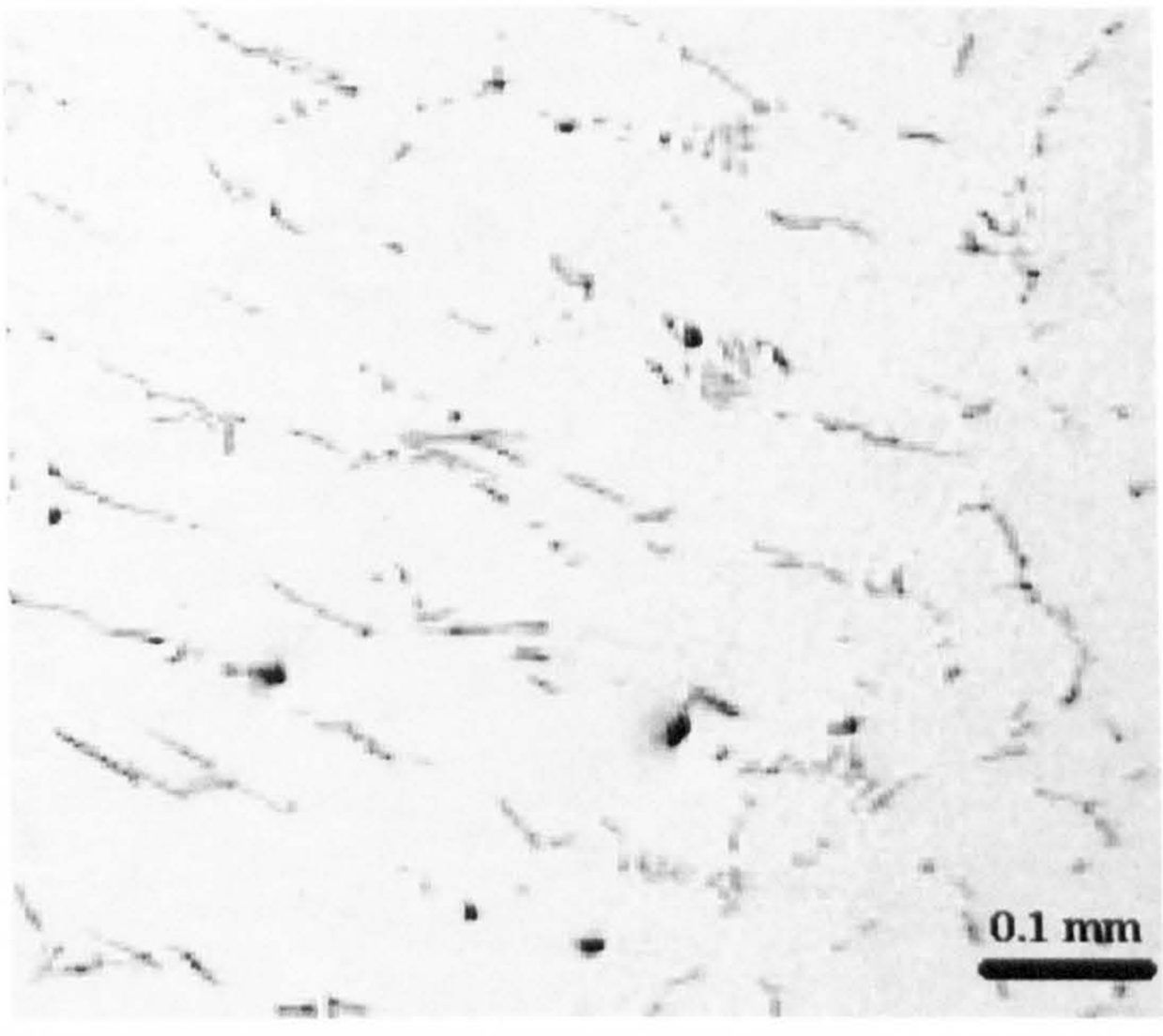

Figure 5.14. Unhomogenised structure of alloy 451 (0.69 wt % Mg, 0.35 wt % Si, 0.77 wt % Fe)

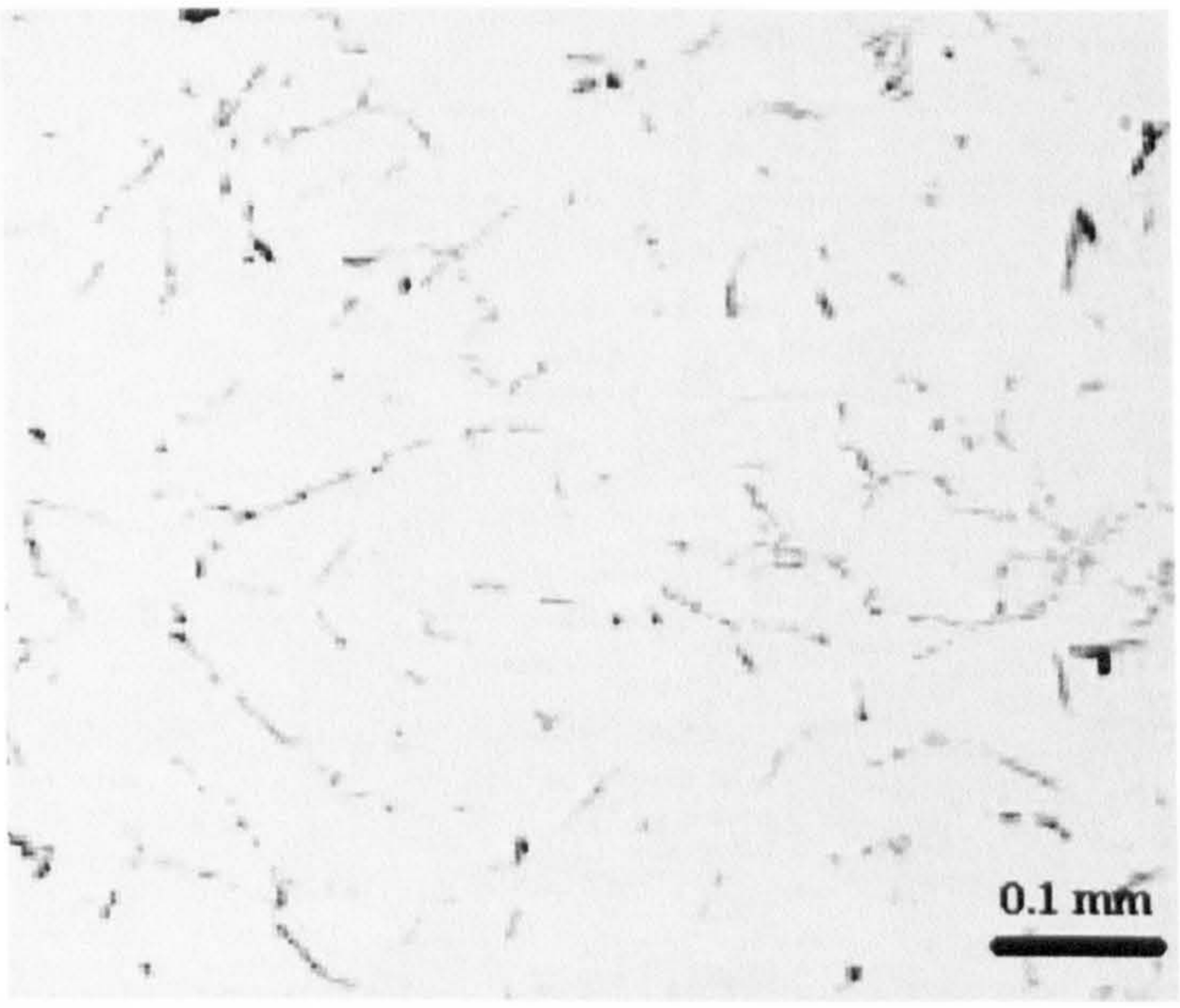

Figure 5.15. Homogenised structure of alloy 451 (0.69 wt % Mg, 0.35 wt % Si, 0.77 wt % Fe).

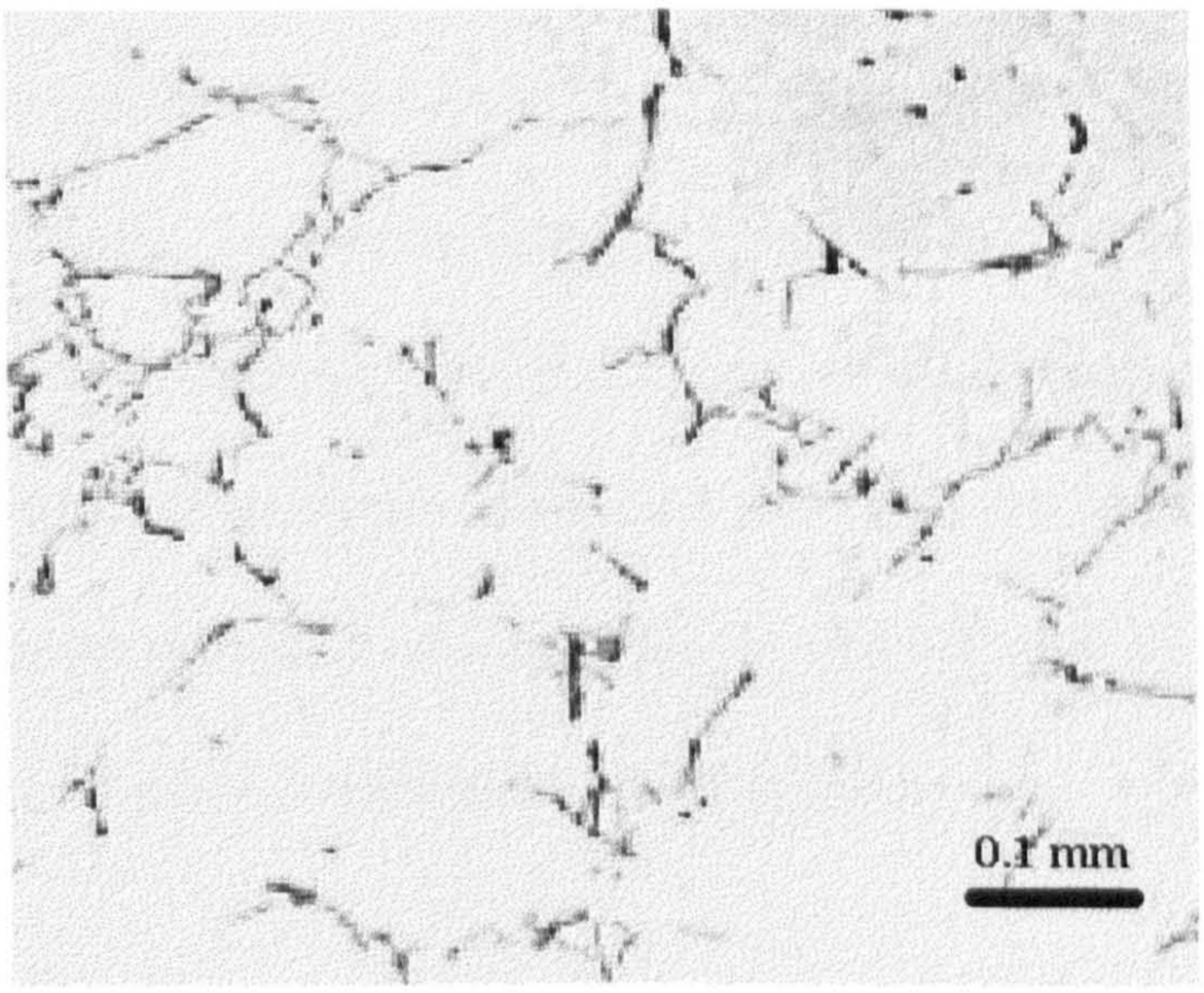

Figure 5.16. Unhomogenised structure of alloy 454 (0.64 wt % Mg, 1.3 wt % Si, 0.8 wt % Fe).

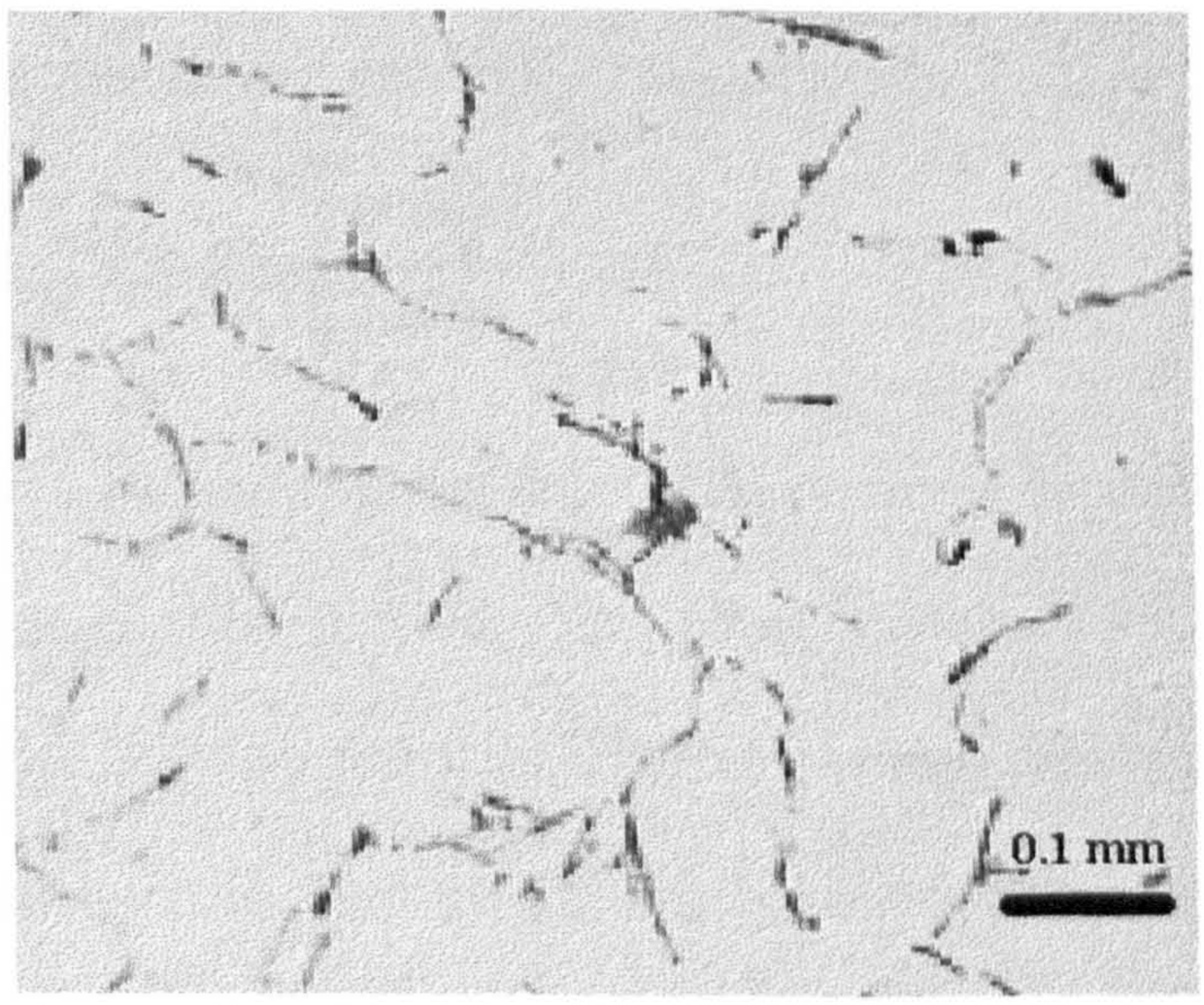

Figure 5.17. Homogenised structure of alloy 454 (0.64 wt % Mg, 1.3 wt % Si, 0.8 wt % Fe).

The second alloy (454) contains a great deal of excess Si (about 1 % over that required to create the Mg_2Si, given the amount of Mg in the system). This leads to larger amounts of Fe phase present in the matrix, than the previous alloy (451), which has the Si balanced with the Mg. Comparing figures 5.14 and 5.15, the amount of iron phase particles seems to have lessened from the former to the latter (unhomogenised to homogenised). This leads to the conclusion that, although, the homogenising process aids the β to α transformation, it also increases the amount of Si in solid solution, as would be expected for a heat treatment above the solvus.

From alloy to alloy, the density of the AlFeSi phase in the structure may change - higher Fe contents, such as the ones shown in the figures above, result in a much higher density of Fe phase in the structure, as do higher Si contents. However, the mode of transformation of the β- to α-AlFeSi is similar for all alloys.

5.4.1.2. Alleviation of Segregation

Figure 5.18 shows a number of grains close to the centre of the casting which have a large amount of segregation in them. This effect is common to all cast alloys as discussed in chapter 2. Note that the intermetallic phases arise around the dendrite arms, where solute rejection from the freezing dendrite is at its highest. The liquid around the dendrites is high in solute concentration and, thus, the intermetallic phases - mainly the AlFeSi phases - are more likely to be nucleated in these areas rather than anywhere else.

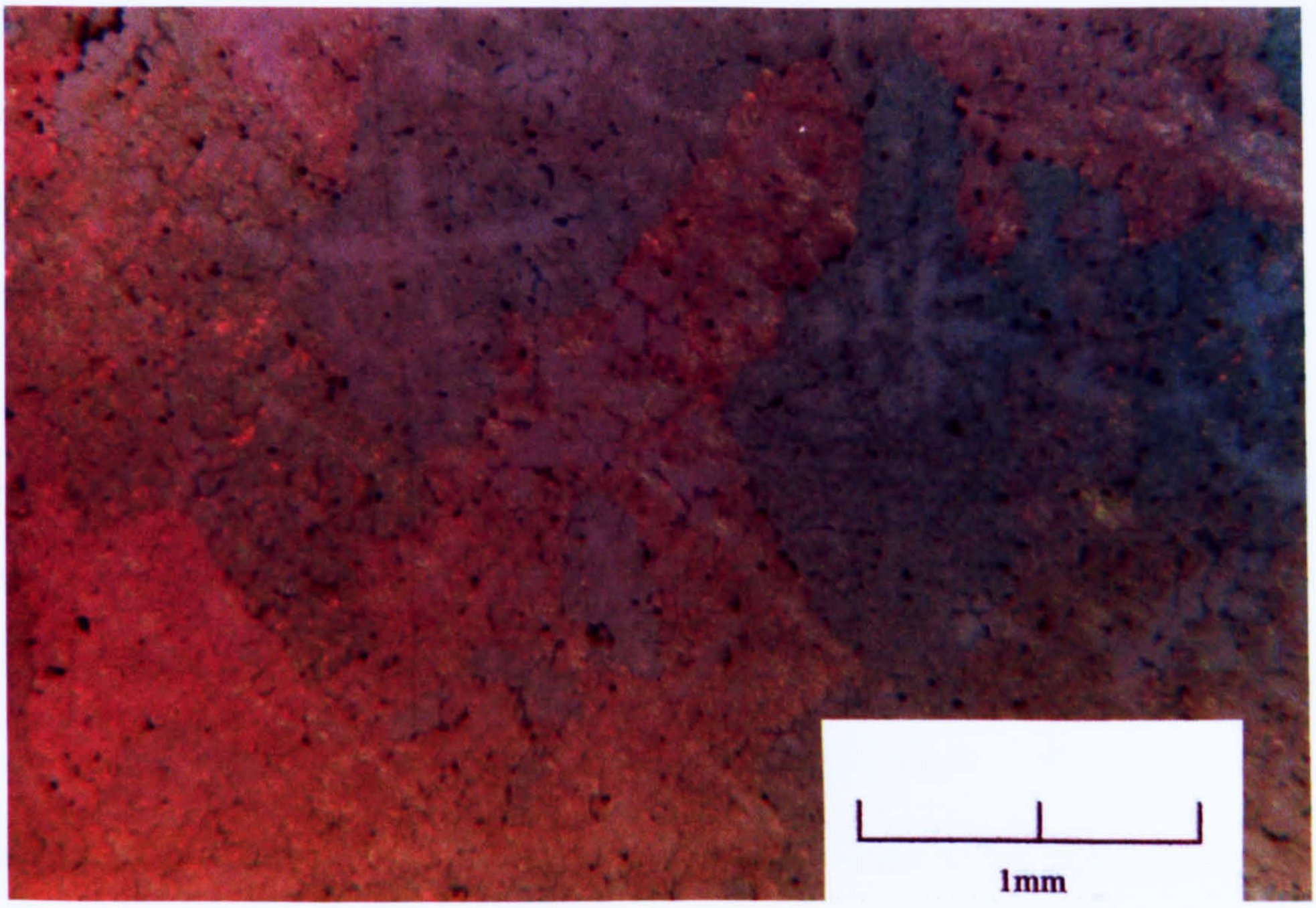

Figure 5.18. Grain structure of as-cast alloy 444

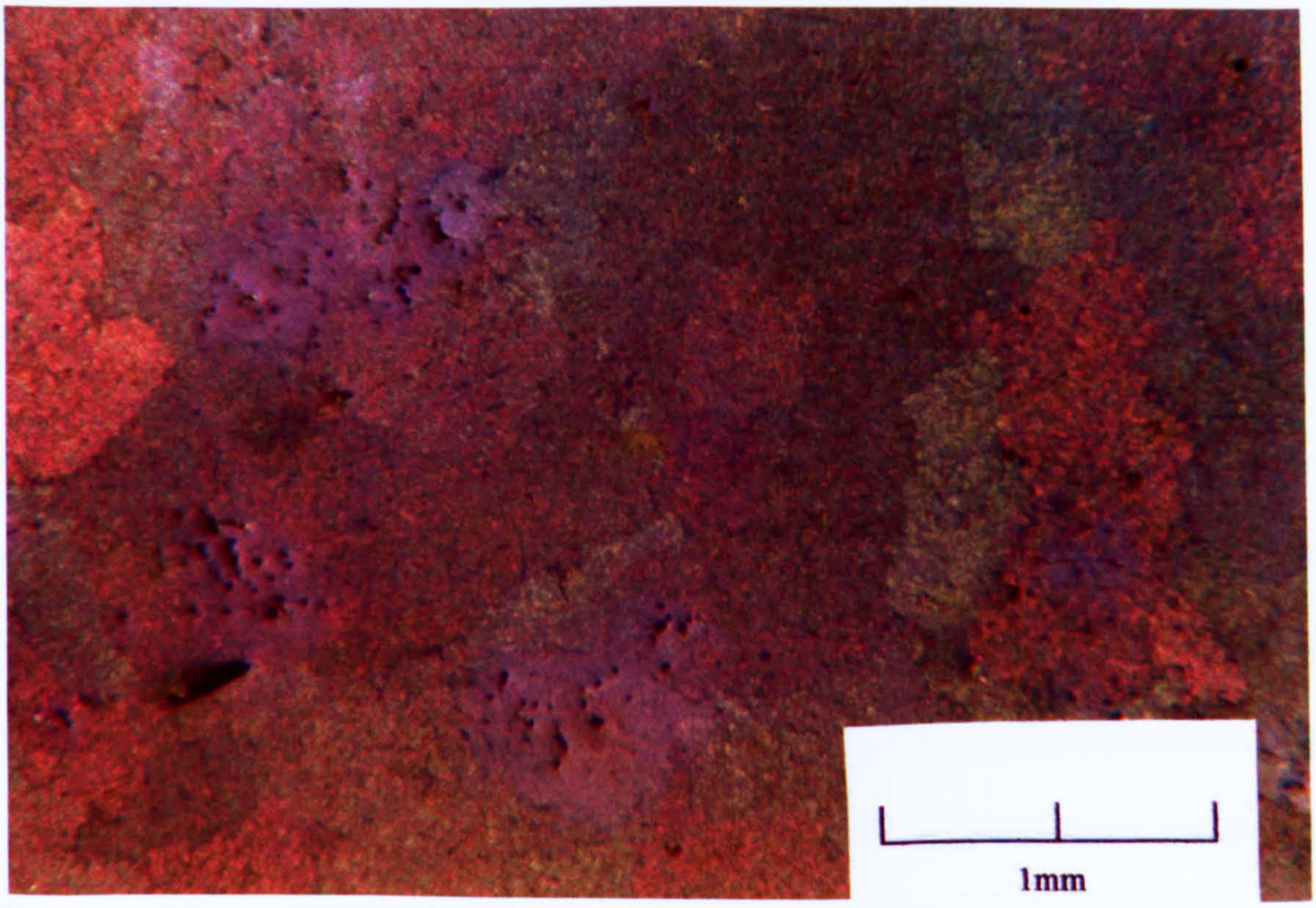

Figure 5.19. Grain structure of homogenised alloy 444

Comparing the structure of the as-cast and the homogenised samples (figure 5.19) it is observed that the coring (the colour variation within a single grain) is now absent. This indicates that the homogenising heat treatment has successfully managed to alleviate the coring and segregation, which was previously present in the cast structure.

As mentioned in section 2.2, the castings used in the present study are prone to amounts of macro segregation, which is common in gravity castings. The segregation will manifest itself as high solute concentration areas at the centre of the billet, as solute rich melt is rejected ahead of the solidification front. Such segregation is expected to affect the L_1/L_2 ratio since flow of the centre of the billet occurs mainly through the large hole (see figure 5.20). A higher solute concentration increases the alloy resistance to deformation, so L_1/L_2 will be smaller for such a billet compared to one with no segregation. However, this effect is universal for all the billets extruded in this study and will not be considered as a factor affecting extrudability.

The structure shown in figure 5.19 shows a great deal of porosity. This is due to imperfections in the casting process. As mentioned previously, the billets used for the extrusion were not cast industrially, but were manufactured using a simple gravity die technique in the laboratory. This process involved an increase in the temperature of the die throughout the day, which caused a corresponding decrease in the solidification rate of the alloys. It was not possible to keep the die at a constant temperature because of the continuous introduction of liquid metal into it. A ceramic filter was used to alleviate the velocity gradient as the metal entered the part of the die, which

formed the billet. This filter created a number of small bubbles in the structure, which could not escape and resulted in the porosity, which is seen in the figure above.

5.4.2. Development of the DMZ

6xxx series alloys have major uses in cosmetic applications and architectural trim. As such, the surface defects, which are common to extrusion products ('pick-up', 'die lines') should be suppressed as much as possible. It has been shown [63] that in order to achieve minimum occurrence of surface defects during extrusion, the products should be generated from the inner areas of the billet while avoiding the use of the surface of the billet. For this reason, it is common to use no lubricant while extruding 6xxx series alloys to introduce sticking friction at the interface between the billet and the tooling. Hence, the material adjacent to the interface remains immobile during the stroke, forming what is known as the Dead Metal Zone (DMZ). This volume of metal extends from the front part of the billet back at an angle typically around 45° as shown in figure 5.20.

Behind the DMZ is a region of highly deformed grains, known as the deformation region. This region forms the inner boundary of the DMZ and extends towards the back of the billet in a hemispherical pattern. The material originating from this region forms part of the surface of the extrudates. The surface of the extrudates emerging from the centre of the die, (i.e. the area where the holes are closest to each other) is generated from a small deformation region, which surrounds the DMZ between the holes.

In figures 5.20-5.22, the discards of billets extruded to about 50 % through each die are shown. Note the size of the Dead Metal Zone on each side of the die.

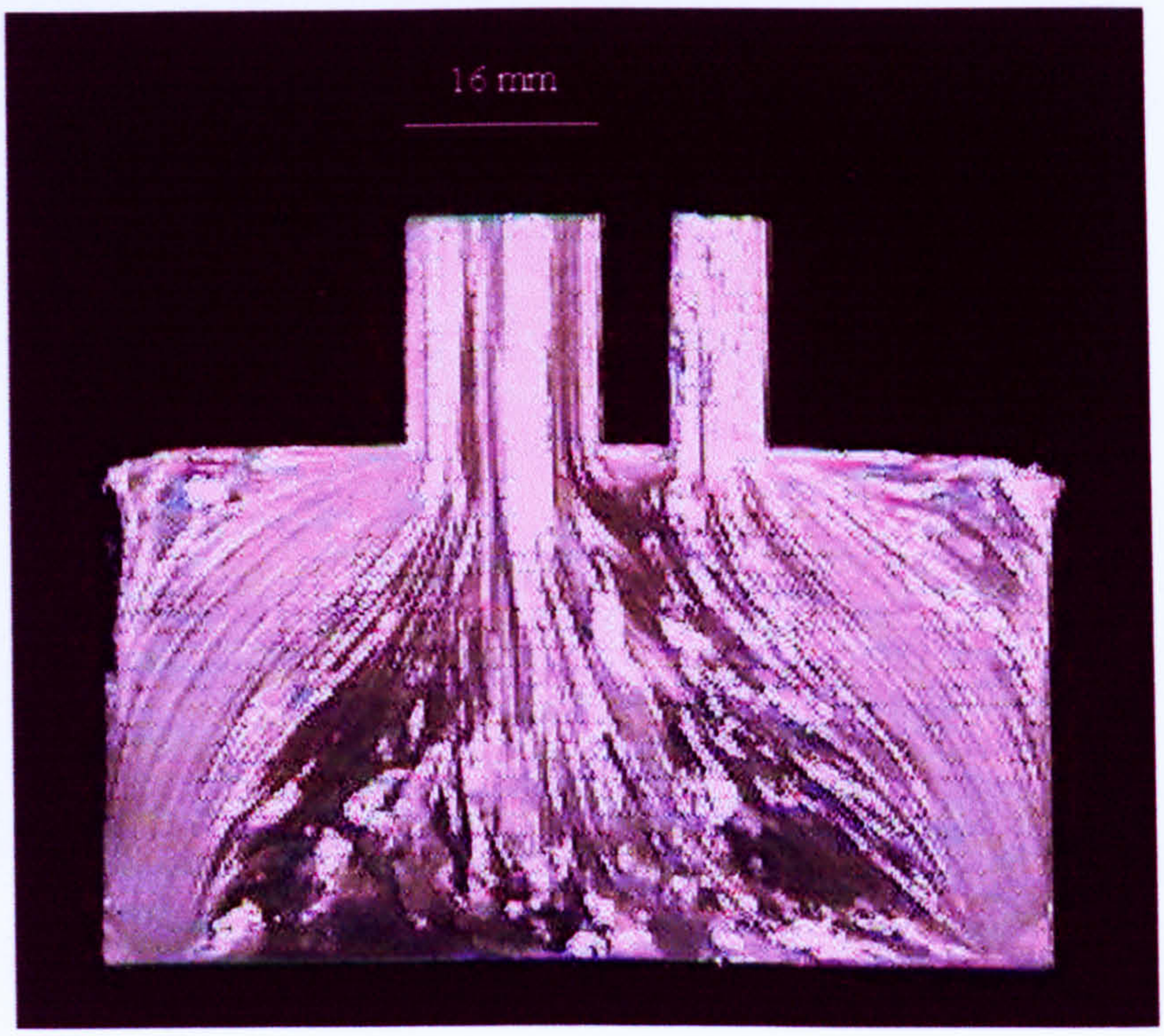

Figure 5.20. Partial extrusion through die 1.

It is evident that the size of the DMZ, i.e. how far into the billet it extends, is appreciably greater on the side of the smaller extrudate. What is also evident is how the DMZ depth increases as the hole decreases in diameter. It is unclear whether this is due to the decreasing size of the aperture or the increasing distance to the edge of the die. There also seems to be a slight increase in the depth of the DMZ on the side of the larger hole. As the holes are the same diameter for all the dies, the reason for this can only be the slight shift towards the centre of the die.

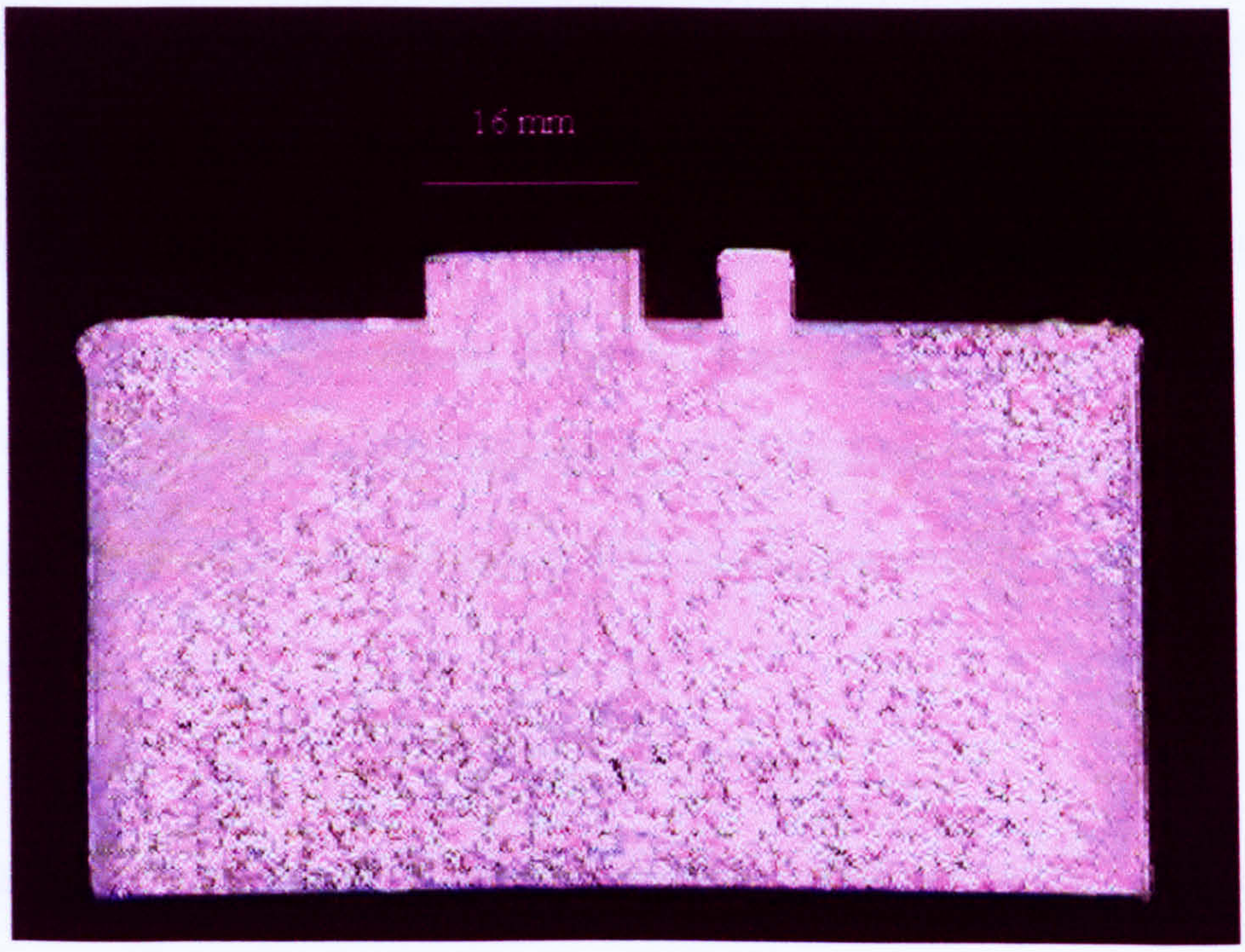

Figure 5.21. Partial extrusion through die 2.

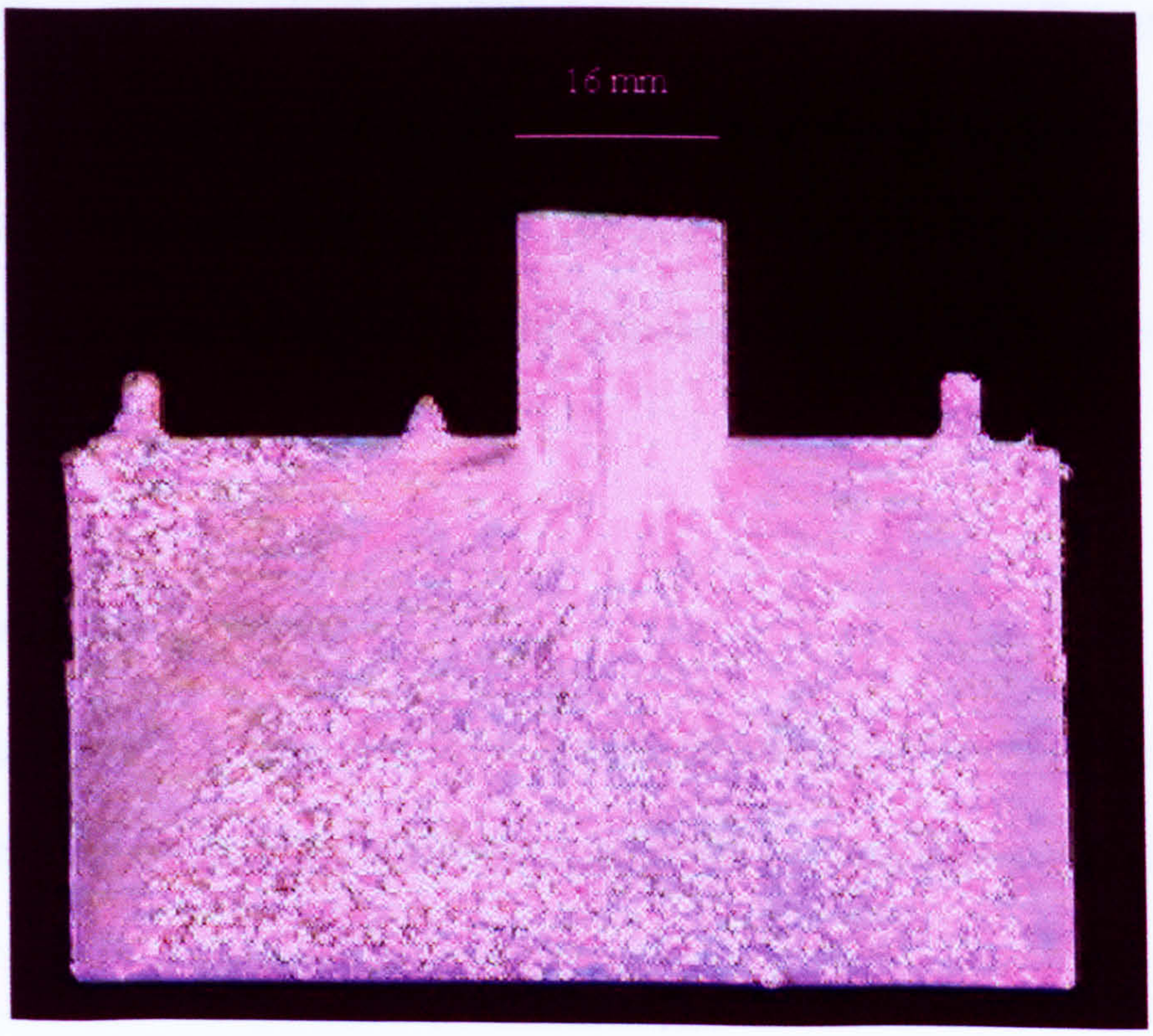

Figure 5.22. Partial extrusion through die 3.

In the region between the die orifices there is very little DMZ development. As noted by Valberg [123], this is due to the close proximity of the holes and the ability of the alloy to undergo internal shear relatively easily. Partial extrusions were only performed on a single alloy - commercial AA6063 - and, thus, any similar effects in other alloys will remain speculations. However, based on other observations in similar studies [123, 124] it is safe to assume that the depth of the DMZ will increase (as will the probability of observing a funnel shaped DMZ between the holes) as the extrudability decreases.

The difference in grain structure - large in figure 5.20, but very fine in figures 5.21 and 5.22 - can be attributed to the grain refiner present in the billets, which were remelted to cast the AA6063 alloys. The structure shown in the figures is that of the pre-extruded billet, not created by the extrusion process. The longer the billets were left in the melting furnace prior to casting, the less effect the grain refiner (TiB_2) would have once the billets were eventually cast [122]. The alloys in the latter two figures were cast early in the casting day while the first one was cast much later, leading to the effects seen in the figures above.

5.4.3. Restoration processes

Comparing figure 5.20 with two other partial extrusions, shown together in figure 5.23, the striking feature is the difference in grain size between the three partials.

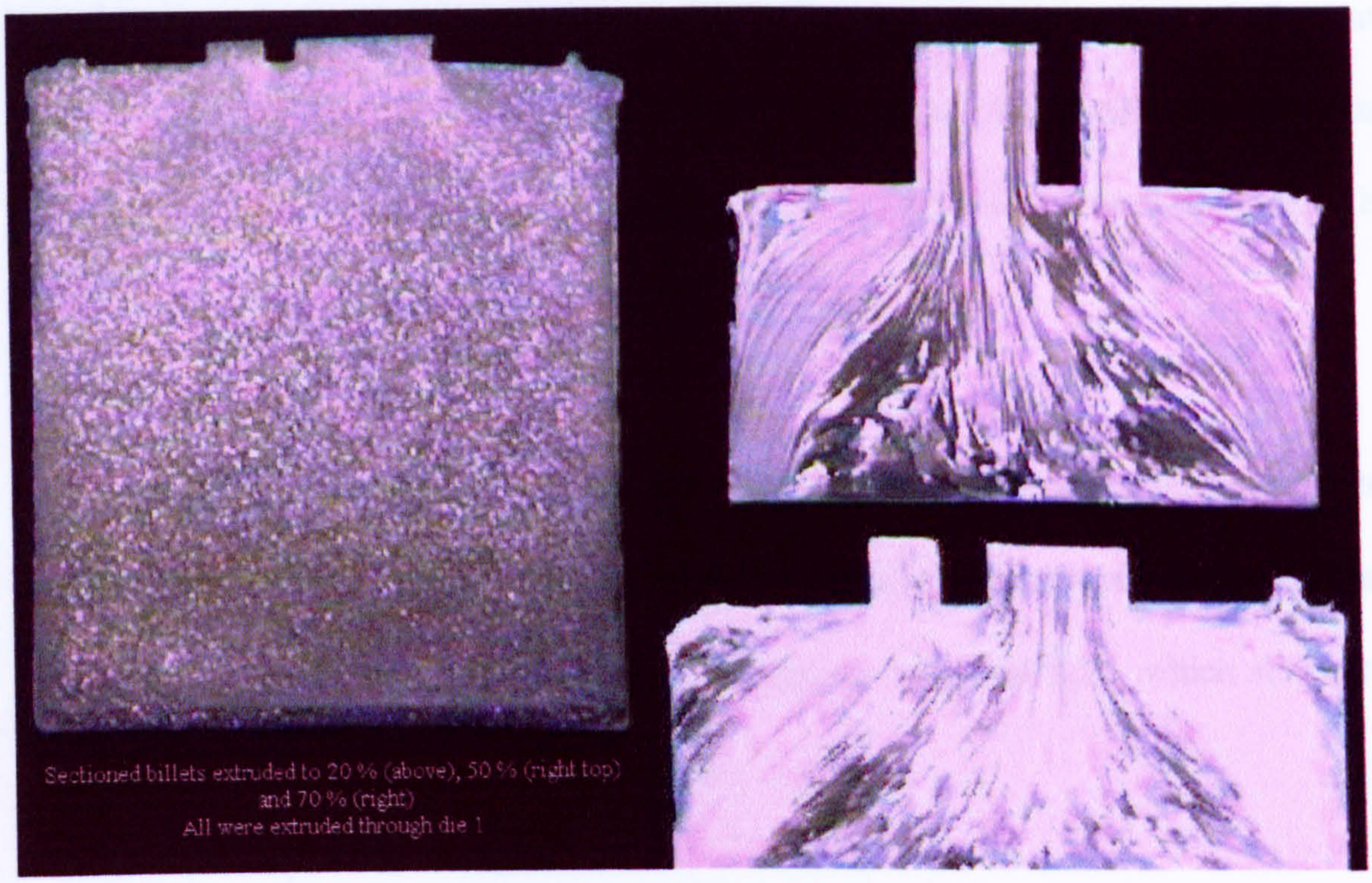

Figure 5.23. Sectioned billets extruded to (clockwise from left) (a) 20, (b) 50 and (c) 70 %. All were extruded through die 1.

No recrystallisation is observed in the figures above. Any static recrystallisation would have resulted in small grains growing in the highly strained areas next to the DMZ. Aluminium alloys do not tend to recrystallise dynamically [129, 130], although some workers [131] have observed a variation of the dynamic mechanism (which they called "*Geometric* Dynamic Recrystallisation") occurring in high alloying content Al alloys at high strains. The difference in grain size is due to the effect described in the previous section regarding the effects of the grain refiner. However, recrystallisation is observed to take place in the extrudates as seen below.

As may be evident in figure 5.23 b and c, the large extrudate has a tendency to be asymmetrically deformed, i.e. one side of the extrudate is more heavily deformed than the other. This can be seen more clearly in figures 5.25 and 5.26, which show the grain structure at either end of the extrudate.

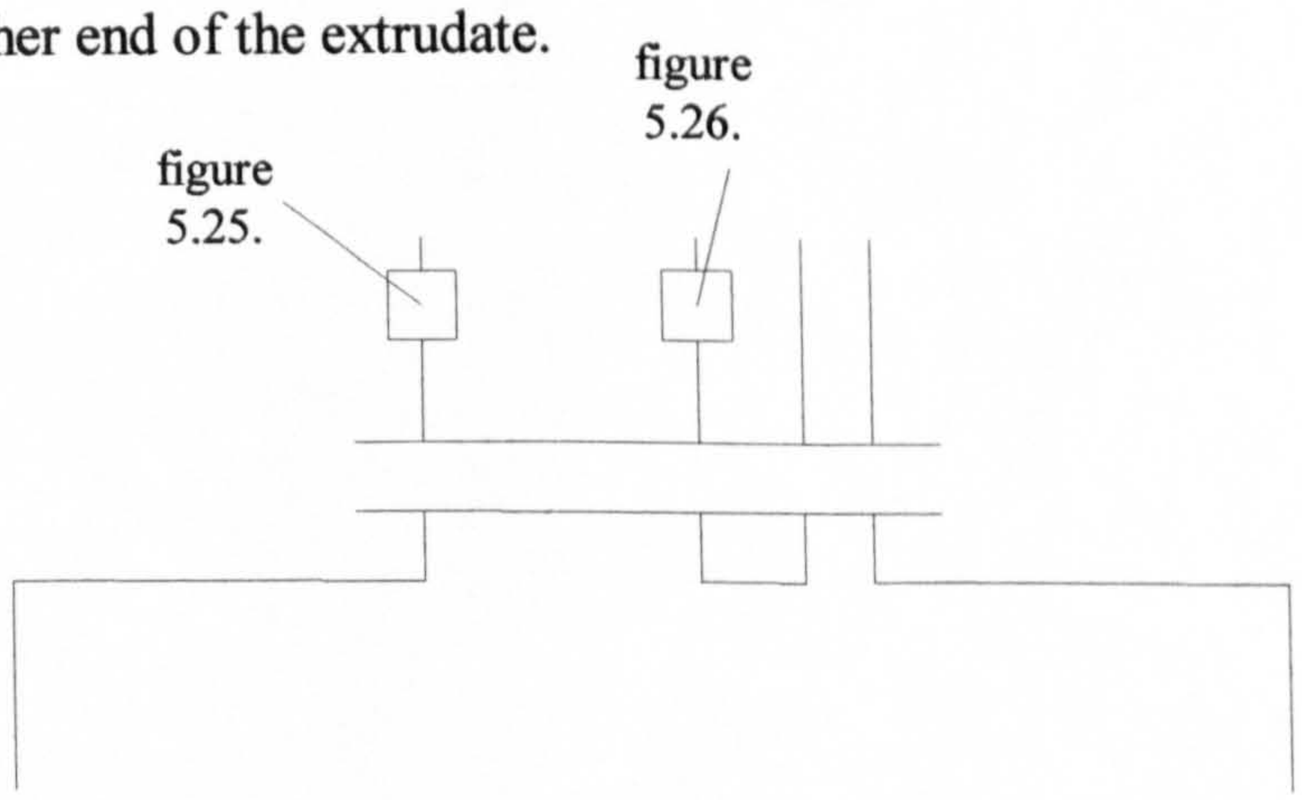

Figure 5.24. Schematic indicating the position of the structures shown in figures 5.25 and 5.26.

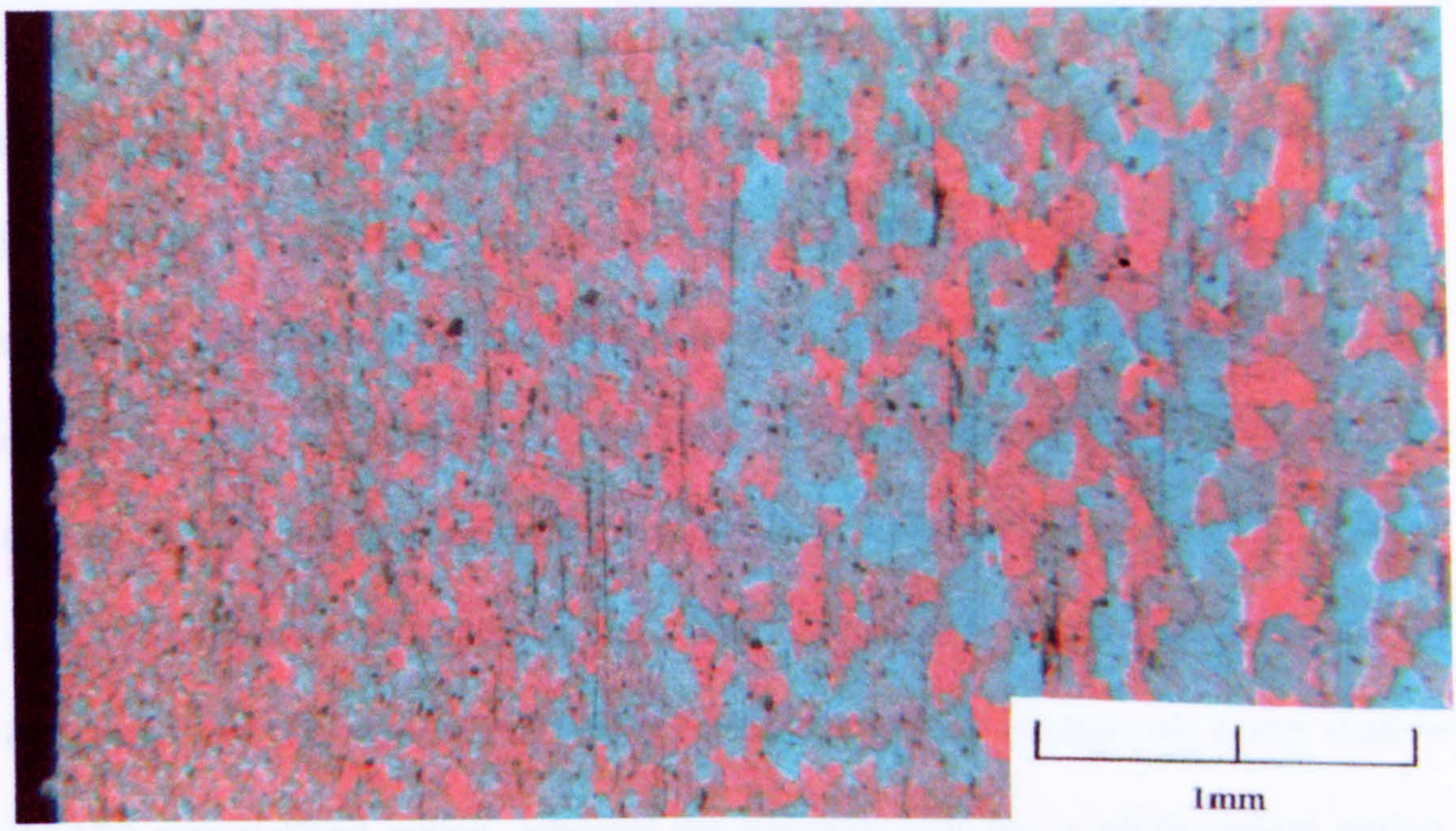

Figure 5.25. Longitudinal section showing the grain structure of alloy 521 (1.18 wt % Mg, 0.67 wt % Si, 0.33 wt % Fe)

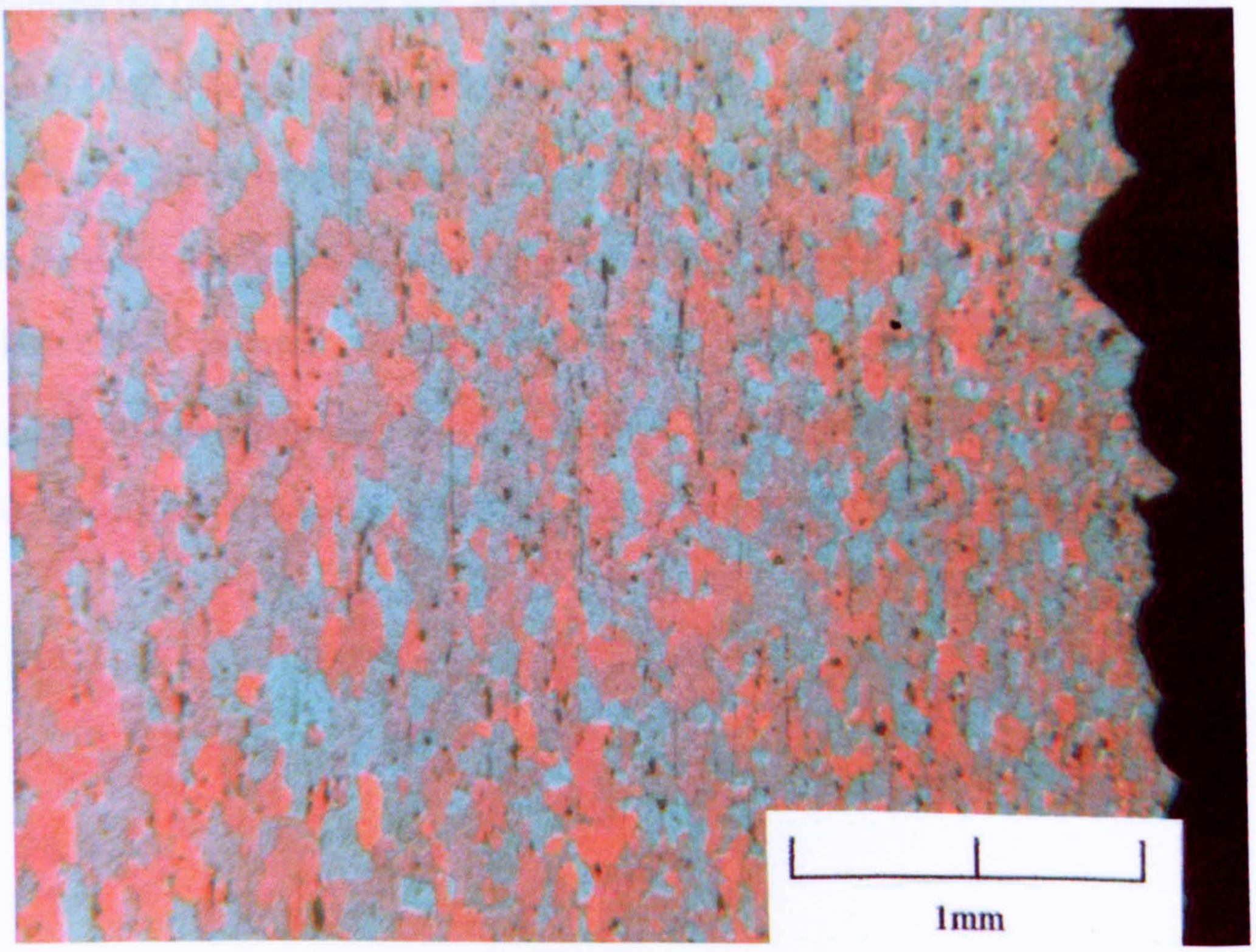

Figure 5.26. Longitudinal section showing the grain structure of alloy 521 (1.18 wt % Mg, 0.67 wt % Si, 0.33 wt % Fe)

It is evident from the fine recrystallised structure at the edges of both figures above, that the high degree of deformation close to the surface of the extrudate provides a large driving force for static recrystallisation. The effects of prior deformation on the recrystallisation rate were examined in a previous study [5]. It was noted that at small deformations, no recrystallisation could occur even at the highest temperatures. As the amount of deformation increases the recrystallisation rate increases. It is interesting to note the difference in depth of the finely recrystallised areas either side of the extrudate. The side close to the smaller extrudate (figure 5.26) has only a very shallow (highly) recrystallised region, whereas the opposite side has a much deeper region. This is due to the flow characteristics of the two-hole dies. High shear is induced, in forming the DMZ, on either side, but because of the proximity of the holes, only a very small DMZ is formed between the holes. Thus only the material forming the extreme surface of the extrudate on that side will be as highly strained as the material on the other side. The large amount of deformation applied to these areas, and the resulting high dislocation density provide a large driving force for nucleation of recrystallised grains, which alleviate the dislocation sub-structure and create grains with a dislocation density orders of magnitude lower than worked grains (10^6-10^8 dislocations/cm^2).

5.5. Conclusions

It has been shown in this chapter that extruding an alloy through a series of asymmetric two-hole dies can provide an idea of the tendencies for flow of the material. The dies can be analysed using an eccentricity theory, which quantifies, in a unitless variable, the distance of a hole from the centre of the die. The ratio of the lengths extruded through each hole can be used as an indication of the extrudability of the material. The present work goes some way to explaining the variations presented by different hole sizes and process parameters. A standard test can be formulated to assess the comparative extrudability of any aluminium alloy. For the purposes of this study, the standard test has the following characteristics:

Test Billet Diameter: 75 mm

Die: Die 3

Temperature: 450 °C

Tooling Temperature: 425 °C

Ram Velocity: 12 mm/s

The resulting length ratio of the produced extrudates constitutes the extrudability factor.

From observations of the grain structure of the extrudates, it has also been shown that static recrystallisation cannot take place unless a certain amount of deformation has been performed, indicating that prior deformation is important in the nucleation of recrystallised grains.

Chapter 6

Effect of alloying elements on two-hole extrusion

Nomenclature – Chapter 6

A	Constant
B	Constant
C_j	Amount of element j in solid solution in wt %
D_0	Diffusion coefficient of element j
D_j	Diffusivity of element j in the aluminium matrix
G	Universal gas constant
P	Extrusion pressure
p	Lattice parameter
R	Extrusion ratio
T	Absolute temperature
ΔH	Activation energy
$\bar{\sigma}$	Flow stress
σ^*	Thermal (short range) component of flow stress
σ_E	Athermal (long range) component of flow stress
σ_y	Yield stress of the alloy

6. Effect of alloying elements on two-hole extrusion

Introduction:

In the previous chapter, the analysis performed pertained to a single alloy - AA6063.

However, it is beneficial to perform the same analysis on a variety of other alloys, commercial and not, to ascertain how the individual alloying elements - primarily magnesium, silicon and iron - affect the extrudability, and the other extrusion variables, of the 6xxx series of alloys.

But what is extrudability? Most published extrudability studies define extrudability as the maximum exit velocity, which can be attained before surface tearing occurs [8, 10, 18, 36]. As outlined in chapter 5, extrudability should be defined as a scalar quantity, unique for a single alloy, which describes its ability to undergo extrusion at high speeds without adverse effects on its surface finish or mechanical properties. As mentioned in section 5.5, because of the different method of extrusion utilised in the present study and the limitations of the press, a measure of extrudability will be defined as the length ratio of the extrudates acquired through die 3.

All the alloys manufactured by the gravity die process were extruded through the dies mentioned in the previous chapter. Three billets of each alloy (54 alloys in total) were available for extrusion.

6.1 Effect of Mg_2Si

It was mentioned in chapter 2, that Mg_2Si - the main hardening phase in 6xxx series alloys - has been reported to decrease the extrudability of the alloy [18, 132]. The workers, though, failed to specify their definition of extrudability, simply allowing the maximum possible extrusion speed to guide them to this inference. Results from the present study seem to contradict this observation, stating that Mg_2Si, on its own, has practically no detrimental effect, and can even be seen to slightly increase the extrudability of the alloy. This can be seen in figure 6.1.

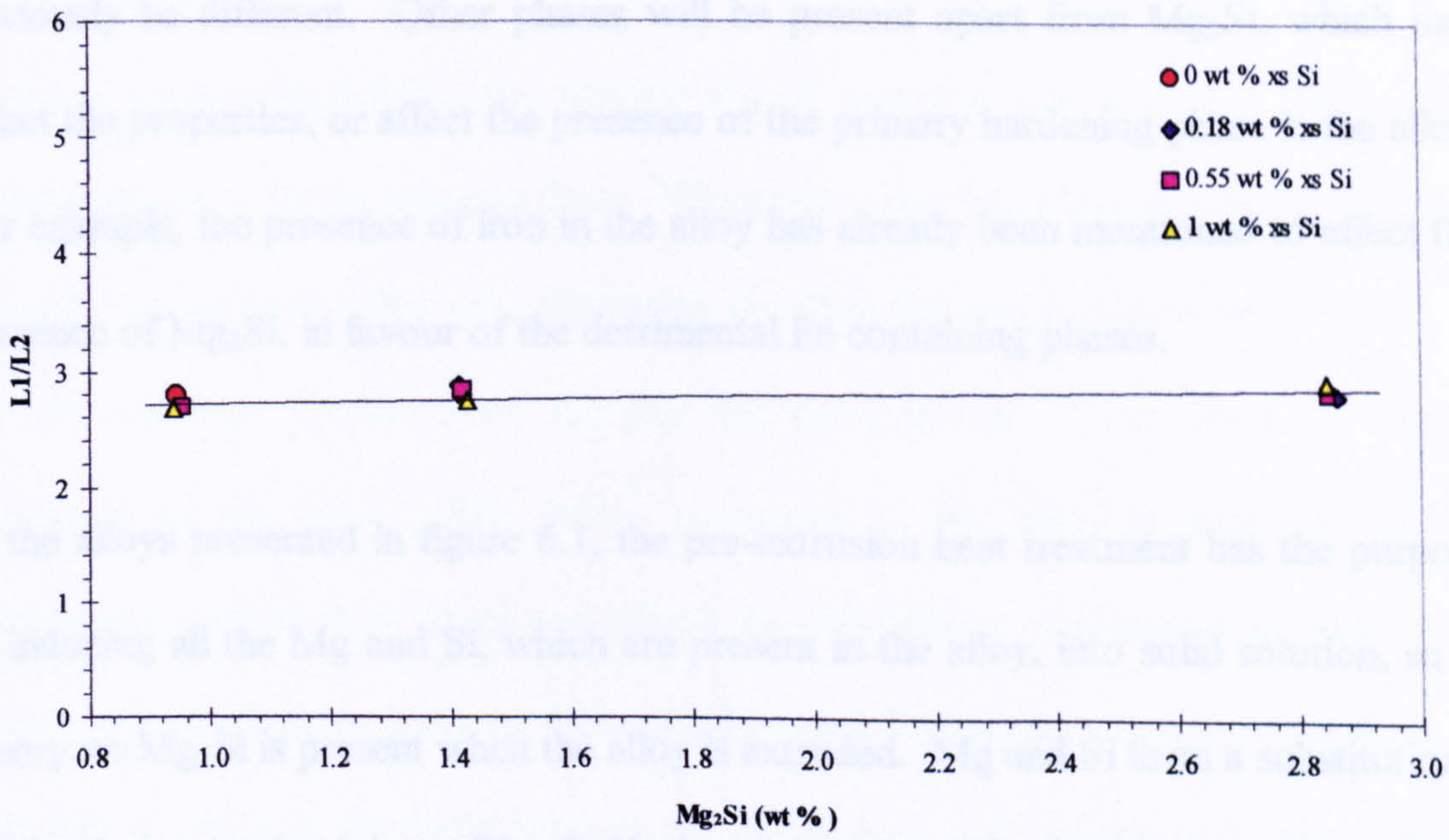

Figure 6.1. Extrudability Vs Mg_2Si content for alloys containing no Fe

All the compositions which appear in figure 6.1 are super-pure Al (99.999 % pure) based and contain no Fe. The situation changes drastically once Fe is added to the equation, but that will be addressed later in this chapter. The reason for the

discrepancy between these results and those mentioned elsewhere could be simply the definition of extrudability and how the maximum extrusion velocity is limited.

If the extrusion ram velocity is limited by the surface finish quality of the product then the two results are not mutually exclusive; in the extrusions performed for the present study the ram velocity was a constant 12 mm/s, and the surface quality of all the extrudates was within acceptable parameters of die line density and pick-up. No surface tearing was observed. Another possible reason for the discrepancy could be the content of the alloys. If commercial alloys were used for the tests, or custom alloys, based on commercially pure (CP) Al (99.5 % pure), then the result will obviously be different. Other phases will be present apart from Mg_2Si, which may affect the properties, or affect the presence of the primary hardening phase in the alloy. For example, the presence of iron in the alloy has already been mentioned to affect the presence of Mg_2Si, in favour of the detrimental Fe containing phases.

In the alloys presented in figure 6.1, the pre-extrusion heat treatment has the purpose of inducing all the Mg and Si, which are present in the alloy, into solid solution, so in theory no Mg_2Si is present when the alloy is extruded. Mg and Si form a substitutional solid solution in aluminium. The Goldschmidt atomic radii of Al, Mg and Si are 1.43, 1.60 and 1.17 Å respectively [133-135]. It is obvious that a solid solution containing the three elements will contain areas of local compression around the Si atoms and local tension around the Mg atoms. However, overall, these areas balance out and a slight increase in the alloying content of both these elements will result in little or no increase in the solution strength.

At the temperatures involved in the extrusion process, diffusion of solute atoms in the matrix is relatively fast, as determined by Fick's first law (equation 6.1).

$$D_j = D_0 \exp\left(\frac{\Delta H}{GT}\right) \qquad (6.1)$$

where D_j is the diffusivity of element j in the aluminium matrix at temperature T, ΔH is the activation energy and G is the universal gas constant. D_0 is the diffusion coefficient of element j. The diffusivities of Mg, Si and Fe in the Al matrix at 450 °C can therefore be calculated to be 8.05×10^{-12}, 5.8×10^{-10}, and 1.11×10^{-18} m^2/s respectively [5]. It can be seen therefore that diffusion of these elements is fairly rapid compared to room temperature values.

Areas of local compression and tension are of opposite sign and thus, there exist mutual attractive forces between them. When two come into close proximity they tend to partly cancel each other out, alleviating the drag the atoms would have applied to the dislocations. Furthermore, alloying has been shown [136] to affect the lattice parameter of the alloy. The lattice parameter of the alloy is important in the determination of its flow stress and affects the diffusivities of elements present in the matrix. As the distance between the atoms increases, the activation energy for vacancy diffusion – which is the main process by which both dislocations and solute atoms migrate in the matrix – increases, causing the applied stress, required to move a dislocation through the matrix, to rise. The lattice parameter of alloys in the AlMgSi family can be seen to follow the rule shown below, which was extrapolated from data presented in earlier studies [5, 136, 137].

$$p = 4.049 + 0.050C_{Mg} - 0.0019C_{Si} \qquad (6.2)$$

where p is the lattice parameter measured in Å, C_{Mg} and C_{Si} are the amounts of Mg and Si in solid solution, in weight %. Note that magnesium and silicon have opposite effects on the lattice parameter, so any change that is effected by an increase in the Mg is partly negated by an increase in the Si. This is the reason for the absence of any significant change in the extrudability of the material with increase in Mg_2Si.

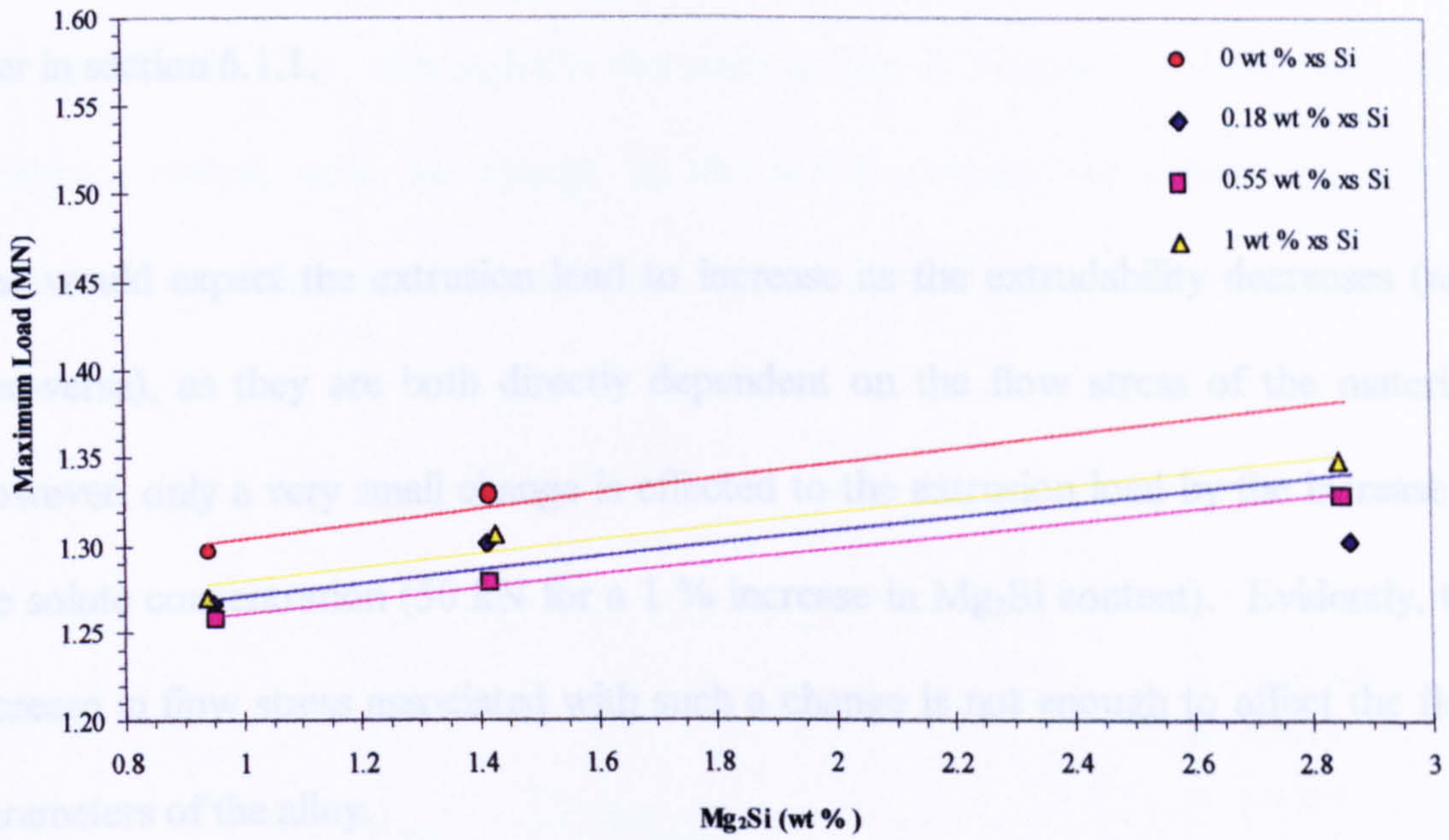

Figure 6.2. Effect of Mg_2Si content on the Maximum Extrusion Load for alloys containing no Fe.

Figure 6.2 shows the variation in extrusion load with increasing Mg_2Si content for alloys containing no iron. It can be suggested that there is a shallow increase in the load induced by the addition of more magnesium and silicon to the alloy. The loads were calculated using the values of the experimentally measured loads, which were normalised based on the overall strain (ln R) produced through each die. The normalisation is justified by using the modified general pressure equation [63], viz.

$$\frac{P}{\sigma_y} = A + B \ln R \qquad (6.3)$$

The reason for the increase is the solution strengthening effects of the Mg and Si in the lattice. With a misfit of -12 and +18 %, the strain fields around the solute atoms are large enough to impede dislocation motion more and more as the density of the solute atoms in the matrix increases. It has also been reported [81] that alloying reduces the stacking fault energy of alloys causing the sub-boundaries to become more diffuse and thus more susceptible to the effects of particle pinning. This effect is expanded on later in section 6.1.1.

One would expect the extrusion load to increase as the extrudability decreases (and vice-versa), as they are both directly dependent on the flow stress of the material. However, only a very small change is effected to the extrusion load by the increase in the solute concentration (50 kN for a 1 % increase in Mg_2Si content). Evidently, the increase in flow stress associated with such a change is not enough to affect the flow parameters of the alloy.

A different approach to explaining the increase in extrusion load, can be made through Taylor's Relation [138], who, after deriving a theoretical model linking the flow stress of a metal to the dislocation density, introduced the concepts of long and short range components to the flow stress, as follows:

$$\bar{\sigma} = \sigma^{*} + \sigma_{E} \qquad (6.4)$$

Where σ^{*} is the thermal, or short-range, component of the flow stress which is effected by the thermal vibrations of the lattice and σ_E is the long-range, or athermal, component, which is affected by work hardening effects such as dislocation density. The latter involves the movement of dislocations through stress fields that are

enormous on an atomic scale, hence it is little affected by lattice vibrations due to temperature changes. In the present situation, obviously due to the hot working involved, the dislocation density increases, decreasing the average distance between dislocations and increasing the long-range flow stress component. On the other hand, the heat generated through friction and deformation causes the short-range component to drop. So two competing mechanisms are taking place to determine the flow stress of the material. Thus, although the thermally activated component of the flow stress remains constant with the change in the solute content the other, long range, component increases as the interaction of the dislocations with the solute atoms increases.

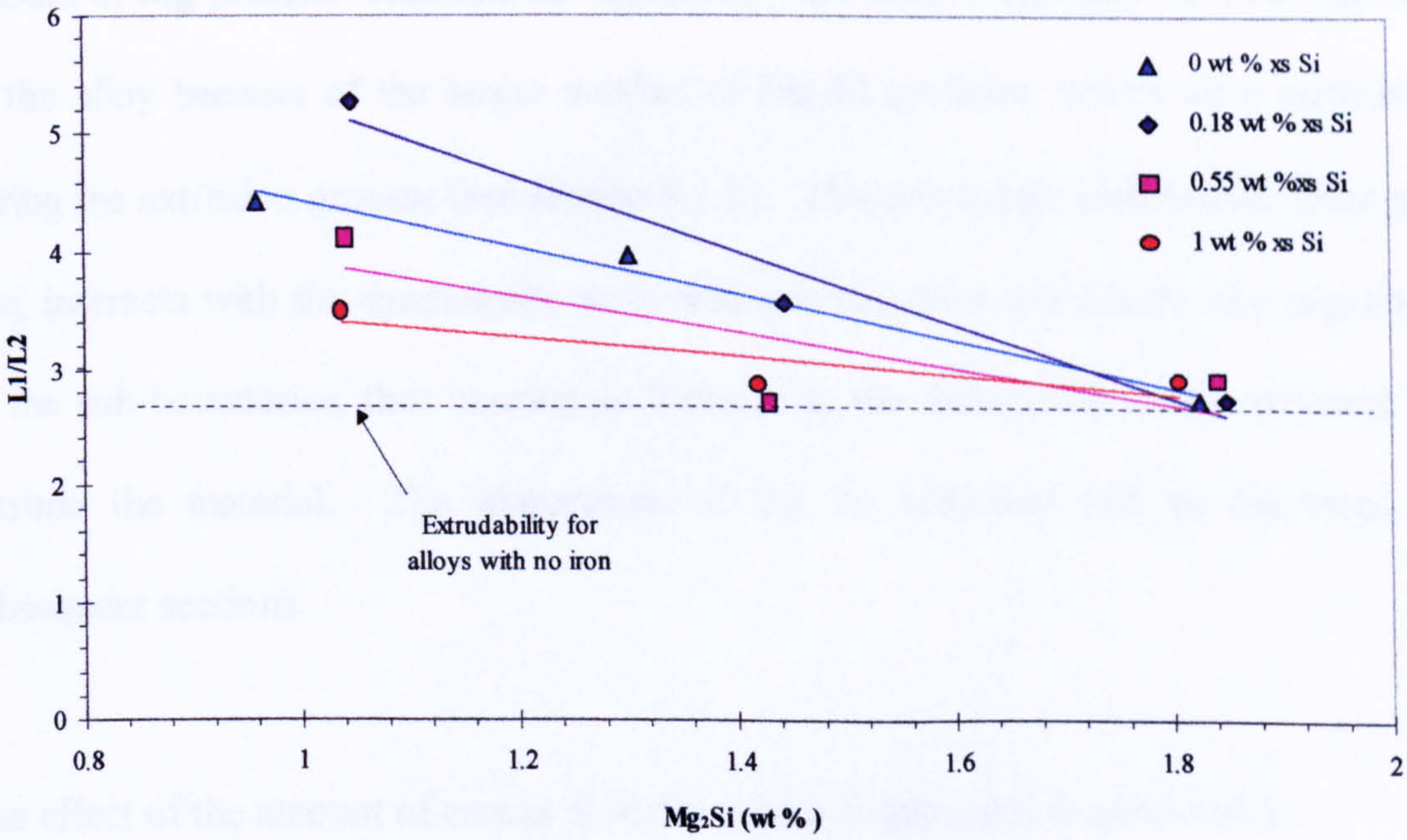

Figure 6.3. Effect of Mg_2Si on the extrudability of alloys containing 0.3 wt % Fe

The situation changes drastically once as little as 0.3 % Fe is added to the equation. It is proposed, by observing the trends shown in figure 6.3, that when only small amounts

of Mg_2Si are present, small additions of Fe can increase the extrudability of the alloy. As more and more Mg_2Si is added, the extrudability gradually decreases, as has been reported elsewhere [18, 132].

The reason for this lies in the affinity of Fe for the available Si. As iron is added to the alloy, it tends to tie up the Si, which would otherwise be in solid solution, forming the AlFeSi phases, mentioned in previous sections. This relieves the matrix of solute Si atoms and adds large Fe phase particles, which nucleate heterogeneously in the solute rich melt around the solidifying aluminium rich dendrites, as described in section 2.2. It should be stressed that the % Mg_2Si presented in the figures above takes no account of the Si tied up in the α-AlFeSi phase. It is the phenomenological % based on the amount of Mg present. Addition of Mg and Si were seen to decrease the extrudability of the alloy because of the larger number of Mg_2Si particles, which were nucleated during the extrusion process (see section 6.1.1). This precipitate distribution, although fine, interacts with the dynamically recovered sub-structure and inhibits the migration of the sub-boundaries, thus causing an increase in the deformation force required to extrude the material. The importance of the Fe additions will be discussed in subsequent sections.

The effect of the amount of excess Si in the matrix is discussed in section 6.2.

6.1.1. Dynamic Precipitation

The pressures involved in extrusion can cause the precipitation of the hardening phase during the manufacturing process. This is especially evident in alloys devoid of iron,

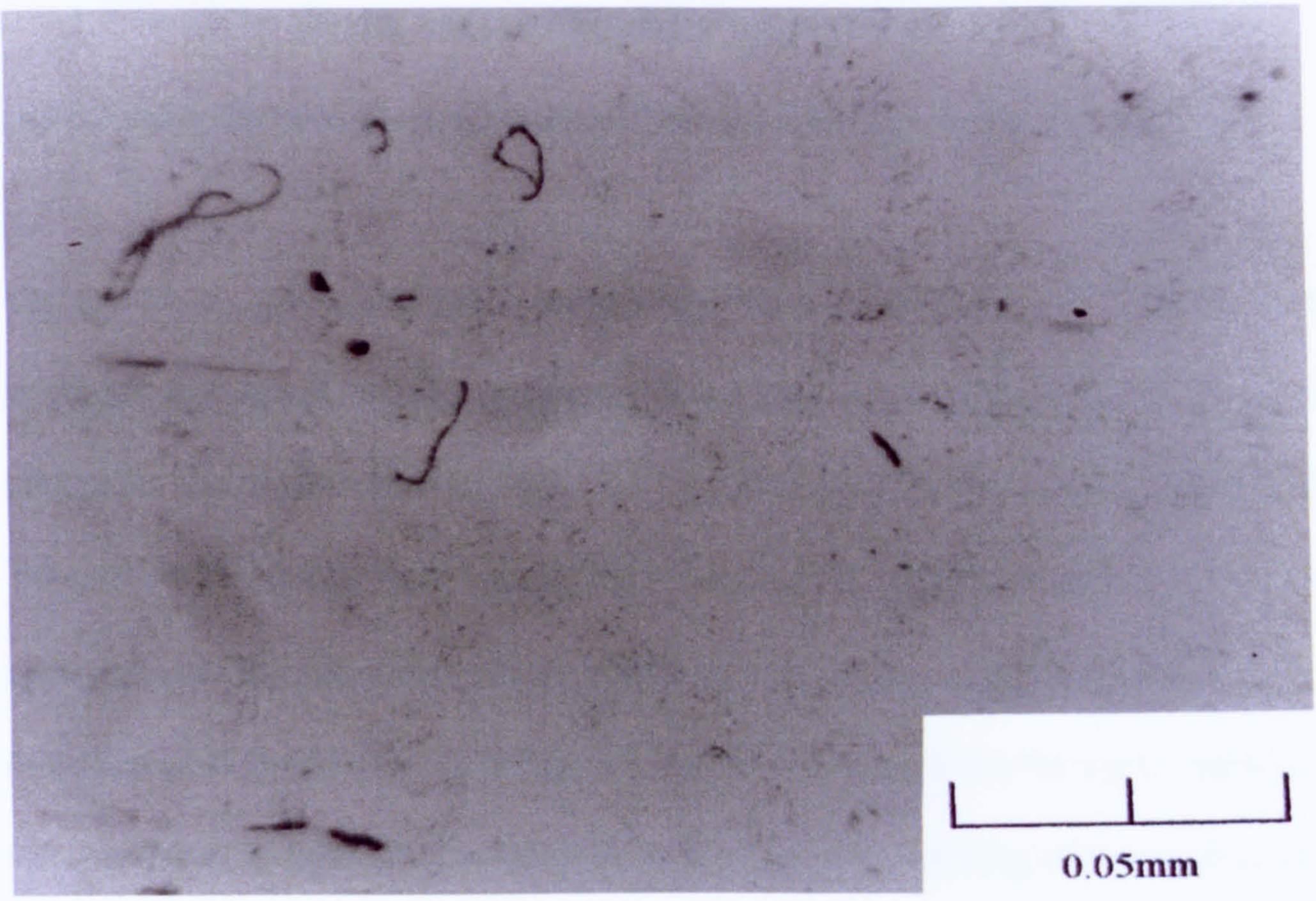

Figure 6.4. Homogenised structure of alloy 662 (0.6 wt % Mg, 0.63 wt % Si). Note the absence of any precipitates

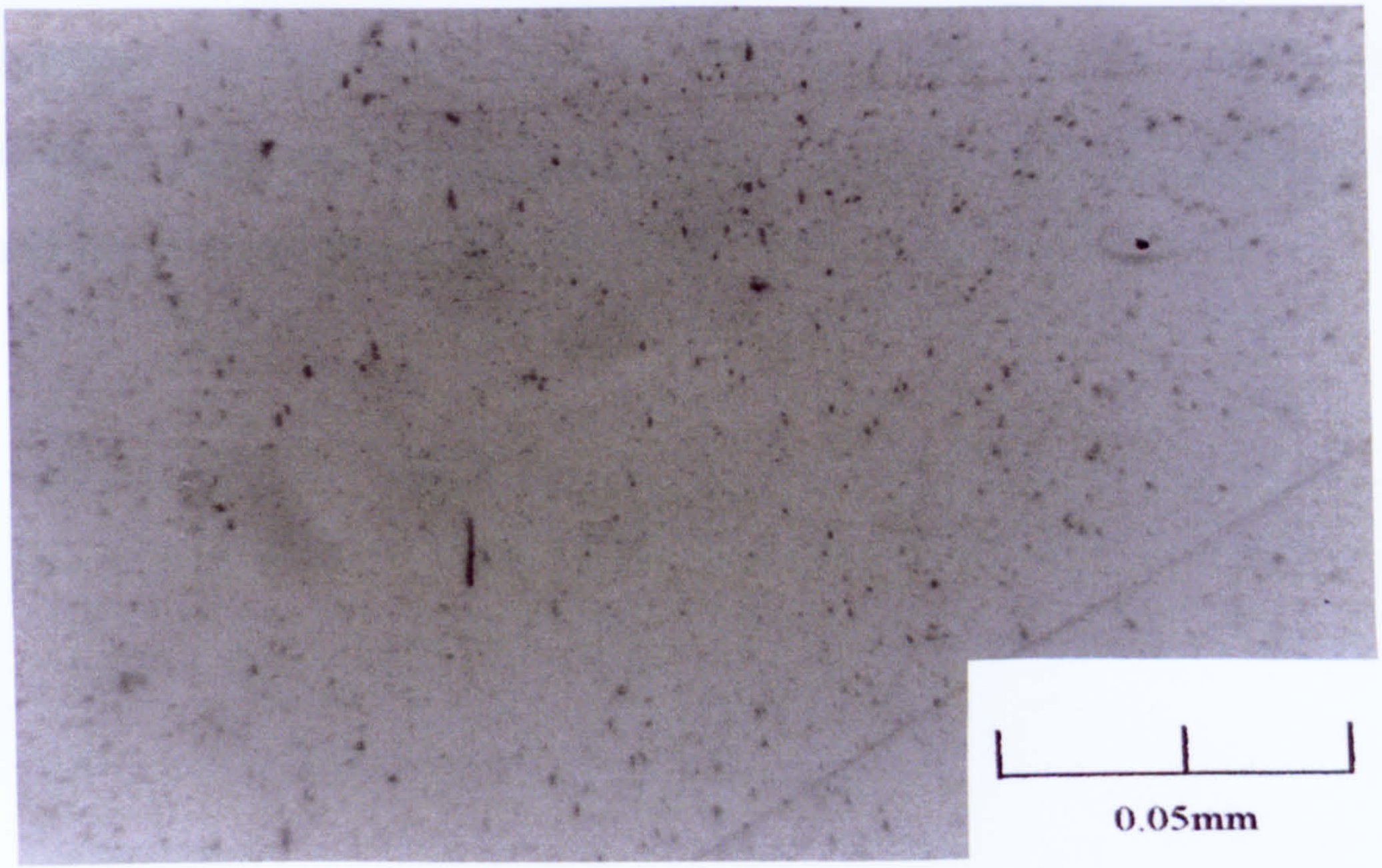

Figure 6.5. Post-extrusion structure of alloy 662 (0.6 wt % Mg, 0.63 wt % Si) (Longitudinal section). Note the fine precipitates of Mg_2Si in the structure.

which have all the alloying additions in solid solution prior to extrusion. Figures 6.4 and 6.5 show the precipitate structures of such an alloy before and after extrusion.

The extrudates were quenched to room temperature 40 mm beyond the die exit, using water jets and, hence, no post-extrusion transformations would be expected. Thus, the precipitate distribution seen in figure 6.5 can be attributed to dynamic precipitation. To compound this argument and eliminate the counter argument that the precipitates appeared after the extrusion - during natural ageing - figure 6.6 shows the load trace of extrusion of alloy 662 (0.6 wt % Mg, 0.63 wt % Si). Comparing the traces below with the one shown in figure 5.1, it can be seen that for iron containing alloys, such as alloy 422 (0.63 wt % Mg, 0.62 wt % Si, 0.1 wt % Fe), a drop in extrusion force occurs immediately after peak conditions are reached. In this case, a shallow increase in load continues even after the peak has been reached (at around 1 second). The increase continues until around halfway through the stroke, when all the Mg_2Si has precipitated and then the load begins to fall as the friction with the container is reduced.

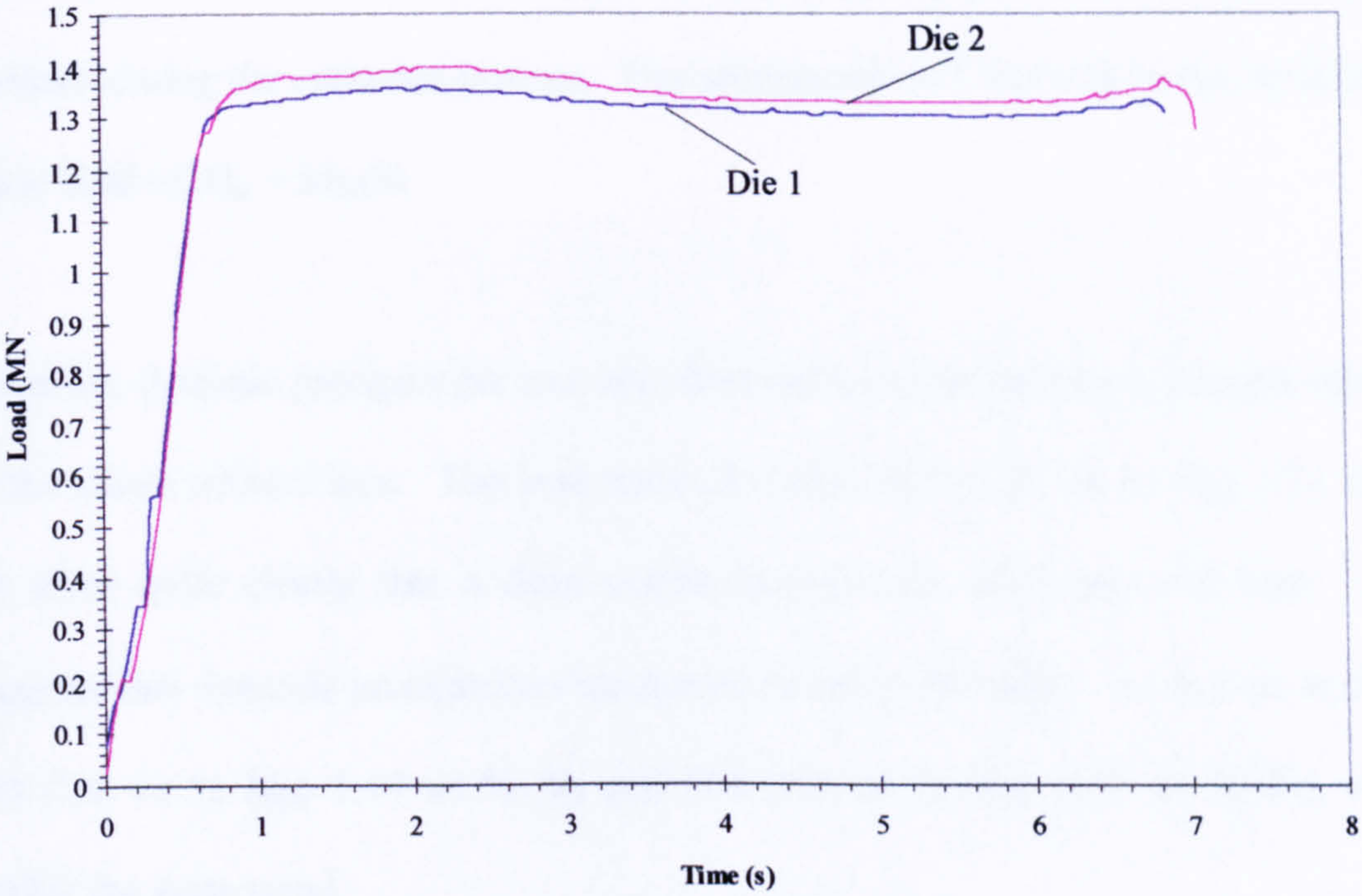

Figure 6.6. Load-time traces for the extrusion of alloy 662 through dies 1 and 2.

The increase in the alloy strength is caused by the particles inhibiting the movement of the dislocation substructure, which is created during dynamic recovery. Particles, as small as the ones seen in figure 6.5, effectively pin the sub-boundaries, causing an increase in the applied stress required to free the dislocations.

It is noteworthy that the load required to extrude increases after the peak, although the force required to overcome the frictional drag of the container is decreasing. Dynamic precipitation is induced in alloys with all their magnesium and silicon in a super-saturated solid solution - i.e. amounts beyond those specified in the equilibrium phase diagram (figure 2.4(b)) [5]. The application of pressure and the initiation of deformation, increase the vacancy concentration and allow faster diffusion of the solute atoms. Hence, at the extrusion temperature - 450 °C - where the solubility limit of Mg_2Si is 0.75 wt % (well below the 0.95 wt % present in alloys 661-4 and the 1.42

wt % in alloys 671-4), the excess Mg_2Si is rapidly precipitated as a fine dispersion of particles during the extrusion process. The aforementioned alloys lie in the equilibrium phase field of Al_{ss} + Mg_2Si.

However, dynamic precipitation was not observed to occur in the most highly alloyed of the alloys without iron. The load traces for alloy 702 (1.81 wt % Mg, 1.21 wt % Si) show quite clearly that a drop occurs immediately after the peak load. This suggests that dynamic precipitation has not occurred in this alloy - as well as in alloys 703 (1.8 wt % Mg, 1.49 wt % Si) and 704 (1.8 wt % Mg, 1.95 wt % Si), which exhibit the same trend.

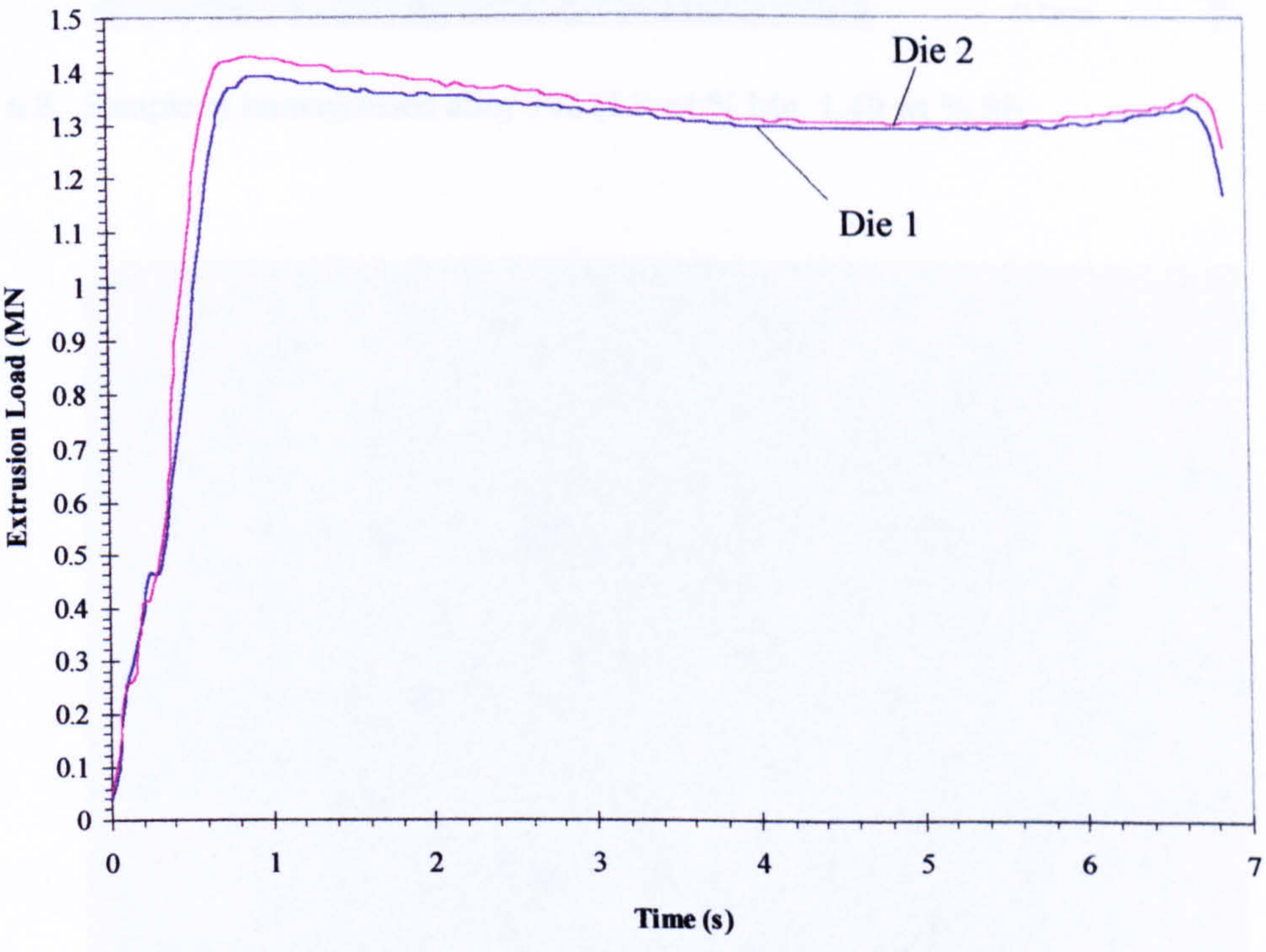

Figure 6.7. Load traces for extrusion of alloy 702 through dies 1 and 2.

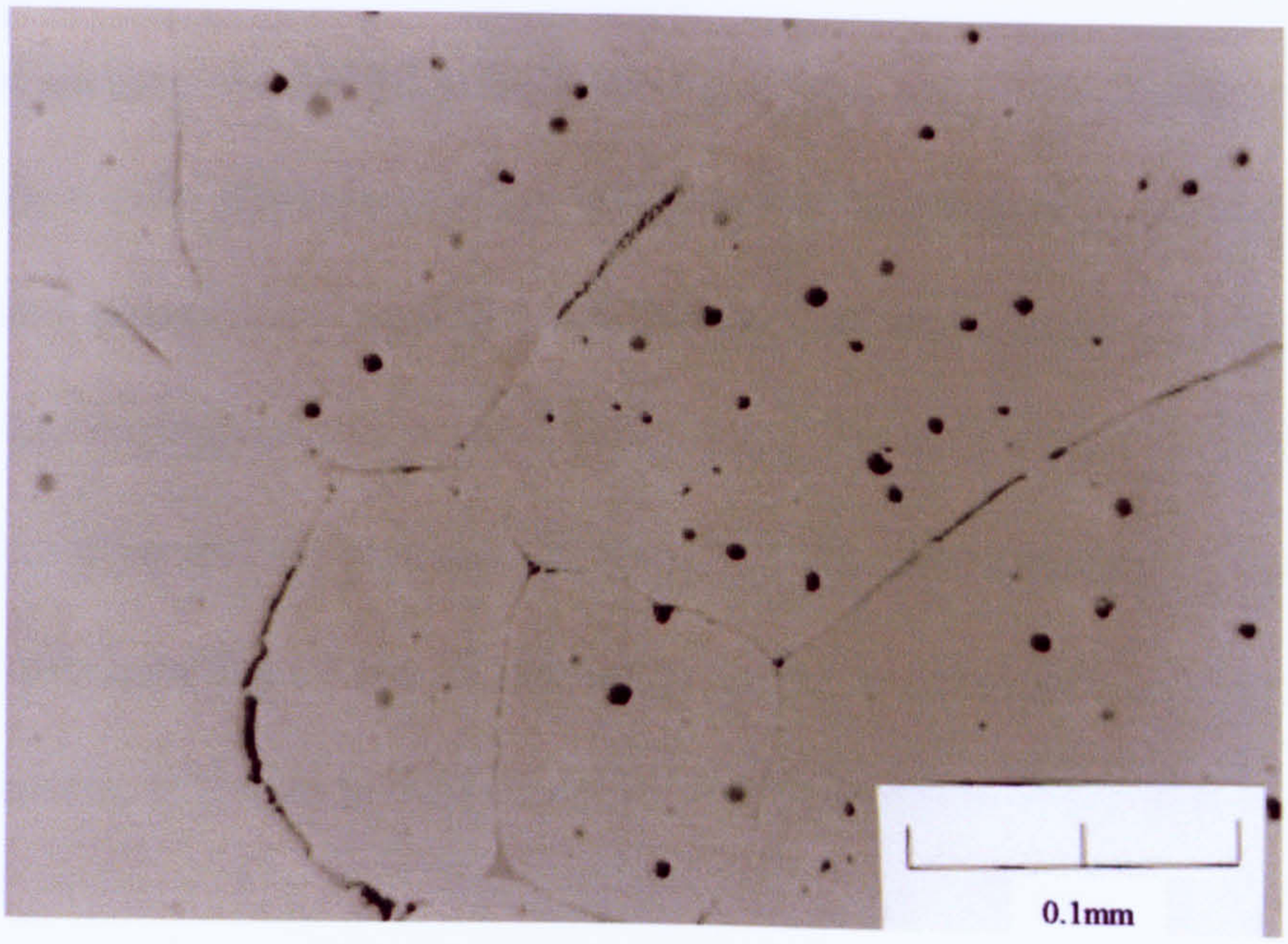

Figure 6.8. Sample of homogenised alloy 702 (1.8 wt % Mg, 1.49 wt % Si)

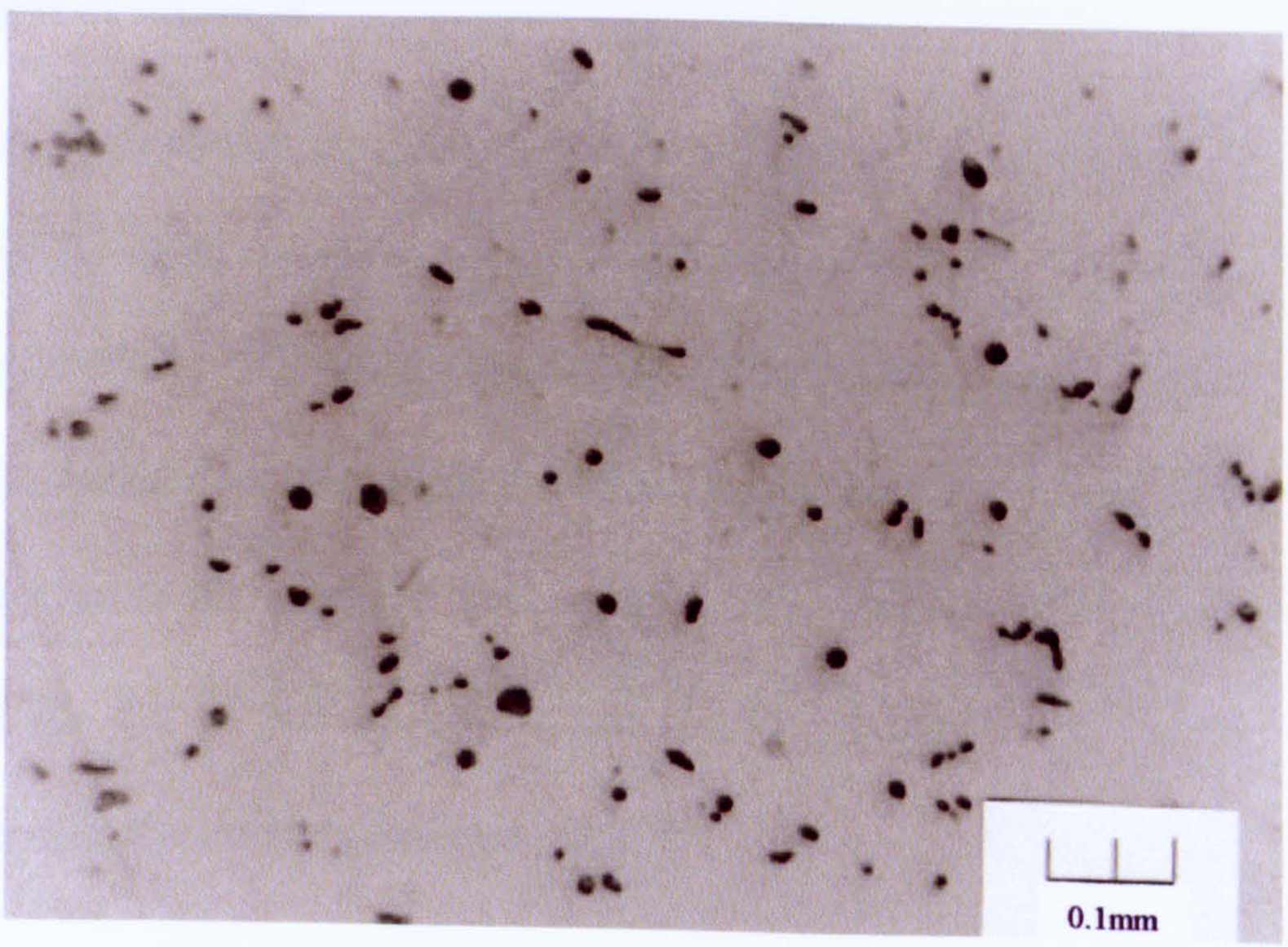

Figure 6.9. Post extrusion structure of alloy 702

Microstructural evidence from alloy 702 indicates that there is no dynamic precipitation but does show a number of large particles, both in the homogenised and the extruded section. Alloys 702-4 lie in the Al_{ss} + Si + Mg_2Si equilibrium phase field. Figure 6.8 shows the structure of alloy 702 before it was extruded. Note the amount of undissolved silicon (dark particles), the Mg_2Si particles (lighter coloured) and the silicon that has segregated to the grain boundaries. Because of the amount of silicon out of solid solution and the existing Mg_2Si, the driving force for dynamic precipitation is low and precipitation of Mg_2Si during extrusion is inhibited. A section of the extruded material is shown in figure 6.9 and the absence of dynamic precipitation is confirmed.

6.2 Effect of excess Si

Si is another element that is added to the 6xxx series alloys to improve their strength but has widely been reported to have a detrimental effect on the extrudability characteristics [10, 16, 35-37]. Most commercial AlMgSi alloys have a certain amount of excess Si, i.e. more than that required to form Mg_2Si with the magnesium present. As before the excess Si contents presented in this chapter are calculated without accounting for the Si tied up in the iron phase particles. The reason for this is consistency with previously published work [10].

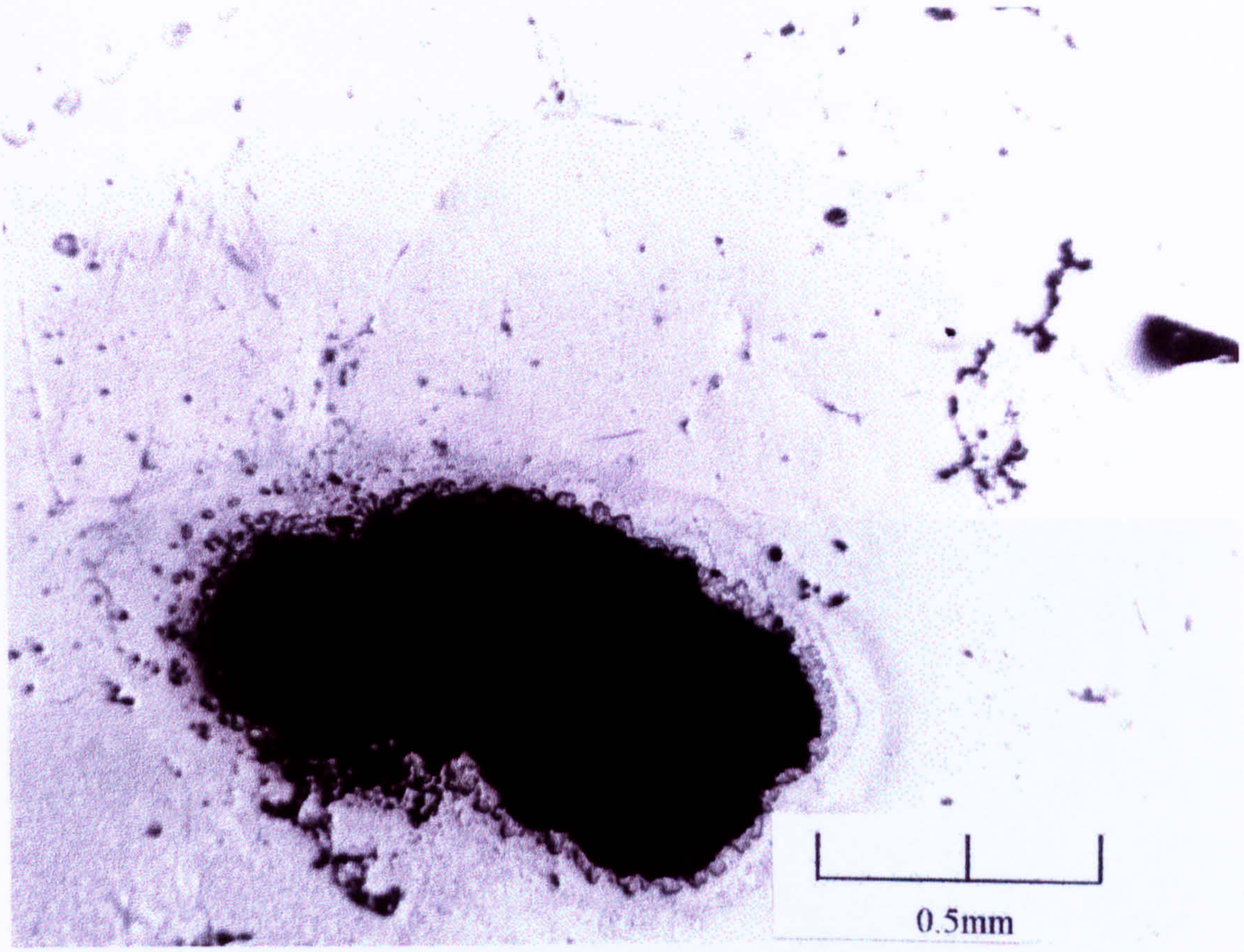

Figure 6.10. Large undissolved Si particle in homogenised alloy 702 (1.21 wt % Si).

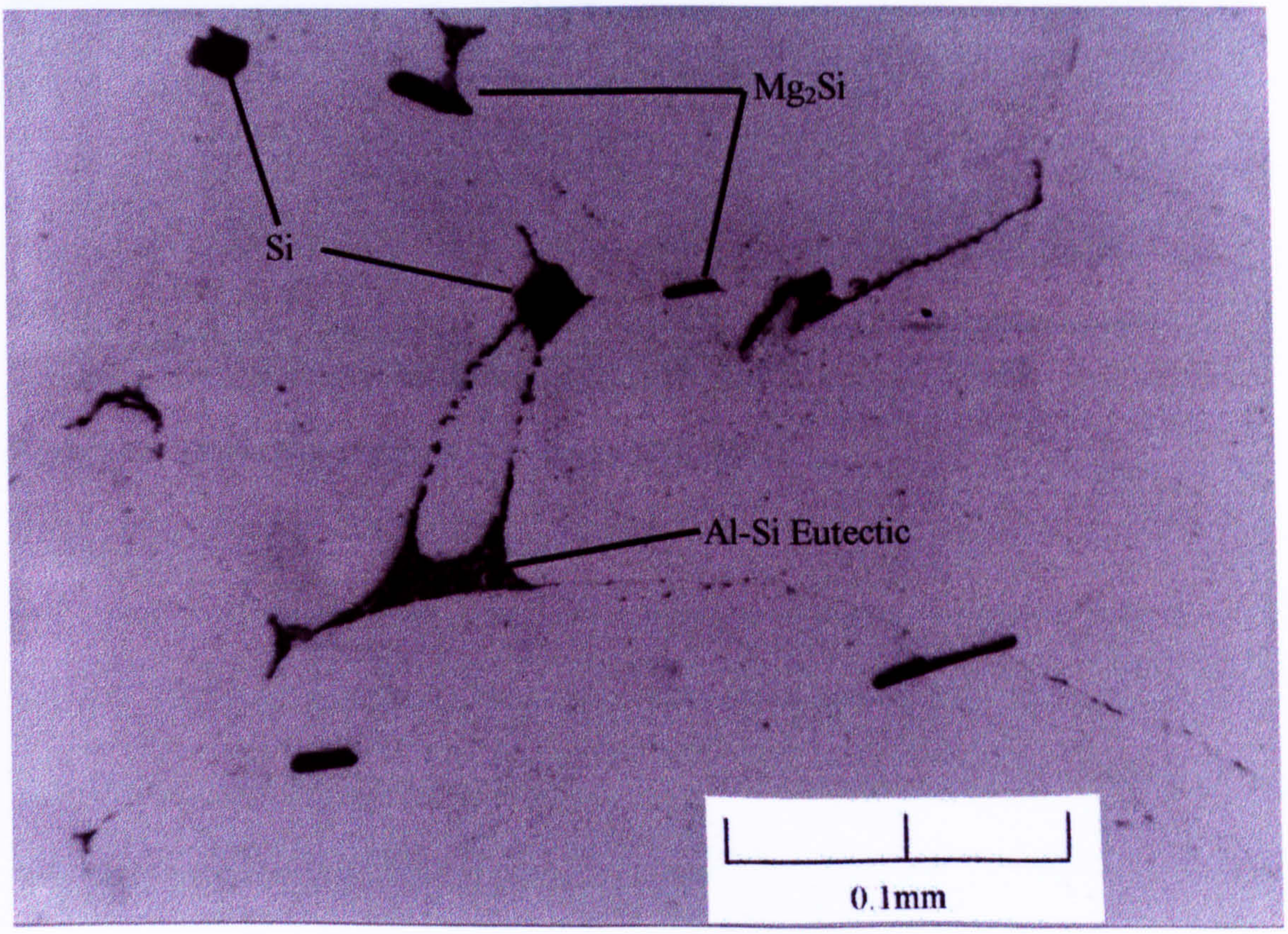

Figure 6.11. Undissolved Si particles in homogenised alloy 424 (1.53 wt % Si).

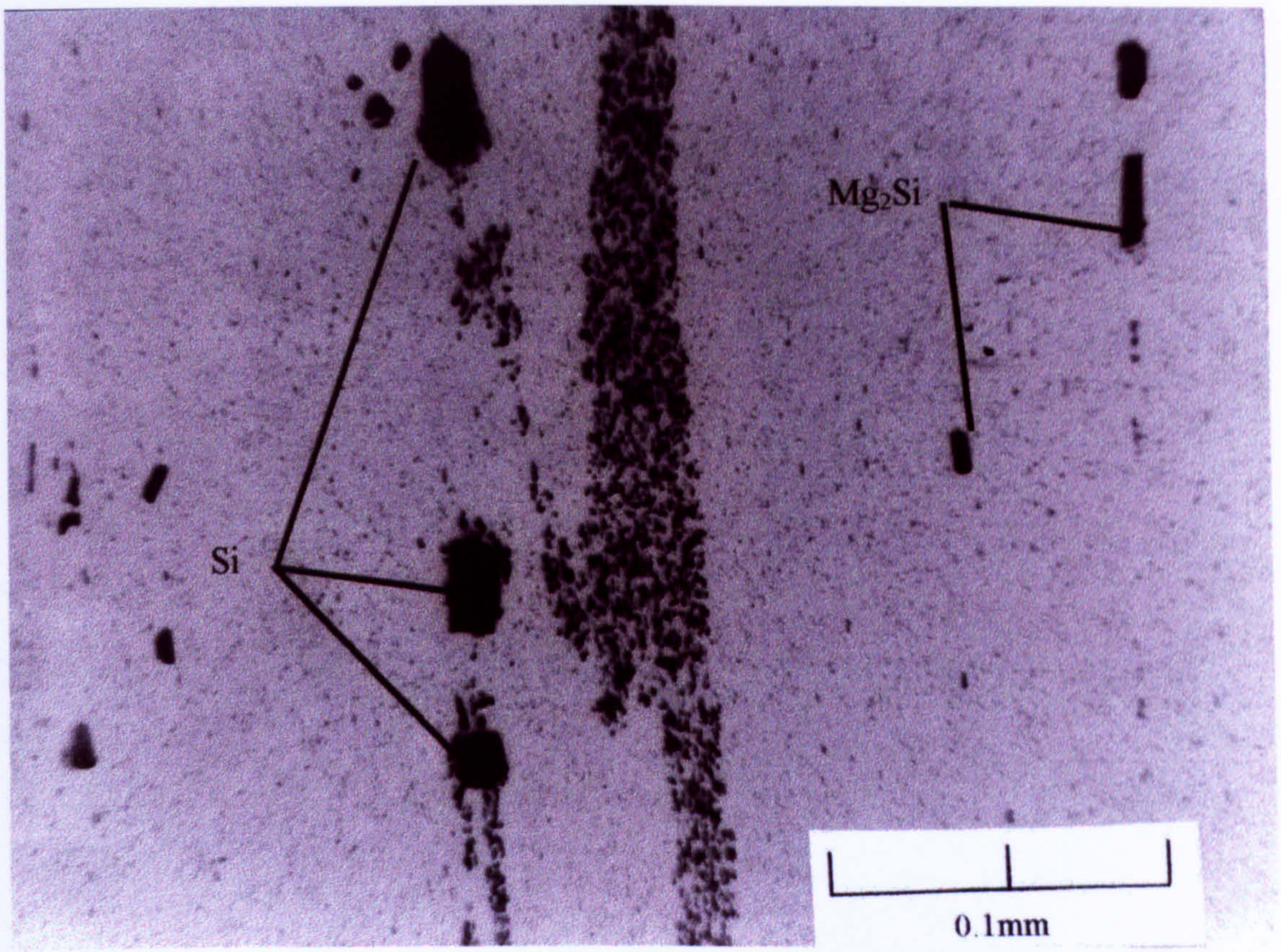

Figure 6.12. Trail left by Si particle in extrusion 424B (die 1).

It should be noted that some silicon, which was added to the melt as pure granules, had not fully dissolved in certain alloys, which had high contents of the addition. The high homogenising temperatures were not enough to fully disperse the undissolved granules, although some small reduction in size was noted. An extreme example of elemental Si in the matrix can be seen in figure 6.10 and more regular occurrences of it in figure 6.11.

Note the presence of the Al-Si eutectic in figure 6.11. When the alloy was homogenised, the high concentration of elemental silicon at the grain boundaries caused a large driving force towards local equilibrium conditions. This driving force caused the creation of areas of Al-Si eutectic.

When extruded, these Si particles tend to break up and leave a wake of very fine particles behind them. It is then easy to follow the progress of a Si particle through the extrudate. Figure 6.12 shows one such example very clearly, indicating the presence of part of the particle, which caused the phenomenon.

The fragmentation of the silicon precipitates, described above is similar to the process suggested by Clode and Sheppard [11], to explain the formation of micro die lines. The workers observed that large AlFeSi precipitates in the subcutaneous layers of the extrudate tended to fragment into smaller particles, which would be interspersed with a large number of cavities, that are identified on the surface of the extrudate as micro die lines. Based on these observations, the dissolution of all the silicon during casting and

the avoidance of reprecipitation of elemental Si, is essential to ensure that such particles do not affect the surface finish of the alloy.

As was shown in figure 6.1, excess Si has no effect on the extrudability of an alloy if no Fe is present. One would expect a change in the flow stress with increase in Si content. This was reflected in figure 6.2, and can be interpreted from the trends that are shown in figures 6.13 and 6.14, which show the variation of the length ratio of the extrudates with the amount of excess Si in the matrix. Due to limitations in the experimental procedure, it was only possible to extrude one billet of each alloy condition through each die. Thus, the phenomenological trends shown in the figures are discussed by observing a large amount of data and are not specific to a single point.

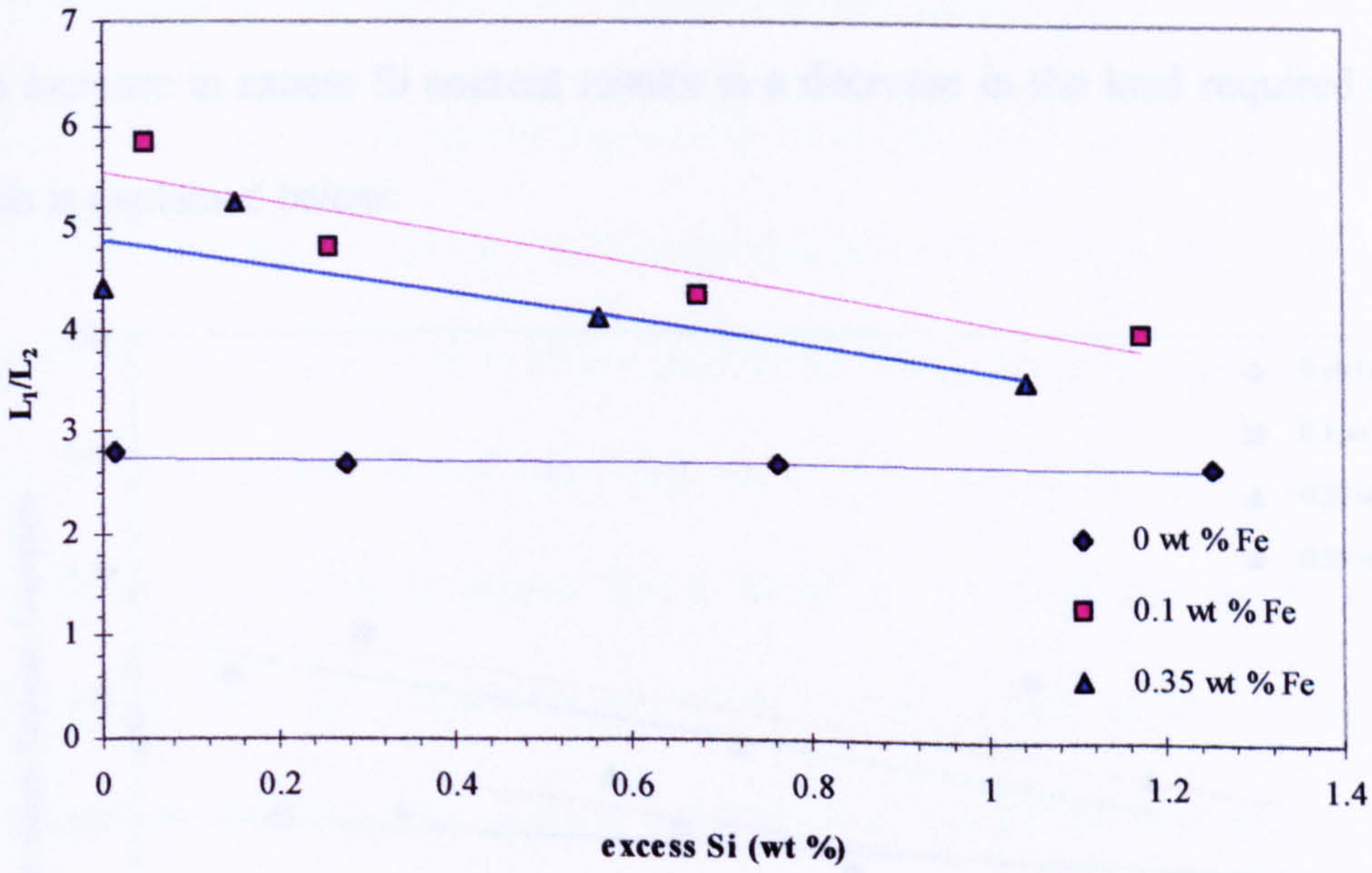

Figure 6.13. Effect of excess Si on the extrudability of alloys containing 1 wt % Mg_2Si.

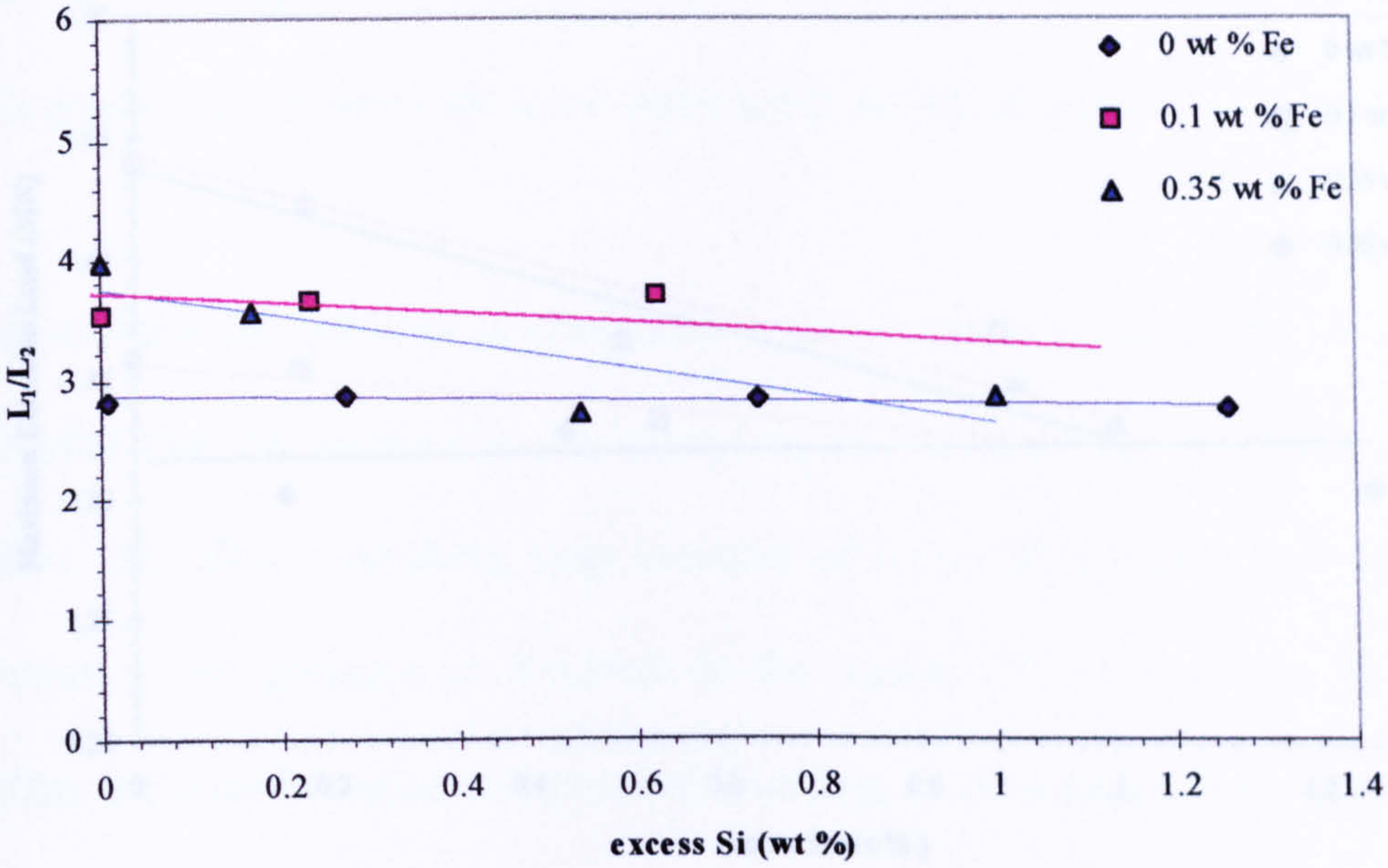

Figure 6.14. Effect of excess Si on the extrudability of alloys containing 1.4 wt % Mg_2Si.

Figures 6.15 and 6.16 reflect the same phenomenological trend in the extrusion loads: An increase in excess Si content results in a decrease in the load required to extrude. This is explained below.

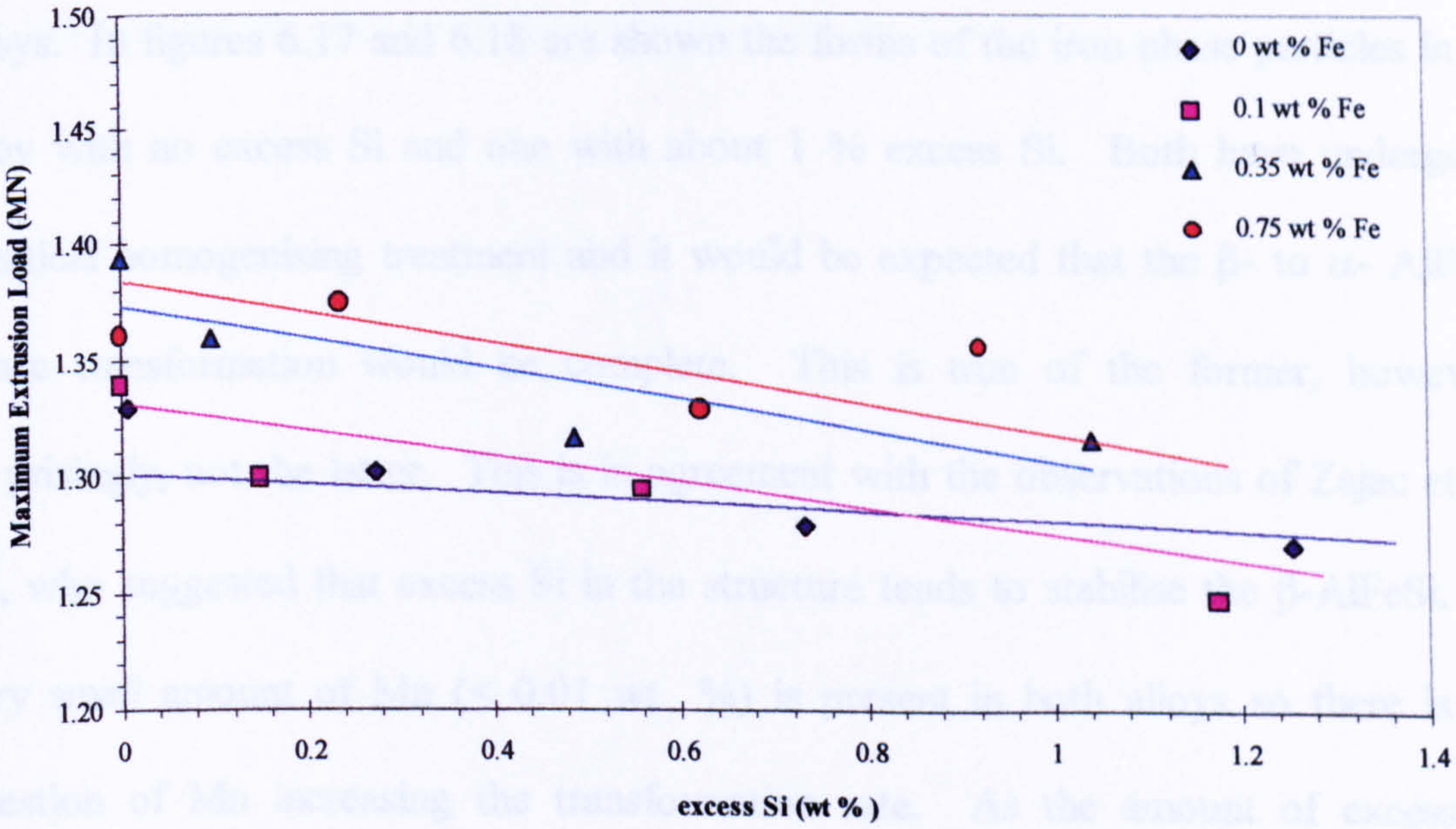

Figure 6.15. Effect of excess Si on the extrusion load required for alloys containing 1 wt % Mg_2Si.

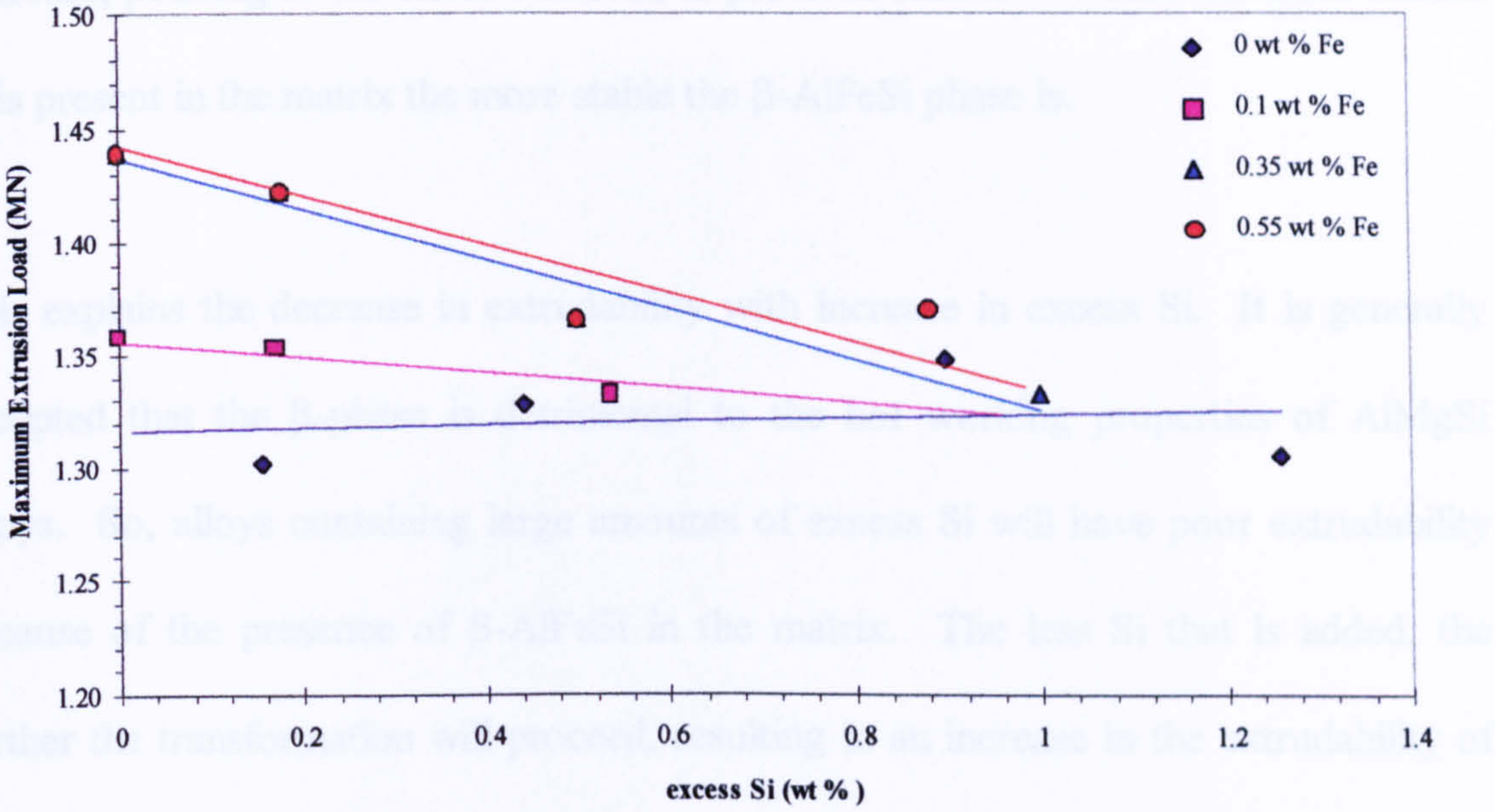

Figure 6.16. Effect of excess Si on the extrusion load required for alloys containing 1.4 wt % Mg_2Si.

6.2.1. Excess Si and the β- to α- AlFeSi phase transformation

It seems from the above figures that excess Si in the matrix decreases the extrudability of the alloys as more is added. This must also be verified by the microstructures of the alloys. In figures 6.17 and 6.18 are shown the forms of the iron phase particles in an alloy with no excess Si and one with about 1 % excess Si. Both have undergone identical homogenising treatment and it would be expected that the β- to α- AlFeSi phase transformation would be complete. This is true of the former, however, surprisingly, not the latter. This is in agreement with the observations of Zajac et al. [39], who suggested that excess Si in the structure tends to stabilise the β-AlFeSi. A very small amount of Mn (< 0.01 wt %) is present in both alloys so there is no question of Mn increasing the transformation rate. As the amount of excess Si increases in the matrix the rate of transformation during homogenising seems to

decrease, pointing to the effect observed in previous studies [39]: That the more excess Si is present in the matrix the more stable the β-AlFeSi phase is.

This explains the decrease in extrudability with increase in excess Si. It is generally accepted that the β-phase is detrimental to the hot working properties of AlMgSi alloys. So, alloys containing large amounts of excess Si will have poor extrudability because of the presence of β-AlFeSi in the matrix. The less Si that is added, the further the transformation will proceed, resulting in an increase in the extrudability of the alloy.

Because of the peritectic nature of the reaction and the time required for the diffusion of Si and Fe in the matrix, the possibility exists that, in low Si containing alloys, before homogenising, the transformation of the α- to β- phase particles does not reach completion (see table 2.3 for the temperatures of the solid state reactions). Thus there is a smaller amount of β- particles to transform in the lower Si containing alloys.

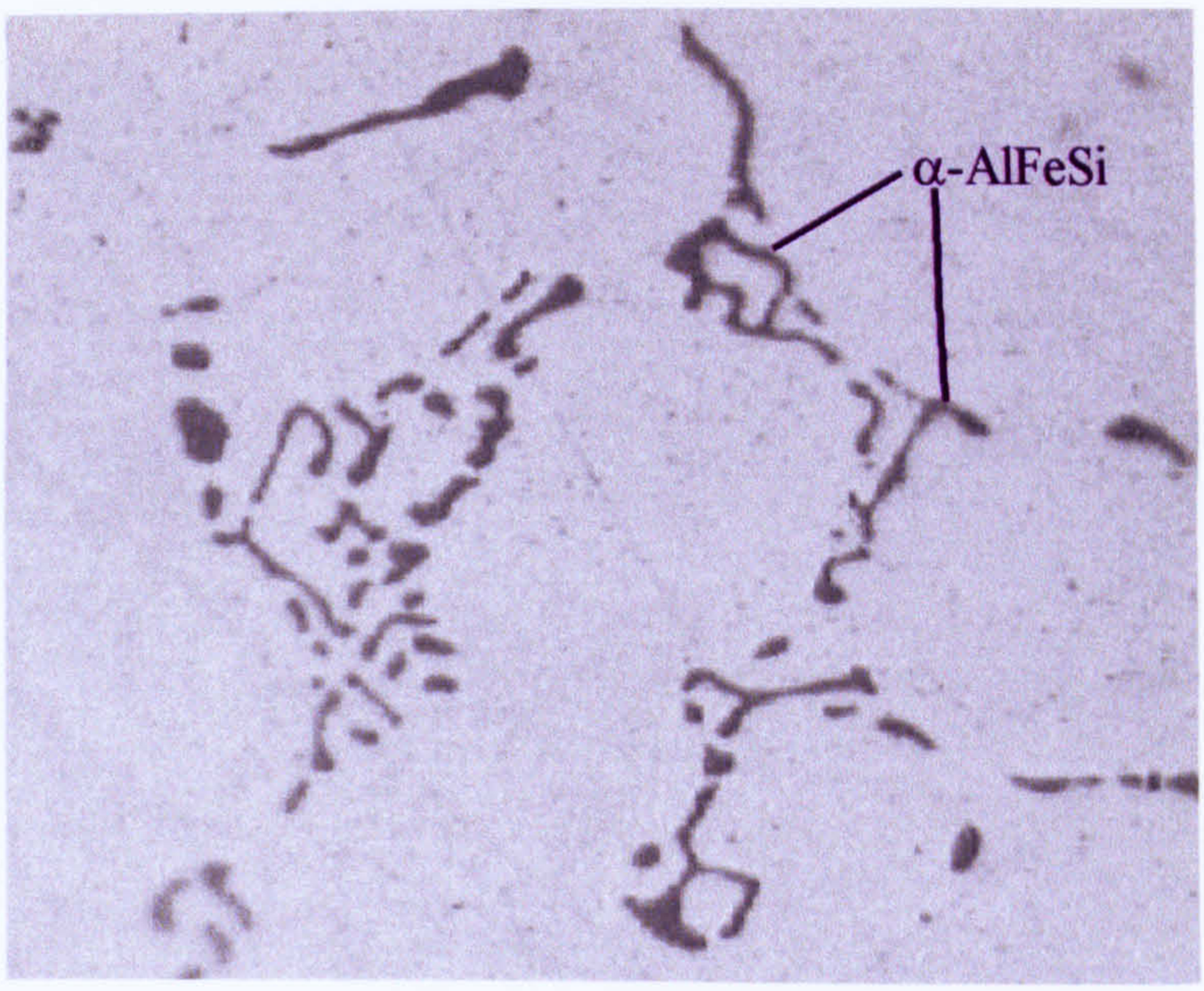

Figure 6.17. Microstructure of homogenised alloy 451 showing the characteristic Chinese script particles (α-AlFeSi). (x 600)

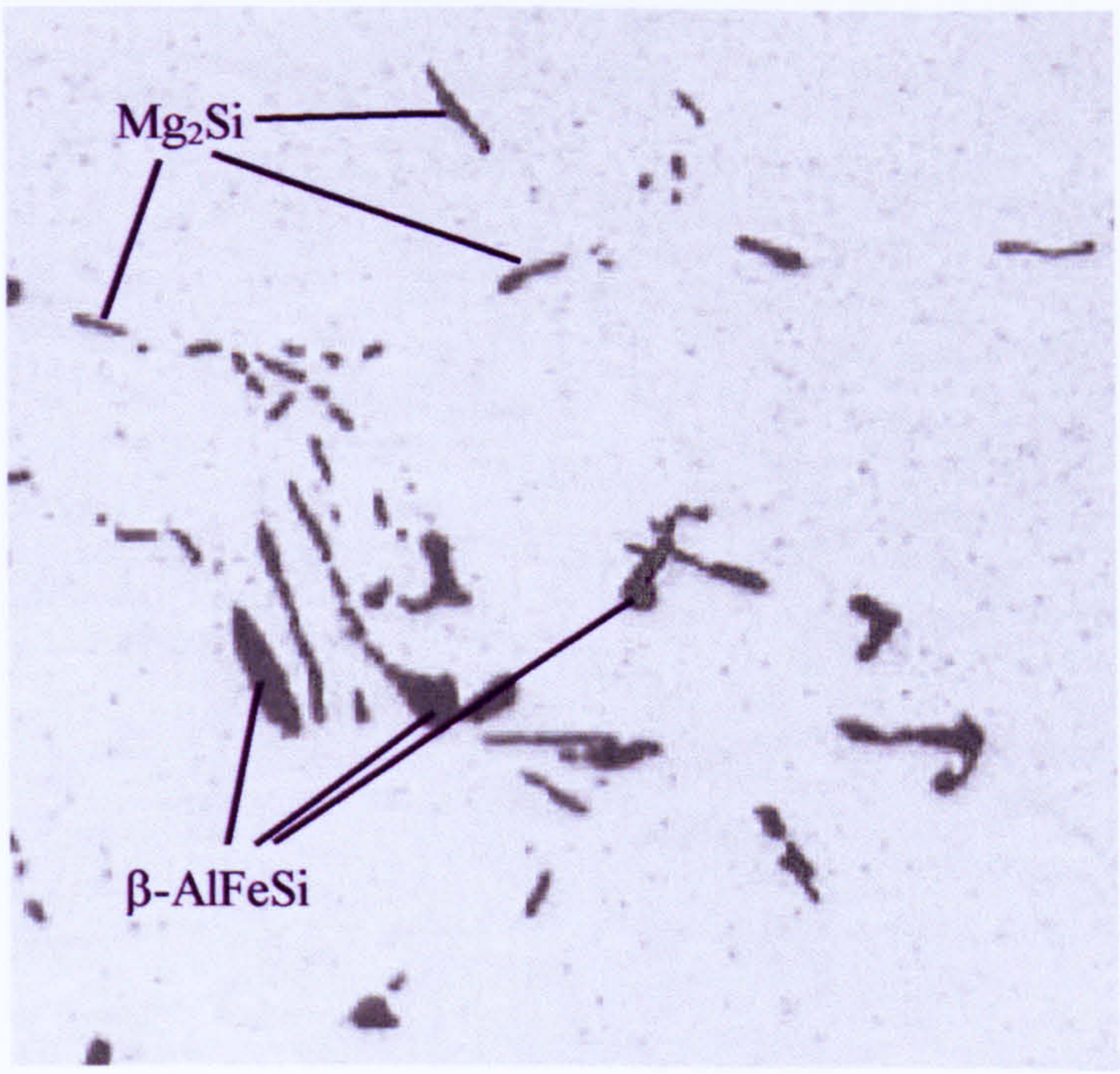

Figure 6.18. Microstructure of homogenised alloy 454 showing the presence of β-AlFeSi particles. (x 600)

6.2.2. Comparison of the extrudability variations which arise from excess Mg and Si

It has been suggested [139] that the extrudability of an alloy, with a Si/Mg ratio exceeding 0.58 and billet temperatures around 400 °C, varies linearly with the function $(2.7Mg + Si)^{-1.5}$. This effect, shown in figure 6.19, reflects the much more deleterious effects of excess Mg on the extrudability of the alloys under these conditions.

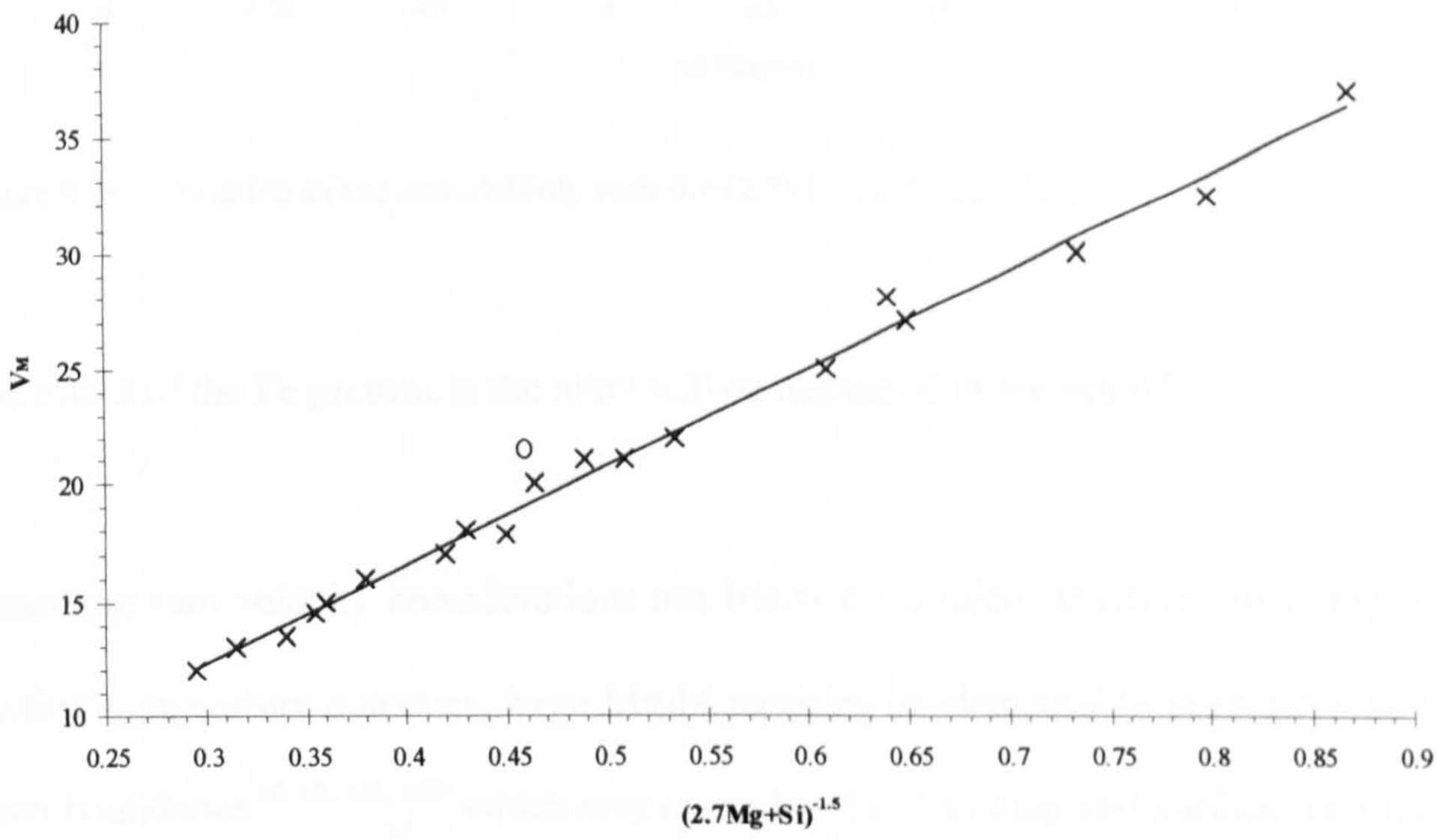

Figure 6.19. Variation of the maximum extrusion speed (extrudability) with the $(2.7Mg+Si)^{-1.5}$ function. (After Baumgarten [139])

From the present study, this theory maybe expanded to the extrudability of excess Si alloys, as shown in figure 6.20. However it is important to note, again, the absence of any variation in the extrudability of the alloys which do not contain any iron.

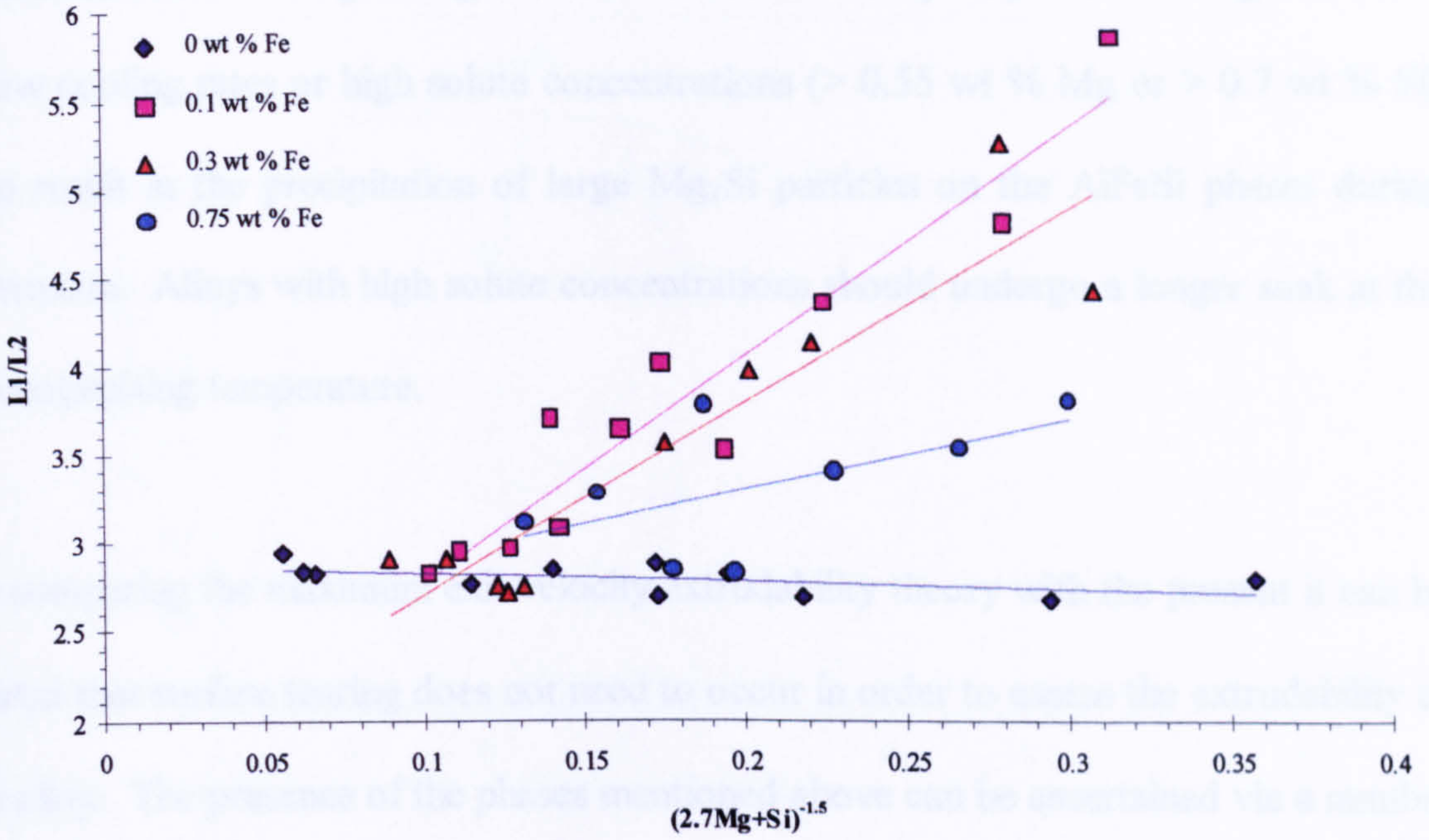

Figure 6.20. Variation of the extrudability with the $(2.7Mg+Si)^{-1.5}$ function.

The effect of the Fe present in the alloy will be discussed in section 6.3.

Maximum ram velocity considerations are based on a microstructure containing low melting temperature eutectics, large Mg_2Si particles or elemental Si segregated to the grain boundaries [8, 10, 140, 141] which may cause localised melting and surface fracture or interfacial cracking leading to a greater likelihood of tearing during extrusion at the stresses associated with large extrusion velocities. Tearing has been reported to occur by two different methods [10, 142]: Type 1 tearing is initiated within the Al matrix and Type 2 is initiated, at lower stresses, at the interface between the matrix and Mg_2Si particles which were not dissolved during the billet pre-heat. Obviously, type 2 tearing should be avoided because it effectively lowers the extrudability of the alloy. There are various ways of avoiding these phases in extrusion billets, which have been extensively discussed elsewhere [8, 10, 16, 36, 83, 142]. In short, a cooling rate of >100 °C/h must be

maintained after homogenising to avoid the chance of reprecipitation during extrusion. Slow cooling rates or high solute concentrations (> 0.55 wt % Mg or > 0.7 wt % Si) can result in the precipitation of large Mg_2Si particles on the AlFeSi phases during extrusion. Alloys with high solute concentrations should undergo a longer soak at the homogenising temperature.

In comparing the maximum exit velocity extrudability theory with the present it can be stated that surface tearing does not need to occur in order to assess the extrudability of an alloy. The presence of the phases mentioned above can be ascertained via a number of metallographic techniques and their importance to the extrudability may be extrapolated from existing data. It is important to note that even at the lower stresses associated with lower speed extrusion, there is still a variation in the extrudability which is not dependent on eutectic melting or interfacial tearing.

6.2.3. Excess Si and dynamic precipitation

It was stated earlier, that alloys with little or no Fe tend to exhibit dynamic precipitation, i.e. the precipitation of the primary hardening phase (Mg_2Si) during the extrusion process. It can further be observed, that as the amount of excess silicon increases in the alloy, the effects of dynamic precipitation become less pronounced.

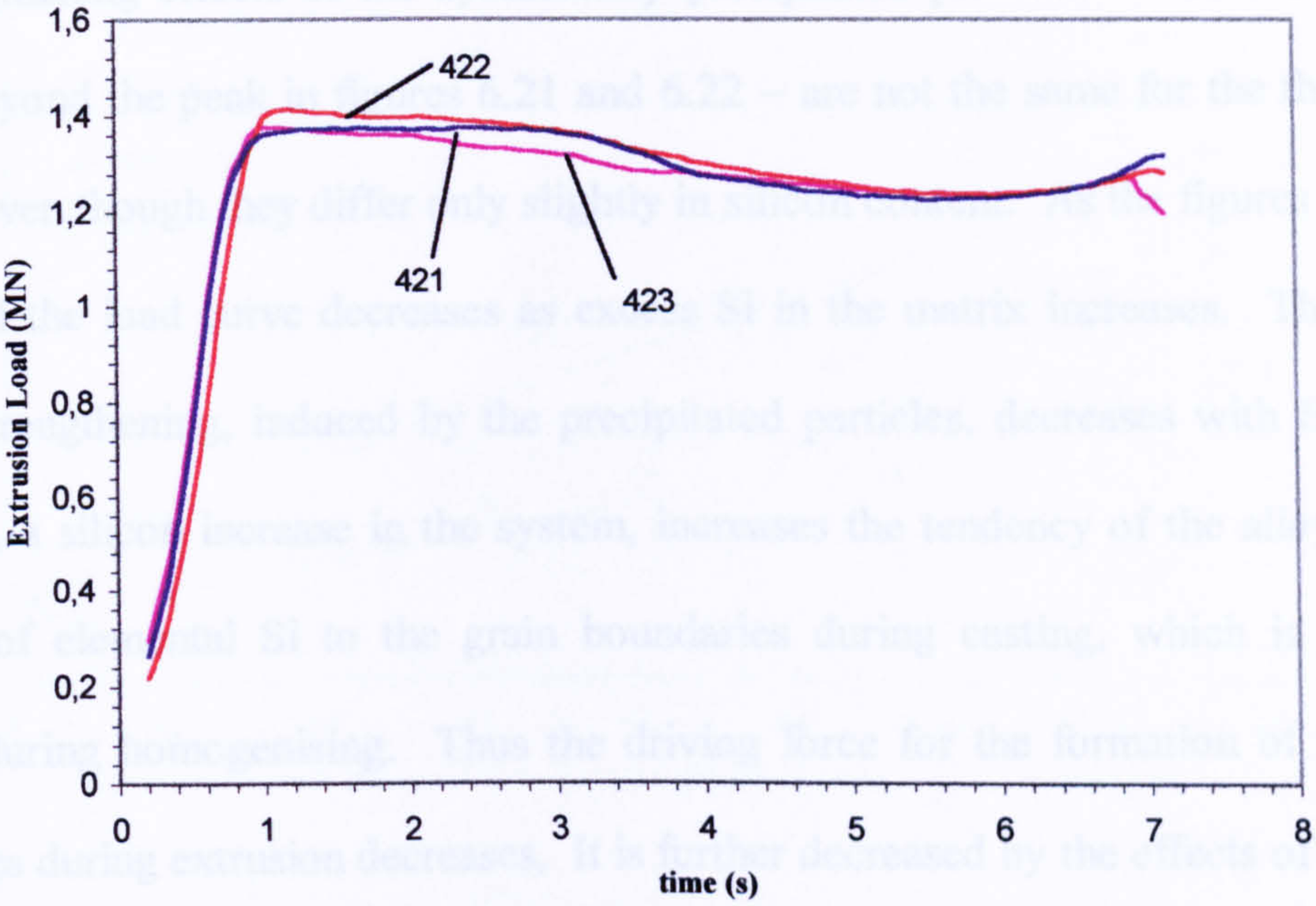

Figure 6.21. Load traces for extrusion of alloys 421-423 (421: balanced, 422: 0.2 wt % xs Si, 423: 0.5 wt % Si. All contain 0.6 wt % Mg and 0.1 wt % Fe) through die 1.

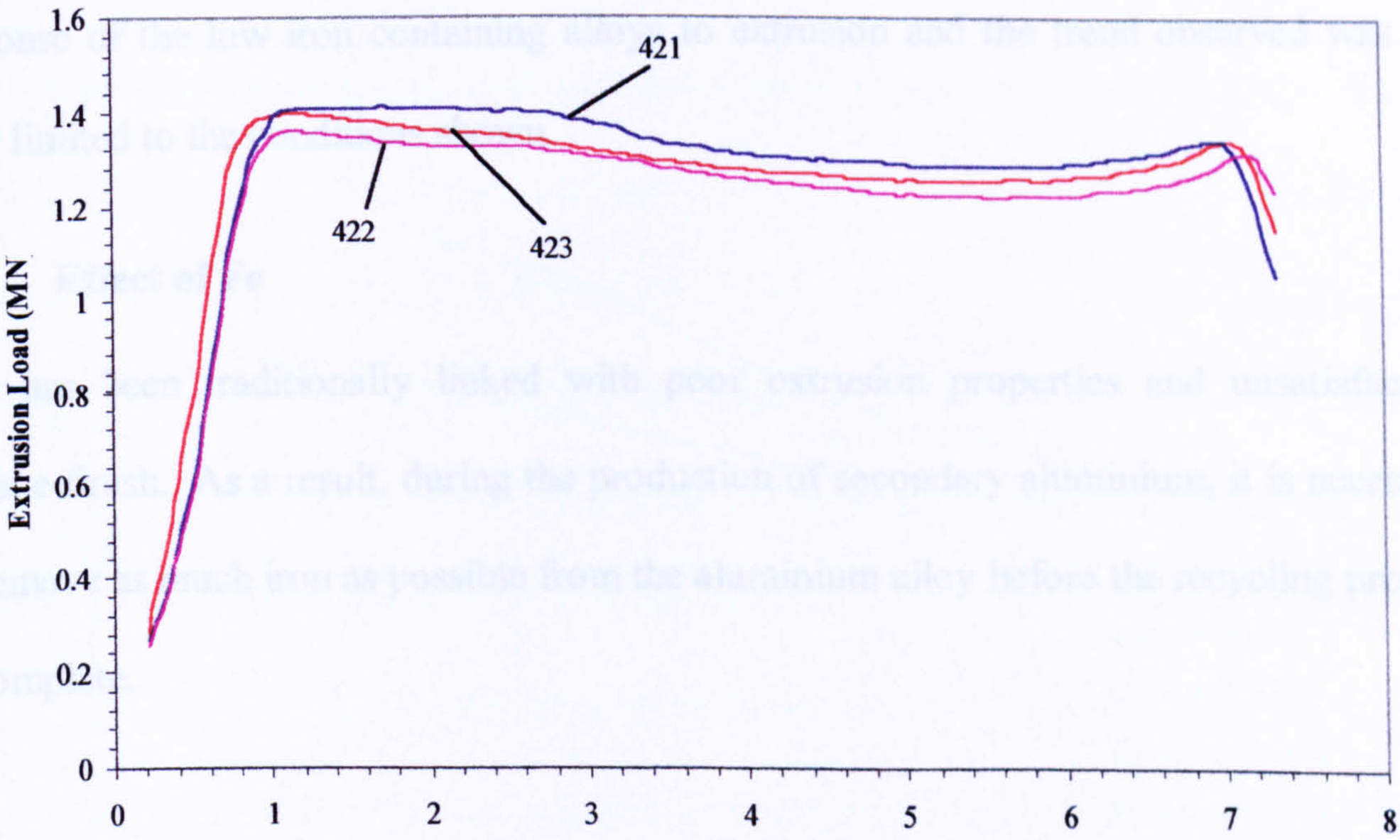

Figure 6.22. Load traces for extrusion of alloys 421-423 (421: balanced, 422: 0.2 wt % xs Si, 423: 0.5 wt % Si. All contain 0.6 wt % Mg and 0.1 wt % Fe) through die 2.

The strengthening effects of the dynamically precipitated particles – which are evident directly beyond the peak in figures 6.21 and 6.22 – are not the same for the three alloys pictured, even though they differ only slightly in silicon content. As the figures show, the gradient of the load curve decreases as excess Si in the matrix increases. This implies that the strengthening, induced by the precipitated particles, decreases with Si content. As before, a silicon increase in the system, increases the tendency of the alloy to cause rejection of elemental Si to the grain boundaries during casting, which is unable to dissolve during homogenising. Thus the driving force for the formation of the Mg_2Si precipitates during extrusion decreases. It is further decreased by the effects of the excess Si on the β- AlFeSi phase. β- AlFeSi is richer in Si than the corresponding α phase, resulting in a drop in the free silicon available to form Mg_2Si, thus the thermodynamic driving force for its formation is also decreased. Figures 6.21 and 6.22 are typical of the response of the low iron containing alloys to extrusion and the trend observed was not only limited to the conditions shown.

6.3 Effect of Fe

Iron has been traditionally linked with poor extrusion properties and unsatisfactory surface finish. As a result, during the production of secondary aluminium, it is necessary to remove as much iron as possible from the aluminium alloy before the recycling process is complete.

Figures 6.23 and 6.24 show the variation of the extrudability and the maximum extrusion load with iron content in the alloy. There is a discrepancy between the two parameters in that the maximum load shows a steady increase with iron content, whereas the extrudability tends to decrease after a sharp peak with the first additions of Fe.

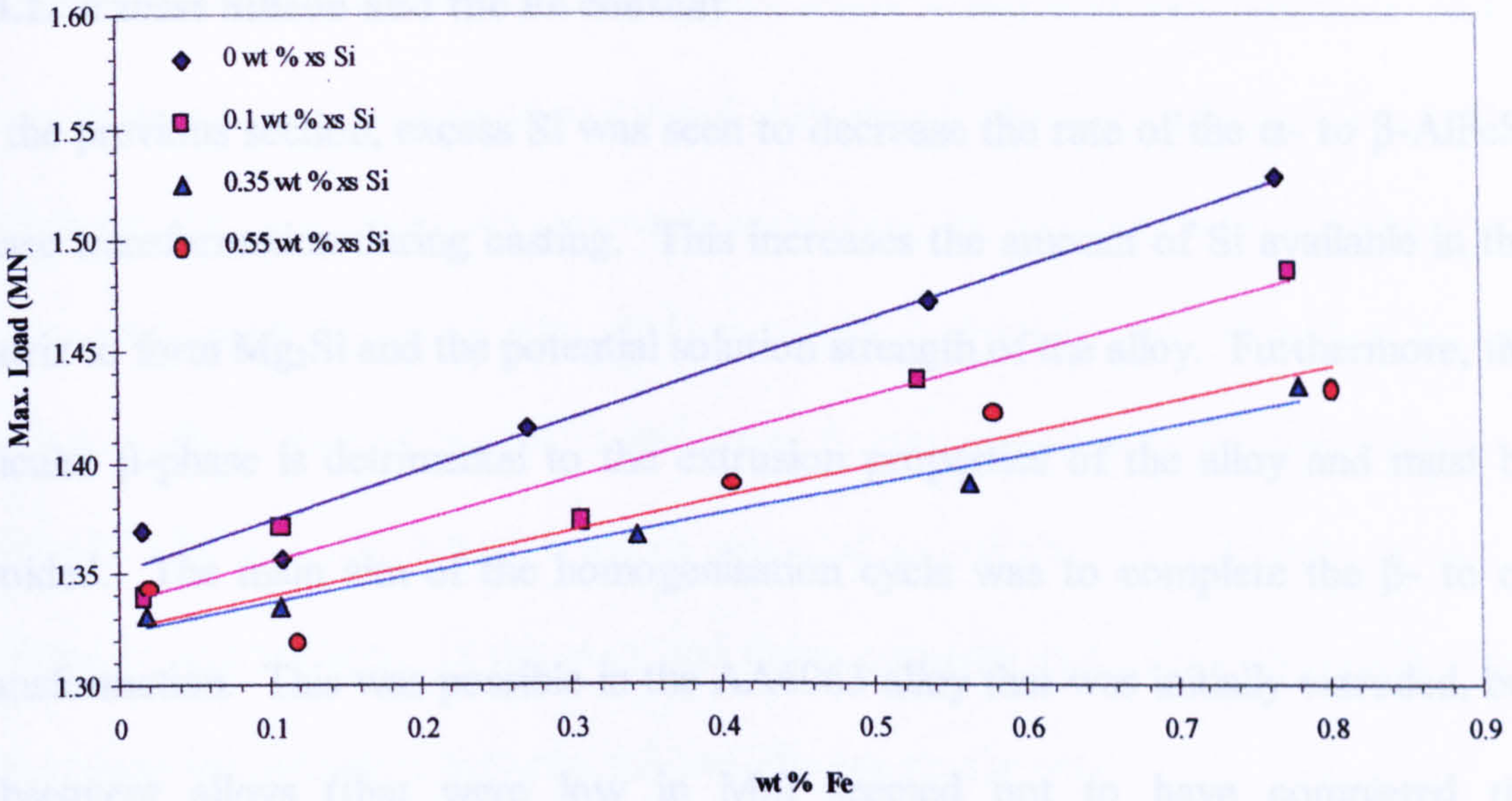

Figure 6.23. Variation of the maximum extrusion load with iron content for alloys containing 1 wt % Mg_2Si.

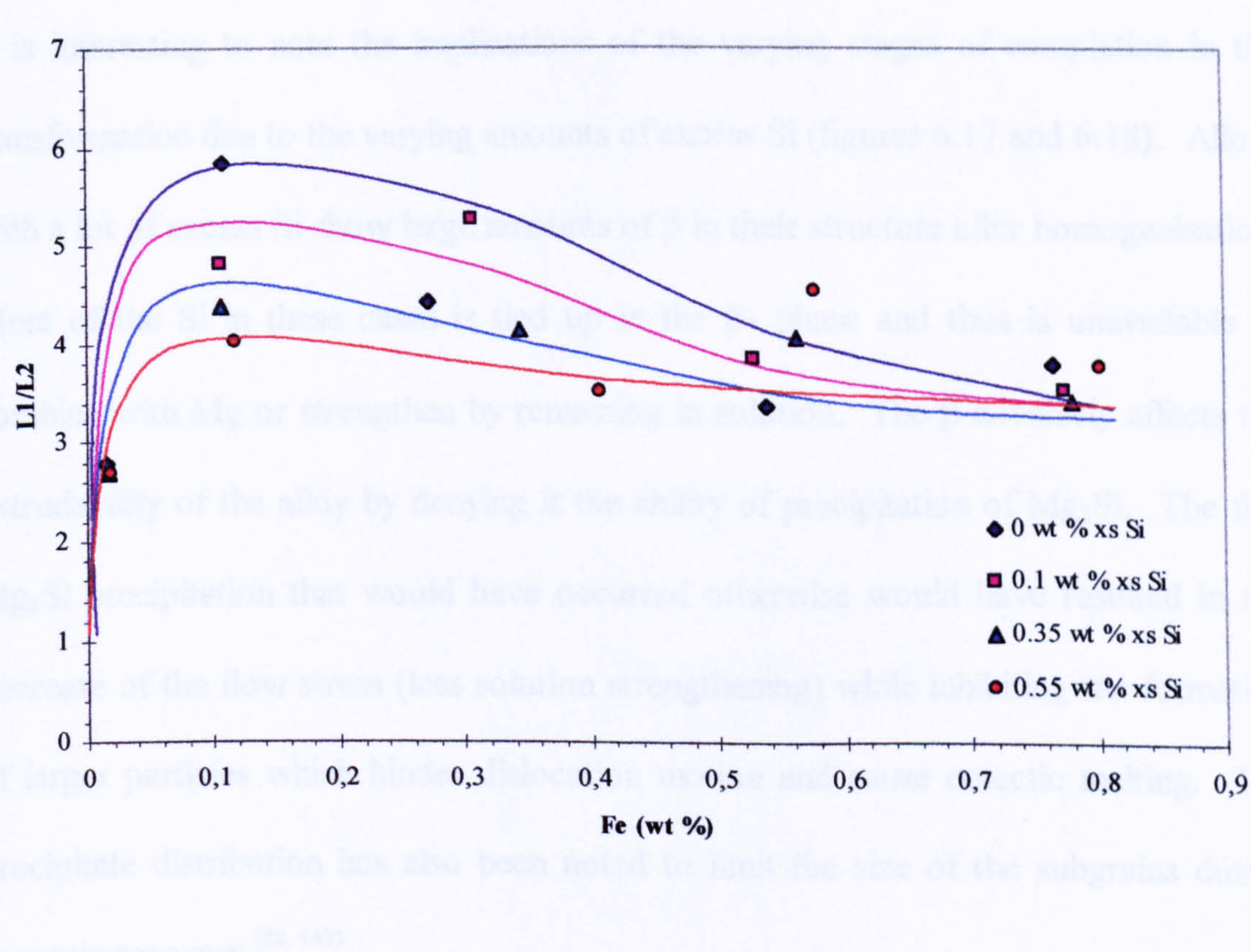

Figure 6.24. Variation of the extrudability with iron content for alloys containing 1 wt % Mg_2Si.

6.3.1. Excess Silicon and the Fe content

In the previous section, excess Si was seen to decrease the rate of the α- to β-AlFeSi phase transformation during casting. This increases the amount of Si available in the matrix to form Mg_2Si and the potential solution strength of the alloy. Furthermore, the acicular β-phase is detrimental to the extrusion properties of the alloy and must be avoided. The main aim of the homogenisation cycle was to complete the β- to α-transformation. This was possible in the AA6063 alloy that was initially extruded, but subsequent alloys (that were low in Mn) seemed not to have completed the transformation. This is consistent with previous observations [16, 39] that a homogenisation temperature of 555 °C would take around 20 h to completely convert the β- AlFeSi (compared with 6 h at 585 °C in the present study).

It is interesting to note the implications of the varying stages of completion in the transformation due to the varying amounts of excess Si (figures 6.17 and 6.18). Alloys with a lot of excess Si show large amounts of β in their structure after homogenisation. Most of the Si in these cases is tied up in the β- phase and thus is unavailable to combine with Mg or strengthen by remaining in solution. The β adversely affects the extrudability of the alloy by denying it the ability of precipitation of Mg_2Si. The fine Mg_2Si precipitation that would have occurred otherwise would have resulted in the decrease of the flow stress (less solution strengthening) while inhibiting the formation of larger particles which hinder dislocation motion and cause eutectic melting. The precipitate distribution has also been noted to limit the size of the subgrains during dynamic recovery [28, 143].

Recrystallisation has also been noted to play a part in the final microstructure of the alloys in this study. It has been mentioned elsewhere [5] that the Fe/Si ratio in an alloy is probably the most important parameter controlling the recrystallisation temperature. A low ratio, such as that of alloy 424, shown in figure 6.25, causes a slow rate of recrystallisation, whereas higher Fe and lower Si contents such as the composition of alloy 521 (figure 6.26) induce a higher recrystallisation rate. The change in rate is effected by the variation of the start and finish temperatures of the recrystallisation. The greater the difference between the two, the slower the rate.

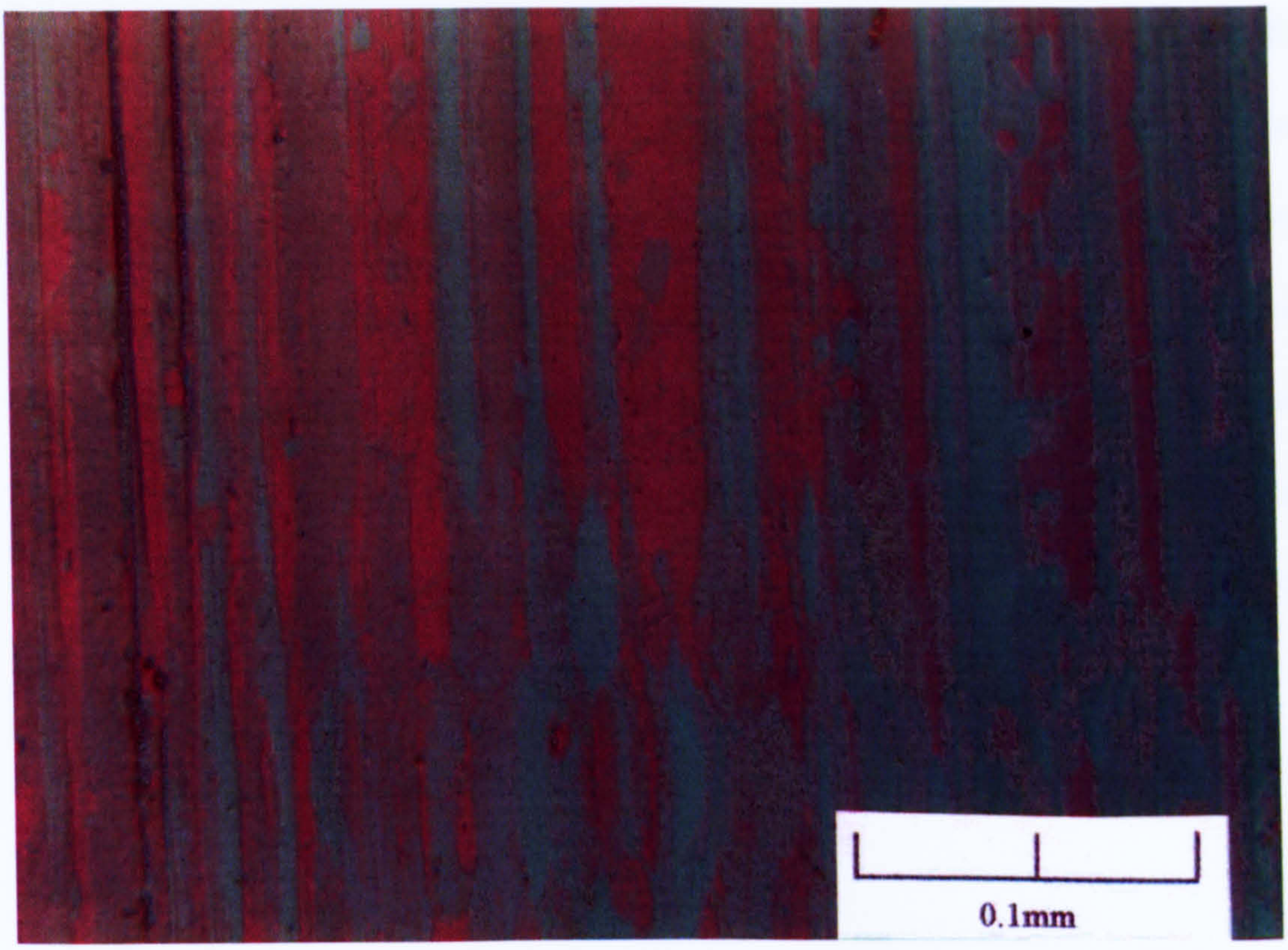

Figure 6.25.Longitudinal section through extrudate of alloy 424 (Fe/Si = 0.077)

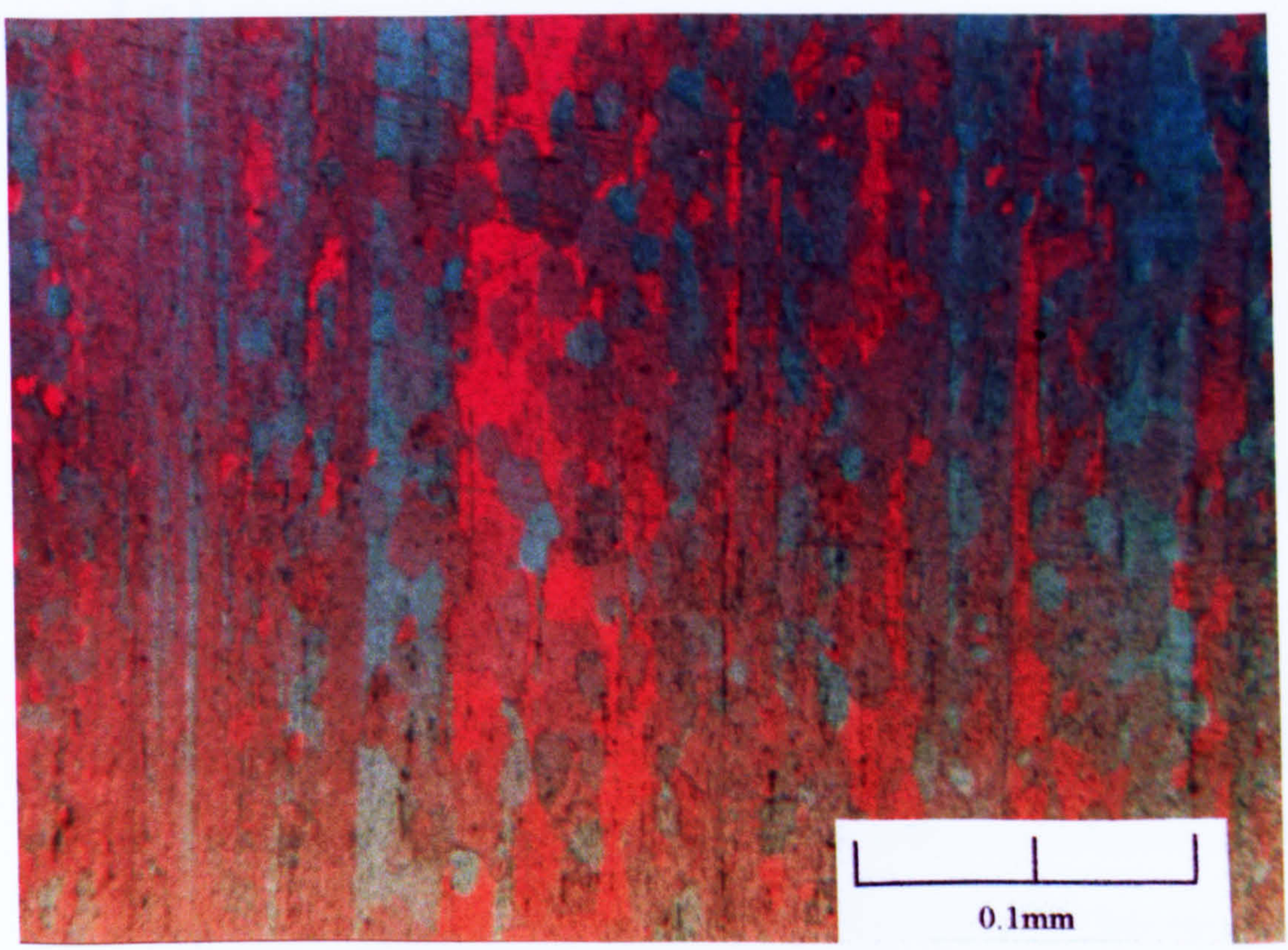

Figure 6.26.Longitudinal section through extrudate of alloy 521 (Fe/Si = 0.487)

The rate at which the alloy reaches the peak load during extrusion– which was found from the slope of the load against time traces – is affected by both the presence of Fe and that of Si. This rate is akin to the rate of work hardening and depends on the rates of dislocation generation and annihilation during the repolygonisation process. An indication of how this rate is affected by the alloying content of the extruded material is given in figure 6.27. Note that there exists a sharp increase in the rate at a certain Fe content, which varies depending on the amount of excess Si present in the matrix.

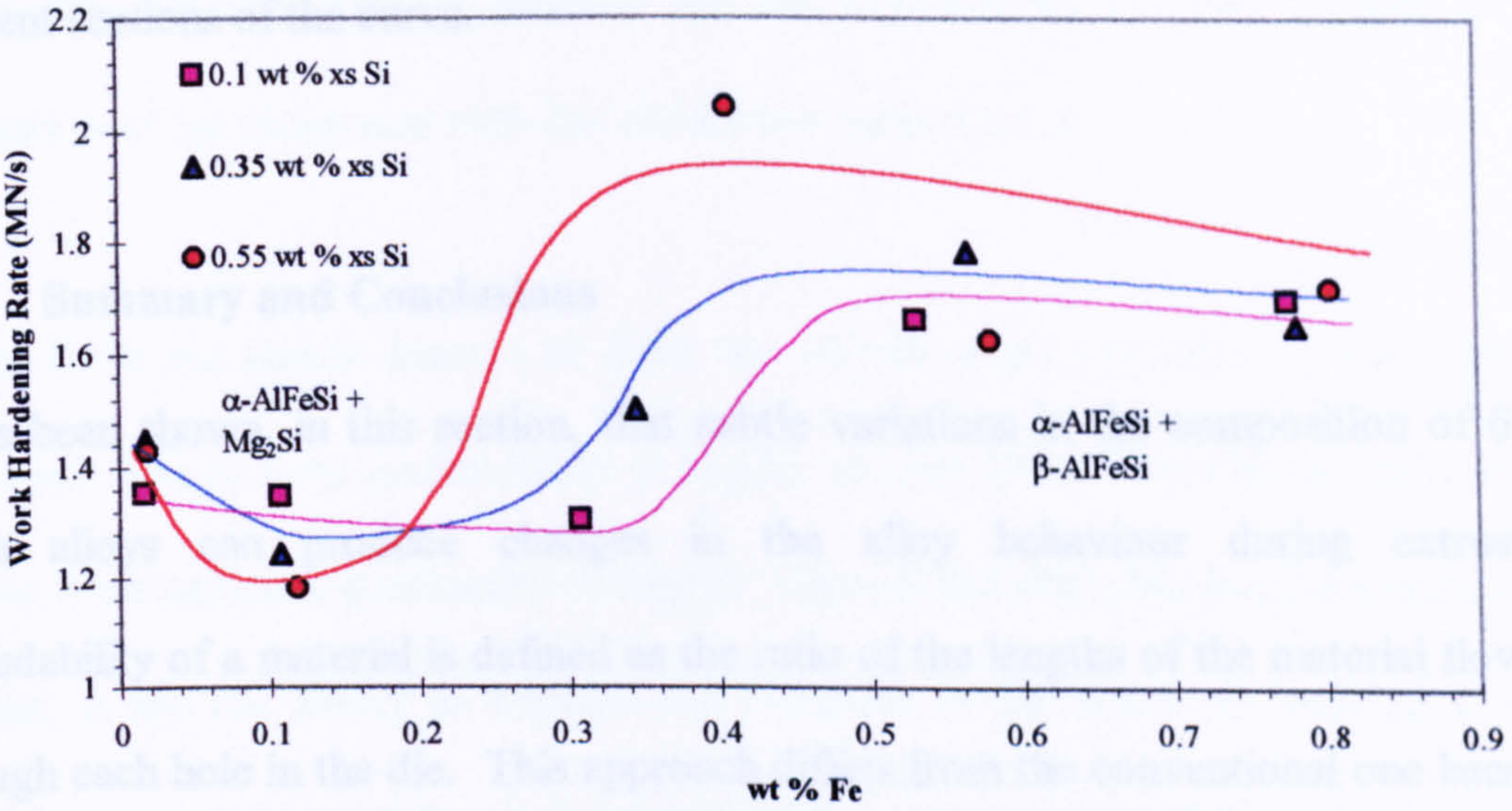

Figure 6.27. Effect of Fe on the rate at which the peak extrusion load is reached for alloys containing 1 wt % Mg_2Si, indicating the phase fields, which exist in the billets.

As the silicon content of the alloy increases, less Fe is required to effect this increase in the rate. Generally, the slope of the initial part of the load – time diagram (section I in figure 2.5), would increase because of the introduction of particles into the matrix, or the existence of smaller grains (or subgrains), thus inhibiting dislocation motion. In the case shown above, at low Fe contents, precipitates exist in the form of α-AlFeSi and

Mg_2Si. However, at the other end of the scale, with high Fe alloys, the precipitation of Mg_2Si is suppressed and β-AlFeSi is formed instead. This is due to the large driving forces, for the formation of these phases, induced by the high Fe contents.

Figure 6.27 indicates that as the Si content of the alloy increases, less Fe is required to effect the rapid increase in the rate. As mentioned in section 6.2.1, as the amount of Si increases in the matrix, any β-AlFeSi becomes more stable. Thus the required driving force for its formation decreases. Hence, less Fe is required to induce the change in precipitate structure from α-AlFeSi + Mg_2Si to α-AlFeSi + β-AlFeSi, in the two different sections of the curve.

6.4. Summary and Conclusions

It has been shown, in this section, that subtle variations in the composition of 6xxx series alloys can produce changes in the alloy behaviour during extrusion. Extrudability of a material is defined as the ratio of the lengths of the material flowing through each hole in the die. This approach differs from the conventional one because only material parameters are considered. The ram velocity, which is definitely important to the industrial extruder – since that is what determines the productivity – is not considered as an extrudability limiting factor. For a certain material, there exists a ram velocity that will render the surface finish unacceptable. This has been discussed by other workers. The tendencies for flow of the material, though, are also affected by the alloying content and the particular phases, which exist in the structure during extrusion. The phases which precipitate in these alloys are the main hardening phase,

Mg_2Si, the iron phase particles – α- and β-AlFeSi, and in high Si-low Mg alloys, elemental Si.

Mg_2Si alone in the structure, with no Fe, does not appreciably affect the extrudability of the alloy. However, when small amounts of Fe are added, the extrudability has been shown to improve because of the depletion of Si – due to the formation of the AlFeSi phase - from the solid solution and the inability of Mg to form the hardening phase. During extrusion, it has been shown that in certain alloys, especially those with low Si contents and devoid of Fe, a fine dispersion of Mg_2Si precipitates is formed. This causes the extrusion load to increase and the extrudability to drop because of the interaction of the dispersion with the dislocation substructure.

Si and Fe in the matrix interact to form the AlFeSi phase particles. These particles have been seen to form preferentially to Mg_2Si, so only alloys with high Si contents are able to form substantial amounts of Mg_2Si. Also, if the alloy has large amounts of Si present, it has the ability to stabilise the β-AlFeSi in the structure, making it more difficult to transform, through homogenisation, into the less detrimental α phase. Results in this study have shown that Si is less detrimental, to the extrudability of 6xxx series alloys, than Mg, confirming the findings of previous workers. As more Fe is added to the alloy, the tendency for the formation of Mg_2Si decreases and that for β-AlFeSi increases causing an increase in the rate at which the peak extrusion load of the alloy is reached.

Chapter 7

Accelerated ageing for 6xxx series alloys

Nomenclature – Chapter 7

C	Constant
C_0	Number of available nucleation sites
D	Self-diffusion coefficient
G	Universal gas constant
N^*	Particle nucleation rate
T	Absolute temperature
t	Time
ΔH^*	Free energy associated with the formation of a stable nucleus
ΔH_m	Activation energy for atomic migration
ΔH_v	Volume free energy
ΔH_ε	Misfit strain free energy
ΔX_0	Supersaturation of the alloy
γ	Surface energy of the nucleus
ν^*	Rate of precipitate growth
ω	Constant

7. Accelerated ageing for 6xxx series alloys

Introduction:

It is well known that 6xxx series alloys constitute the largest percentage of all extruded sections. A significant proportion of these are AA6063 architectural type alloys. The mechanical properties of such alloys may be improved after extrusion by employing a low temperature heat treatment known as artificial ageing. Numerous papers have been published discussing ageing but surprisingly few discuss the accelerated (two stage) form of the process. The aim of the present work is to decrease the time required to artificially age profiles after they have been extruded by using two separate temperatures.

7.1. Conventional Ageing of PERAl

7.1.1. Microstructural Evolution during Ageing

It is still not fully understood how the change in the structure of the particles occurs.

The question that must be posed is: Do subsequent precipitates nucleate after, or during, the dissolution of the previous phase or does the growth of a certain precipitate result in the change in structure and coherency to give a new phase?

From the results presented in a number of studies [110-113, 144-146], it is possible to speculate as to the sequence of changes in the structure of the metastable precipitates.

Consider a typical ageing curve of a commercial AlMgSi alloy (AA6063) shown in figure 7.1.

An initial dip in the mechanical properties can be seen which may be attributed to the dissolution of the GP zones which were formed during the natural ageing of the samples before the artificial ageing process had begun, and the subsequent formation of the β″ particles. During natural ageing GP zones form homogeneously in the matrix. Because of their low surface energy, the free energy required to create a stable nucleus is low. Now, when the temperature is raised to the ageing temperature, the matrix can no longer maintain these nuclei because the higher temperature has induced an increase in the minimum possible size of a stable nucleus [114]. This effect - a temporary drop in properties on temperature change - is sometimes called *reversion*. In 7xxx series alloys (AlMgZn) this effect is particularly evident. The magnitude of the dip varies depending on the length of time between solutionising and ageing (termed 'incubation period' or 'storage time'). The incubation period also affects the steady state mechanical properties of the alloy after the ageing cycle is complete [147-152]. This effect is of particular importance where industrial extrusions are concerned: Industrial extrudates are typically subjected to varying incubation periods after they have been extruded. This can cause a variation in the mechanical properties within the same batch of extrudates, which are supposed to be identical. The dip was present in the first ever age hardening curve published by Alfred Wilm in 1911 [153]. However, Wilm did not attempt an explanation and subsequent studies, by other workers, did not involve the first half-hour or so of the curve. The variation of hardness at the beginning of the ageing process is shown in figure 7.2.

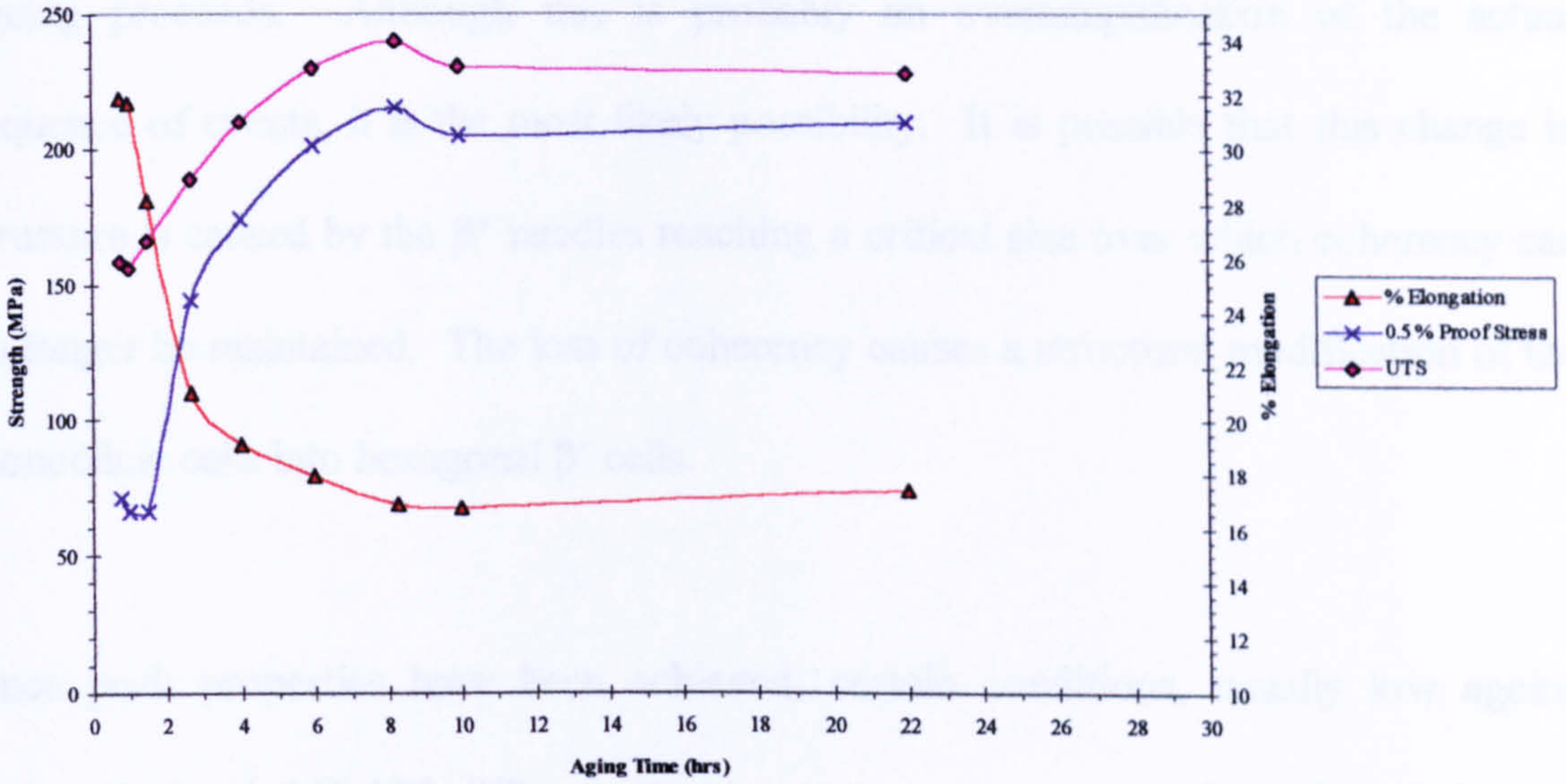

Figure 7.1. Typical ageing characteristics of a PERAl AA6063 alloy (solutionised: 540 °C, aged: 175 °C).

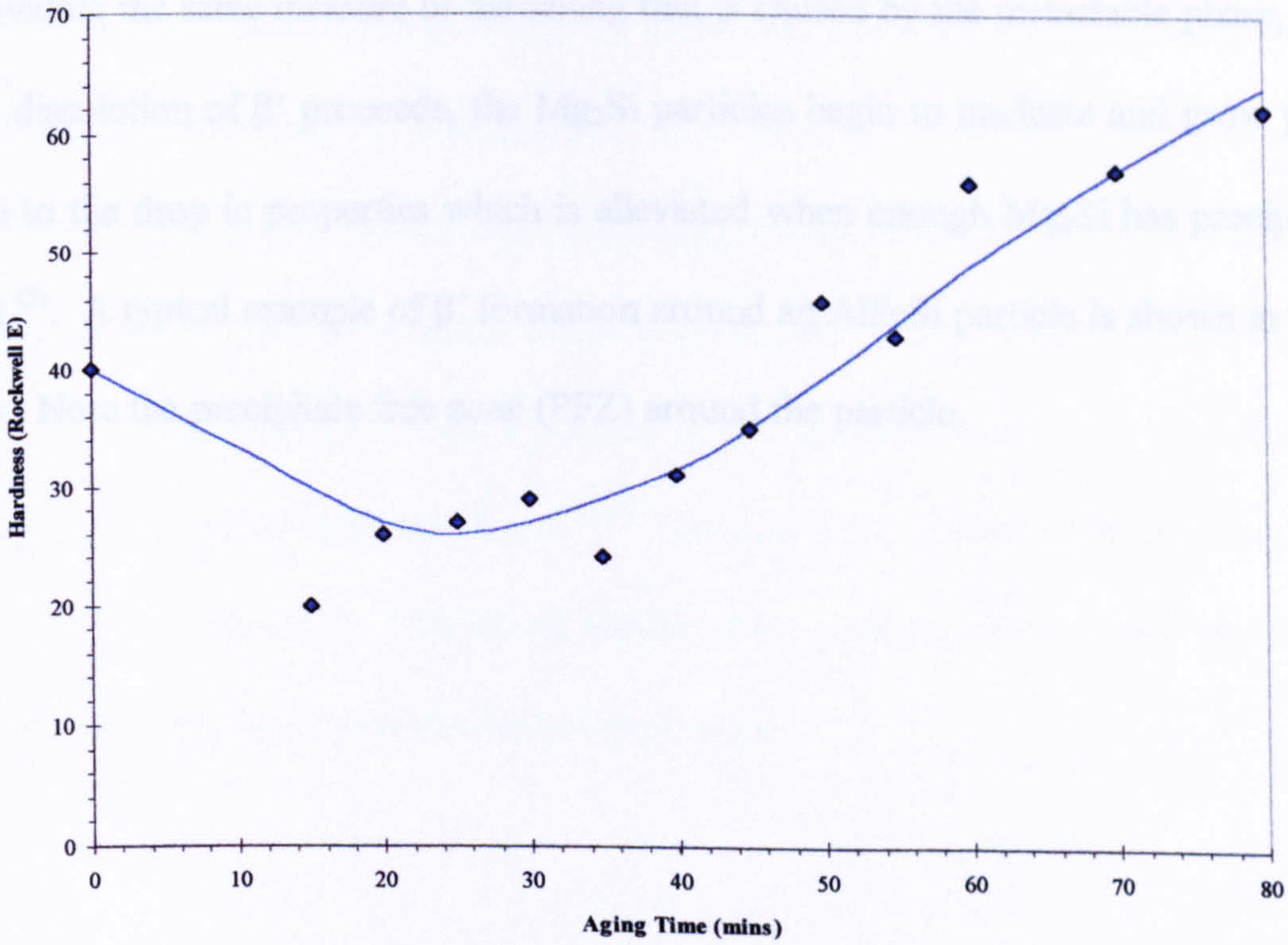

Figure 7.2. The dip observed in the properties of an aged sample during the fist stages of the process (Sol T: 560 °C, Ageing T: 203 °C)

The transition from β″ to β′ seems to be a simple change in structure, which occurs as ageing proceeds. Although this is probably an oversimplification of the actual sequence of events, it is the most likely possibility. It is possible that this change in structure is caused by the β″ needles reaching a critical size over which coherency can no longer be maintained. The loss of coherency causes a structural modification of the monoclinic cells into hexagonal β′ cells.

Once peak properties have been achieved, certain conditions, usually low ageing temperatures (~165-175 °C), seem to cause a temporary drop in mechanical properties. This is most probably due to the dissolution of the β′ phase before the formation of the equilibrium Mg_2Si. The equilibrium platelets are not capable of providing the same measure of hardening that is caused by the metastable phase, so as the dissolution of β′ proceeds, the Mg_2Si particles begin to nucleate and grow giving rise to the drop in properties which is alleviated when enough Mg_2Si has precipitated out [5]. A typical example of β′ formation around an AlFeSi particle is shown in figure 7.3. Note the precipitate free zone (PFZ) around the particle.

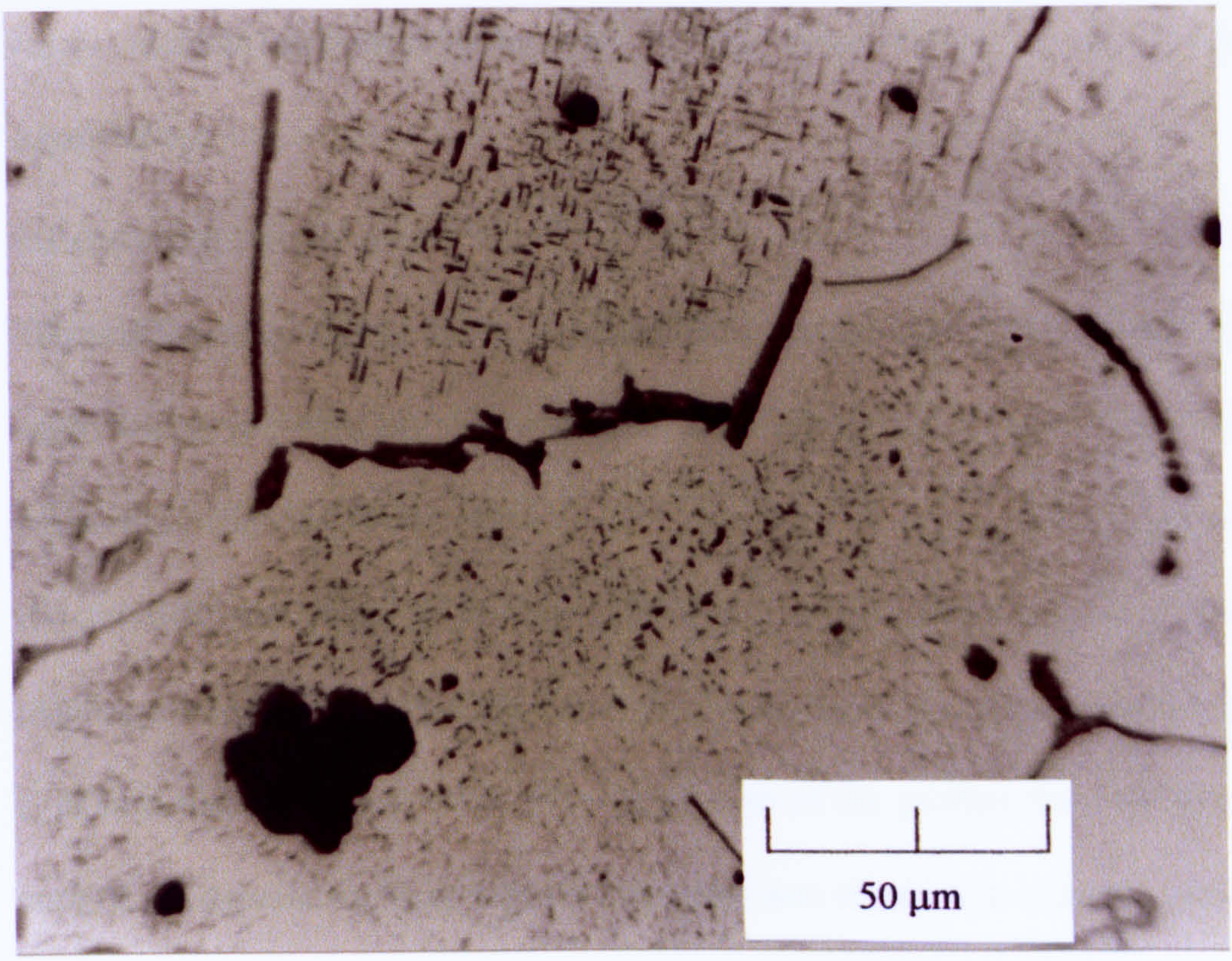

Figure 7.3. Typical β' precipitate formation including a PFZ.

However, other conditions tend to give a permanent drop in the mechanical properties (termed 'age softening' or 'overageing'). It is widely accepted that Mg_2Si cannot, as mentioned earlier, provide the same hardening effects as β′. This would lead one to believe that the explanation given above is erroneous. It is possible, though, that this effect may indirectly prove the existence of the alternate form of β precipitates as suggested by Westengen and Ryum [111] (Section 2.7). Cubic particles would pose more of an obstacle to dislocation motion than platelets of the same phase, thus incurring an increase in the mechanical properties.

7.1.2. Effects of Solutionising and Ageing Temperature on the Properties of Aged Alloys

Solutionising Temperature:

The solutionising temperature, to which alloys are subjected before ageing, has not been widely considered as a possible parameter, which affects the mechanical properties. This is probably because solutionising is not necessarily a separate step in the industrial processing of an alloy. However, in microstructural terms, solutionising may be considered to be a static parallel of the extrusion process - and its importance is akin to that attributed to the exit temperature of the profiles from the press. In the case of the present study, a solution treatment was required in order to place as much of the solute into solid solution as possible, because all the samples were provided in already aged to T4. In an industrial environment, depending on the alloy, a separate solution treatment may not be required because adequate solutionising could be achieved through quenching at the press. Press quenching is an important part of the extrusion process and in most cases of 6xxx series alloy extrusions gives adequate solutionising [22, 154]. In other cases, such as most 7xxx series alloys and the high copper containing 2xxx series, a separate solution treatment is required because of the inadequate response of such alloys to the press quenching treatment.

Specimens, which were given different solutionising treatments, but identical ageing treatment, exhibited a variation in steady state properties. This was demonstrated by hardness testing and tensile measurements. Specifically, the final hardness/strength was found to increase with increasing solutionising temperature, below the solvus (if the solutionising temperature is above the solvus temperature of the alloy, then no significant hardening is observed). Typically a 20°C increase in the solutionising

temperature resulted in a corresponding increase in the proof strength of around 5 %. The solutionising temperature was also seen to have an effect on the time taken to reach peak hardness. The higher the solutionising temperature, the faster the peak conditions are achieved. This is demonstrated in figure 7.4. Figures 7.5 and 7.6 show the variation of the peak hardness and time required to reach peak properties, respectively, with ageing temperature.

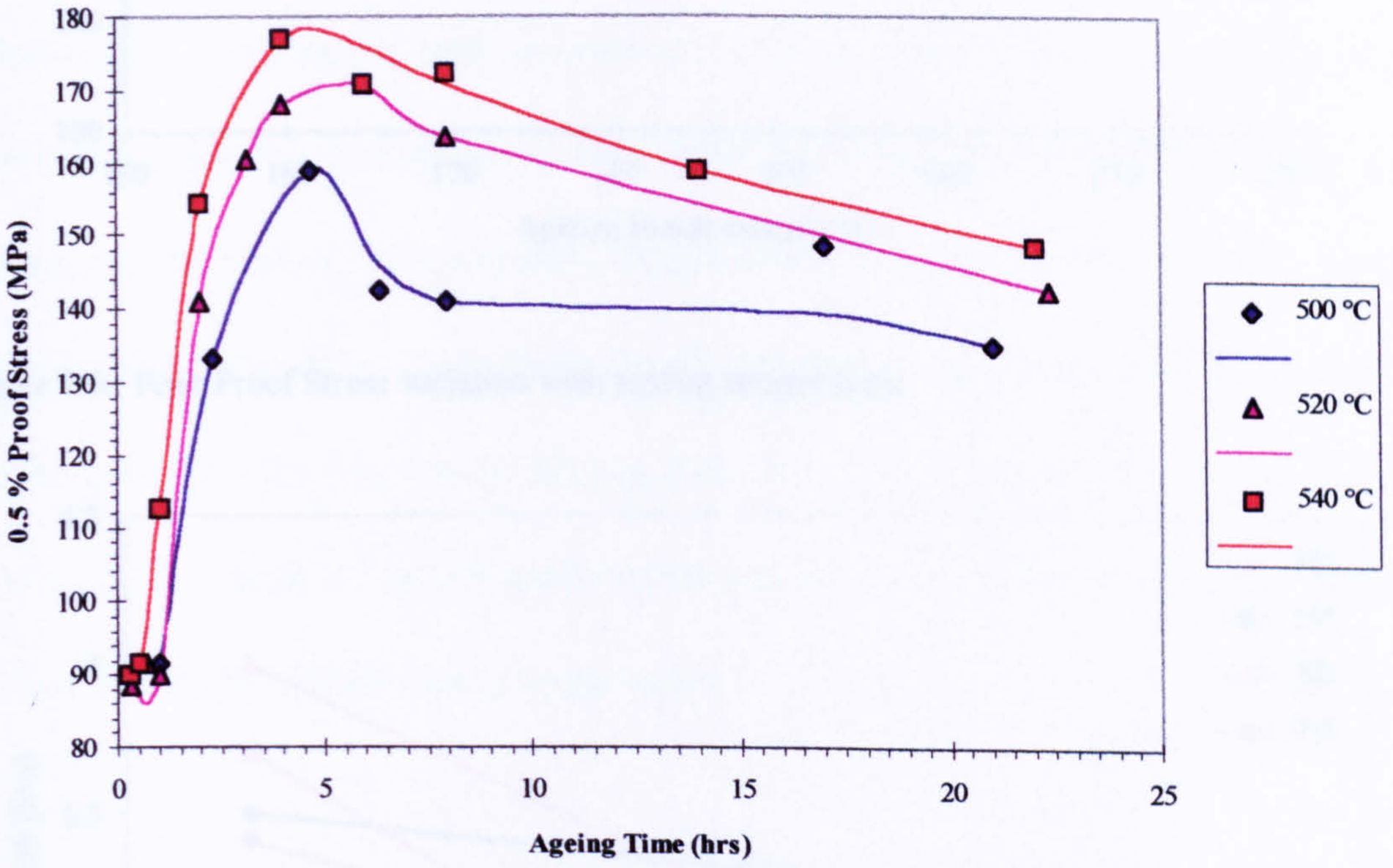

Figure 7.4. Ageing curves of samples aged at 205 °C

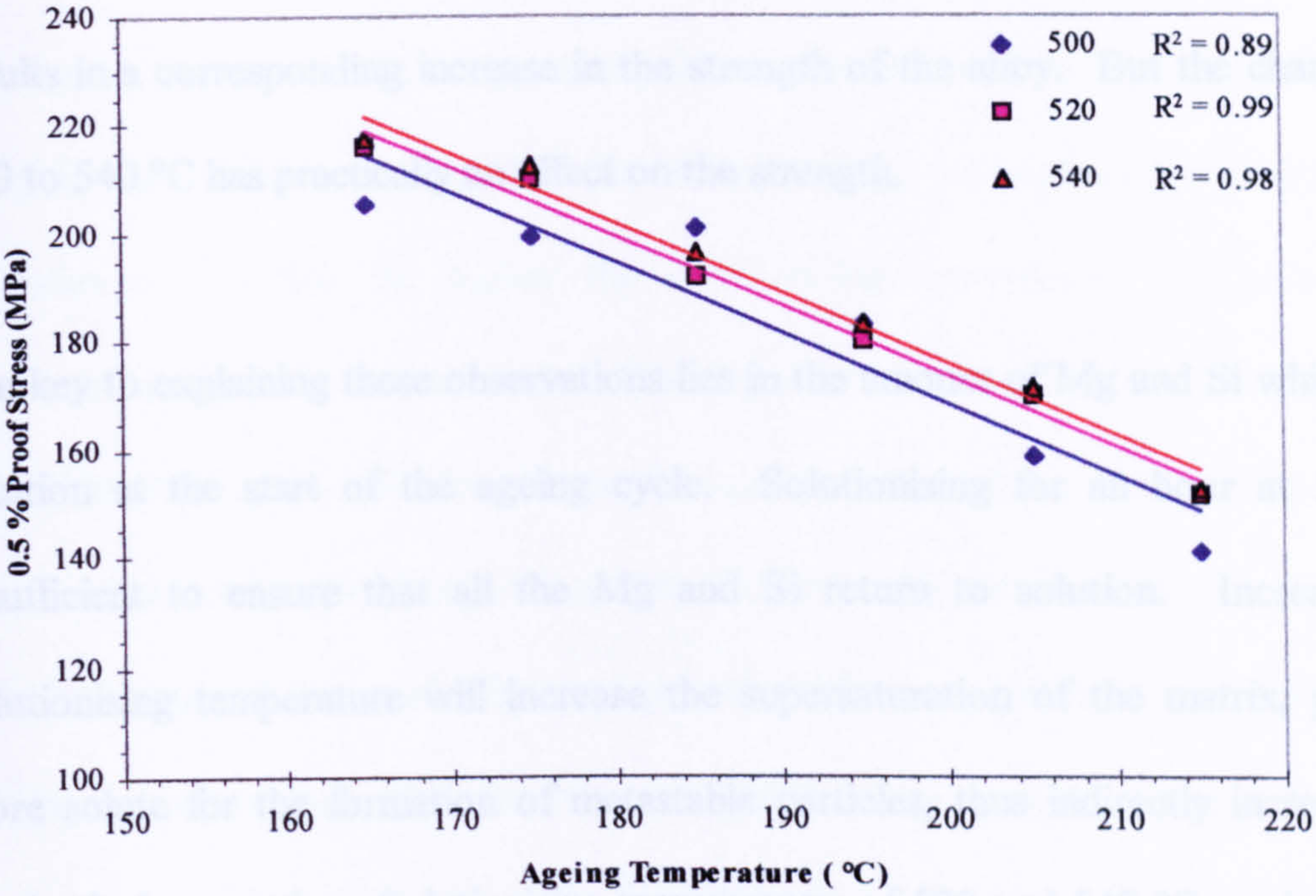

Figure 7.5. Peak Proof Stress variation with ageing temperature.

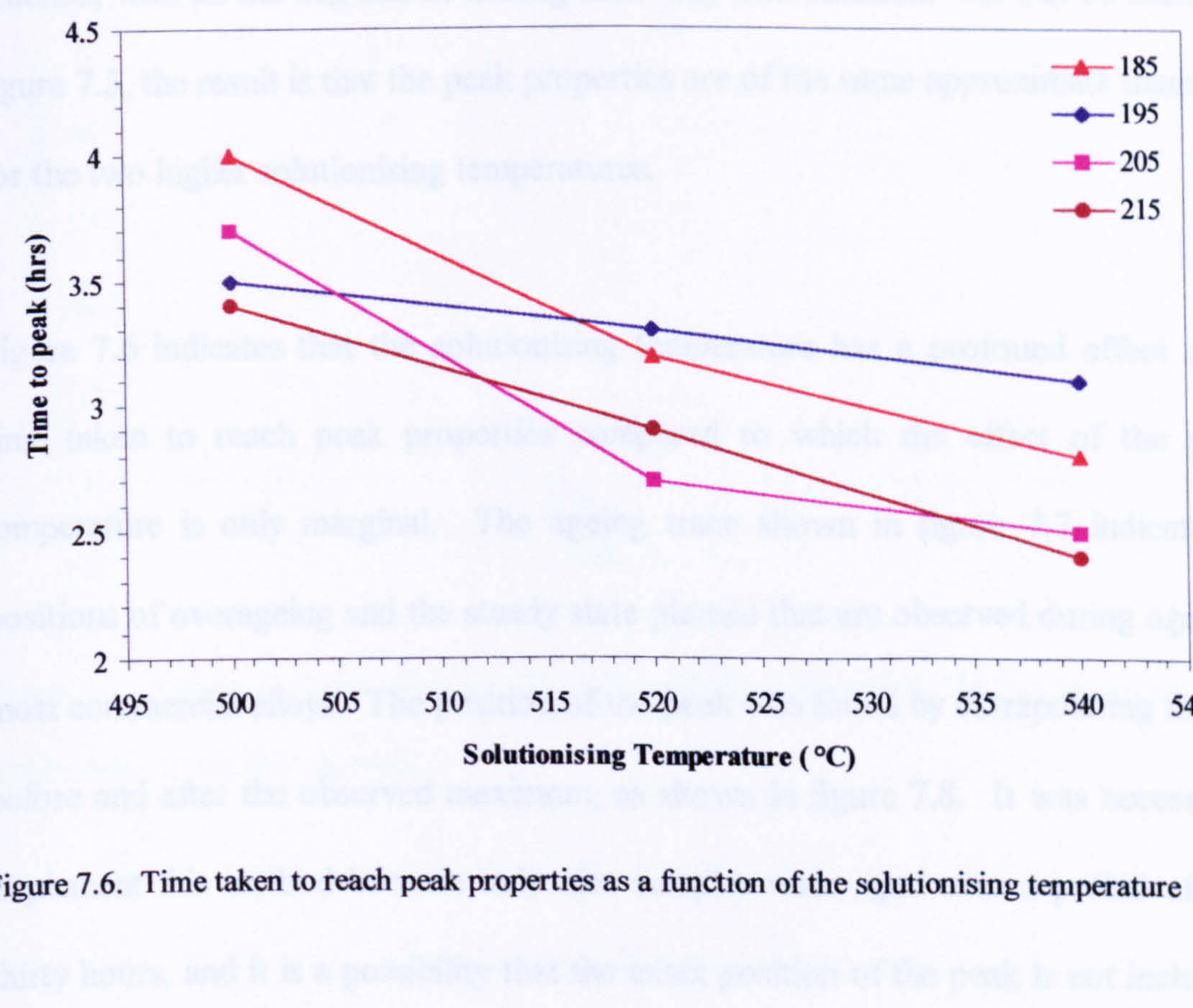

Figure 7.6. Time taken to reach peak properties as a function of the solutionising temperature

As is seen in figure 7.5, increasing the solutionising temperature from 500 to 520 °C results in a corresponding increase in the strength of the alloy. But the change from 520 to 540 °C has practically no effect on the strength.

The key to explaining these observations lies in the amount of Mg and Si which are in solution at the start of the ageing cycle. Solutionising for an hour at 500°C is insufficient to ensure that all the Mg and Si return to solution. Increasing the solutionising temperature will increase the supersaturation of the matrix, providing more solute for the formation of metastable particles, thus indirectly increasing the mechanical properties. Solutionising temperatures of 520 and 540 °C are both above the solvus (for the alloy in question), so the maximum supersaturation of the matrix is reached, with all the Mg and Si finding their way into solution. As can be seen from figure 7.5, the result is that the peak properties are of the same approximate magnitude for the two higher solutionising temperatures.

Figure 7.6 indicates that the solutionising temperature has a profound effect on the time taken to reach peak properties compared to which the effect of the ageing temperature is only marginal. The ageing trace shown in figure 7.7 indicates the positions of overageing and the steady state plateau that are observed during ageing of most commercial alloys. The position of the peak was found by extrapolating the lines before and after the observed maximum, as shown in figure 7.8. It was necessary to implement this method because only nine samples were aged over a period of up to thirty hours, and it is a possibility that the exact position of the peak is not included in the samples taken.

The reason for the variation in time-to peak is the increased vacancy concentration induced by the increase in temperature, shown schematically in figure 7.9. Since the samples were cooled very rapidly after solutionising, the vacancies were effectively *quenched-in*, so that the higher the solutionising temperature the more excess vacancies are present in the matrix. These quenched-in vacancies have the effect of greatly increasing the diffusion rate at the ageing temperatures - because as the solid solution is a substitutional one, the atomic sites available for an adjacent atom to jump into are increased - so nucleation and growth of the metastable precipitates increases leading to a shortening of the time-to-peak with increase in solutionising temperature.

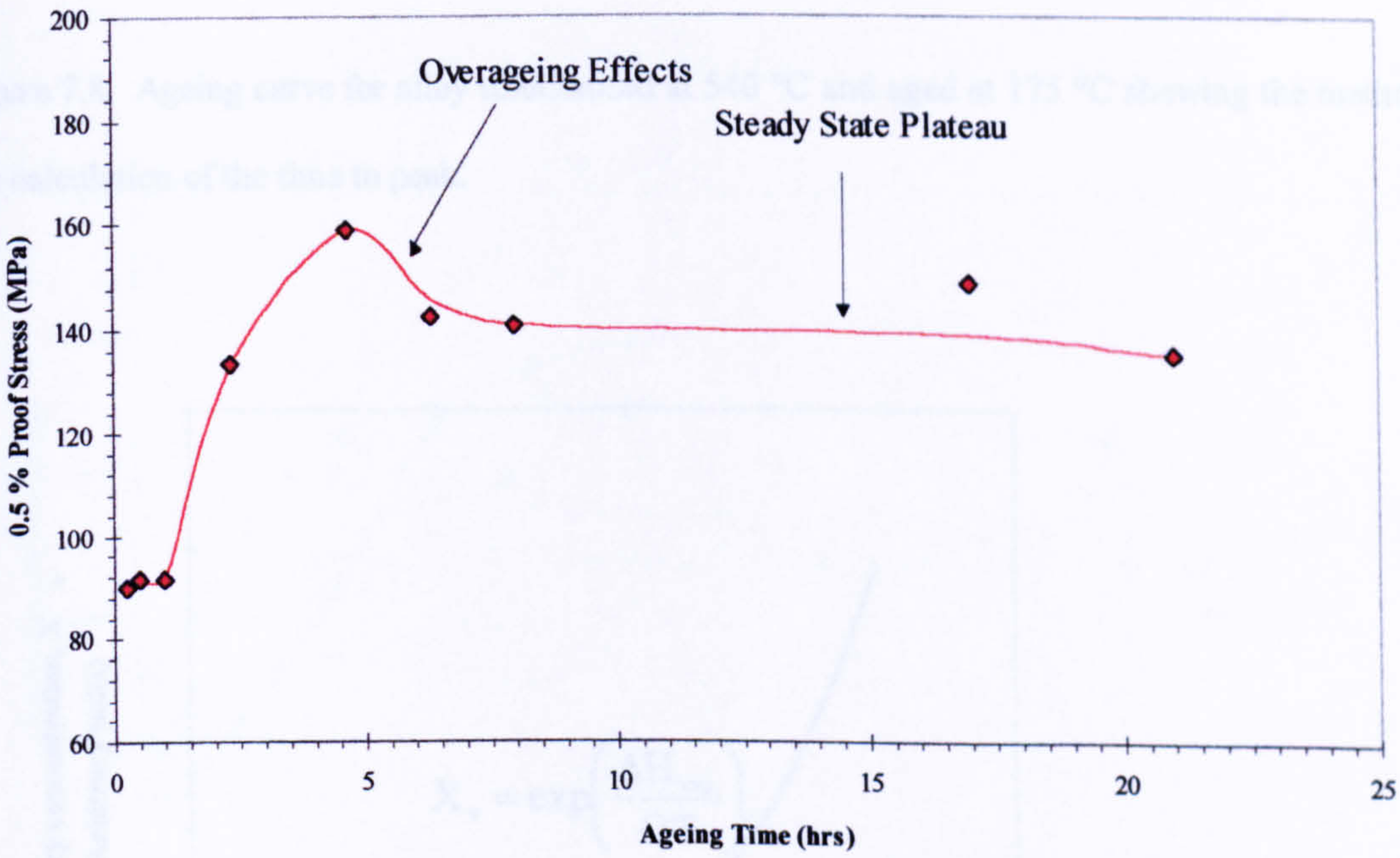

Figure 7.7. Ageing curve for alloy solutionised at 500 °C and aged at 205 °C, demonstrating the steady state plateau after the peak.

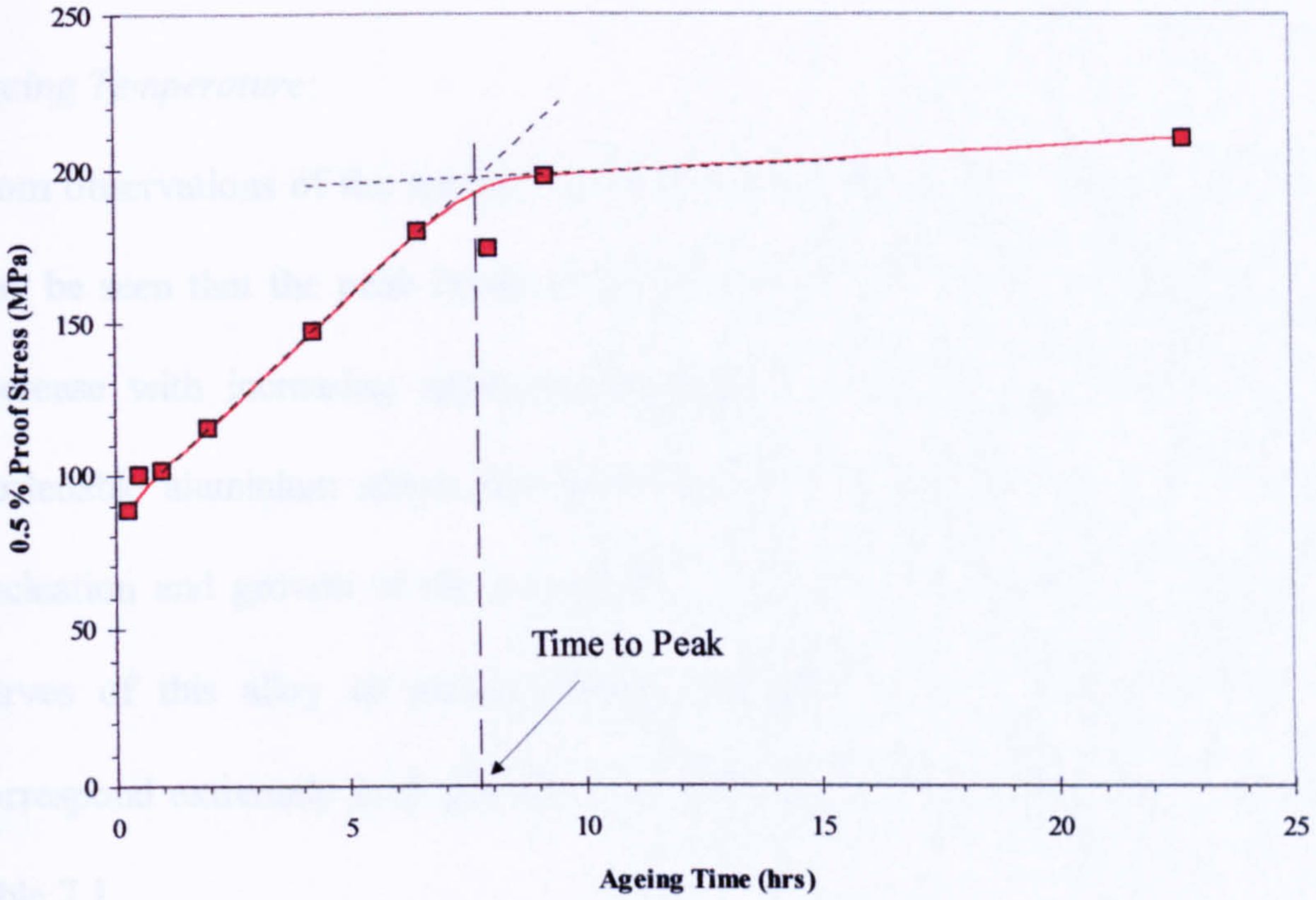

Figure 7.8. Ageing curve for alloy solutionised at 540 °C and aged at 175 °C showing the method for the calculation of the time to peak.

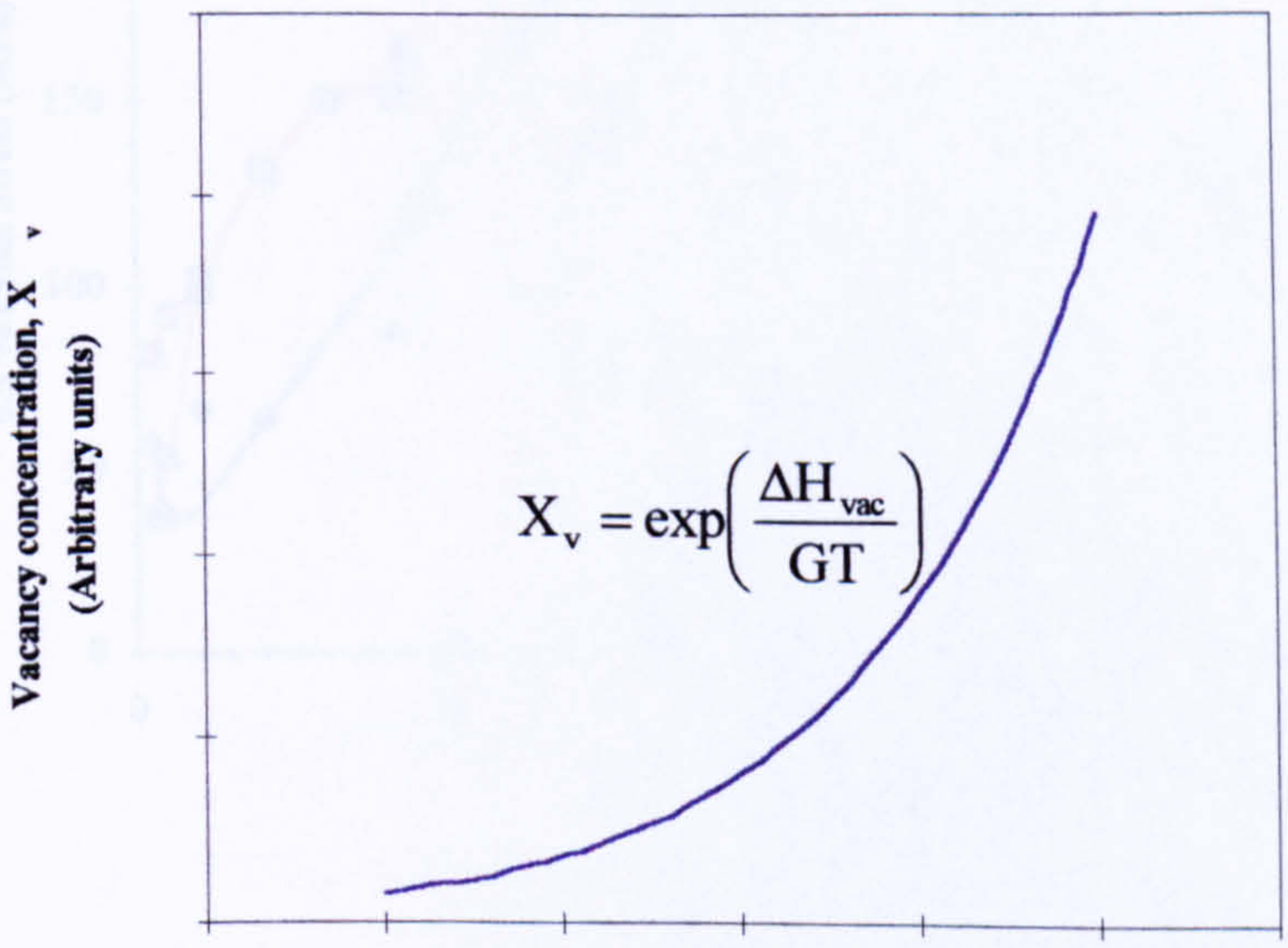

Figure 7.9. Variation of the vacancy concentration with solutionising temperature. X_v is the fraction of vacancies to atoms of the alloy, ΔH_{vac} is the change in free energy per vacancy, G is the Gas Constant (8.314 kJ/mol/K) and T is the absolute temperature.

Ageing Temperature:

From observations of the ageing curves of the AA6063 alloy utilised in this study, it may be seen that the peak hardness and the time taken to reach peak hardness both decrease with increasing ageing temperature. This effect is common to all age hardenable aluminium alloys and has been established to be due to the kinetics of nucleation and growth of the precipitates. Figure 7.10 displays the relative ageing curves of this alloy at various ageing temperatures. The curves shown below correspond extremely well with those presented in a previous study [143] as shown in table 7.1.

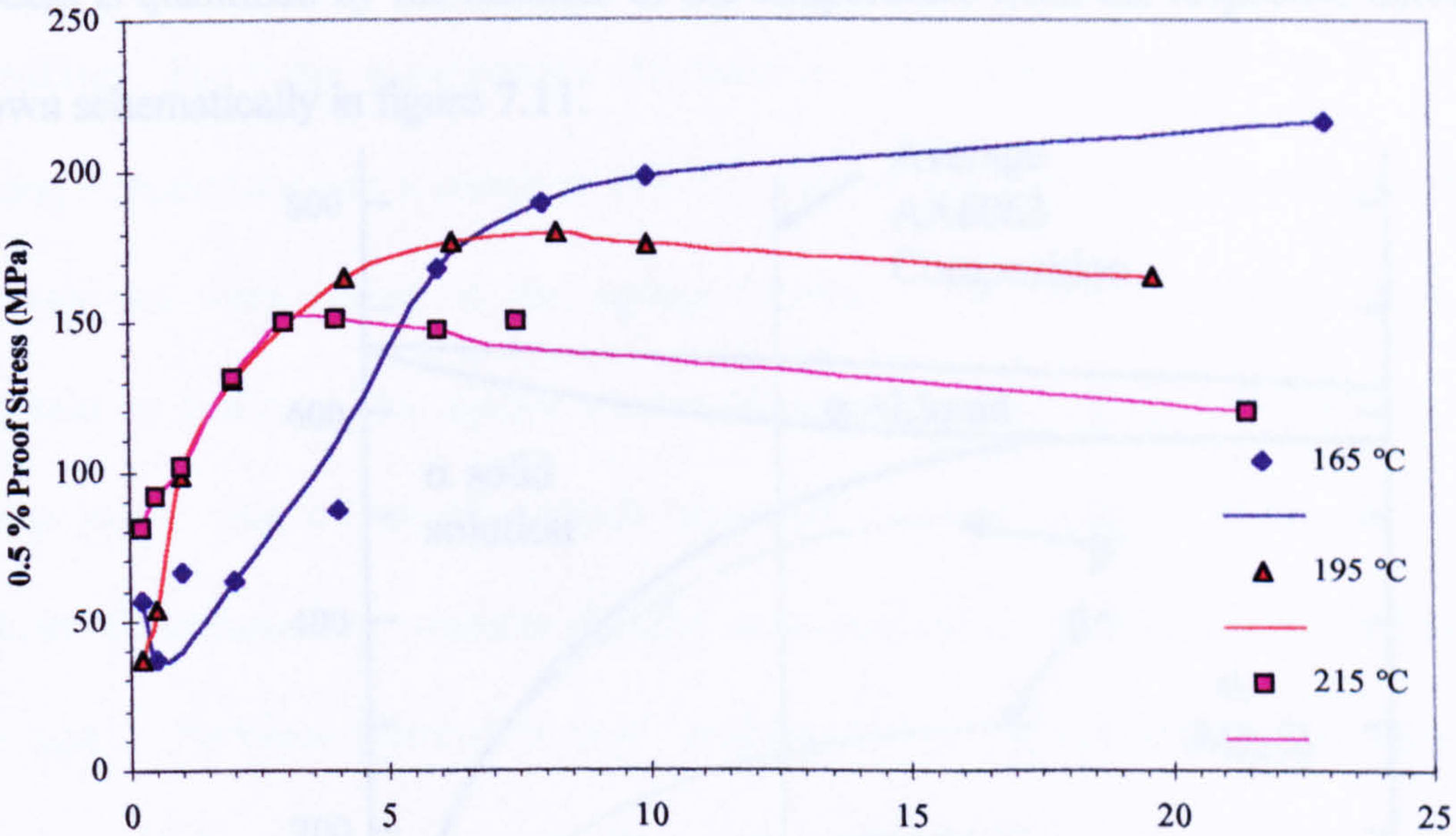

Figure 7.10. Relative ageing curves of samples solutionised at 520 °C

Ageing Temp. (°C)	Yield Stress at peak (MPa)		Time to reach peak (hrs)	
	Present study	Hains [143]	Present study	Hains [143]
165	225	-	25+	-
170	-	220	-	20+
175	208	-	6.5	-
185	201	200	4	5
195	186	-	3.7	-
200	-	190	-	4
205	179		3.5	-
215	161	170	3	2.5

Table 7.1. Comparison of data gained from the present study with corresponding data from a previous study

The thermodynamic driving force for nucleation of any phase during the ageing process is quantified by the distance of the temperature from the respective solvus, as shown schematically in figure 7.11.

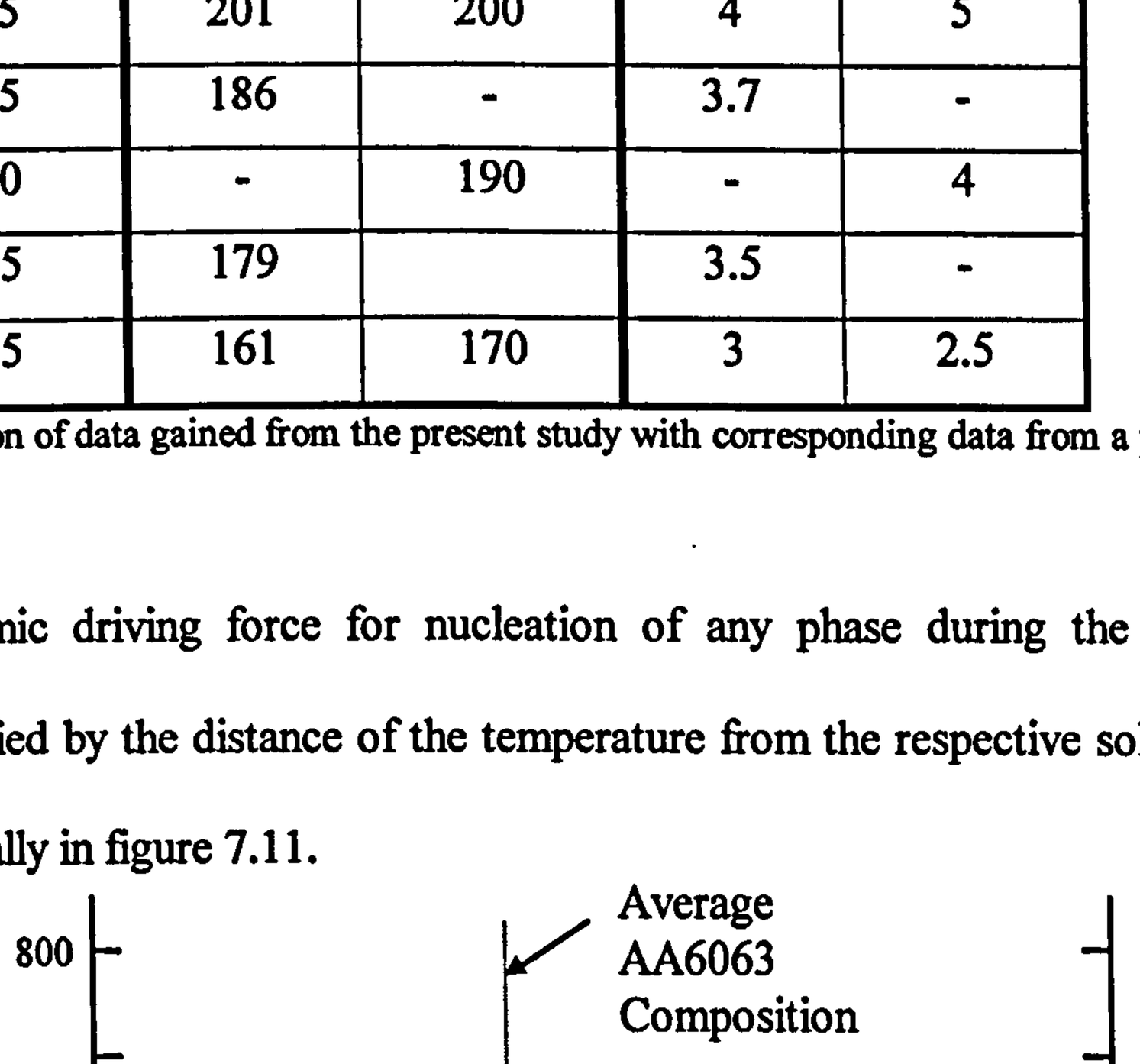

Figure 7.11. Psedo-binary phase diagram of the Al-Mg_2Si system, including the metastable solvuses, the positions of which were approximated based on the Al-Cu system[114]

As the ageing temperature increases the driving force for the nucleation of the β″ (or β′) phase is reduced and thus it forms a coarser dispersion than it would at lower temperatures. This makes it easier for the mobile dislocations in the matrix to bow around the particles. Also the potential maximum volume fraction of the β″/β′ would decrease. Both these factors cause the peak hardness of the alloy to decrease [114]. However, the higher temperature causes an increase in the rate of diffusion. Consequently heterogeneous nucleation of the hardening phase is achieved faster, leading to the peak being achieved at shorter ageing times.

7.2. Effects of Pre-strain on the ageing characteristics of AA6063

A significant number of samples were aged after they had been cold worked by means of rolling. For these experiments, the samples were solutionised at 525 °C and the ageing temperature was a constant 195 °C. The rolling took place immediately before the samples were placed in the ageing furnace. All other parameters were kept constant as before. The ageing curves of samples pre-strained to 5 and 10 % are compared to that of samples which underwent no pre-strain in figure 7.12. In an industrial extrusion environment profiles are subjected to tensile straining before they are aged. Previous studies on cold working before ageing turned out contrasting results. It has been suggested that cold working enhances the age hardenable properties [116-117, 155-156], but also that it accelerates ageing while reducing the age hardening characteristics [5]. A similar method of cold working was used in a previous study [157] and was found to accelerate metastable precipitate growth by providing a dislocation sub structure which aided nucleation of the particles. From these results it may be inferred that pre-straining has differing effects for different alloys.

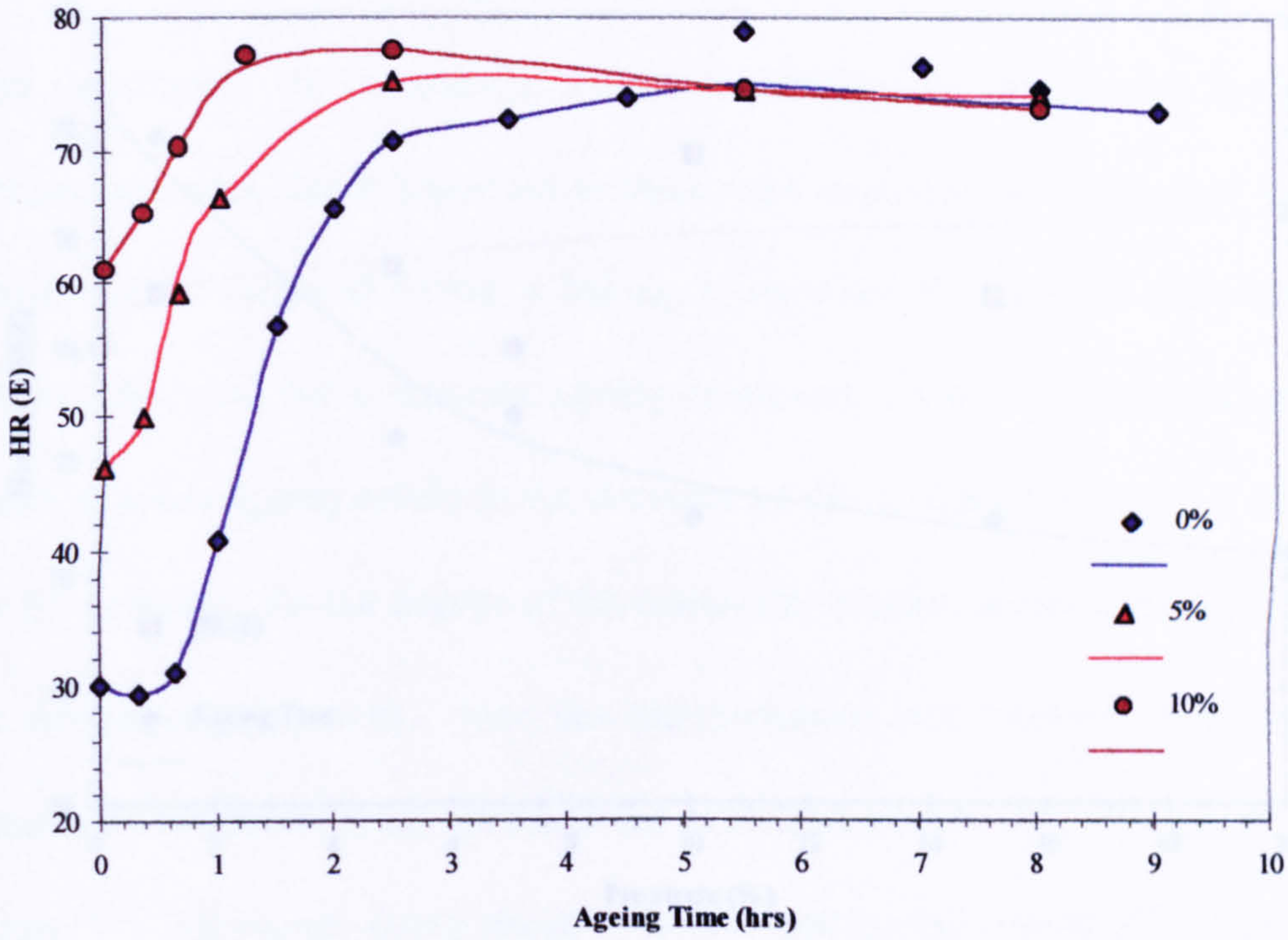

Figure 7.12. Comparative ageing curves of samples pre-strained to 0, 5 and 10 %.

The immediate reaction is that the initial hardness of the alloy increases with working. This is obviously due to the increased dislocation density induced by the rolling. Another point, which is seen in the curves above, is the absence of the 'dip' in the pre-strained samples. As was mentioned above the reason for the presence of the 'dip' is the dissolution of the GP zones and the subsequent formation of the β″ particles. Where pre-straining has been applied, the β″ particles form on the masses of dislocations which are present in the matrix and do not have to wait for the dissolution of the zones.

The relative position of the peaks in the pre-strained samples can be seen in figure 7.13.

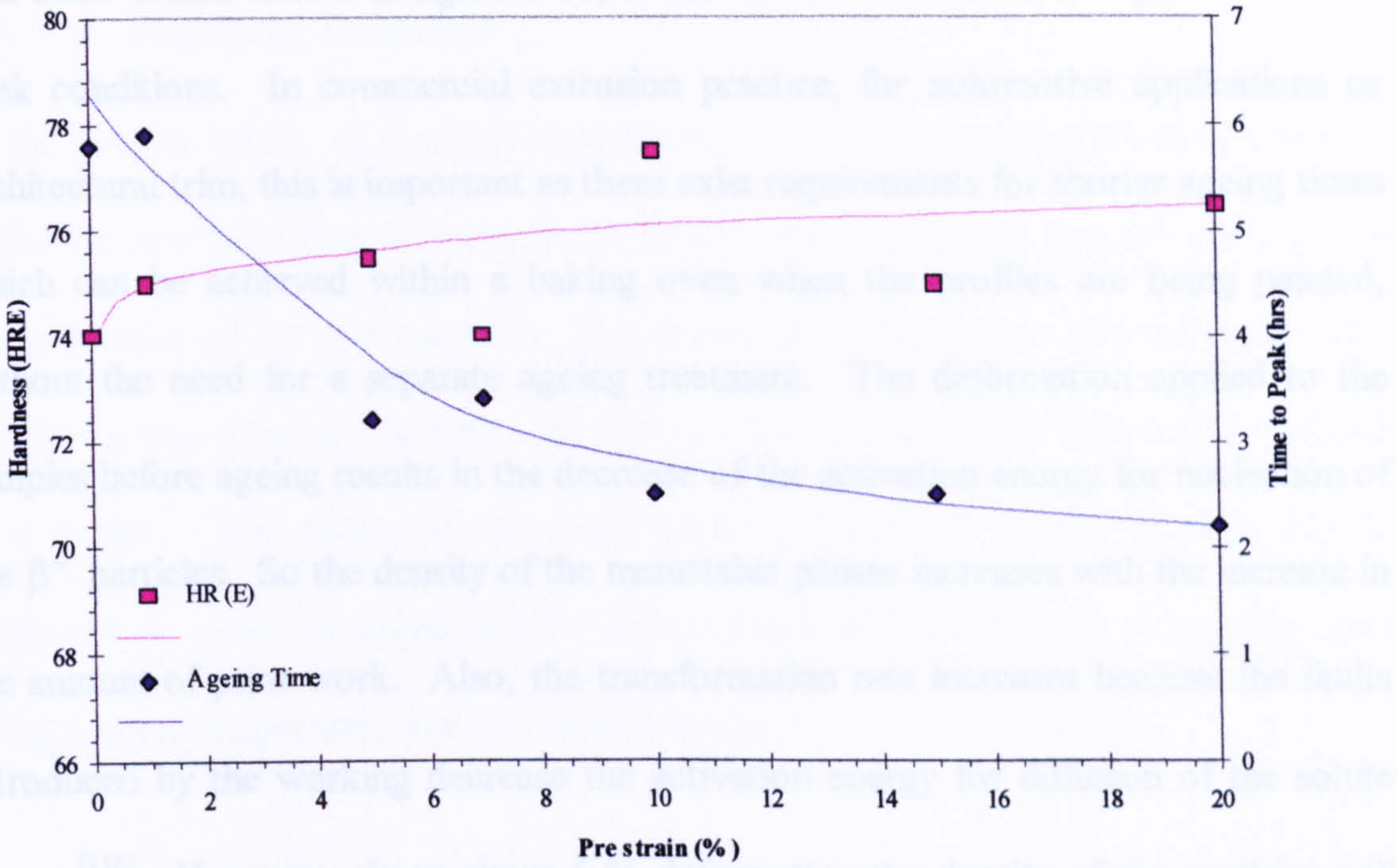

Figure 7.13. Peak magnitudes and time to reach peak conditions for the pre-strained samples.

Observing the phenomena presented in figure 7.13, it is proposed that an increase in the magnitude of the peak is observed with pre-strain of the samples. The increase in peak magnitude with pre-straining was also noted in a recent study by Zhen and Kang [116]. The increase in hardness seen in figure 7.13 could be due to one or both of the following reasons: (a) The increase in dislocation density induced by the rolling and (b) An increase in the precipitation strength because of the increased β″ density which resulted from the larger number of available nucleation sites (dislocations). Previous studies [116-117, 155] have suggested that the natural ageing process, which precedes the ageing, causes the formation of clusters of solute atoms with the aid of quenched in vacancies. This clustering effect - essentially the formation of GP zones - is affected by the cold working of the alloy, so the increase in strength can not only be attributed to one of the factors mentioned above but is a result of the combination of the two.

The other effect, shown in figure 7.13, is the decrease of the time required to reach peak conditions. In commercial extrusion practice, for automotive applications or architectural trim, this is important as there exist requirements for shorter ageing times which can be achieved within a baking oven when the profiles are being painted, without the need for a separate ageing treatment. The deformation applied to the samples before ageing results in the decrease of the activation energy for nucleation of the β″ particles. So the density of the metastable phases increases with the increase in the amount of prior work. Also, the transformation rate increases because the faults introduced by the working decrease the activation energy for diffusion of the solute atoms [116]. However, above about 5 % deformation the density of the particles will begin to decrease because their coarsening rate also increases. Thus, it is seen that for large amounts of deformation, both the peak hardness and the time required to reach the peak become nearly constant.

The hardness results shown above should, however, be viewed with some caution, as it is possible that the deformation applied by the rolling process is restricted to the surface layers of the samples and the hardness readings are not representative of the overall harness because the indentations applied by the Rockwell Hardness tester are only surface deep. This was another reason why Rockwell was preferred to Vickers hardness testing: Rockwell applied a much deeper indentation (using a far larger load).

7.3. Two-stage heat Treatment

In the present study, as well as studying the conventional ageing characteristics of PERAl, a new technique was developed to accelerate the ageing process and improve the properties of the said material. This technique, is termed accelerated ageing and involves a two-stage ageing cycle, the first at a low ageing temperature and the second at a higher. The details of the experimental process are shown in table A.2 in Appendix A. This treatment resulted in a strength higher than that of an alloy aged using a single temperature in a far shorter time, as shown in figure 7.14.

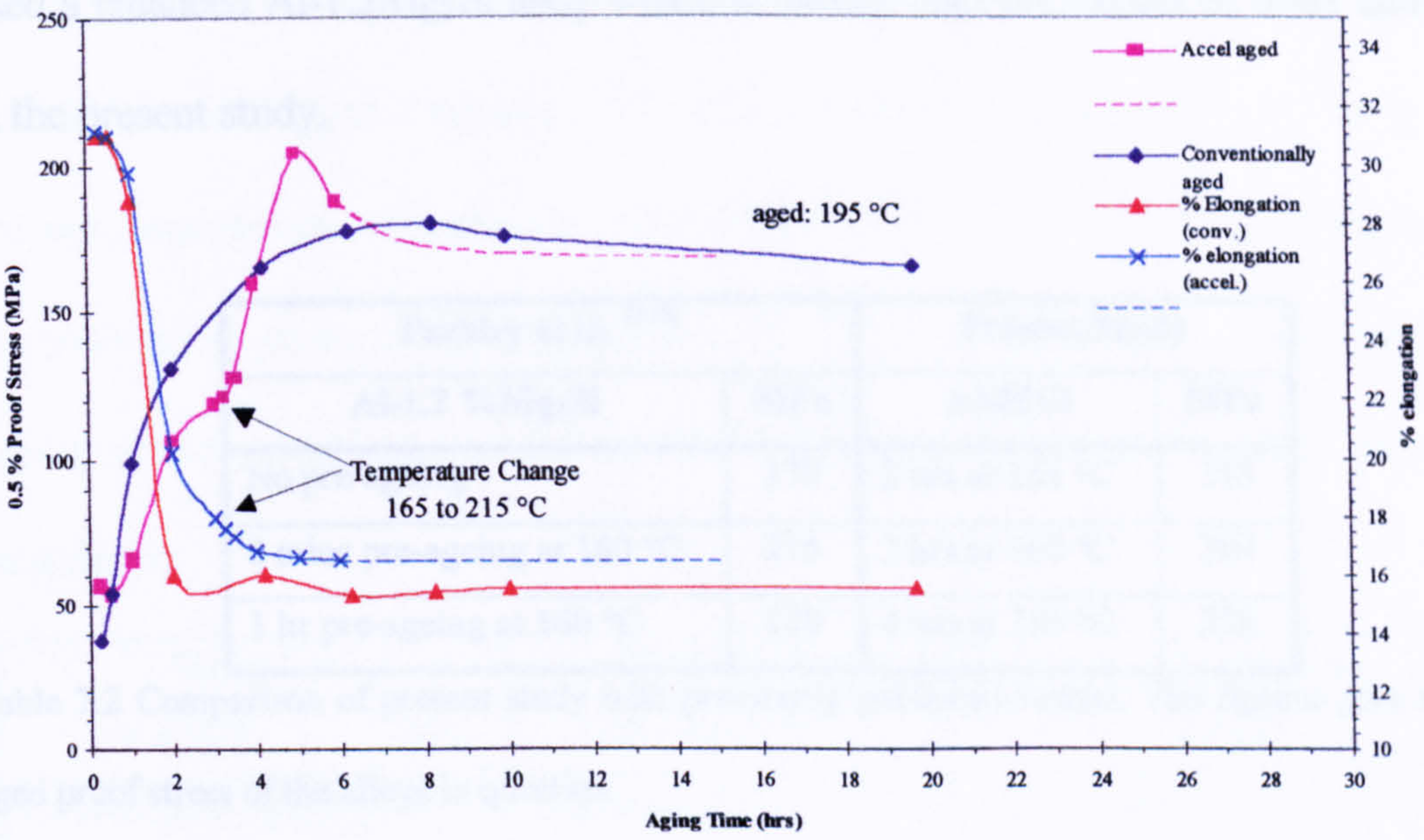

Figure 7.14. Comparison of the ageing characteristics of the conventional and the accelerated ageing processes. Both alloys were solutionised at 520 °C

Notice that the conventionally aged alloy reaches its peak some three hours later than the other. Of course, using accelerated ageing greatly decreases the margin for error involved in the timing of the removal of the profiles from the ageing furnace. There only exists a window of around 20 minutes during which the alloys have peak strength.

Delay, or premature removal could prove costly to the alloy properties. This is to be expected, as the transformation kinetics are enhanced at the higher 215 °C, due to the increased rate of diffusion.

A step ageing process, first suggested by Pashley et al.[115], can be construed to be similar to the process used in the present study. This involved the pre-ageing of a sample at the intended ageing temperature (160 °C) immediately after solutionising, storing for given period and then ageing as normal. The results of the two studies are shown in table 7.2 along with corresponding results in the present study. The workers used a balanced Al-1.2Mg_2Si alloy which is harder than the excess Si 6063 alloy used in the present study.

Pashley et al. [115]		Present Study	
Al-1.2 %Mg_2Si	MPa	AA6063	MPa
No pre-ageing	170	2 hrs at 165 °C	195
8 mins pre-ageing at 160 °C	216	3 hrs at 165 °C	204
1 hr pre-ageing at 160 °C	230	4 hrs at 165 °C	208

Table 7.2 Comparison of present study with previously published results. The figures give the peak aged proof stress of the alloys in question.

The data presented in table 7.2 points to the fact that both processes can result in an increase in the mechanical properties of alloys compared to conventional ageing. The increase in strength given by pre-ageing is based on an increase in the solute clusters which are nucleated during the three day storage period thus giving rise to an increase in the nucleation sites available for β″ and β′ precipitates during the ageing process itself. The higher strengths observed compared to the present study are due to the

more concentrated alloy (more Mg and Si available to form the metastable precipitates) and the lower ageing temperature selected by the workers. Step ageing is more common for 7xxx series alloys – mainly to improve corrosion resistance – but benefits are also observed in mechanical properties. The process was studied by Fridlyander et al. [118, 158] on the Russian alloy V95 (AA7075). The ageing treatment consisted of 3 hours at 120 °C followed by a prolonged treatment at 175 °C. In this case the AlMgZnCu alloy is shown to perform far better than conventional ageing if an ageing treatment using two temperatures is applied. Table 7.3 compares the yield strength values stated by Hatch [159] with those observed by Fridlyander [118] and the trend presented in the present study. Hatch [159] states that a step ageing program (for AA7075) consisting of 4 hours at 100 °C followed by 8 hours at 160 °C can result in the same amount of strengthening as 24 hours at 120 °C. It is important to note that the pre-ageing process employed previously [115] is not the same as the accelerated ageing process employed in the present study as will be explained in subsequent paragraphs.

Hatch [159]		**Fridlyander et al.**		**Present Study**	
AA7075	**MPa**	**V95 (AA7075)**	**MPa**	**AA6063**	**MPa**
Conventional ageing (120 °C)	490	Conventional ageing (120 °C) [158]	470	Conventional ageing (195 °C)	186
Conventional ageing (135 °C)	470	Conventional ageing (160 °C) [158]	350	2 hrs at 165 °C	195
Conventional ageing (160 °C)	460	Conventional ageing (200 °C) [158]	260	3 hrs at 165 °C	204
Step Ageing	475	Step Ageing [118]	490	4 hrs at 165 °C	208

Table 7.3 Comparison of present study with previously published results. The figures give the peak aged proof stress of the alloys in question.

In certain cases (for 7xxx series alloys), if it is not feasible to use a two step treatment, the same result can be achieved if slow heating is employed. The slower heating rate allows the formation of a distribution of GP zones which is stable at higher temperatures, thus emulating the first step ageing conditions.

The theory behind the accelerated ageing process lies with the nucleation and growth rates of the particles involved in the process [160]. As has been mentioned before, the major hardening constituent in 6xxx series alloys is β′, which tends to nucleate heterogeneously in the matrix. However, precluding the formation of these, the GP zones must be formed. It is unlikely that the high coherency and the similarity in structure between the zones and the surrounding matrix leads to homogeneous nucleation, for GP zones, so these also form heterogeneously on sites such as vacancies, dislocations and stacking faults.

So, initially, a low temperature is employed to increase the nucleation rate of the zones. The nucleation rate is governed by the following equation [114]:

$$N^{\bullet} = \omega C_0 \exp\left(-\frac{\Delta H_m}{GT}\right)\exp\left(-\frac{\Delta H^{\bullet}}{GT}\right) \qquad (7.1)$$

where $N^{\bullet}$ is the nucleation rate in nuclei per m^3 per s, ω is a constant that includes atomic vibration frequency and critical nucleus size, C_0 quantifies the available nucleation sites, ΔH_m is the activation energy for atomic migration, T is the absolute temperature and G=8.314 kJ/mol/K is the gas constant. $\Delta H^{\bullet}$ is the free energy associated with the formation of a stable nucleus and can be calculated as follows:

$$\Delta H^{*} = \frac{16\pi\gamma^{3}}{3(\Delta H_{v} - \Delta H_{\varepsilon})^{2}} \qquad (7.2)$$

where γ is the surface energy of the nucleus, ΔH_v and ΔH_ε are the volume free energy and the misfit strain free energies respectively. The volume free energy, for dilute alloys, (such as the one that was used in the present study) can be approximated by:

$$\Delta H_{v} \propto \Delta X_{0} \qquad (7.3)$$

$$\Delta X_{0} = X_{0} - X_{e}$$

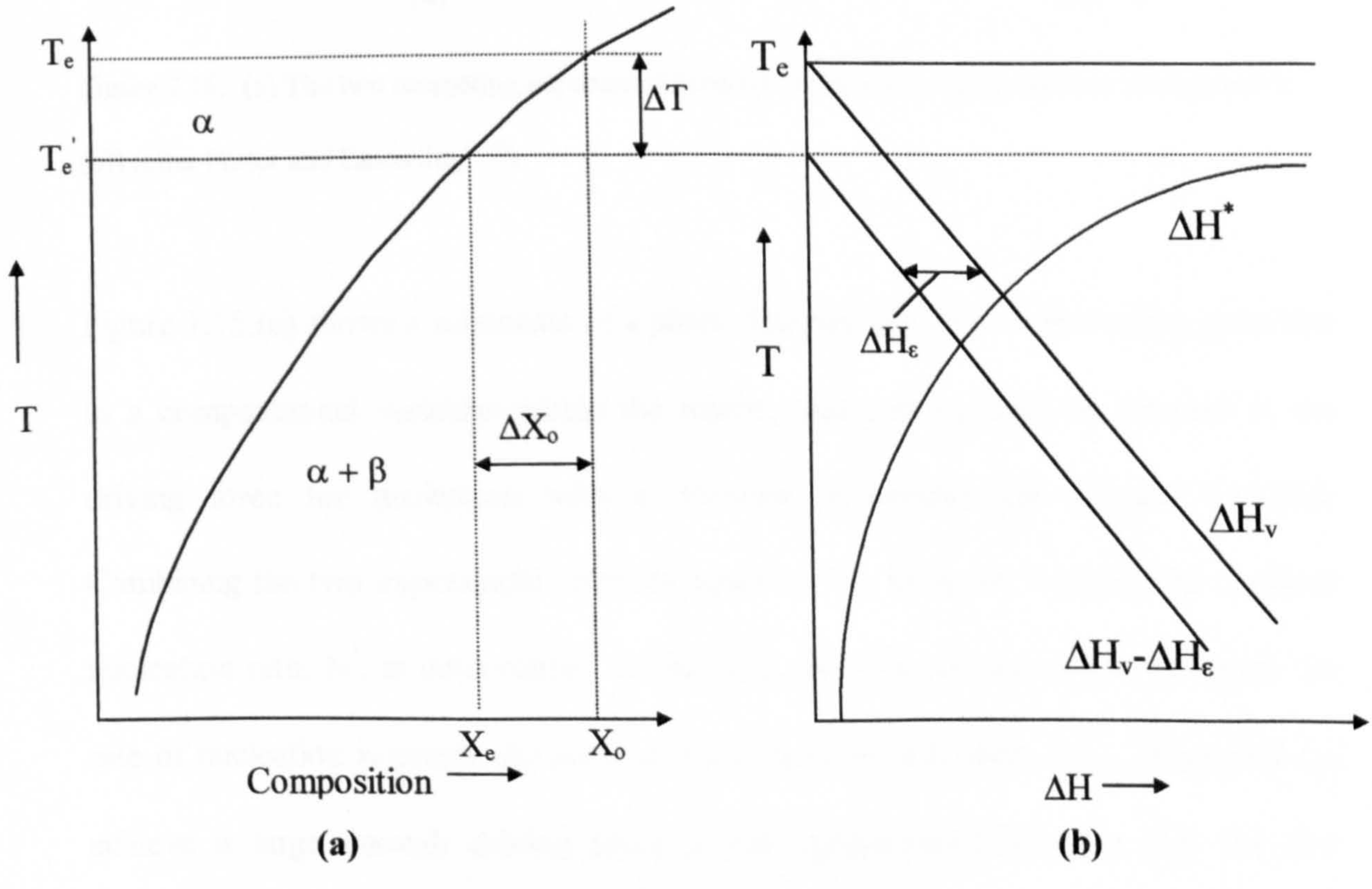

Figure 7.15. (a) Phase field annotation, (b) Variation of the volume free energy and generation of a pseudo-equilibrium temperature due to the misfit strain energy. (after Porter and Easterling [114])

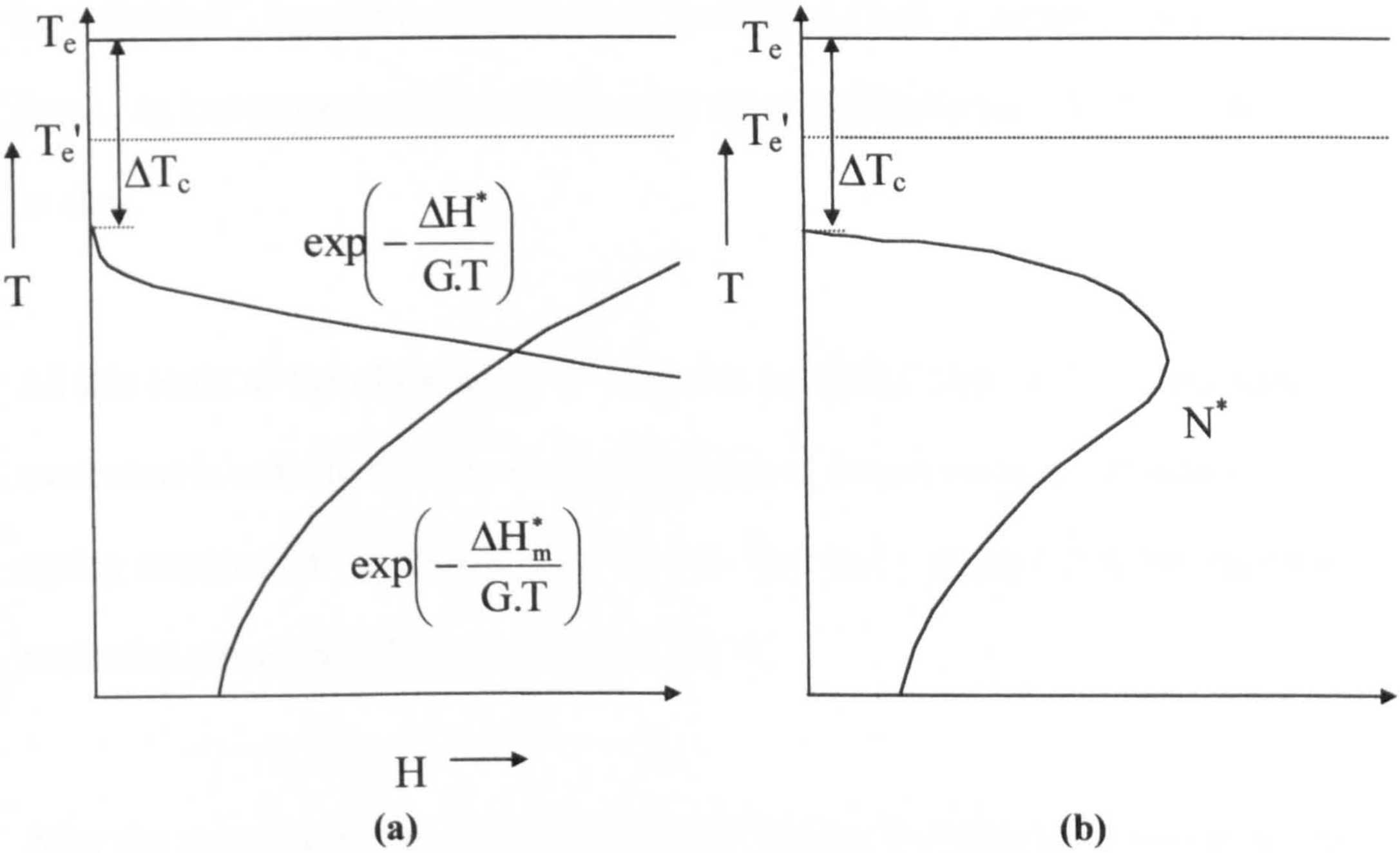

Figure 7.16. (a) The two competing exponential terms that determine the nucleation rate (shown in (b)) (after Porter and Easterling[114])

Figure 7.15.(a) shows a schematic of a phase diagram and how undercooling gives rise to a compositional variation within the matrix, and consequently an increase in the driving force for nucleation with a decrease in temperature (Figure 7.15.(b)). Combining the two exponential terms of equation 7.1, in figure 7.16.(a), the resultant nucleation rate, N^*, is determined. Notice that, as with nucleation from a liquid, the rate of nucleation is practically zero until a critical undercooling, ΔT_c, is reached (to achieve a large enough driving force in the supersaturation); after that the first exponential term, $\exp\left(-\Delta H^*/GT\right)$ – which essentially is the potential concentration of nuclei – rises rapidly. The other exponential term quantifies the mobility of the atoms within the matrix. This rises with increasing temperature, as one would expect since the energy term, ΔH_m, is constant. Thus the resultant nucleation rate rises rapidly once the critical undercooling is reached (any undercooling less than the critical would result

in negligible $N^{\bullet}$, because the driving force would be so low), it reaches a peak and then drops. At low temperatures nucleation rates are negligible because the diffusion rate is so slow.

All this leads to the observation [160] that the nucleation rate of the zones must be maximised in order to optimise the ageing process. Experimental observations, of the ageing response of the PERAl alloy used in this study, suggest that the maximum nucleation rate of the GP zones is around 165 °C.

After the zones have been nucleated, the case remains that they must now grow into β″ and then β′ to complete the hardening cycle. This is achieved by elevating to a higher temperature. The reason for this is explained below, using particle growth thermodynamics [114]:

Growth of a particle is described by the following relationship:

$$\nu^{\bullet} = C\Delta X_0\sqrt{\frac{D}{t}} \qquad (7.4)$$

where $\nu^{\bullet}$ is the rate of growth of the precipitate, C is a constant, D is the self-diffusion coefficient, and ΔX_0 is the supersaturation of the alloy, as shown in figure 7.15.(a). Figure 7.17 shows the relative variation of the different parameters that give rise to $\nu^{\bullet}$, and the resultant growth rate.

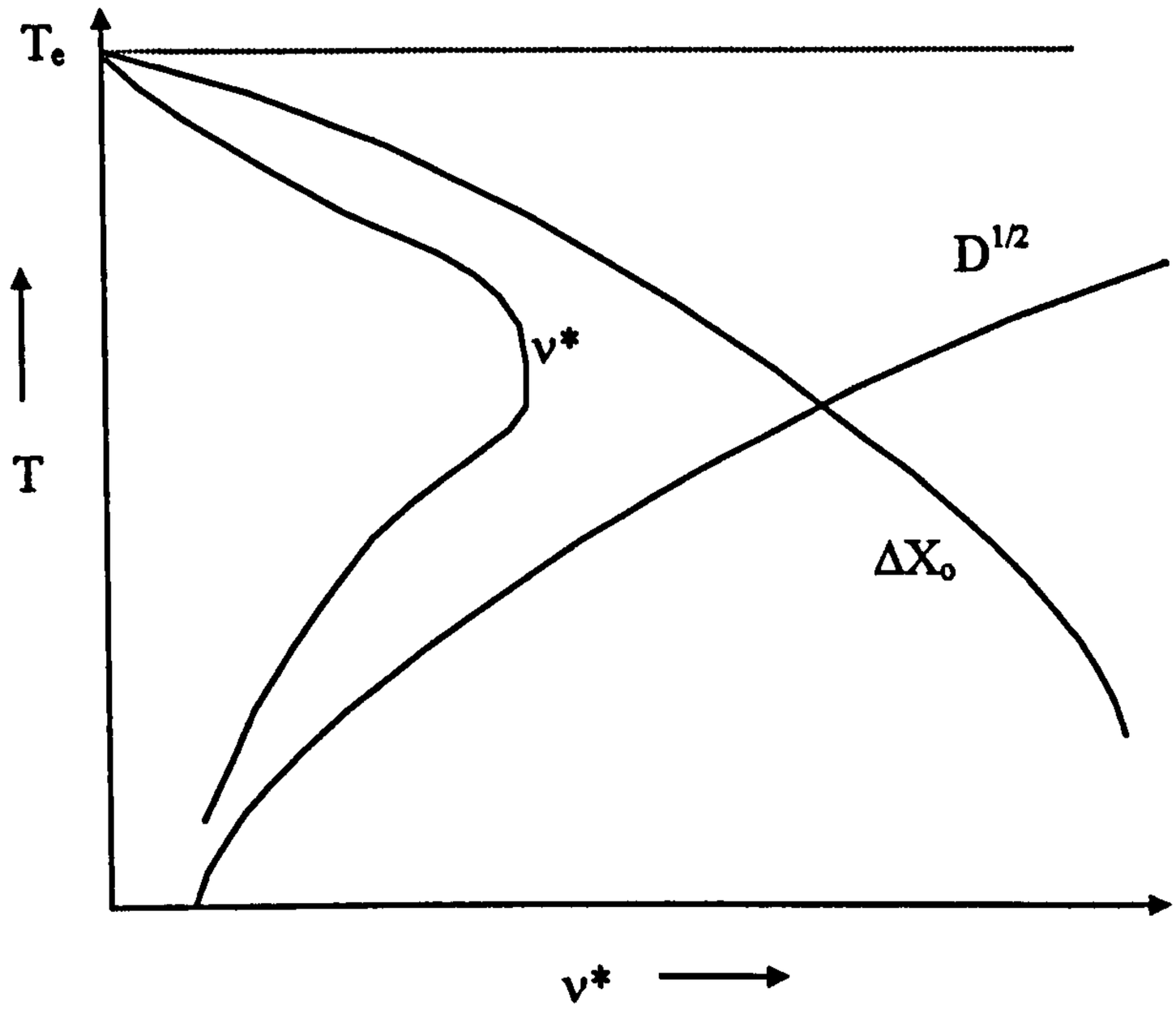

Figure 7.17. Determination of the growth rate of the precipitates.

As with the rate of nucleation, at low levels of undercooling $\nu^{\bullet}$ is small because the driving force for particle growth is small. Similarly, at high levels of undercooling, the growth rate is small because diffusion is slow. The maximum value of $\nu^{\bullet}$ lies between the two regions at some moderate level of undercooling. It is this temperature that must be found for the second part of the ageing process. The overall accelerated ageing process can be described as shown in figure 7.18. The difference from the pre-ageing process described elsewhere [115] is in the nature of the precipitate which is induced. The present study induces the rapid precipitation of the β′ particles, whereas the pre-ageing process causes the increase in the number of the GP zones which act as nucleation sites for the β′ particles.

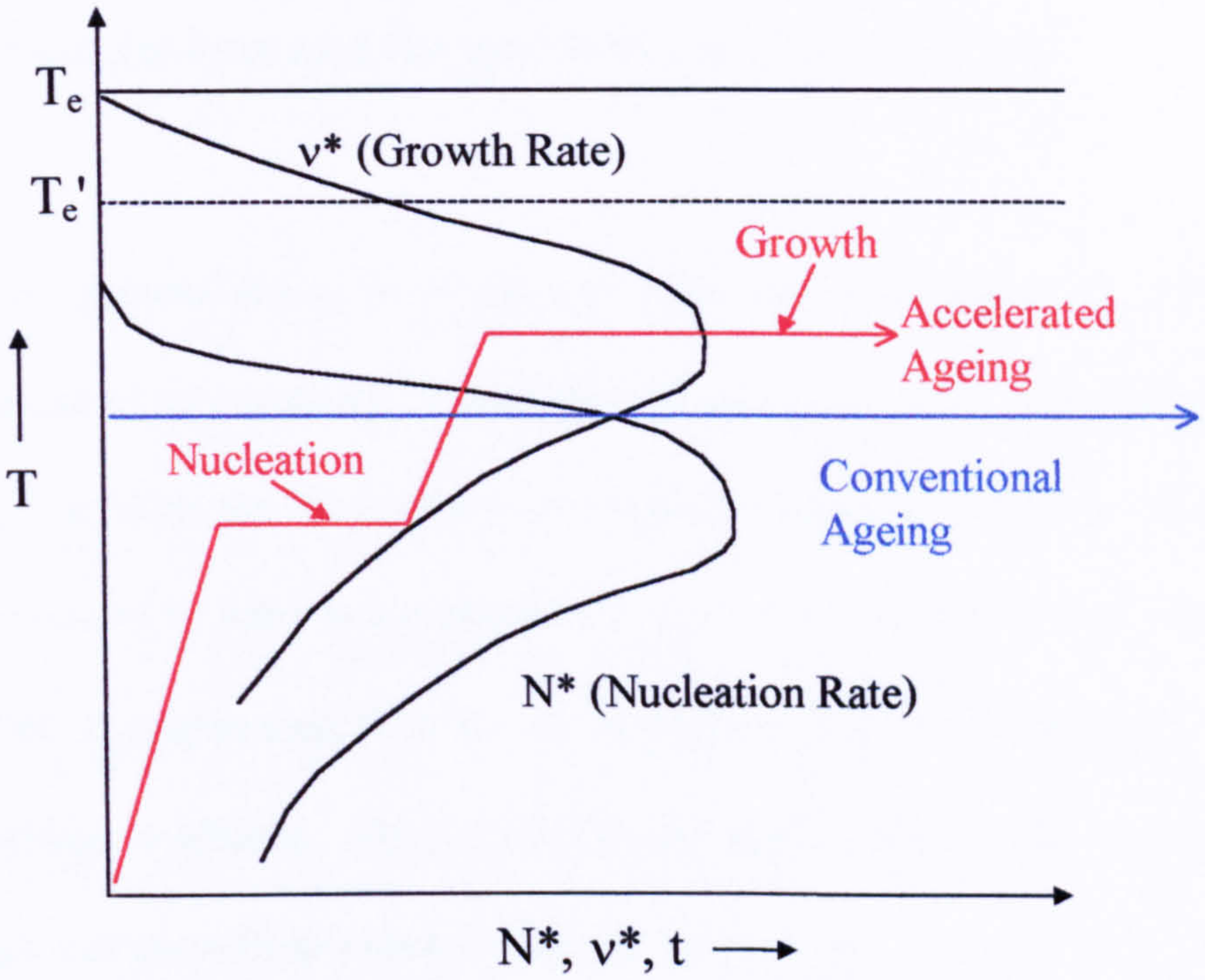

Figure 7.18. Nucleation and growth rates against temperature and comparison of the process involved in conventional (blue line) and accelerated (red line) ageing.

7.4 Conclusions: Comparison of conventional and accelerated ageing processes

The implementation of accelerated ageing on an industrial scale could spell the end to the bottleneck in the extrusion process, which has traditionally been ageing. With cleaner alloys, more powerful presses and better dies being introduced all the time to increase the speed of extrusion, the ageing process should also be improved to meet the increasing demands of the extruder and decrease the idle time of the press. Accelerated ageing has been implemented at an extrusion facility in the Midlands (BOAL UK) and was found to work just as well under industrial conditions, as it does in the laboratory.

Chapter 8

Conclusions and suggestions for further work

8. Conclusions and Suggestions for Further Work

In the present study, two-hole extrusion has been shown to provide an adequate measure of extrudability. A material will tend to extrude more through one hole - the one that offers the least resistance - as its extrudability increases. This is not, however, intended to be used as a replacement of the maximum extrusion velocity measure, but rather in conjunction with it. It determines relative extrudability of alloys without reaching conditions, which would compromise surface finish or overall productivity (high extrusion temperature or fast extrusion speed).

Subtle changes in alloying can have a profound effect on extrudability. Addition of small amounts of Fe can prove advantageous to slow speed extrusion, contrary to the present beliefs. However, at higher speeds, the extrudability will be limited by the surface finish of such alloys. AlFeSi particles adversely affect the surface finish and cause surface tearing. Local weakness at the Mg_2Si/Al matrix boundary causes tearing which will limit the speed at which Fe containing alloys can be extruded, because the AlFeSi particles provide nucleation sites for Mg_2Si precipitates.

Dynamic precipitation of the major hardening phase (Mg_2Si) has been proved to increase the pressure required to extrude the alloys, and should be avoided. Such precipitation is especially prominent in alloys with very little or no iron. The effects of dynamic precipitation are dependent on the amount of excess silicon present in the alloy. Higher Si contents result in less precipitation during extrusion.

Also excess Si was shown to stabilise the β-AlFeSi phase, which is detrimental to the extrusion properties of the alloy, by increasing the driving force for its formation.

After extrusion, static recrystallisation occurs in the extrudates. The most highly deformed regions of the extrudate, i.e. closest to the surface, showed the smallest grain size indicating that prior deformation is important in the development of the extrudate microstructure. Recrystallisation is also affected by the alloying content, or, more specifically, the Fe/Si ratio, of the alloy. The recrystallisation rate is accelerated by high Fe/Si ratios, and retarded by lower ones.

More work is required before this method can provide definitive extrudability calculations. To attain such a model, an extensive study must be carried out using a large number of dies. These dies should differ in hole size and die land length as well as in the distance between the holes. Hole area ratios of 16 or above should be used. It has been shown in the present study that smaller hole area ratios (dies 1 and 2) result in extrudate lengths which show only very subtle variations that cannot be distinguished from experimental error.

Due to the large number of compositional variations used in the present study, it was not possible to minimise the scatter in the results. It is recommended if similar studies are carried out in the future, numerous tests are conducted using identical extrusion parameters in order to minimise the possible errors. Also to assess the process, the alloys used should be commercial and not custom so as a comparison can be made to the existing extrudability tables. It is also a good idea to used choked dies in order to be sure that the whole die land is being utilised.

Ideally, extrudability should be defined by a weighting system from a matrix of parameters, such as surface finish and extrusion velocity, which an extruder can apply, given the requirements of the customer, to give the conditions that should be used for the alloy.

In the present study, a two-step artificial ageing program was developed which was proved, through laboratory experiments, to perform better than the existing single temperature one. The program is based on using a low temperature first to induce a high nucleation rate, followed by a higher temperature to give a high growth rate of the metastable precipitates.

Although this process is now being used in an industrial plant, further research could be performed in order to ascertain the exact temperatures at which the maximum precipitate nucleation and growth rates are effected.

Chapter 9

References

9. References

1. Gooding, K. 'Aluminium', *Financial Times* '*Survey*', 22nd Oct.1997
2. Dick, G. Alexander, Patentschrift No. 83388 Klasse 49: Mechanische Metallbearbeitung, 1895
3. Emley, E. F., *Int. Met. Rev.*, vol. 21, p.75, 1976
4. Campbell, J., 'Castings', Pub: Butterworth Heinmann, Oxford, 1991
5. Mondolfo, L.F. 'Aluminium: Structure and Properties', Pub: Butterworth, 1976
6. Philips, H. W. L., *J.I.M.*, vol. 72, pp. 151-227, 1946
7. Beatty, E. C., *Proc. 2nd Int Al Ext Tech Sem*, Aluminium Association, Washington, vol. 1, pp. 225-228, 1977
8. Reiso, O., *Proc. 4th Int Al Ext Tech Sem*, Aluminium Association, Washington, vol 1, pp.287-295, 1988
9. Agrawal, B. K.; Singh, J. P., *Proc. 4th Int Al Ext Tech Sem*, Aluminium Association, Washington, vol. 2, pp. 395-401, 1988
10. Reiso, O., *Proc. 3rd Int Al Ext Tech Sem*, Aluminium Association, Washington, vol 1, pp. 31-40, 1984
11. Clode, M. P., Sheppard, T., *Mat. Sci & Tech.*, vol 6, pp. 755-763, 1990
12. Markides, C. A., MSc. Project, University of London, 1994
13. Deiter, E. G., 'Mechanical Metallurgy', 2nd Ed., Pub: McGraw-Hill, 1988
14. Shewmon, P. G., 'Transformations in Metals', p.41, Pub: McGraw-Hill, New York, 1969
15. Langerwerger, J., *'Aluminium Technology'*, Ed: T. Sheppard, Inst. Metals, London, pp.216-222, 1986
16. Traenkner, F. O., *Proc. 2nd Int Al Ext Tech Sem*, Aluminium Association, Washington, vol. 1, pp. 339-347, 1977
17. Scharf, G.; Grzemba, B., *Proc. 3rd Int Al Ext Tech Sem*, Aluminium Association, Washington, vol 1, pp. 47-52, 1984
18. Scharf, G., *Metallkde.*, vol. 55(12), pp.740-744, 1964
19. Pashley, D. W.; Jacobs, M. H.; Vietz, J. T., *Phil. Mag.*, vol 16, p. 51, 1967
20. Gullotti, D. B.; Crane, J.; Setzer, W. C., *Proc. 2nd Int Al Ext Tech Sem*, Aluminium Association, Washington, vol. 1, pp.249-256, 1977
21. Mondolfo, L. F.; Peel, A. R., *Proc. 2nd Int Al Ext Tech Sem*, Aluminium Association, Washington, vol. 1, pp. 323-330, 1977
22. Hains, R. W., *Proc. 3rd Int Al Ext Tech Sem*, Aluminium Association, Washington, vol 1, pp. 81-88, 1984
23. Gjestland, H.; Dons, A. L.; Lohne, O.; Reiso, O, Proc. conf. *'Al alloys: their physical and mechanical properties'*, Charlottesville, VA, USA, vol. 1, pp. 359-370, 1986
24. Kaneko, J.; Sultan, M. M.; Horiuchi, R. Z., *Metallkde*, vol. 67. pp.8-10, 1976
25. Marchive, D., *Aluminium Review*, vol 12, pp. 437-446, 1980

26. Akeret, R. Z., *Metallkde*, vol. 61. pp.3-10, 1970

27. Evangelista, E.; Gabrielli, F.; Mengucci, P.; Quadrini, E., *'Strength of Metals and Alloys'*, ICSMA 8, Ed: Kepttunen, P. et al., Pub: Pergamon Press, Oxford, vol. 2, pp. 977-982, 1988

28. Evangelista, E.; Forcellese, A.; Gabrielli, F.; Mengucci, P., *'Hot Deformation of Al alloys'*, Ed: Langdon, T. G. et al, TMS-AIME, Warrendale, PA, pp. 121-129, 1991

29. Evangelista, E.; Gabrielli, F.; Mengucci, P.; Quadrini, E.; Argioni, G., *'Innovation for Quality'*, Italian Assoc. Met., Milan, pp. 205-214, 1988

30. McQueen, H.J.; Xia, X.; Sakaris, P.; Meng, O.; Cui, Y.; Li, B., *Report No. 307*, Mech. Eng., Concordia University, 1996

31. Sakaris, P., McQueen, H. J.; Meng, O.; Cui, Y.; Li, B.; *'Advances in Production and Fabrication of Light Metals'*, Ed: Avedesian, M. M. et al., CIM, Montreal, pp. 605-617, 1992

32. Sakaris, P., McQueen, H. J., *'Aluminium alloys: their Physical and Mechanical Properties'*, ICAA3, Ed: Arnberg, L. et al., Trondheim, Norway, vol.2, pp. 276-281, 1992

33. Akeret, A.; Kunzli, A. Z., *Metallkde*, vol. 57, pp.789-792, 1966

34. Barry, W. J.; Heins, R. W.; *Proc. 2nd Int Al Ext Tech Sem*, Aluminium Association, Washington, vol. 1, pp. 271-284, 1977

35. Evans, D. W.; Autcote, J., *Proc. 3rd Int Al Ext Tech Sem*, Aluminium Association, Washington, vol. 1, pp. 53-62, 1984

36. Langerwerger, J., *Proc. 3rd Int Al Ext Tech Sem*, Aluminium Association, Washington, vol. 1, pp. 41-45, 1984.

37. Langerwerger, J., *Proc. 4th Int Al Ext Tech Sem*, Aluminium Association, Washington, vol. 2, pp. 381-384, 1988

38. Sperry, P. R., *Proc. 3rd Int Al Ext Tech Sem*, Aluminium Association, Washington, vol. 1, p. 21, 1984

39. Zajac, S.; Hutchinson, B.; Johanson, A.; Gullman, L. O., Mat Sci. & Tech., vol. 10(4), pp. 323-333, 1994

40. Gullman, L. O.; Zajac, S.; Johanson, A., *Proc. 5th Int Al Ext Tech Sem*, Aluminium Association, Washington, vol. 1, pp. 71-77, 1992

41. Thanabonsumbut, B.; Sanders, B., *'Aluminium alloys: their Physical and Mechanical Properties'*, ICAA4, Ed: Sanders, T.; Starke, E., Atlanta, GA, vol. 3, pp. 197-205, 1994

42. Maitland, A.; Ried, A., *Proc. 2nd Int Al Ext Tech Sem*, Aluminium Association, Washington, vol. 1, pp. 297-300, 1977

43. Barry, W. G.; *Proc. 3rd Int Al Ext Tech Sem*, Aluminium Association, vol. 1, p. 7, 1984

44. Ohori, K. Takeuchi, Y; Matsuyama, H., *Proc. 3rd Int Al Ext Tech Sem*, Aluminium Association, Washington, vol. 1, pp. 63-67, 1984

45. Walters, R. V.; Franz, E. C., *Proc. 3rd Int Al Ext Tech Sem*, Aluminium Association, Washington, vol. 1, p. 75, 1984

46. Lang, G. Castle, A. F., *Proc. 2nd Int Al Ext Tech Sem*, Aluminium Association, Washington, vol. 1, pp. 293-296, 1977

47. Dimayuga, F. C.; Mulazimoglu, H.; Closset, B.; Gruzleski, I., *Proc. 5th Int Al Ext Tech Sem*, Aluminium Association, Washington, vol. 1, pp. 519-528, 1992

48. Sanders, R. E., *Proc. Int. Conf. on 'Aluminium alloys: Physical and Mechanical Properties'*, Charlottesville, VA, Engineering materials Advisory Service, Warley, U.K. (1941), 1986

49. Perlitz, H., *Nature*, Vol. 154, p. 606, 1944

50. Sampson, S., *Acta Crystallog.*, vol. 19, p. 41, 1965

51. Hultgren, R.; Desai, P. D.; Hawkins, D. T.; Gleiser, M., Kelly, K. K., 'Selected Values of Thermodynamic Properties of Binary Alloys', ASM, Metals Park, Ohio, 1973

52. Novotny, H.; Komark, K.; Kramer, J.; Berg, U., *Hüttenmänn Monatsh Montan Hochschule Leoben*, vol. 96, pp. 161-169, 1951

53. Phragmén, *J. I. M.*, vol. 77, pp. 489-552, 1953

54. Nedreberg, M. L.; Andersson, B., *'Aluminium alloys: their Physical and Mechanical Properties'*, ICAA3, Ed: Arnberg, L. et al., Trondheim, Norway, vol.2, pp. 55-60, 1992

55. Robinson, K; Black, P. J.; *Phil. Mag.*, vol. 44, pp. 1392-1397, 1953

56. Perlitz, H.; Westgren, A., *Arkiv. Kemi.*, Min. Geol., vol 15(B), p. 16, 1942

57. Sheppard, T., *Proc. 2nd Int Al Ext Tech Sem*, Aluminium Association, Washington, vol. 1, pp. 331-337, 1977

58. Feltham, P., *Metals Treatment and Drop Forging*, vol. 23, p.440-444, 1956

59. Sheppard, T.; Patterson, S. J., *J. Mech. Working*, vol. 7, pp. 39-56, 1982

60. Alexander, J. M., *J.I.M.*, Vol. 90, pp. 193-200, 1961-2

61. Vierod, R. P., PhD Thesis, University of London, 1983

62. Castle, A. F.; Sheppard, T., *Met. Tech.*, vol. 3, pp. 465-475, 1976

63. Clode, M. P., PhD. Thesis, University of London, 1987

64. Lauè, K.; Stenger, H., 'Extrusion: Processes, Machinery, Tooling', Am. Soc. for Metals, Metals Park, Ohio, 1981

65. Sheppard, T., *Met. Tech*, Vol. 8, pp. 130-141, 1981

66. Sheppard, T., Proc. 8th Light Metals Congress, Ed: Jeglitsch, J et al., the University, Leoben, pp. 301-311, 1987

67 Sheppard, T.; Wood, E. P., *Met. Tech*, Vol. 7, pp. 58-66, 1980

68. Wilson, W. R. D., *Int. J. Mech. Sci.*, vol. 13, p.17, 1971

69. Ziegler, W.; Siegert, K., *Z. Metallkde*, vol. 64, p. 224, 1973

70. Ashcroft, K.; Lawson, D., *J.I.M.*, vol. 89, p.369, 1960

71. Farag, M. M.; Sellars, C. M., *J.I.M.*, vol. 101, pp. 137-145, 1973

72. Avitzur, B., 'Metal Forming Process and Analysis', Pub: McGraw-Hill, New York, 1968

73. Dodeja, L. C.; Johnson, W., *J. Mech. Phys. Solids*, vol. 5, pp.267-281, 1957

74. Hirst, S.; Ursell, D. H., *Met. Treatment and Drop Forging*, vol. 25, pp. 409- 416, 1958

75. Tutcher, M. G., PhD. Thesis, University of London, 1979

76. Tutcher, M. G.; Sheppard, T, *Met. Tech.*, vol 7, pp.488-493, 1980

77. Chandra, T; Jonas J. J., *Met. Trans.* vol 2, pp.877-881, 1971

78 Clode, M. P.; Sheppard, T., *Mat. Sci & Tech.*, vol 9, pp.313-318, 1993

79 Scharf, G; Lossack, E, *Proc. 2nd Int Al Ext Tech Sem*, Aluminium Association, Washington, vol. 1, pp. 311-320, 1977

80 Musulin, I; Dietz, D.; *Proc. 5th Int Al Ext Tech Sem*, Aluminium Association, Washington, vol. 1, pp. 25-33, 1992

81. Reed-Hill, R. E., 'Physical Metallurgy Principles', 2nd Ed., Pub: PWS Engineering, Boston, 1973

82 Faunce, J. P.; Watts, J. M., *Proc. 4th Int Al Ext Tech Sem*, Aluminium Association, Washington, vol. 1, pp. 165-171, 1988

83. Ricks, R. A.; Parson, N. C.; Yiu, H. C.; Court, S. A., ., *Proc. 5th Int Al Ext Tech Sem*, Aluminium Association, Washington, vol. 1, pp. 57-69, 1992

84. Bondarev, B. I.; Davydov, V. G.; Zakharov, V. V., *Proc. 3rd Int Al Ext Tech Sem*, Aluminium Association, Washington, vol. 1, pp. 495-501, 1984

85. Laue, K., *Z. Metallkde*, vol. 54, p.667, 1963

86. Sheppard, T., 'Extrusion of Aluminium Alloys', Kluwer Academic Publishers, London, 1999

87. Mondolfo, L. F.; Peel, A. R.; Marcantonio, J. A., *Met. Tech.*, vol. 2, p. 433, 1975

88. Keife, H., *J. Mat. Processing Tech.*, vol. 37, pp. 189-202, 1993

89. Keife, H., *J. Mat. Processing Tech.*, vol. 36, pp. 321-331, 1993

90. McQueen, H. J.; Jonas, J. J., 'Metal Forming: Interrelation Between Theory and Practice', Ed: Hoffman, A., Pub: Plenum Press, New York, pp. 393-428, 1971

91. Sheppard T.; Wright, D. S., *Met. Tech.*, vol. 6, pp. 215-223, 1979

92. Sheppard, T.; Wright D. S., *Met. Tech.*, vol. 6, pp. 224-229, 1979

93. McQueen H. J.; Celliers, O., *Materials Forum*, vol. 17, pp. 1-13, 1993

94. Teggart, W. J. McG., Seminar for Ductility, ASM, 1967

95. Jonas, J. J.; Cellars, C. M.; Teggart, W. J. McG., *Int. Met. Rev.*, vol. 14, p. 1, 1969

96. Cellars, C. M.; Teggart, W. J. McG., *Int. Met. Rev.*, vol. 17, p. 1, 1972

97. Philips, V. A.; Adler, J. F., *J.I.M.*, vol. 83, pp. 80-86, 1954-1955

98. Buhler, H.; Wagener, H. W., *Z. Metallkde*, vol. 57, p.825, 1966 (in German)

99. Buhler, H.; Wagener, H. W., *Z. Metallkde*, vol. 58, p. 136, 1967 (in German)

100. Wong, W. A.; Jonas, J. J., *Trans Met Soc. AIME*, vol. 242, pp. 2271-2280, 1968

101. Zhou, M.; Clode, M. P., Internal Report, TIEPERA, KCL08, 1997

102. Shi, H., McLaren, A. J.; Cellars, C. M.; Shahani, R.; Bolingbroke, R., *MST*, vol. 13(3), pp. 210-216, 1997

103. McQueen H. J., *J. O. M.*, vol. 32(2), p.17, 1980

104. McQueen, H. J.; Wong, W. A.; Jonas, J. J., *Can. J. Phys.*, vol. 45, pp. 1225-1234, 1967

105. Cockcroft, M. G.; Latham, D. H., *J. Inst. Met.*, vol. 96, pp.33-39, 1968

106. Hull, D.; Bacon, D. J., 'Introduction to dislocations', Pub: Pergamon Press, 3rd Ed., 1984

107. Gay, P.; Hirsh, P. B.; Kelly, A., *Acta Crystallog.*, vol. 7, p. 41,. 1951

108. Sheppard, T., Personal Communication, 1997

109. Guinier, A.; Lambot, H., *Compt. Rend.*, vol. 227, p.74, 1948

110. Thomas, G., *J.I.M.*, vol. 19, pp. 57-63, 1961-62

111. Westengen, H.; Ryum, N., *Z. Metallkde*, vol. 70, pp. 528-535, 1979

112. Jacobs, M. H., *Phil. Mag.*, vol. 26., pp. 1-13, 1972

113. Dumolt, S. D.; Laughin, D. E.; Williams, J. C., *Scripta Met.*, vol. 18, pp. 1347-1350, 1984

114. Porter, D. A.; Easterling, K. E., 'Phase Transformations in Metals and Alloys', 1st Ed., Pub: Chapman-Hall, London, 1981

115. Pashley, D. W.; Rhodes, J. W.; Sendorek, A., *J. Inst. Met.*, vol 94, pp. 41-48, 1966

116. Zhen, L.; Kang, S. B., *Mat. Sci &Tech.*, vol 14 (4), pp. 317-321, 1998

117. Zhen, L.; Kang, S. B.; Kim, H. W., *Mat. Sci. & Tech.*, vol 13(11), pp. 905-910, 1997

118. Fridlyander, I. N.; Sandler, B. S.; Borovskikh, S. N.; Vlaskina, I. I., *Met. Sci. & Heat Treatment*, vol 24, pp.811-814, 1982

119. Romanova, R. R.; Senatorova, O. G.; Uksysinkov, A, N.; Fridlyander, A. N., *Fisika Metallov i Metallovedenie*, vol 80 (4), pp.110-118, 1995 (paper in Russian)

120. Smagorinskii, M. E., *Met. Sci & Heat Trearment*, vol 31(7-8), pp. 539-544, 1989

121. Orowan, E., 'Dislocations in Metals', AIME publication, p. 69, 1954

122. Barry Price, Deeside Aluminium, Personal Communication, 1998

123. Valberg, H; Coenen, F. P.; Kopp, R., *Proc. 6th Int Al Ext Tech Sem*, Aluminium Association, Washington, vol. 2, pp. 113-124, 1996

124. Romana, S.; Zasadzinski, J., *Archivum Hutnictwa*, vol. 28, pp. 231-240, 1983

125. Castle, A. F., PhD. Thesis, University of London, 1974

126. Castle, A. F.; Flory, R.; Gagg, J., *Proc. 4th Int Al Ext Tech Sem*, Aluminium Association, Washington, vol. 2, pp. 25-34, 1988

127. Miles, N.; Evans, G.; Middleditch, A., *J. Mat. Processing Tech.*, vol. 72, pp. 162-176, 1997

128. Baker, B., 'Aluminium Extrusion Die Design', Kaiser Aluminium & Chemical Sales Inc., 1963

129. Nussbaum, A. I., *Light Metal Age*, pp. 8-33, 1990

130. Jonas, J. J.; Sellars, C. M.; McG. Tegart, W. J., *Int. Met. Rev.*, vol. 14, p. 1, 1969

131. McQueen, H. J.; Knustad, O.; Ryum, N.; Solberg, J. K., *Scripta Met.*, vol. 19, pp. 73-78, 1985

132. Scharf, G.; Grzemba, B., *Proc. 3rd Int Al Ext Tech Sem*, Aluminium Association, Washington, vol. 2, pp. 45-48, 1984

133. Bondi, L., *American J. of Physical Chemistry*, vol. 64, p. 444, 1964

134. Sutton, L. (ed.), Special Publications Nos: 11 & 18, The Chemical Society, London 1958, 1965

135. Smithells, C. J., 'Metals Reference Book', 4th Ed., vol. 1, p.140, Pub: Butterworths, London, 1967

136. Pearson, W. B., 'Handbook of Lattice Spacings and Structures of Metals', Pub: Pergamon Press, 1967

137. Barrett, C. S.; Massalski, T. B., 'Structure of Metals: Crystallographic Methods, Principles and Data', 3rd Ed., Pub: Pergamon Press, 1980

138. Taylor, G. I., *Proc. Royal Soc.*, vol. A145, pp. 362-388, 1934

139. Baumgarten, J., *Proc. 3rd Int Al Ext Tech Sem*, Aluminium Association, Washington, vol. 2, pp. 45-48, 1984

140. McQueen, H. J.; Celliers, O., *Canadian Metallurgical Quarterly*, vol. 39, pp. 73-86, 1997

141. Scharf, G., *Proc. Int Al Ext Tech Sem*, Aluminium Association, Washington, pp. 1-18, 1969

142. Wert, J. A., *Proc. 5th Int Al Ext Tech Sem*, Aluminium Association, Washington, vol. 1, pp. 393-401, 1992

143. Evangelista, E.; Gabrielli, F.; Mengucci, P.; Quadrini, E., 'Strength of Metals and Alloys' ICSM A8 (Ed. Kettunen, P. et al.), Pub: Pergamon Press, Oxford, vol. 2, pp. 977-982, 1988

144. Shercliff, H. R.; Ashby, M. F., *Acta Met.*, vol. 38(10), pp. 1789-1802, 1990

145. Shercliff, H. R.; Ashby, M. F., *Acta Met.*, vol. 38(10), pp. 1803-1812, 1990

146. Hains, R. W., *Proc. 2nd Int Al Ext Tech Sem*, Aluminium Association, Washington, vol. 1, pp. 285-291, 1977

147. Gayler, M. L. V.; Preston, G. D.; *J.I.M.*, vol. 1, p. 191, 1929

148. Brenner, P.; Kostron, H., *Z. Metallkde.*, vol. 31, p. 89, 1939

149. Nock, J. A., *Iron Age*, vol. 159, p. 48, 1947

150. Harris, I. R.; Varley, P. C., *J.I.M.*, vol. 82, p. 379, 1953-54

151. Philips, V. A.; *J.I.M.*, vol. 82, p. 625, 1953-54

152. Kawachi, R., *Light Metals (Japan)*, vol. 14, p. 47, 1955

153. Wilm, A., *Metallergie*, vol. 8, p.225, 1911

154. Sheppard, T., *Mat. Sci &Tech.*, vol 4 (7), pp. 635-643, 1988

155. Zhen, L.; Kang, S. B., *Scripta Materialia*, vol 36(10), pp. 1089-1094, 1997

156. Zhen, L.; Sun, D. L., Yang, D. Z.; Cui, Y. X., *Proc. 6th Int Conf on 'Aluminium Lithium Alloys'*. Garmisch-Partnkirchen, Germany, p. 471, 1991

157. Ismail, Z. H., *Scripta Metallurgica et Materialia*, vol. 32(3), pp. 457-462, 1995

158. Fridlyander, I. N., *Met. Sci & Heat Trearment*, vol 22, pp. 564-571, 1980

159. Hatch, J. E., 'Aluminum', pub.: ASM, Metals Park, Ohio

160. Markides, C. A.; Clode, M. P., *Proc. Int. Conf. 'Aluminium 2000'*, Limassol, Cyprus, (1997)

161. Polmear, I. J., 'Light Alloys', pub.: Edward Arnold, London, 1989

162. Baba, Y. Yoshida, H. , *Proc. 2nd Int Al Ext Tech Sem*, Aluminium Association, Washington, vol. 1, pp. 301-306, 1977

163. Hollrigi, G., Bichsel, H. Zoller, H., *Proc. 3rd Int Al Ext Tech Sem*, Aluminium Association, Washington, vol. 1, pp. 125-131, 1984

Chapter 10

Appendices

Appendix A: Experimental Conditions and Results

Smpl. no	wt % Mg	wt % Si	% Fe	Smpl. no	wt % Mg	wt % Si	% Fe
421	0.64	0.42	0.108	501	0.90	0.51	0.707
422	0.63	0.62	0.107	502	0.91	0.70	0.750
423	0.61	1.03	0.107	503	0.89	1.04	0.742
424	0.62	1.53	0.118	504	0.89	1.45	0.761
431	0.68	0.35	0.272	511	1.13	0.61	0.154
432	0.66	0.54	0.307	512	1.16	0.79	0.164
433	0.66	0.94	0.345	513	1.16	1.18	0.166
434	0.66	1.43	0.407	514	1.14	1.48	0.163
441	0.69	0.31	0.538	521	1.18	0.67	0.326
442	0.67	0.49	0.530	522	1.17	0.86	0.347
443	0.66	0.87	0.564	523	1.17	1.27	0.355
444	0.65	1.32	0.579	524	1.14	1.91	0.359
451	0.69	0.35	0.766	531	1.27	0.69	0.524
452	0.67	0.58	0.775	532	1.27	0.83	0.548
453	0.66	0.90	0.781	533	1.25	1.25	0.539
454	0.64	1.30	0.803	534	1.26	1.66	0.557
471	0.01	0.46	0.149	661	0.60	0.36	0.015
472	0.91	0.50	0.155	662	0.60	0.63	0.016
473	0.95	0.79	0.170	663	0.60	1.12	0.018
474	0.93	1.17	0.176	664	0.59	1.60	0.019
481	0.89	0.48	0.319	671	0.90	0.53	0.012
482	0.91	0.70	0.364	672	0.90	0.80	0.013
483	0.91	1.06	0.368	673	0.90	1.26	0.015
484	0.90	1.52	0.386	674	0.90	1.79	0.018
491	0.93	0.52	0.536	702	1.81	1.21	0.006
492	0.94	0.73	0.579	703	1.80	1.49	0.007
493	0.93	1.04	0.577	704	1.80	1.95	0.008
494	0.93	1.42	0.594				

Table A.1. Variable element compositions of the alloys cast for the present study. In all alloys, the balance is aluminium.

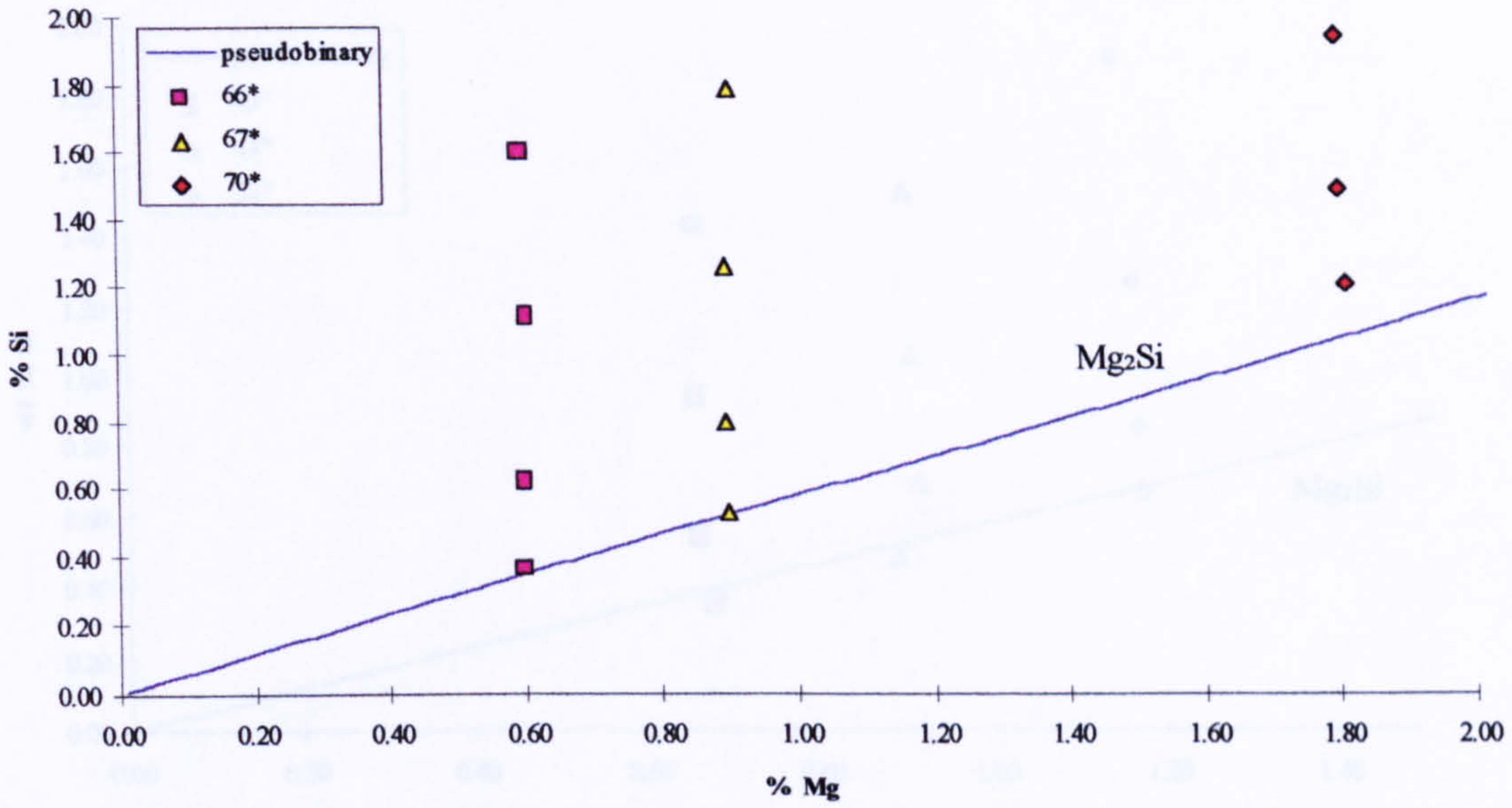

Figure A.1 Compositions of alloys containing no Fe

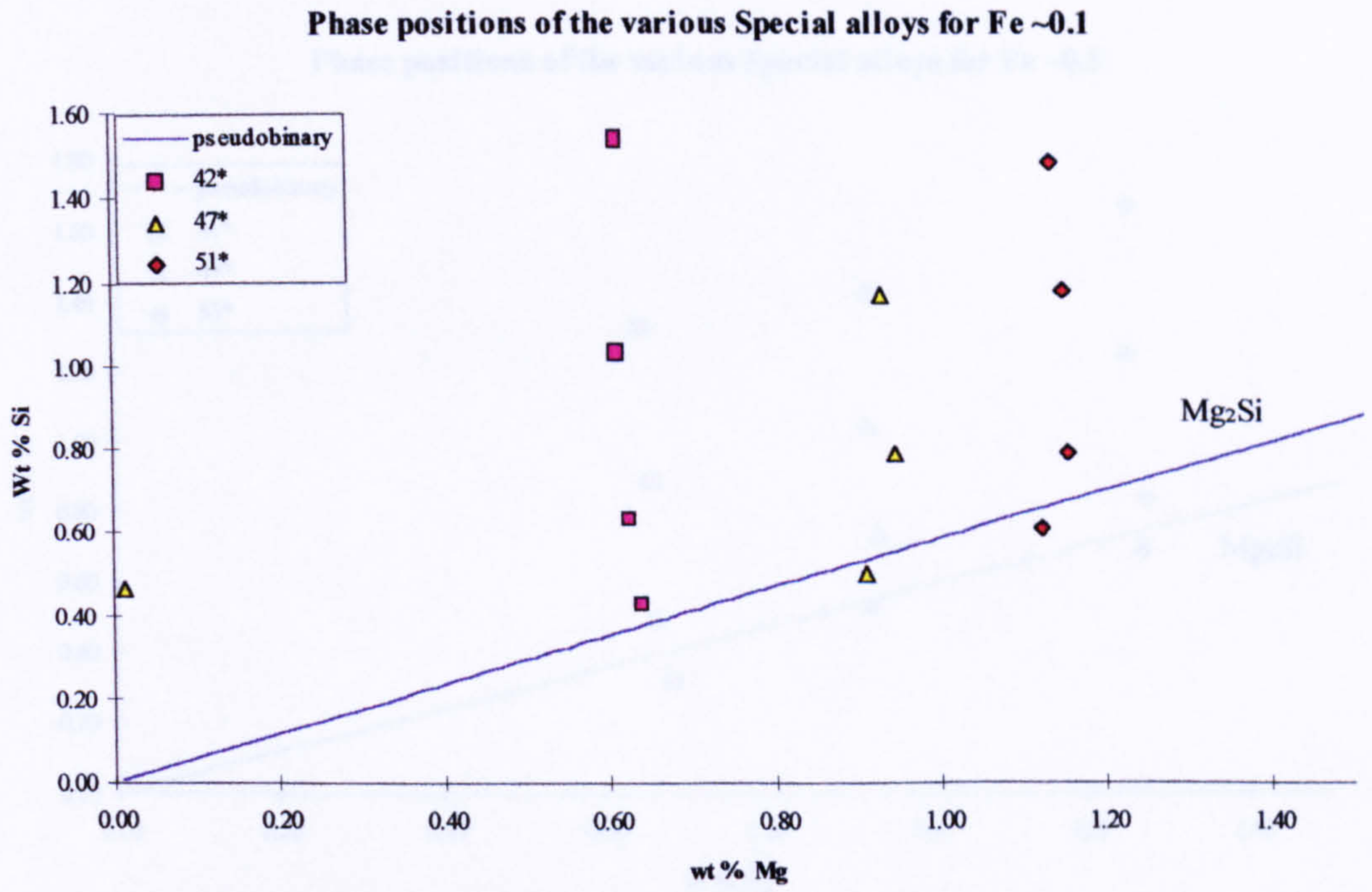

Figure A.2 Compositions of alloys containing 0.1 wt % Fe

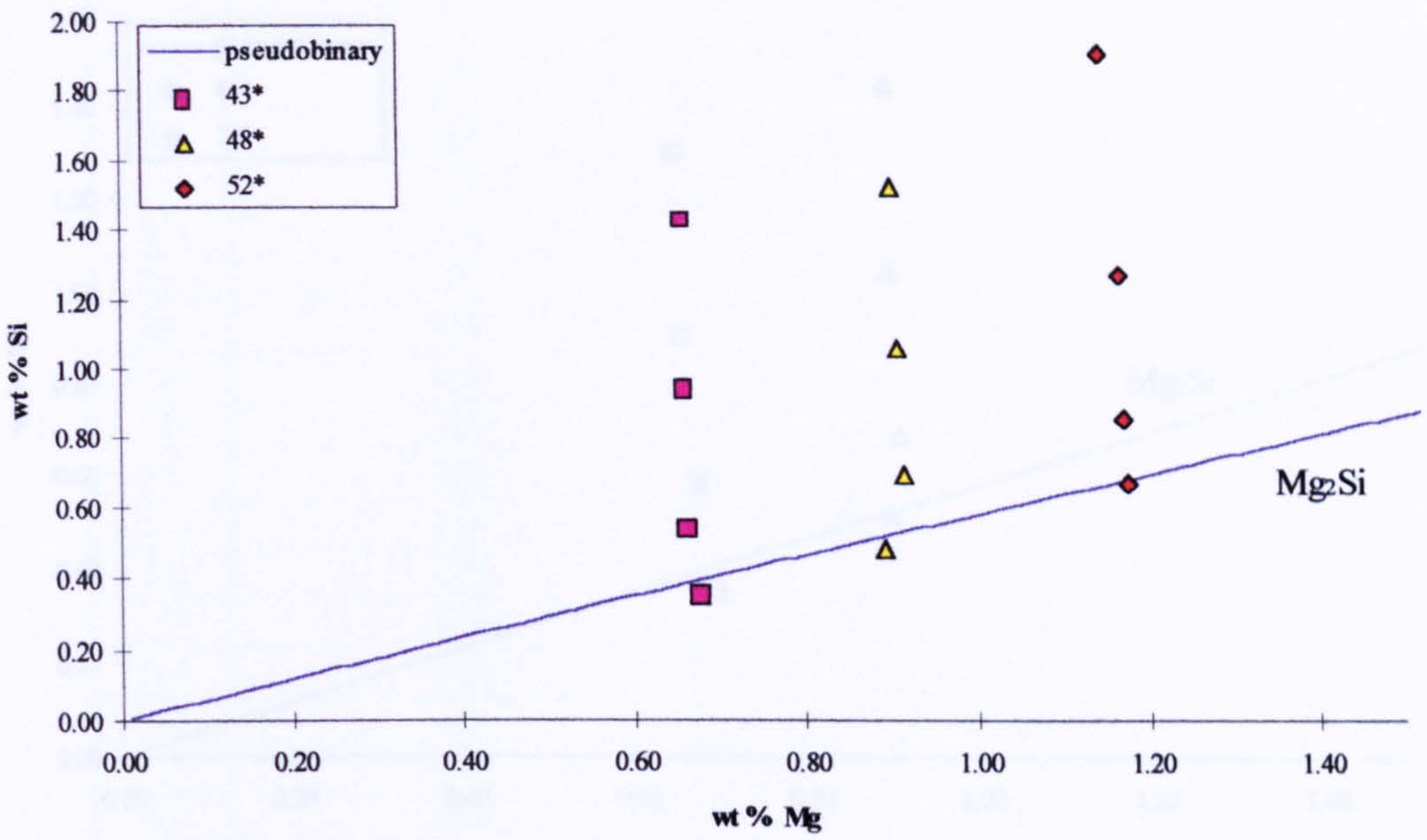

Figure A.3 Compositions of alloys containing 0.35 wt % Fe

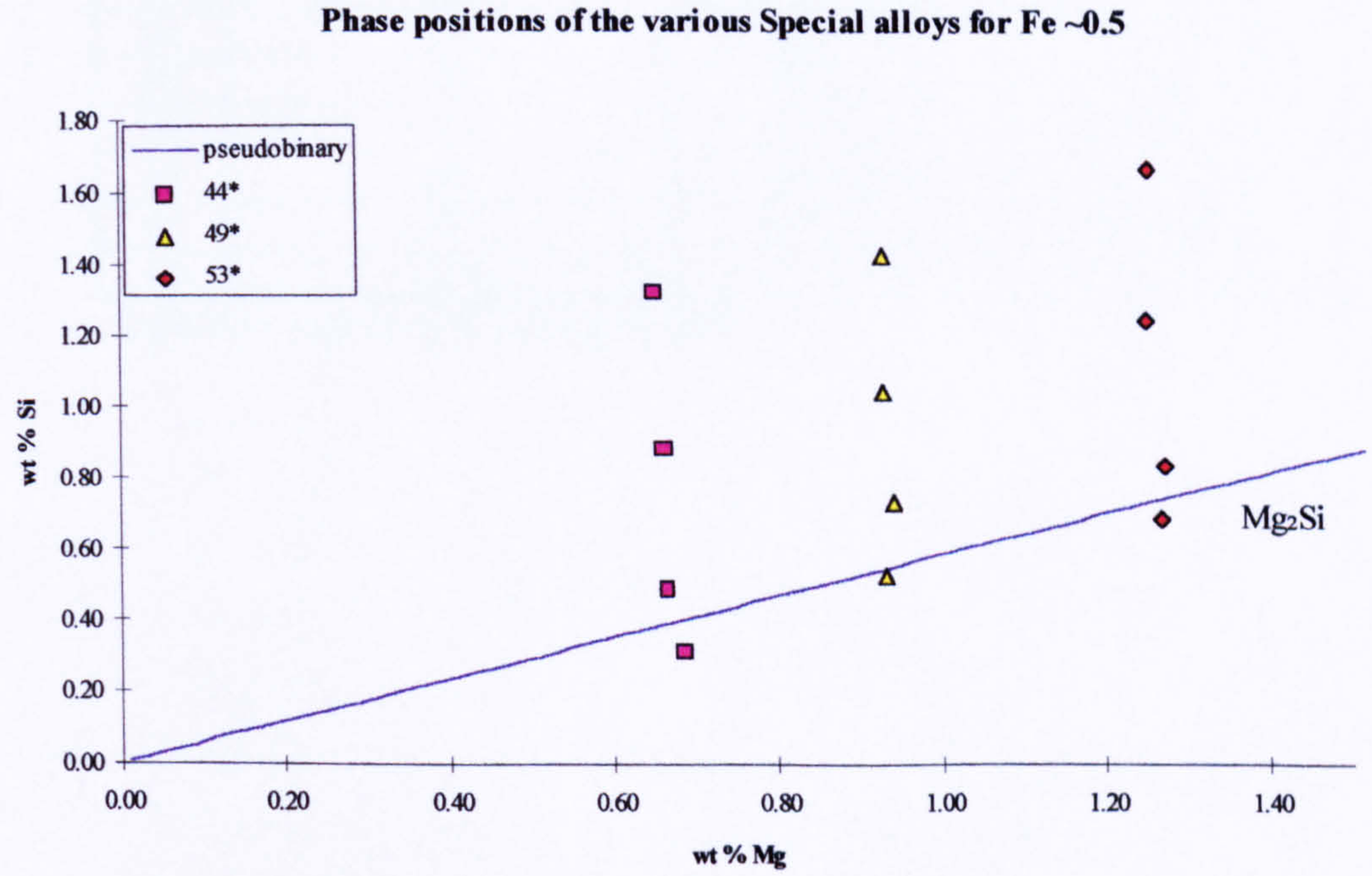

Figure A.4 Compositions of alloys containing 0.5 wt % Fe

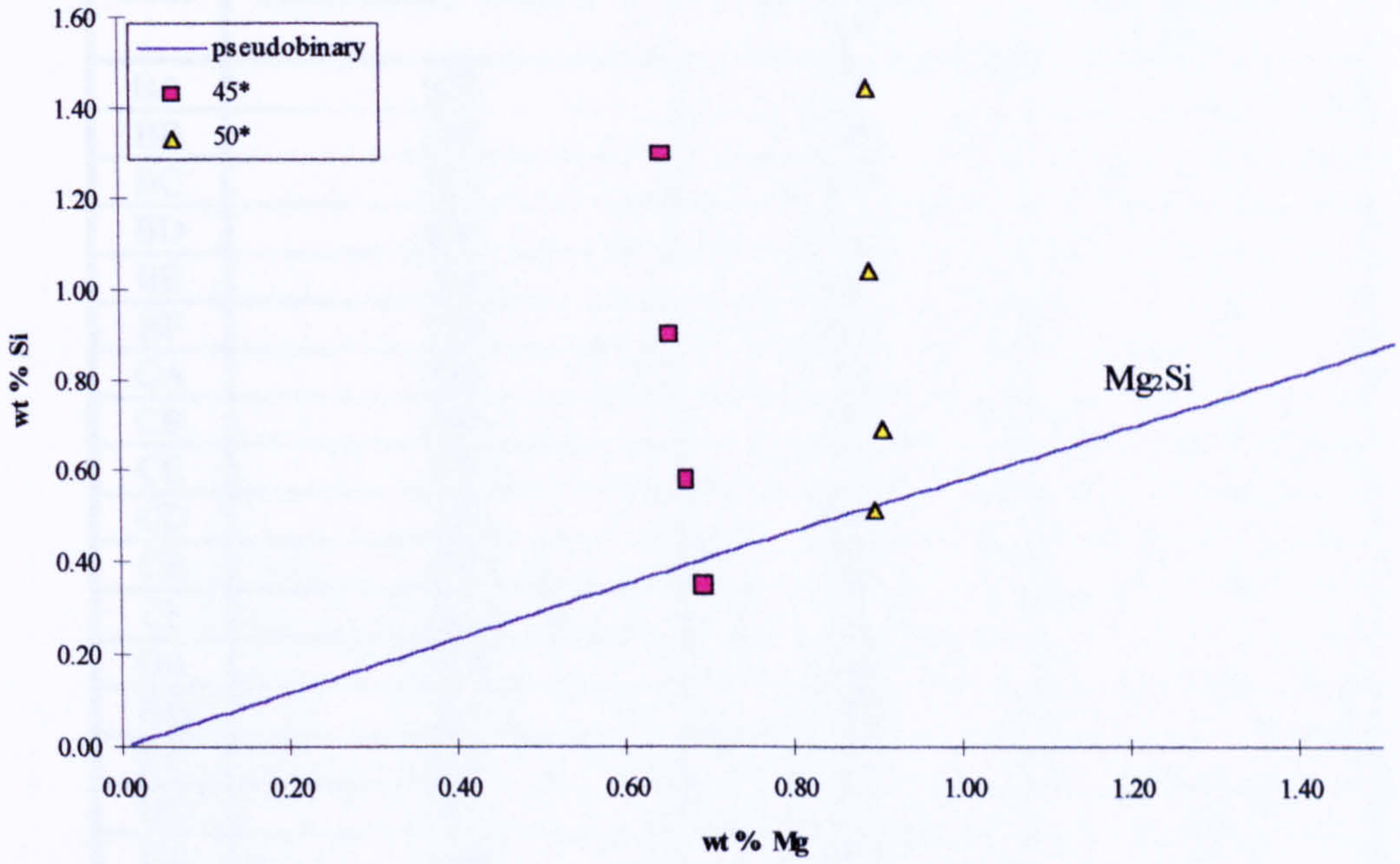

Figure A.5 Compositions of alloys containing 0.75 wt % Fe

Code	Solutionising Temp. (°C)	Ageing Temp 1 (°C)	Ageing Temp 2 (°C)
BA	500	165	-
BB	500	175	-
BC	500	185	-
BD	500	195	-
BE	500	205	-
BF	500	215	-
CA	520	165	-
CB	520	175	-
CC	520	185	-
CD	520	195	-
CE	520	205	-
CF	520	215	-
DA	540	165	-
DB	540	175	-
DC	540	185	-
DD	540	195	-
DE	540	205	-
DF	540	215	-
G2	500	165 (2 hrs)	215 (up to 3)
G3	500	165 (3 hrs)	215 (up to 3)
G4	500	165 (4 hrs)	215 (up to 3)
H2	520	165 (2 hrs)	215 (up to 3)
H3	520	165 (3 hrs)	215 (up to 3)
H4	520	165 (4 hrs)	215 (up to 3)
F2	540	165 (2 hrs)	215 (up to 4)
F3	540	165 (3 hrs)	215 (up to 4)
F4	540	165 (4 hrs)	215 (up to 4)

Table A.2. Ageing combinations utilised

Appendix B: Extrusion Results

extrusion #	Work Done per second (W)	Maximum Load (MN)	Time to peak (s)	Ram Speed (mm/s)	Total Ram Disp. (mm)	Total Test Time (s)	Load (normalised) (MN)
421T	1463855	1.38	1.51	12.02	82.06	6.97	1.3824
422T	1467840	1.42	1	12.13	85.37	7.43	1.4208
423T	1441532	1.38	0.9	12.19	80.56	6.88	1.3824
424T	1233890	1.33	2.65	12.02	34.27	2.85	1.3296
431T	1482673	1.44	1.05	12.01	81.16	6.88	1.4352
432T	1457027	1.41	1.11	12.02	84.47	7.32	1.4064
433T	1397836	1.37	0.96	12.02	81.76	7.02	1.3728
434T	1464429	1.40	0.95	12.01	85.67	7.28	1.4016
441T	1490046	1.50	1	12.07	85.07	7.33	1.5024
442T	1456168	1.44	1	12.07	84.47	7.18	1.44
443T	1399806	1.42	0.85	12.19	88.68	7.43	1.4208
444T	1438181	1.44	0.86	12.14	85.07	7.47	1.44
451T	1578189	1.57	0.9	12.13	85.67	7.43	1.5696
452T	1543352	1.51	0.95	12.07	82.97	7.43	1.5072
453T	1456093	1.44	0.75	12.13	82.67	7.43	1.4448
454T	1495756	1.45	0.95	12.13	79.66	7.43	1.4496
472T	1266033	1.41	3.03	10.26	37.88	3.59	1.4112
473T	1327180	1.46	5.15	10.56	63.73	6	1.464
474T	1408320	1.39	0.85	12.13	83.27	7.43	1.3872
481T	1481305	1.48	0.8	12.13	82.67	7.43	1.4832
482T	1457987	1.44	0.85	12.07	82.36	7.43	1.44
483T	1461903	1.42	0.96	12.02	83.57	7.48	1.4208
484T	1452429	1.44	0.75	12.19	82.06	7.43	1.4448
491T	1559975	1.53	0.96	10.24	79.96	8.18	1.5312
492T	1487747	1.50	0.96	12.14	85.07	7.12	1.5024
493T	1429187	1.43	0.8	12.19	81.16	6.93	1.4304
494T	1446821	1.44	0.81	12.02	86.27	7.07	1.4448
501T	1524126	1.54	0.86	12.14	81.76	7.07	1.5408
502T	1494919	1.50	1.01	12.08	88.98	7.02	1.4976
503T	1437626	1.43	0.86	12.27	80.86	6.82	1.4256
504T	1468143	1.45	0.9	12.13	84.17	6.99	1.4544
511T	1596328	1.56	0.9	12.13	87.47	7.74	1.5552

512T	1551562	1.54	0.91	12.14	86.87	7.63	1.536
513T	1470922	1.44	0.8	12.19	82.97	7.14	1.4448
514T	1478299	1.44	0.81	12.26	82.36	7.68	1.4448
521T	1550451	1.55	0.91	12.02	84.17	7.33	1.5456
522T	1584480	1.54	0.9	12.13	84.17	7.13	1.5408
523T	1481103	1.49	0.75	12.19	84.47	7.63	1.488
524T	1493255	1.47	0.9	12.07	84.77	7.18	1.4688
531T	1647082	1.62	0.9	12.25	84.77	7.38	1.6224
532T	1655545	1.62	0.95	12.19	86.57	7.79	1.6176
533T	1539764	1.49	0.95	12.19	84.47	7.13	1.488
534T	1566392	1.52	0.85	12.19	82.36	7.23	1.5216
661T	1510611	1.42	2.02	11.49	78.46	8.33	1.416
662T	1493486	1.36	2.13	12.13	83.57	7.28	1.3632
663T	1419688	1.32	0.95	12.13	84.77	7.58	1.32
664T	1492511	1.38	1.66	12.17	82.97	7.08	1.3776
671T	1505482	1.43	0.81	12.08	85.97	7.32	1.4304
672T	1489945	1.37	1	12.13	83.57	7.33	1.3728
673T	1460427	1.34	1.52	12.11	82.06	7.22	1.344
674T	1497171	1.39	0.96	12.02	84.47	7.33	1.392
702T	1464657	1.39	0.91	12.08	84.17	7.12	1.392
703T	1495629	1.42	1.01	12.08	86.57	7.33	1.4208
704T	1484160	1.42	0.85	12.08	79.06	7.17	1.416

Table B.1. Extrusion parameters for all special alloys extruded through die 1.

extrusion #	Work Done per second (W)	Maximum Load (MN)	Time to peak (s)	Ram Speed (mm/s)	Total Ram Disp. (mm)	Total Test Time (s)	Load (normalised) (MN)
421M	1450762	1.40	0.96	12.02	85.37	7.42	1.440845
422M	1493661	1.42	1.05	12.01	81.76	6.93	1.455648
423M	1416859	1.37	1.1	12.07	86.57	7.43	1.406304
424M	1411579	1.36	1.15	12.07	83.87	7.43	1.396435
431M	1518994	1.47	0.86	12.02	77.86	6.82	1.509926
432M	1460842	1.44	1.1	12.07	84.47	7.58	1.475386
433M	1437297	1.44	0.96	12.20	82.06	7.58	1.48032
434M	1469229	1.45	0.71	12.14	78.16	6.87	1.490189
441M	1539739	1.51	0.95	12.07	77.86	7.03	1.554336
442M	1504749	1.49	0.9	12.13	80.86	7.08	1.534598
443M	1429592	1.43	0.8	12.13	85.07	7.43	1.465517
444M	1524581	1.46	0.9	12.01	83.27	7.43	1.500058
451M	1593196	1.56	1	12.07	84.77	7.43	1.60368
452M	1551006	1.53	0.9	12.07	84.47	7.43	1.569139
453M	1500884	1.48	0.9	12.07	83.27	7.43	1.52473
454M	1492724	1.46	0.85	12.07	82.67	7.43	1.500058
472M	1558257	1.50	0.96	11.90	83.87	7.48	1.539533
473M	1563992	1.50	1	12.07	82.67	7.43	1.544467
474M	1460867	1.44	0.85	12.07	86.87	7.43	1.485254
481M	1486181	1.45	0.96	12.08	86.57	7.48	1.495123
482M	1494341	1.50	0.9	12.13	85.07	7.43	1.539533
483M	1464707	1.44	0.9	12.19	83.57	7.43	1.485254
484M	1455916	1.41	0.85	12.07	84.77	7.43	1.450714
491M	1581474	1.56	0.95	12.13	84.47	7.33	1.608614
492M	1572328	1.56	0.9	12.19	89.58	7.43	1.60368
493M	1534686	1.53	0.85	12.13	85.67	7.53	1.574074
494M	1519301	1.49	0.9	12.13	85.97	7.23	1.534598
501M	1635613	1.60	0.9	12.13	81.76	7.23	1.64809
502M	1577987	1.55	0.86	12.08	82.67	7.43	1.588877
503M	1513011	1.52	0.85	12.13	85.07	7.33	1.55927
504M	1542644	1.55	0.96	12.08	84.77	8.34	1.593811
511M	1594611	1.58	0.95	12.07	83.57	7.54	1.628352

512M	1582636	1.55	0.91	12.02	84.77	7.28	1.588877
513M	1479714	1.45	0.9	12.13	85.37	7.39	1.490189
514M	1500354	1.45	0.95	12.13	84.17	7.13	1.495123
521M	1597844	1.56	1	12.01	82.06	7.33	1.60368
522M	1550021	1.53	0.91	11.96	84.17	7.77	1.569139
523M	1479815	1.50	0.91	12.02	85.97	7.88	1.544467
524M	1495503	1.50	0.85	12.06	82.97	7.88	1.539533
531M	1674644	1.65	0.95	12.19	82.36	7.14	1.697434
532M	1734240	1.68	1	12.19	85.07	7.23	1.72704
533M	1608531	1.61	0.95	12.19	85.07	7.29	1.657958
534M	1565406	1.57	0.9	12.25	85.37	7.23	1.613549
661M	1542420	1.41	2.02	12.09	81.76	7.33	1.445779
662M	1526892	1.40	1.97	12.10	85.97	7.18	1.43591
663M	1514348	1.40	1.72	12.11	82.97	7.67	1.440845
664M	1483009	1.37	1.25	12.27	78.16	6.93	1.411238
671M	1539840	1.47	0.96	12.08	84.17	7.07	1.509926
672M	1533928	1.45	0.85	12.07	83.27	7.23	1.490189
673M	1472792	1.39	0.75	12.19	79.06	7.9	1.430976
674M	1499975	1.42	1.11	12.02	83.57	7.72	1.460582
702M	1488884	1.42	0.8	12.13	78.16	6.94	1.460582
703M	1530594	1.46	0.95	12.19	79.96	7.29	1.504992
704M	1545549	1.49	0.8	12.07	79.66	7.28	1.529664

Table B.2. Extrusion parameters for all special alloys extruded through die 2.

extrusion #	Work Done per second (W)	Maximum Load (MN)	Time to peak (s)	Ram Speed (mm/s)	Total Ram Disp. (mm)	Total Test Time (s)	Load (normalised) (MN)
421B	1461474	1.40	0.96	12.02	81.16	7.43	1.475021
422B	1447453	1.39	1	12.13	81.76	7.43	1.464883
423B	1481457	1.36	0.9	11.95	84.17	7.43	1.439539
424B	1477314	1.38	1	12.01	84.77	7.44	1.454746
431B	1526072	1.46	1.12	11.96	84.17	7.28	1.540915
432B	1462282	1.39	0.95	12.01	83.27	7.43	1.469952
433B	1435225	1.40	0.96	12.08	82.36	7.48	1.48009
434B	1474838	1.44	0.85	12.07	84.77	7.29	1.515571
441B	1564952	1.53	1	12.07	88.68	7.58	1.611878
442B	1551638	1.50	1.05	12.01	81.46	7.43	1.581466
443B	1436362	1.44	0.8	12.19	82.67	7.43	1.52064
444B	1485600	1.49	0.9	12.13	83.57	7.43	1.571328
451B	1590695	1.58	0.91	11.96	81.46	7.48	1.667635
452B	1603149	1.55	0.85	12.01	81.76	7.43	1.637222
453B	1531832	1.49	0.95	12.01	82.67	7.43	1.576397
454B	1495402	1.51	0.85	12.07	81.46	7.44	1.596672
472B	1569272	1.54	0.95	12.01	82.36	7.43	1.622016
473B	1555377	1.52	1.1	12.01	80.26	7.43	1.601741
474B	1479486	1.50	0.95	12.07	83.87	7.23	1.586534
481B	1507074	1.48	0.95	12.19	85.37	7.43	1.566259
482B	1476531	1.47	0.86	12.08	83.57	7.48	1.556122
483B	1515057	1.48	0.8	12.07	82.97	7.43	1.566259
484B	1507326	1.49	0.9	12.13	83.27	7.43	1.571328
491B	1712780	1.60	0.91	12.11	70.94	6.29	1.68791
492B	1662527	1.58	0.85	12.09	71.54	6.26	1.667635
493B	1546105	1.49	0.81	12.08	69.74	6.97	1.576397
494B	1575923	1.54	0.91	12.08	72.75	6.87	1.622016
501B	1683714	1.62	1	12.19	82.97	7.38	1.713254
502B	1619596	1.57	0.95	12.19	82.36	7.18	1.657498
503B	1547242	1.49	0.96	12.08	84.17	7.73	1.576397
504B	1580766	1.57	0.85	12.19	79.36	7.14	1.657498
511B	1635916	1.56	1.05	12.13	84.47	8.29	1.652429

512B	1592463	1.53	1.1	12.07	82.06	7.18	1.616947
513B	1531685	1.43	0.95	12.07	76.65	6.93	1.510502
514B	1537516	1.45	1	12.13	83.57	7.28	1.530778
521B	1618712	1.58	1.1	12.13	85.97	7.33	1.667635
522B	1641297	1.58	0.9	12.07	81.76	7.33	1.667635
523B	1564674	1.53	0.95	12.13	82.97	7.28	1.611878
524B	1565179	1.53	0.95	12.13	83.57	7.13	1.611878
531B	1687478	1.66	0.95	12.13	85.37	7.28	1.748736
532B	1682147	1.61	0.95	12.13	83.57	7.74	1.698048
533B	1569726	1.53	0.81	11.85	66.73	7.28	1.611878
534B	1562072	1.54	0.95	12.13	82.97	7.48	1.622016
661B	1548456	1.40	1.92	11.95	84.17	7.18	1.475021
662B	1499267	1.37	1.26	12.08	81.76	7.42	1.444608
663B	1481406	1.38	0.85	12.08	79.06	7.82	1.459814
664B	1476707	1.39	0.95	12.13	78.76	7.49	1.464883
671B	1510686	1.43	0.85	12.13	82.36	7.28	1.510502
672B	1516345	1.42	0.9	12.07	79.36	6.99	1.500365
673B	1529179	1.44	0.91	12.08	82.97	7.28	1.515571
674B	1549011	1.44	1.26	12.01	83.57	7.34	1.525709
702B	1488657	1.43	0.9	12.19	84.77	7.13	1.510502
703B	1506695	1.44	0.91	12.08	85.97	7.27	1.525709
704B	1562400	1.49	0.91	12.02	80.26	7.17	1.576397

Table B.3. Extrusion parameters for all special alloys extruded through die 3.

extrusion #	Work Done per second (W)	Maximum Load (MN)	Time to peak (s)	Ram Speed (mm/s)	Total Ram Disp. (mm)	Total Test Time (s)	Temperature (° C)
SP01	1563411	1.5552	0.86	12.20	84.47	7.98	450
SP02	1561339	1.4928	1.21	10.74	83.57	8.13	450
SP03	1544968	1.4496	1.46	8.46	81.16	10.13	450
SP04	1501819	1.4064	5.22	5.34	85.07	16.34	450
SP05	1474080	1.3488	5.66	3.54	82.06	25	450
SP06	1501162	1.3632	8.52	2.10	81.76	40.32	450
TEMP01	2545465	2.6304	1.2	12.19	83.57	7.38	350
TEMP02	1965297	1.92	1.01	12.08	80.86	7.07	400
TEMP03	1558080	1.5024	0.76	12.08	83.87	7.28	450
TEMP04	1334223	1.2672	0.66	12.11	82.67	7.57	500
TEMP05	1249213	1.176	0.66	12.14	82.36	7.43	525
TEMP06	1223489	1.152	1.61	12.22	87.47	7.59	550

Table B.4. Extrusion parameters for alloys extruded through die 1, at different speeds and temperatures.